Structures and Stabilities of Nanocrystalline Materials Synthesized by Mechanical Alloying and Modeled as Driven Alloys

Thesis by
Liubo Hong

In Partial Fulfillment of the Requirements
for the Degree of
Doctor of Philosophy

California Institute of Technology
Pasadena, California

1996
(Submitted December 1995)

To my parents
and my wife

Acknowledgments

First and foremost, I would like to express my great and sincere gratitude to my advisor, Professor Brent Fultz. Without his numerous advice and inspiration, constant support and encouragement, this thesis study would not have been possible. His enthusiasm toward and enjoyment of scientific research, and his hard working with joys have been my examples to follow over the years. The years would otherwise have been much longer in both real and relative time units. He is also a good friend to share with, and helped to initiate my push for improving my spoken English in the past one and half years. It has been both a great pleasure and a privilege to be a member of his highly talented and productive group.

I would also like to express my gratitude to Professor William L. Johnson. Throughout my entire graduate study at Caltech, I have enjoyed his constant support and inspiration, through being both a TA or student of his class, and a RA on the nanocrystalline materials project he shared with Professor Brent Fultz and Dr. Channing Ahn. Discussions and chatting with him are not merely pleasant, but stimulating and inspiring as well.

My special gratitude also goes to Dr. Channing Ahn for his support on the project and hands-on teaching and help in the lab. Working with him has been both productive and pleasant. I am appreciative to Mrs. Carol Garland for teaching and helping me with electron microscopes, and to Mrs. Pam Albertson for her assistance in numerous ways.

Many thanks are due to the present and past Fultz group, especially Dr. Zheng-Qiang Gao, Dr. Lawrence Anthony, Dr. Tab Stephens, Dr. Ouyang Hao, Dr. Tim Lindsey, Dr. James Okamoto, Laura Nagel, Charles Whitham, and Professor Chandrahas

Bansal. Collaborating and working with them made my research both more productive and more fun. They are also great resources for help in both my research and my personal life. I would also like to thank Dr. Mohit Jain and various past and present Johnson group members, especially Dr. Yoshi Abe, Dr. Zezhong Fu, Dr. David Lee, Dr. Mo Li, Dr. Marissa La Madrid, Dr. Carl Krill III, Xianghong Lin, Jianzhong Li, Dr. Ralf Busch, Dr. Susanne Schneider, and Professor R. Birringer for their help and friendship.

I would like to thank my friends Dr. Wenbo Yang, Dr. Zhiqiang Alex Zheng, Dr. Wen Jiang, Dr. Zhen Hu, Dr. Weishi Huang, Dr. Xiaodong Song, Dr. Haiming Liang, Dr. Zeng Zheng, Yu Cao, Guangqing Chen, Mei Bin, Qianli Liu, Yibo Jiang for their help and friendship. I would like to thank Mr. and Mrs. Roger Luo, the Woodburry family, the Sun family, my English tutor Mr. Larry Bardwell, Cindy and Charles Lei, and many other friends out of school for their long time support and friendship.

I would like to express my special gratitude to my teachers at my elementary and high schools, especially my high school physics teacher and long time friend Mrs. Xialin Gong, and Mrs. Jinyin Qi, Mr. Zhe Yu and Mr. Xiaoyang Zhou (both passed away 8 years ago). Meeting my demand for knowledge has taken away a great deal of their spare time.

Finally, my never-ending gratitude goes to my parents. During those starving years with an 8 cent wage for 12 hours hard labor, they sold grains and edible oils out of the limited quota and with the risk of confiscation to send their 5 sons and 2 daughters to school, and 3 through college. They set my lifetime examples to be honest, to be proud, to set high goals, to work hard, and to achieve what is impossible. I am especially grateful to my second brother and 2 sisters for supporting their younger brothers through college education both morally and financially without any reservation, and to all my brothers and sisters for sharing hardship and joys with each other.

My ever-lasting gratitude goes to my wife Nalin for building up a happy family with me and supporting my study whole-heartedly. Her love and care are my source of strength. By taking care of almost all the house work besides her job, she contributes a great deal to my high productivity at study. I am thankful to my parents-in-law for caring for our daughter Rachel, and to Rachel for bringing blessings to her parents and grandparents.

Abstract

Nanocrystalline materials (NCM) are single-phase or multi-phase polycrystalline materials with crystal sizes in the nanometer range (2-20 nm). Owing to their very small grain size, NCM have enhanced or novel physical and mechanical properties compared to conventional materials, making NCM attractive for various technical applications. Mechanical alloying (MA) is now one of the most commonly used methods to synthesize NCM, among other far-from-equilibrium materials. During mechanical alloying, nanocrystalline materials are sustained in nonequilibrium states by continuous external driving (e.g., collisions, shearing, fracturing, welding, etc.), and can be studied as driven alloys – a simplified model that grasps the essentials of external driving in a general way. In this thesis study, the structures and thermal stabilities of nanocrystalline materials synthesized by mechanical alloying were studied by experimental techniques, and were modeled as driven systems by Monte Carlo simulations.

A general introduction to nanocrystalline materials is given in Chapter 1 and discusses their structures, synthesis methods, characterization techniques, properties and technical applications. In parallel, introductions on phase transformations, driven alloys, and Monte Carlo simulations are given in Chapter 2. Our theoretical and simulational work on critical temperature of ordering transformations of driven square alloys is presented in Chapter 3, while the study on the ordering kinetics and low temperature phase diagrams of driven bcc alloys is presented in Chapter 4. We found that the ballistic (random) atom movements, caused by external driving, suppressed the critical temperature of ordering on square lattices. The decrease in critical temperature was linear only at small driving intensity. The ballistic atom movements also changed both the transient states and the steady states of ordering of bcc alloys. The stability of B32 order was increased with

respect to the stabilities of B2 order and an unmixed state because of the smaller defect enthalpy sustained in B32 phase. In steady state, the B32 phase region encroached into adjacent B2 or unmixed phase regions, and regions of two-phase coexistence were formed. The changes were significant and nonintuitive, and provided useful guidance to the experimental studies presented in Chapter 5, 6, and 7.

In the experimental studies described in Chapters 5, 6, and 7, we studied how the microstructures of NCM prepared by MA depended on milling intensity, temperature, and composition (I, T, c). We found: (1) I — The intensity of MA had little effect on the average grain size or strain, but changed the phase boundaries of Fe-Ni nanocrystalline materials drastically and in nonintuitive ways. Similar to what was found in Monte Carlo simulations, a region of bcc plus fcc two-phase coexistence occurred from MA, and shifted asymmetrically to the bcc side with increased milling intensity. This was attributed to the larger heterogeneities in free energy density in the alloy at higher MA intensity. (2) T — Mechanical alloying of Ni_3Fe and Fe_3X (X=Si, Zn, Sn) at temperatures from 23 °C to 300 °C showed that the effect of milling temperature was little different from the role of temperature itself on the microstructure of NCM. (3) c — The same Hume-Rothery rules for 5% solubility in equilibrium alloys translated to a 25% solubility in nanocrystalline materials Fe_3X (X=Al, As, Ge, In, Sb, Si, Sn, Zn) prepared by MA. Also observed was the transient DO_3 ordering of NCM Fe_3Ge prepared by MA upon annealing at high temperature.

Table of Contents

List of Figures

Chapter 1

Chapter 2

Chapter 3

Chapter 4

Chapter 5

Chapter 6

List of Tables

List of Publications

1. L. B. Hong and B. Fultz, Phys. Rev. B **51**, 2687 (1995).

2. L. B. Hong and B. Fultz, Phys. Rev. B **52**, (1995).

3. L. B. Hong, L. Anthony, and B. Fultz, J. Mater. Res. **10**, 126 (1995).

4. L. B. Hong, C. C. Ahn, and B. Fultz, "The Debye Temperature of Nanocrystalline β-Sn Measured by X-ray Diffraction", J. Mater. Res. **10** (10), (1995).

5. L. B. Hong, C. Bansal, and B. Fultz, Nanostructured Materials, **4**, 949 (1994).

6. C. Bansal, Z.Q. Gao, L. B. Hong, and B. Fultz, J. Appl. Phys.**76**, 5961 (1994).

7. C. C. Ahn, L. Hong, J. Eckert, B. Fultz, and W. L. Johnson, "Energy Filtered Imaging of Nanophase Materials", Proc. 50th Annual Electron Microscopy Society of America, G. W. Bailey, J. Bentley, and J. A. Small Eds. 1196 (Boston, 1992).

8. C. C. Ahn and L. B. Hong, "Ballistic Consolidation of Nanophase Sn Prepared by Inert Gas Condensation", submitted to Nanostructured Mater., 1994.

9. L. B. Hong and B. Fultz, "The Kinetics and Steady States of Driven Systems with Thermodynamic Tendency of Phase Separation", in revision.

10. L. B. Hong and B. Fultz, "Two-Phase Coexistence in Fe-Cu Alloys Prepared by Ball Milling at Two Intensities", in preparation.

11. B. Fultz, C. C. Ahn, S. Spooner, L. B. Hong, J. Eckert, and W. L. Johnson, "Thermal Stability of Nanophase Fe-Cu Alloys Prepared by Mechanical Alloying", submitted to Metall. Trans. A, 1995.

12. L. B. Hong and B. Fultz, "Two-Phase Coexistence in Fe-Ni Alloys Synthesized by Ball Milling at Two Intensities", submitted to J. Appl. Phys, 1995.

Chapter 1. Nanocrystalline Materials

1.1 Introduction to Nanocrystalline Materials

The thermodynamic equilibrium state of a metal or alloy at low temperatures is a perfect crystal, i.e. a three-dimensional periodic array of atoms. However, all engineering materials in service are somewhat out of thermodynamic equilibrium. Great interest has focused on highly nonequilibrium materials since Pol Duwez first synthesized metallic glasses by rapid quenching at Caltech in 1960 [1]. New experimental techniques have been developed to prepare a variety of materials far from thermodynamic equilibrium, such as metallic glasses, nanocrystalline materials, and disordered solid solutions.

Nanocrystalline materials (NCM) [2-7] are single- or multi-phase polycrystalline materials with crystal sizes on the order of nanometers. Because of their very small crystal sizes, nanocrystalline materials have novel physical properties. The property of interest is useful for defining the characteristic size of a nanocrystal, but often this size is 10 nm or below.

A schematic section showing atomic arrangements in a nanocrystalline material is shown in Fig. 1.1 [2-6]. Here we are concerned with atomic arrangement only. There are two types of atoms. The atoms in black are inside individual grains, and have regular nearest neighbor atom configurations. The atoms in white are at grain boundaries and have different nearest neighbor configurations. While the local atomic structure of all atoms in grains of the same phase is identical, the local atomic structures of atoms at and near the grain boundaries are different because the orientation relationships between adjacent grains are different.

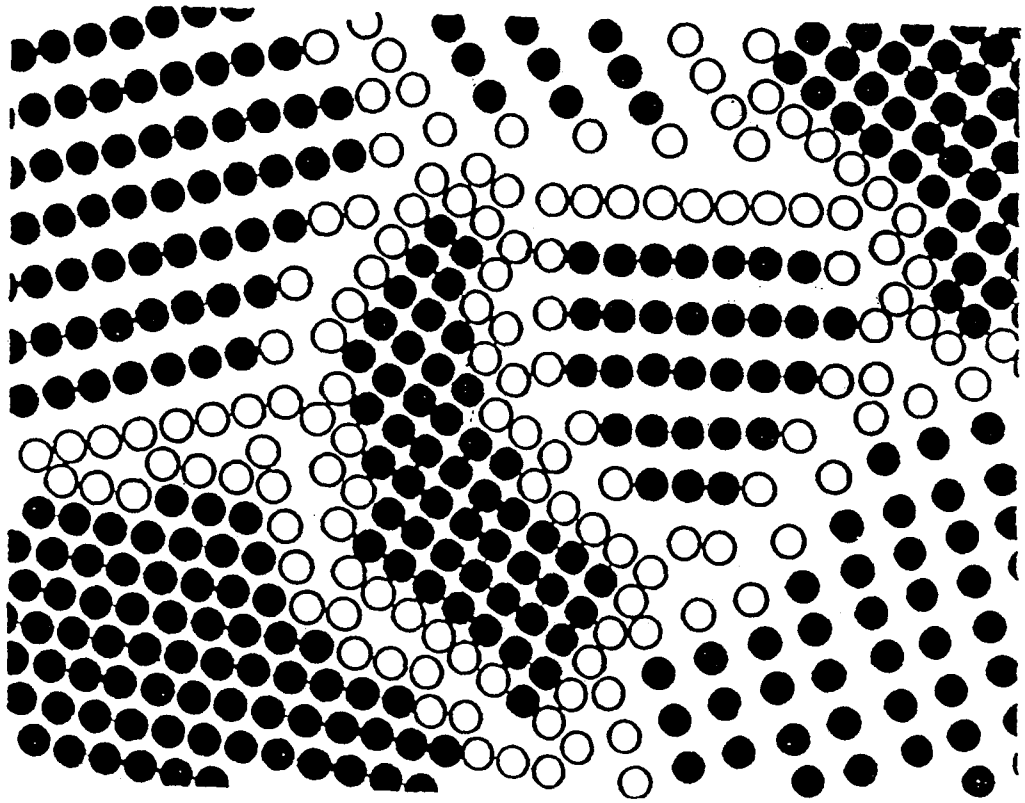

FIG. 1.1. A schematic cross-sectional representation in a hard sphere model of a nanocrystalline material distinguishing between the atoms inside grains (black) and at the grain boundaries (white). The atoms at grain boundaries are shown in regular lattice positions but in reality may relax to form different atomic arrangement [2-6].

Nanocrystalline materials with equiaxed grains belong to a more general class of materials termed Nanostructured Materials (NSM). Nanostructured materials can have nanostructure in one dimension (layered), two dimensions (filamentary or rod-shaped), or three dimensions (equiaxed) [5]. In each case, the small dimensions lead to novel or enhanced physical and mechanical properties compared to conventional crystalline materials. Depending on the chemical composition profile, NSM can be grouped into four families. The chemical composition can be homogeneous all across the crystallites and interfaces, or different for different crystallites (e.g. quantum well structures), or different only between crystallites and interfaces (e.g., after grain boundary chemical segregation in a homogeneous NSM). The fourth family of NSM is formed by nm-sized crystallites (layered, filamentary, or equiaxed) dispersed in a matrix of different chemical composition (e.g., precipitation hardened alloys). Fig. 1.2 summarizes various types of NSM classified according to their dimensionality (shape) and chemical composition profile [7]. In addition, if the core components are glasses instead of crystallites (e.g., in Fig. 1.1, the black atoms form glassy structures instead of crystalites), the material is termed a nanoglass [2-4].

1.2 Synthesis of Nanocrystalline Materials

In principle, any method suitable for preparing a polycrystalline material with a crystal size of a few nanometers and a random texture may be utilized to synthesize nanocrystalline materials. The original inert gas condensation method used by Gleiter et. al., is still used widely. Nevertheless, mechanical attrition by high energy ball milling has become the most frequently used method to synthesize nanocrystalline materials.

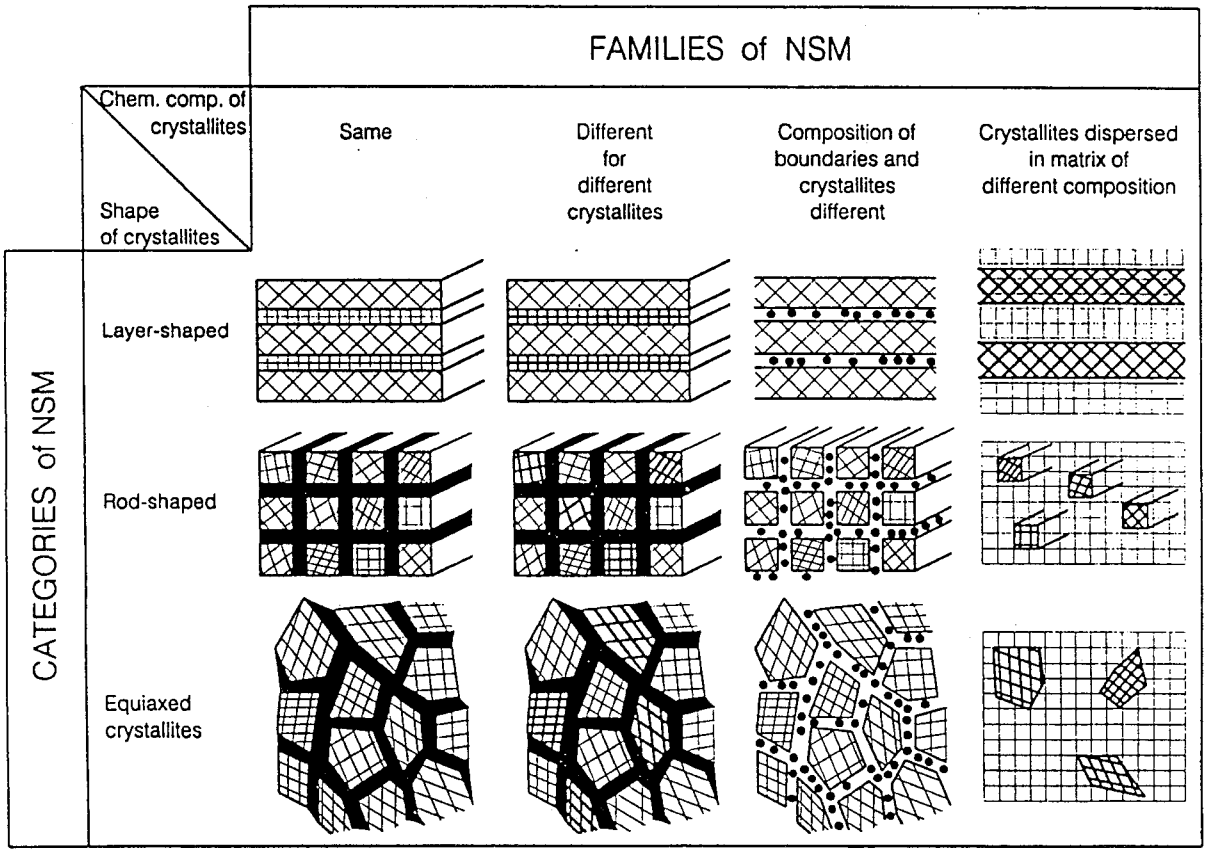

FIG. 1.2. Various types of nanostructured materials (NSM) classified according to their dimensionality (shape) and chemical composition profile [7].

1.2.1 Gas Condensation

The inert gas condensation method [2-4, 6] first used by the Gleiter group includes two steps: generating nanometer-sized clusters, and assembling the clusters by *in-situ* consolidation and sintering. A typical apparatus consists of a gas-condensation chamber and powder consolidation cell as shown schematically in Fig. 1.3 [2-6]. The UHV vacuum chamber is first evacuated and then back-filled with a controlled high purity gas atmosphere at pressures of a few Torr. For producing metal or alloy powders, the gas is typically inert gas, such as He or Ar. N_2 and gas mixtures (H_2 + He) have also been used. Alternatively, a reactive gas or gas mixture can also be used to produce nanometered clusters of ceramic compounds such as oxides. The grain size depends on various experimental parameters, including the gas type, the gas pressure, and the evaporation rate.

During the evaporation of the precursor materials from sources A and/or B, atoms condense into clusters in the supersaturated region close to the Joule-heated sources. The clusters are transported via convection to the liquid-nitrogen cooled cold finger, where they are collected via thermophresis. The clusters deposited on the cold finger are subsequently scraped from the cold finger, collected into a funnel, and consolidated first by a low-pressure compacting device and then by a high-pressure compacting device.

There exist variations of the gas condensation method. Fig. 1.4 depicts schematically our two-chamber system capable of gas condensation in a dynamic flow gas environment [8]. This equipment permits ballistic consolidation of the powders, avoiding the need for mechanically compressing them into a solid. The evaporation chamber and the deposition chamber are connected through a nozzle of small diameter (3 mm to 10 mm). The gas (typically He) flows in the evaporation chamber and is evacuated from the deposition chamber by a Roots pump with a pumping speed of 80 liters/sec and a base pressure below 10^{-5} Torr. A relatively large pressure difference is maintained between the

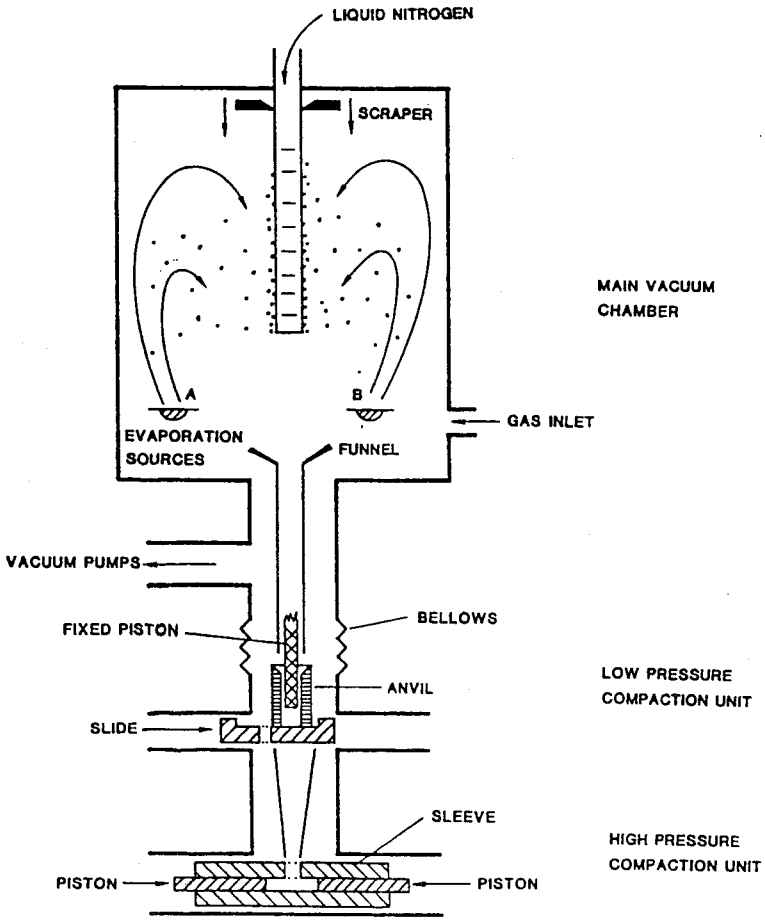

FIG. 1.3. A schematic drawing of a gas-condensation system for the synthesis of nanocrystalline materials [6].

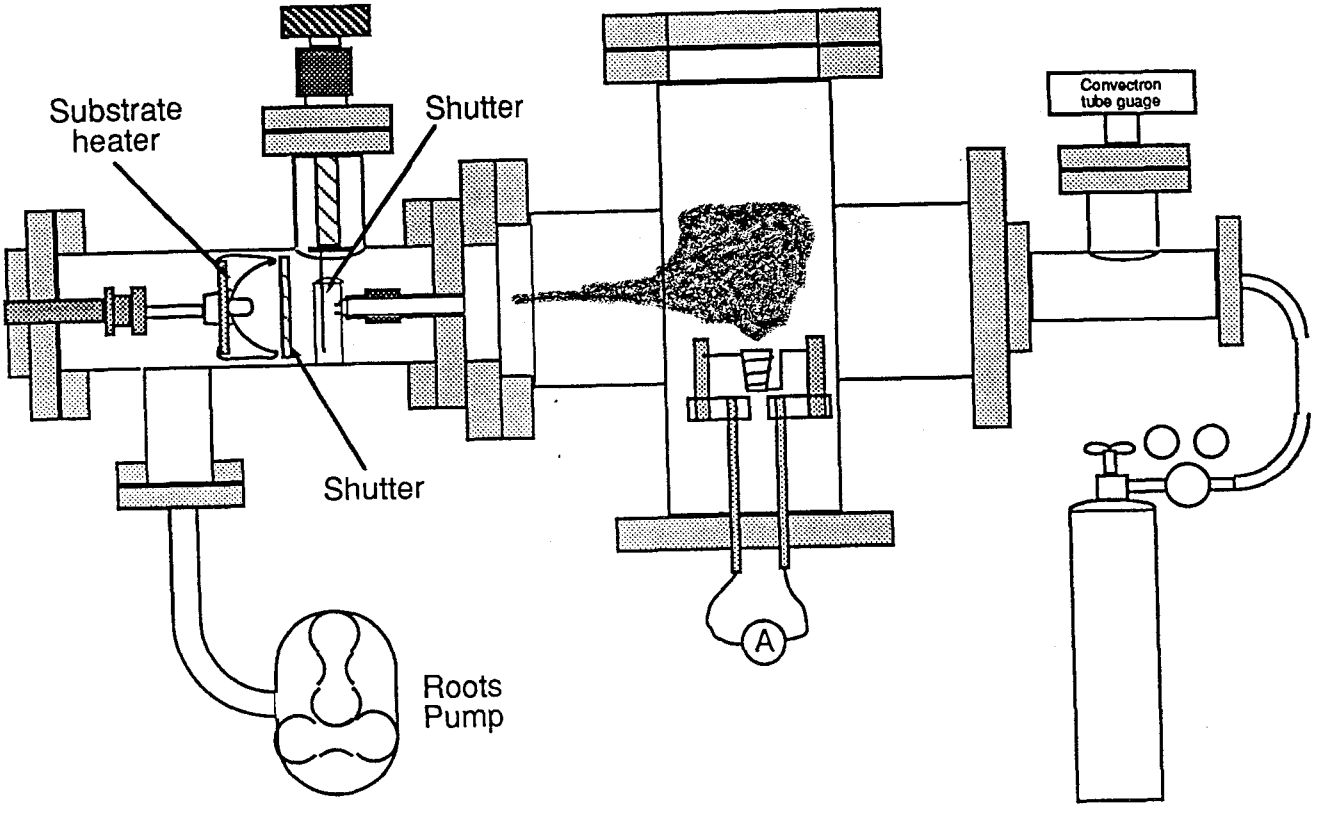

FIG. 1.4. A schematic drawing of our two-chamber gas-condensation system capable of gas condensation in dynamic gas flow and in-situ ballistic consolidation of nanocrystalline materials [8].

two chambers. The pressure differential depends on the gas flux, pumping speed, and the conductance of the nozzle (diameter, length, and geometry). This large pressure difference results in a large velocity for gas flow through the nuzzle (in the range of 30 to 1000 m/s for evaporation chamber pressures of 0.5 to 5 Torr).

During operation of a gas condensation system modified for ballistic consolidation, the precursor materials are evaporated and form nanocrystalline particles in the evaporation chamber. The particles are carried along by the gas flow through the nozzle and attain the high flow velocity. The primary crystallites have a size range of 5 to 10 nm before they are deposited onto the substrate, which is perpendicular to and about 1 cm away from the nozzle. The deposited area has almost the same 1 cm diameter as the nozzle because lateral diffusion of the particles is minimal at high velocities. This directional deposition is an important and useful feature of the method. The deposited materials are dense when there is a high kinetic energy of the depositing nanoparticles. Therefore the nanoparticles are collected and ballistically consolidated *in situ* without the use of thermophoretic collection and subsequent pressing.

A Kapton window was epoxied on the chamber wall near the substrate to allow for *in situ* x-ray diffraction or Mössbauer spectrometry of the deposited material. Through this window, a three-dimensional structure could be observed during deposition and growth.

1.2.2 Mechanical Alloying

Mechanical alloying (MA) or high energy ball milling (BM) was first developed by Benjamin and coworkers in the late 1960s for producing oxide dispersion strengthened (ODS) superalloys [9-13]. These alloys combine the high temperature strength provided by dispersion mechanisms with the intermediate temperature strength and ductility of a selected alloy matrix. Some Fe, Ni, and Al based ODS superalloys have been developed

(a)

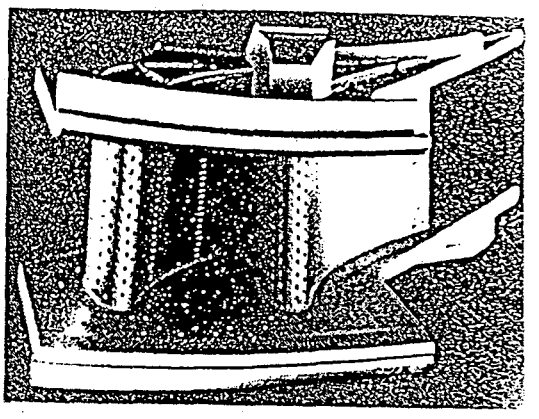

(b)

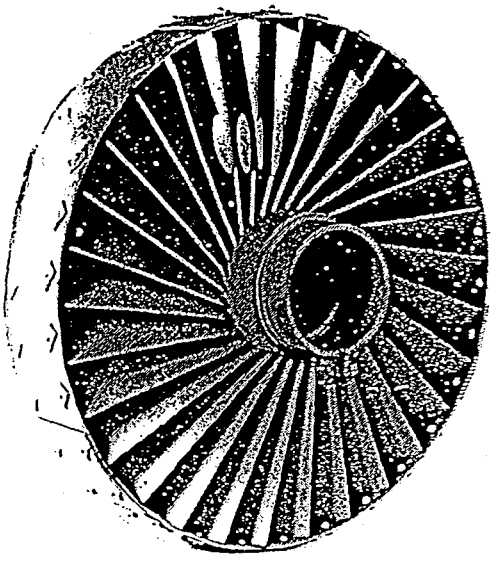

(c)

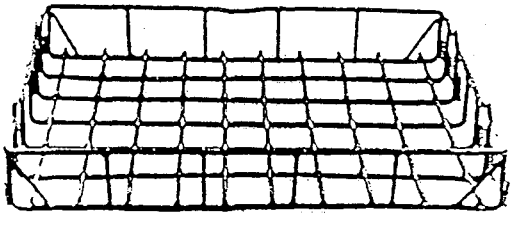

FIG. 1.5. MA ODS superalloy components [13]: (a) a swirler assembly for a power station, INCOLOY alloy MA 956; (b) a heat treatment furnace basket, INCOLOY alloy MA 956; (c) a nozzle guide vane assembly for a gas turbine engine, INCONEL alloy MA 754.

and used for gas turbine vanes, turbine blades, and sheets for use in oxidizing/corrosive environments [13]. Fig. 1.5 shows just a few examples. MA can also be used to alloy elements that are normally difficult or impossible to combine by conventional melting techniques. Recently it has attracted much attention from the materials science community, in large part because of the discovery that MA can cause solid-state amorphization [14-24] and produce nanocrystalline materials [25-29]. Many types of phase transformations have been observed during ball milling, such as polymorphous transformations of compounds and disordering of ordered alloys [30-37]. It is also well-established that high energy ball milling can be used to synthesize alloy phases with extended solid solubilities [25-27, 38-54], for which the Hume-Rothery systematics for size and electronegativity may be relevant [49].

Many collisions between balls or ball and vial wall take place during mechanical alloying. The sample particles trapped between the colliding parts are subject to severe plastic deformation repeatedly. They are flattened, work hardened, and broken up. The mechanical alloying process includes repeated welding and fracturing of powder particles. If the starting material is a mixture of two or more kinds of powders, strong chemical reactions such as alloying and amorphization take place. These phenomena are shown schematically in Fig. 1.6.

There are three typical types of ball mills for mechanical alloying as shown in Fig. 1.7. The vibratory mill is the most common one used in research laboratories and has become the *de facto* standard. A vial sealed with samples and balls is shaken violently, thus causing collisions between balls or a ball and the vial wall. The sample powders are alloyed and broken into nanometer structures by these collisions. Very high ball milling intensities are obtained with this type of ball mill. The Spex 8000 mills and the Super-Misuni NEV-MA8 shaker mill (Fig. 6.1) used in this study are of this type. Typically four

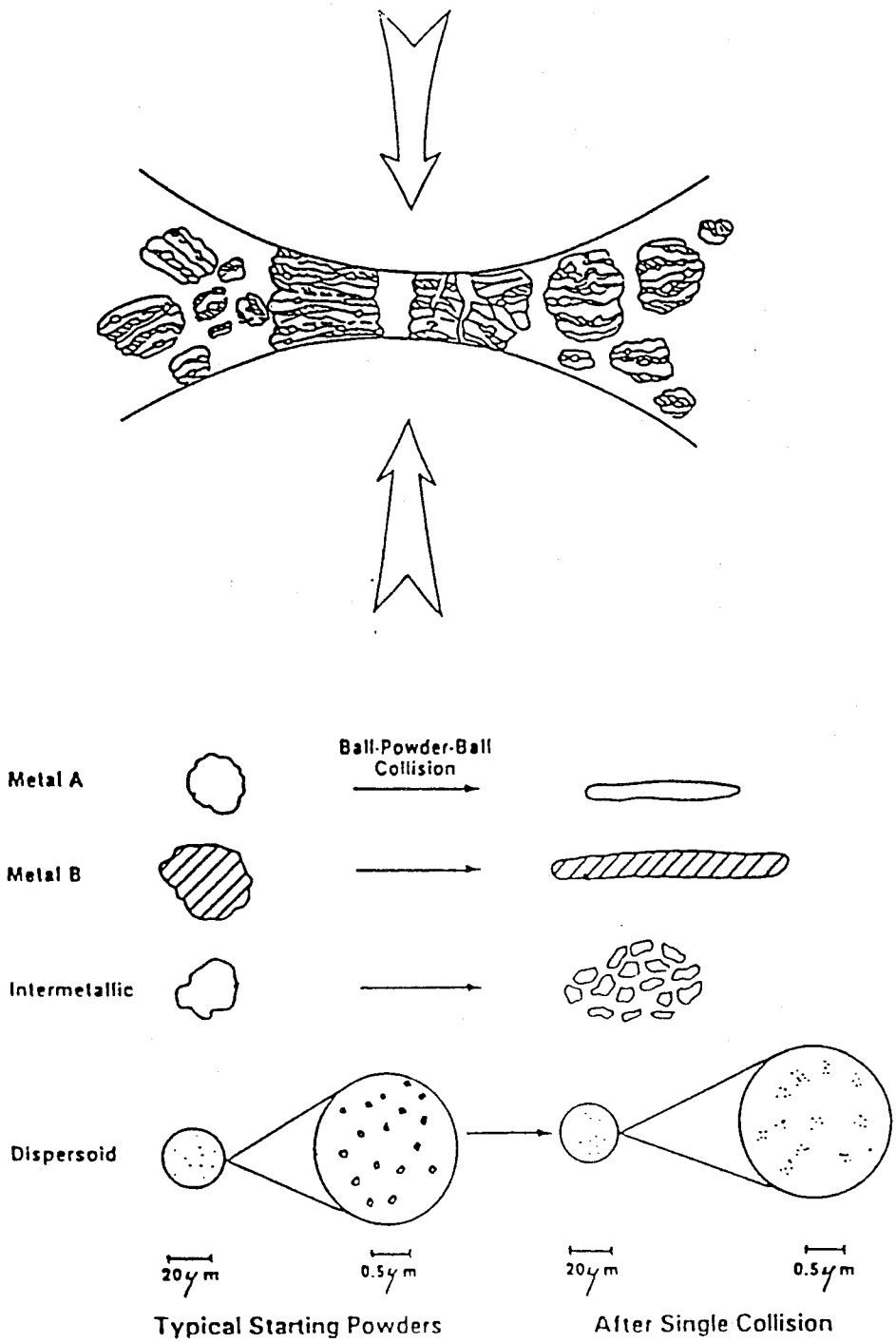

FIG. 1.6. Schematic drawing of the mechanism of ball milling. Powder particles sandwiched between colliding parts are flattened, broken up, and alloyed due to the collision.

steel balls (two 10 mm and two 3 mm in diameter) and starting powders with a ball-to-powder weight ratio of 5:1 are sealed in the vial in an Ar atmosphere. The starting materials are either elemental powders (Fe, Ni, Si, etc.) with 99.9% purity mixed at designated atomic ratios or powders filed from pre-alloyed ingots (Ni_3Fe, $Fe_{75}Ni_{25}$, etc.). During milling, the vial temperature is kept either below 60 °C by forced air cooling if the Spex 8000 mill is used, or at constant elevated temperatures (300 °C, 200 °C, or 100 °C) by heating with a feed-back controlled heater or at room temperature by cooling with flowing cold water if the NEV-MA8 mill is used. After the milling is stopped, the vial is cooled for a few hours before opening. These are the typical experimental procedures of ball milling. More specific information and details on control of temperature and intensity are provided in Chapter 6 and 5, respectively. Although chemical contamination from the vial and balls is unavoidable, the amount of Fe enrichment was not large and usually not a problem.

The attritor mill (also shown in Fig. 1.7) was invented by Szegavi and is often called a *Szegvari Attritor*. The rotation of the rotary mixer bar and the arms on it agitate the balls sealed in the container. The shear force between two rotating balls or a ball and the wall of the container crushes and alloys the sample powders. The milling intensity is relatively low and longer milling times are needed compared with the vibratory mills. However, attritor mills are capable of large quantity production because they allow continuous feeding of raw materials and extraction of products. Attritor mills with capacities for 0.5 to 100 kg of powder have been used in industrial production.

A planetary ball mill shown in Fig. 1.7 has a revolving table with vials mounted in several rotating stages. It is more similar to the conventional rotary ball mills than a vibratory or attritor mill. Rotary mills can rotate on a central horizontal axis. High energy can be achieved by using large mills and high rotation speed. Large batches of powders

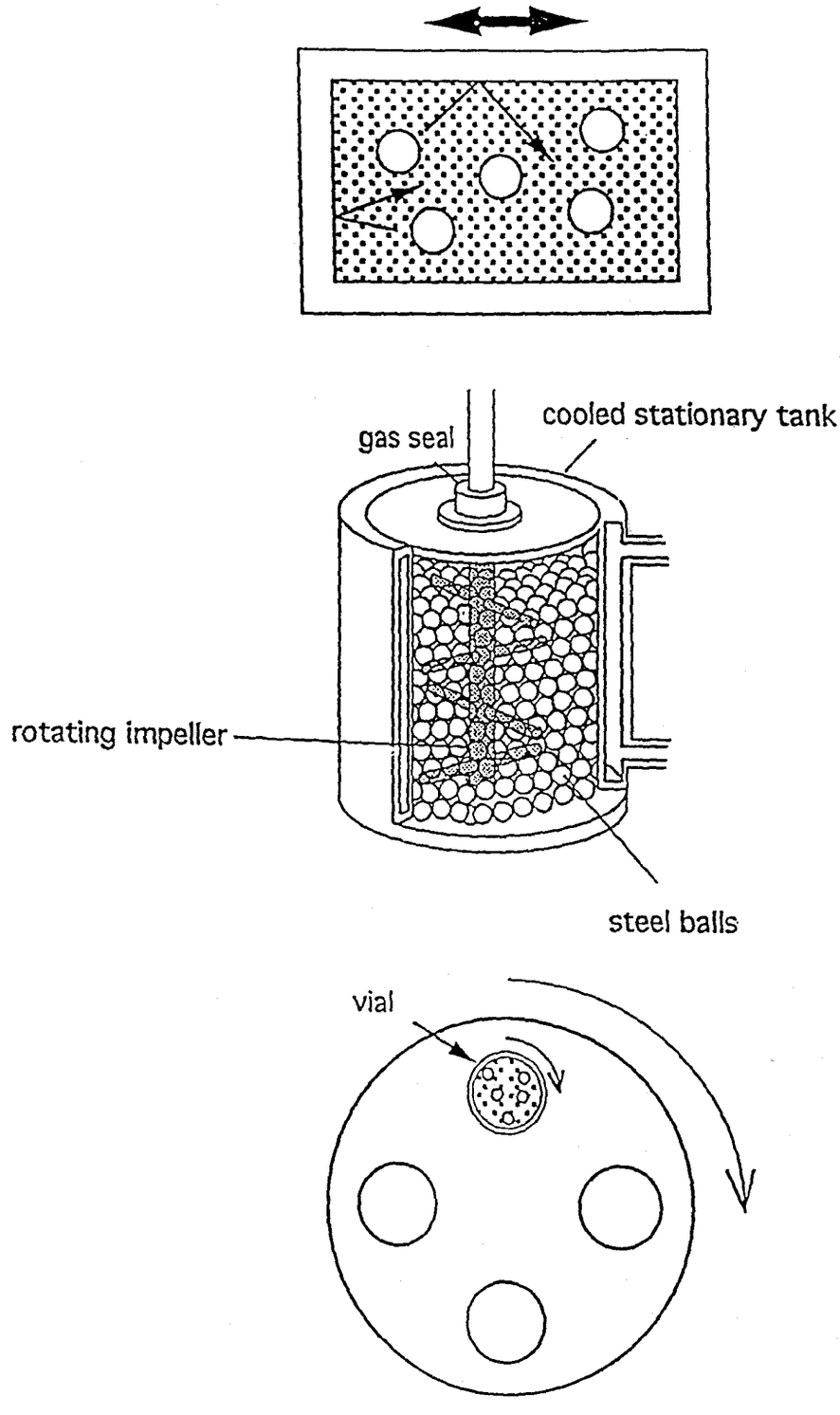

FIG. 1.7. Schematic drawing of typical ball mills. (a) vibratory mill, (b) attritor mill, and (c) planetary mill [10].

(up to about 2,000 kg) can be processed [13]. Mechanical driving forces for alloying and nanocrystallization are provided by shear forces.

Mechanical alloying (high energy ball milling) has a bright promise as a method for producing novel phases such as nanocrystalline and amorphous materials, alloying difficult-to-alloy elements, and inducing chemical reactions at low temperatures. Unlike many methods of far-from-equilibrium processing, mechanical alloying is scalable to commercial production quantities [13,55]. However, scaling up and the relation of the process parameters for different alloy systems are not direct or intuitive, and require further research. This is part of the goal of this current study.

1.2.3 Other Techniques

Besides the two experimental methods described above, gas condensation and mechanical alloying, there are quite a few other methods to prepare nanocrystalline materials. A brief description of some of these methods is provided[2,5,56].

In the sol-gel technique, crystalline sols of the final equilibrium phase are introduced in a matrix as seeds for nucleation to lower the nucleation energy. This method does not need high temperature as the nucleation energy is relatively low. It is especially suitable for preparing stoichiometric compounds containing one or more components with a high vapor pressure, such as (BaPb)TiO_3 ferroelectrics.

The mixalloy processing method utilizes the turbulent mixing of impinging alloy streams and *in-situ* chemical reactions. For example, mixing of turbulent streams of molten Cu-B alloy and Cu-Ti alloy results in nanocrystalline TiB_2 in the zone of mixing, which can become nanocrystalline dispersions in fine-grained material after subsequent rapid solidification.

Chemical vapor deposition (CVD) has been used to synthesize nanocrystalline nitrides and carbides of titanium and silicon. RF-plasma CVD was used to grow nanocrystalline carbon films and filaments. Crystal sizes as small as 2 to 3 nm could be obtained. There are other deposition methods as well, such as electron beam vapor deposition and electrochemical deposition processes [57,58].

Rapid quenching from the liquid state can also give fine equiaxed nanostructures, with the finest microstructures obtained at the highest solidification rates [59]. Amorphous phases obtained at extremely high solidification rates in this technique can be used as precursors to produce nanocrystalline materials by annealing them at relatively low temperatures for chemical unmixing and nucleation [60].

A new thermo-mechanical processing technique has been recently developed at Caltech to produce ultrafine grained 304 stainless steel ($\approx$ 200 nm grain size) [61]. This technique has two key processing steps: formation of ultrafine dislocation cell structure by deformation at room and liquid N_2 temperatures and subsequent low temperature annealing, and the conversion of dislocation cells into grains with medium to high misorientation by deformation at low strain rates and high temperatures, which initiates grain boundary sliding in the microstructure .

1.3 Characterization of Nanocrystalline Materials

To understand interrelationships among processing, structures, and properties, the materials must be characterized both during the process and after the process, and on both atomic and nanometer scales. Features of importance include: crystal structures, grain size distribution and morphology, nature of grain boundaries and interfaces, defects, chemical composition and chemical homogeneity.

1.3.1 X-ray Diffractometry and Data Analysis

All x-ray diffractometry work was performed on an INEL CPS-120 diffractometer system (Debye-Scherrer optics) with a curved position sensitive detector (PSD) spanning 127° in 2θ angle. The Co Kα incident radiation was monochromated with a flat graphite monochromater. From x-ray diffraction, we can identify the various phases present in the sample, such as bcc or fcc phases. When there are multiple phases present simultaneously, the phase fraction of each phase can also be determined. For example, in the study of mechanical alloying of Fe-Ni nanocrystalline alloys, the phase fractions of bcc and fcc phases in the bcc/fcc two-phase alloys were calculated from the intensities of the bcc (200) and fcc (220) peaks, which were reasonably immune to problems of overlap with broadened neighboring peaks. Detection limits for the bcc and fcc phases in this study were set primarily by the statistical quality of data, and are estimated to be about 0.5 %.

To calculate phase fractions of bcc and fcc phases, however, the measured peak intensities have to be corrected for Lorentz-polarization, multiplicity, and structure factors, which was done in a standard way [62]. Sample absorption also needs to be corrected, and it is different for our flat samples with Debye-Scherrer optics from that for a Bragg-Brentano (θ-2θ) diffractometer [63,64]. In comparison, an additional correction factor of $\frac{\sin\phi + \sin(2\theta-\phi)}{\sin(2\theta-\phi)}$ is needed, with φ the glancing incidence angle for the x-ray beam on the flat sample, which was 15°. The corrected peak intensity, I_{cor}, is:

$$I_{cor}(\theta) = \frac{\sin\theta \sin 2\theta}{1+\cos^2\theta} \frac{V_c^2 \mu \rho}{m F^*(k) F(k)} \frac{\sin\phi + \sin(2\theta-\phi)}{\sin(2\theta-\phi)} I(\theta) \quad , \qquad (1.1)$$

where V_c is the volume of the unit cell, μ is the mass absorption coefficient, ρ is the density of the material, m is the multiplicity of the diffracting planes, and F(k) is the structure factor for the unit cell. As usual, $k = 4\pi\sin\theta/\lambda$. With little if any crystallographic texture present in the ball milled samples, the fractions of constituent phases, f_{bcc} and f_{fcc},

were determined by taking ratios of the corrected intensities for the bcc (200) and fcc (220) diffractions:

$$\frac{f_{bcc}}{f_{fcc}} = \frac{I_{cor200}}{I_{cor220}} \tag{1.2}$$

For nanocrystalline alloys, the absorption factors, $\mu\rho$, are the same for both bcc and fcc phases, and therefore cancel in Eq. 1.2. We also assume the same atomic form factors for the atoms in the fcc and bcc phases. Equation 1.2 becomes:

$$\frac{f_{bcc}}{f_{fcc}} = 1.657 \frac{I_{200}}{I_{220}} \quad , \tag{1.3}$$

$$f_{bcc} = \frac{1.657\, I_{200}}{1.657 I_{200} + I_{220}} \quad , \tag{1.4a}$$

$$f_{fcc} = \frac{I_{220}}{1.657 I_{200} + I_{220}} \quad . \tag{1.4b}$$

These are the equations used in calculating the bcc and fcc phase fractions of Fe-Ni alloys in Chapter 5.

X-ray diffraction can also provide useful information on average grain size and strain for nanocrystalline materials. Fig. 1.8 shows an x-ray diffraction pattern from a nanocrystalline Fe_3Si sample mechanically alloyed at 300 °C. Each diffraction peak is fitted into a Lorentzian function, which is typical of an exponential distribution of the grain size (the grain size distribution produced by gas condensation method are usually log-normal) [65]. The insert of Fig. 1.8 shows a very reasonable Lorentzian fitting (solid curve) of the Fe_3Si (200) peak (dotted curve). The average grain size and root-mean-square strain were estimated in two ways from the x-ray diffraction peak broadening.

In the method of Williamson and Hall [66], we measured the diffraction linewidth in k-space, Δk, and the k-vector of all diffraction peaks:

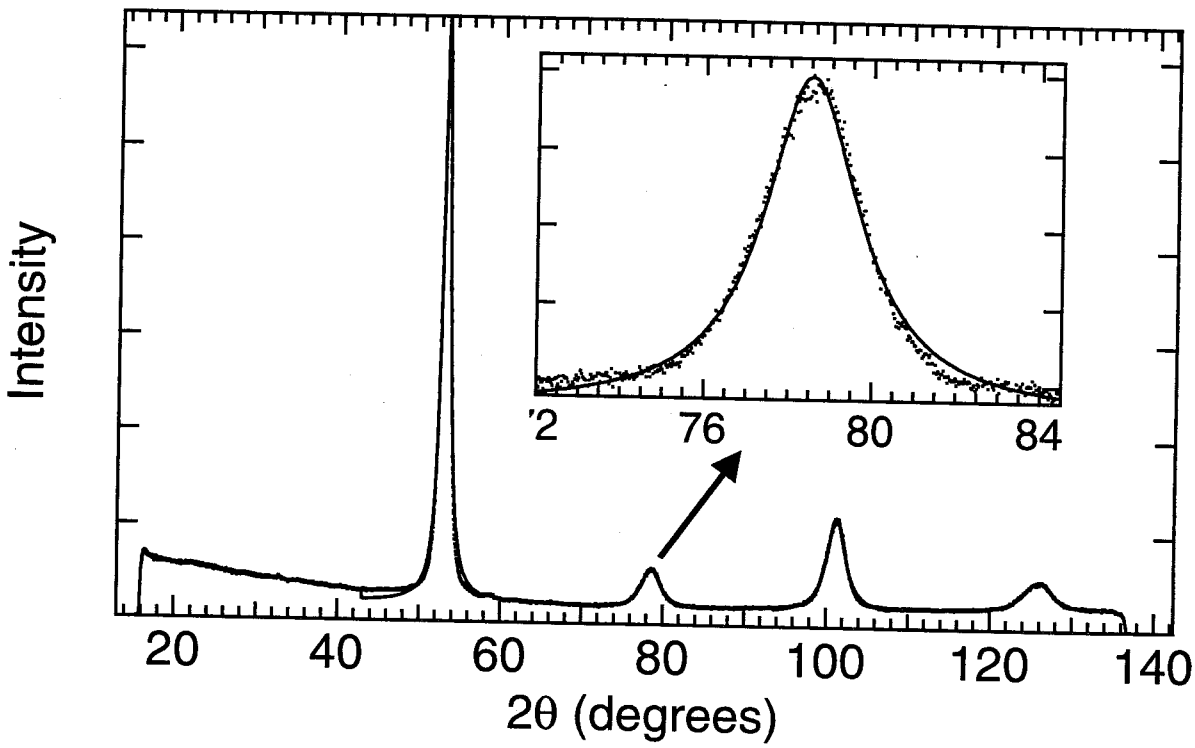

FIG. 1.8. X-ray diffraction pattern of a nanocrystalline Fe_3Si sample mechanically alloyed at 300 °C. The peaks are fitted to Lorentzian functions. The insert shows the (200) peak (dotted) and its fitting (solid).

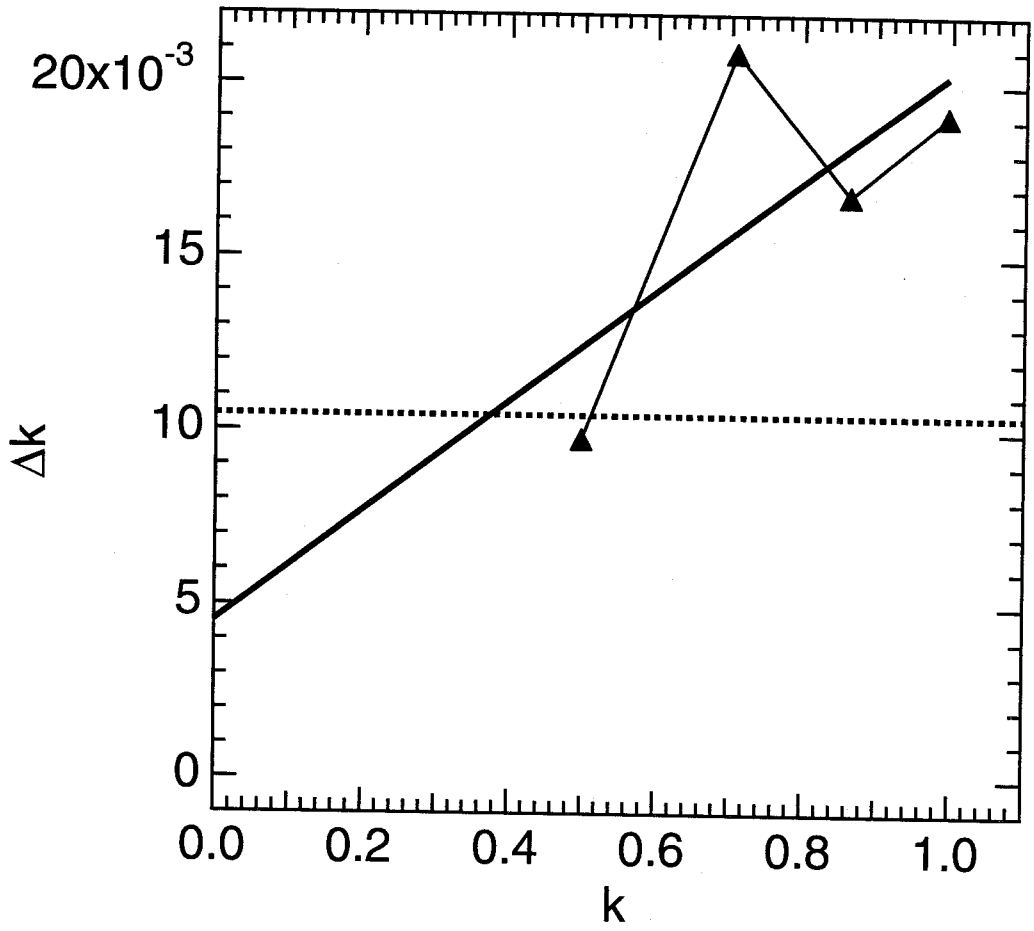

FIG. 1.9. An average grain size and root-mean-square strain analysis from x-ray diffraction peaks shown in Fig. 1.8. Both the Williamson-Hall method (triangles: raw data; thick line: fitted) and the Scherrer method (dashed line) are shown.

$$\Delta k = \frac{\cos\theta \, \Delta 2\theta}{\lambda} \quad , \tag{1.5}$$

$$k = \frac{2 \sin\theta}{\lambda} \quad . \tag{1.6}$$

Here $\Delta 2\theta$ is the full-width-at-half-maximum (in radians) of a Lorentzian function fit to the diffraction peak. Both small grain size and a strain distribution contribute to the peak broadening, i.e., Δk. It was found [67]:

$$\Delta k \equiv \Delta k^{size} + \Delta k^{strain} \cong \frac{1}{d} + 2ek \quad . \tag{1.7}$$

Therefore, a linear curve is expected if Δk is graphed versus k, as in Fig. 1.9 . The curve was fitted to a straight line (thick solid line) and was extrapolated to zero k. The average grain size, d, was obtained as the inverse of the extrapolated y-intercept, and the root-mean-square (RMS) strain, e, as half the slope of the plot of Eq. 1.7. There are a number of problems with this method of Williamson and Hall [67]. In the present study, however, absolute accuracy of grain size or strain was not so important as the ability to detect systematically differences between the specimens. Differential sensitivity was facilitated by using the same procedures / programs for both data collection and analysis for all samples.

In a second method, the average grain size was obtained from the width of Fe_3Si (110) peak with the Scherrer equation [68,69]:

$$d = \frac{0.9 \, \lambda}{\Delta 2\theta \cos\theta} \quad . \tag{1.8}$$

For comparison, this Scherrer method is included as a dash line in Fig. 1.9. Our previous work showed reasonable agreement between the grain size obtained from Eq. 1.8 and the grain size obtained from dark field imaging with a transmission electron microscope

[70,71]. In this thesis, the average grain sizes were calculated from the bcc (110) or fcc (111) peaks with this second method, while the root-mean-squared (RMS) strain was obtained with the Williamson-Hall method.

Lattice parameters can be determined from the x-ray diffraction pattern by the Nelson-Riley extrapolation method [64,72,73]. In this method, the lattice parameter, a_o, obtained from the Bragg angle, θ, for each (hkl) diffraction peak has an error Δa_o:

$$\frac{\Delta a_o}{a_o} \propto \frac{\cos^2\theta}{\sin\theta} + \frac{\cos^2\theta}{\theta} \quad , \tag{1.9}$$

where the error Δa_o comes from specimen shift, variation in x-ray penetration depth, and vertical (out of the diffracting plane) divergence of the x-ray beam. Meanwhile a_o itself is calculated from the Bragg's Law:

$$a_o(\theta) = \frac{\lambda \sqrt{h^2 + k^2 + l^2}}{2 \sin\theta} \quad . \tag{1.10}$$

Extrapolating the curve of $a_o(\theta)$ vs. $\frac{\cos^2\theta}{\sin\theta} + \frac{\cos^2\theta}{\theta}$ to $\theta = 90°$ gives the lattice parameter a_o.

1.3.2 Transmission Electron Microscopy

A Philips EM310 TEM operated at 100 kV and a Philips EM430 operated at 300 kV were used for the TEM studies. The primary use of TEM study was to provide a check on grain size and its distribution through dark field imaging. By this technique, one colleague in our group has confirmed that the grain size distribution after a few hours of ball milling is approximately exponential [65, Fig. 3.7]. Systematical agreement on average grain size between this technique and x-ray diffraction was also confirmed.

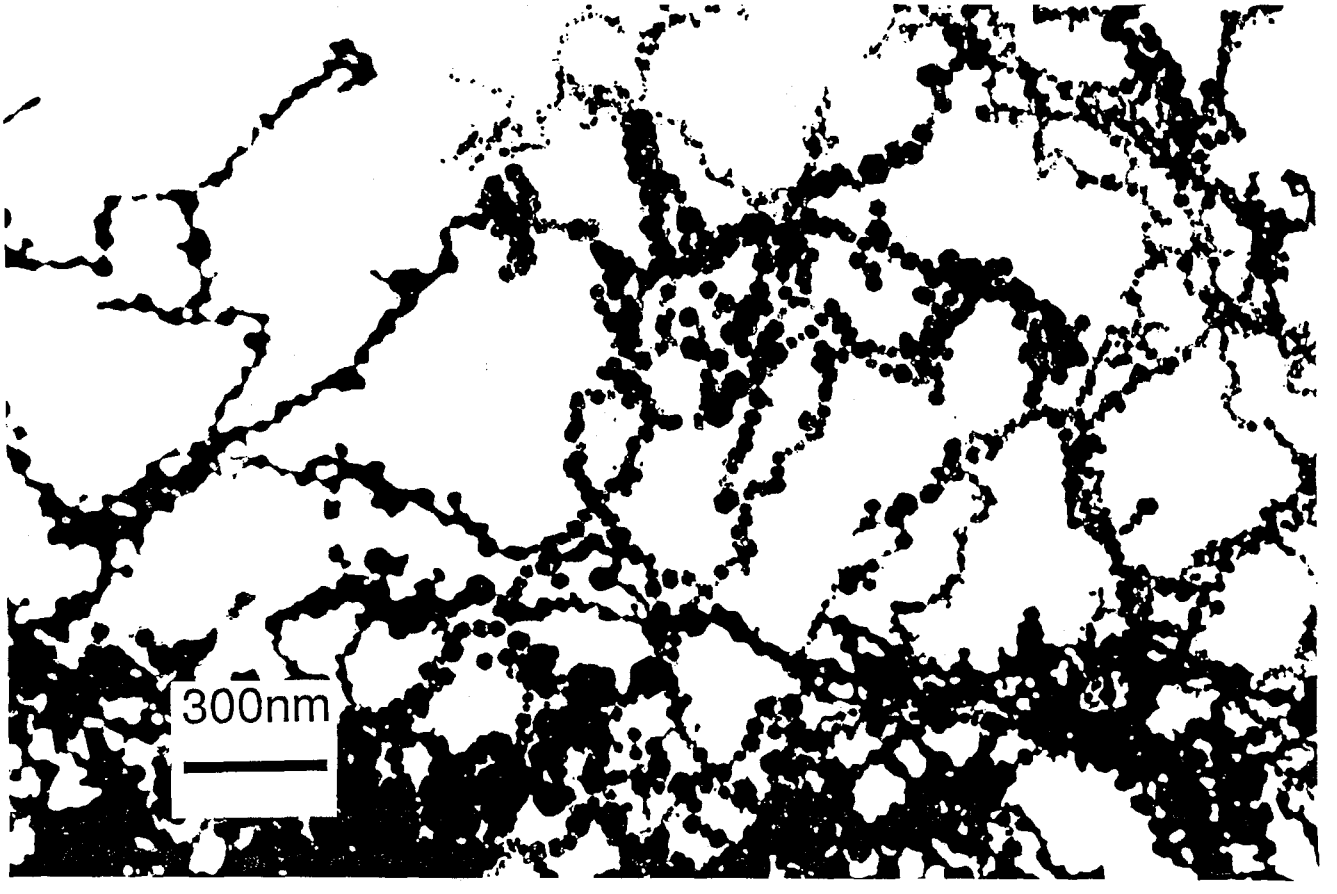

FIG. 1.10. A TEM bright field image of a nanocrystalline Fe prepared by gas condensation in N_2 gas and in a magnetic field. The hexagonal shape and the shell structure (Fe core plus Fe oxide outer shell) of some nanocrystalline Fe particles as well as the interparticle chains are all observed on this TEM picture.

When the grain size becomes so small that the diffraction peaks become very broad, x-ray diffraction alone can not provide definite information on grain size as the broad peaks can also be interpreted as evidence of amorphization. High resolution TEM (HREM), which can show the lattice fringes of crystalline materials, can play special role in such a situation. HREM is the best experimental technique for distinguishing the very-small-grained nanocrystalline materials from amorphous materials.

For studies of microstructural morphology, however, TEM can provide unique information and is especially useful. Fig. 1.10 shows a TEM bright field image of nanocrystalline Fe prepared by gas condensation in N_2 gas and in a magnetic field. The hexagonal shape and the shell structure (Fe core plus Fe oxide outer shell) of some nanocrystalline Fe particles as well as the interparticle chains are all obvious from this TEM picture while other techniques including x-ray diffraction may not be able to provide this information.

1.3.3 Mössbauer Spectrometry

Mössbauer Spectrometry [74-76] is a technique to study the absorption of γ-rays by the nuclei of atoms. It uses the emission of γ-rays (14.41 keV in the case of ^{57}Fe) by radioactive nuclei (an excited state of ^{57}Fe), and the subsequent reabsorption of these gamma-rays by other nuclei (^{57}Fe) of the same kind, with negligible recoil energy transferred to any internal excitation of the lattice. The nuclear emission and absorption energies are changed slightly by the local atomic environment of the nuclei. Mössbauer spectrometry can measure these tiny changes of energy, caused primarily by the first few nearest-neighbor shells of atoms, and provide useful information about the local chemical environment of the ^{57}Fe nuclei.

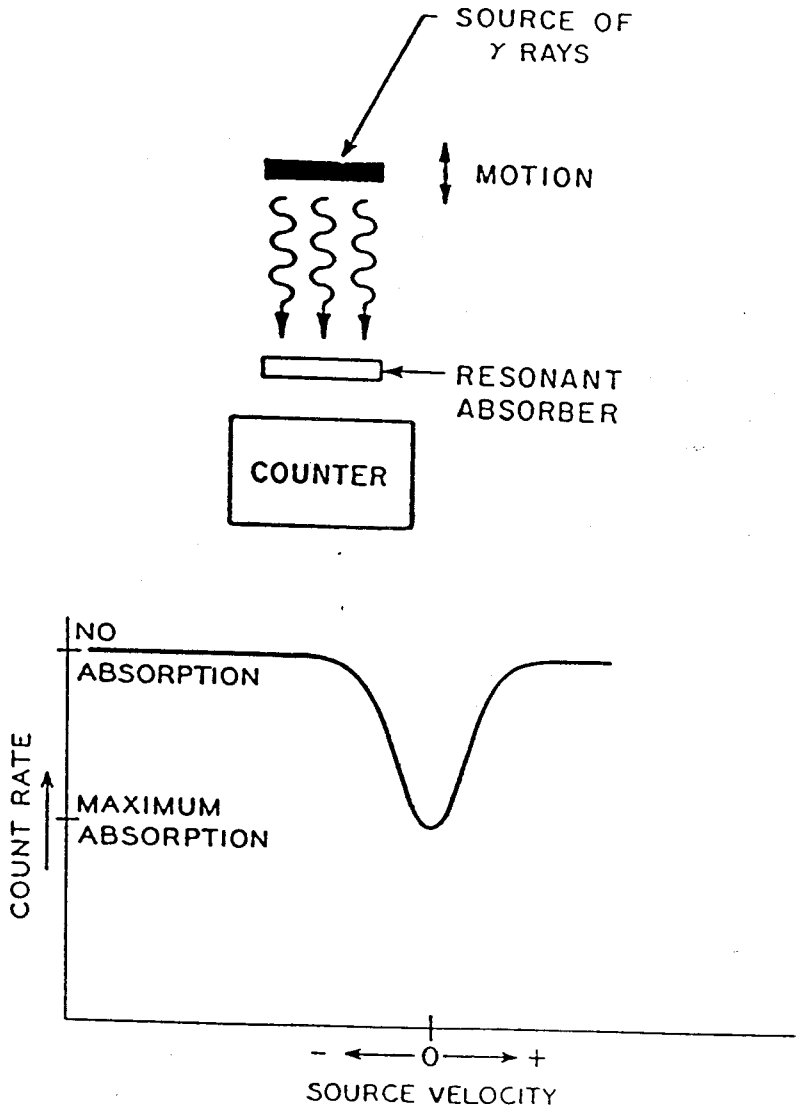

FIG. 1.11. Basic setup for ^{57}Fe Mössbauer spectrometry experiments. The source (^{57}Co in Rh matrix) is moved to vary the γ-ray energy by the Doppler effect. A stronger absorption occurs when the γ-ray is absorbed resonantly by the ^{57}Fe nuclei in the sample, which results in a decreased counting rate.

Many important insights into nanocrystalline materials have been obtained by ^{57}Fe Mössbauer spectrometry. The Saarbrücken groups of Gleiter and Gonser have been particularly active in this field [2-4,77-79], among many other investigators. Almost all of nanocrystalline materials studied in this thesis are Fe-based so that ^{57}Fe Mössbauer spectrometry can be employed.

The basic setup of ^{57}Fe Mössbauer spectrometry experiments is schematically shown in Fig. 1.11. Everything is at room temperature for our room temperature spectra. The source (^{57}Co, typically a few tens of mCi, in Rh matrix) is moved at constant acceleration to vary the γ-ray energy with a Doppler shift. A stronger absorption occurs when the γ-rays are absorbed resonantly by the ^{57}Fe nuclei in the sample. This gives a decreased counting rate in the Ar-CH_4 flow-gas detector.

As an example, a transmission Mössbauer spectrum from a well-ordered Fe_3Si sample (mechanically alloyed at 300 °C for 48 hours, then DSC-scanned to 600 °C at a rate of 20 °C / min) is shown in Fig. 1.12. The raw Mössbauer spectrum (dotted) comprises of a sum of overlapping ferromagnetic sextets, and the distribution of ^{57}Fe hyperfine magnetic field (HMF) can be obtained by processing the spectrum by the method of Le Caër and Dubois [80]. In this method, a set of sextets with progressive HMF were used to fit the experimental raw data. A linear dependence of isomer shift, IS, on the HMF is assumed: IS = A * HMF + B. The constants A and B were determined by the quality of fit of a simulated spectrum (solid curve in Fig. 1.12) to the experimental one. The hyperfine magnetic field distribution obtained from the spectrum of Fig. 1.12 is presented in Fig. 1.13. The peaks at about 310 kG and 200 kG signify DO_3 ordering of the Fe_3Si sample, which was also confirmed by x-ray diffraction.

These two peaks at about 310 kG and 200 kG correspond to the two chemical sites for Fe in the DO_3-ordered Fe_3Si sample. These two sites of Fe have 0 and 4 Si atoms in

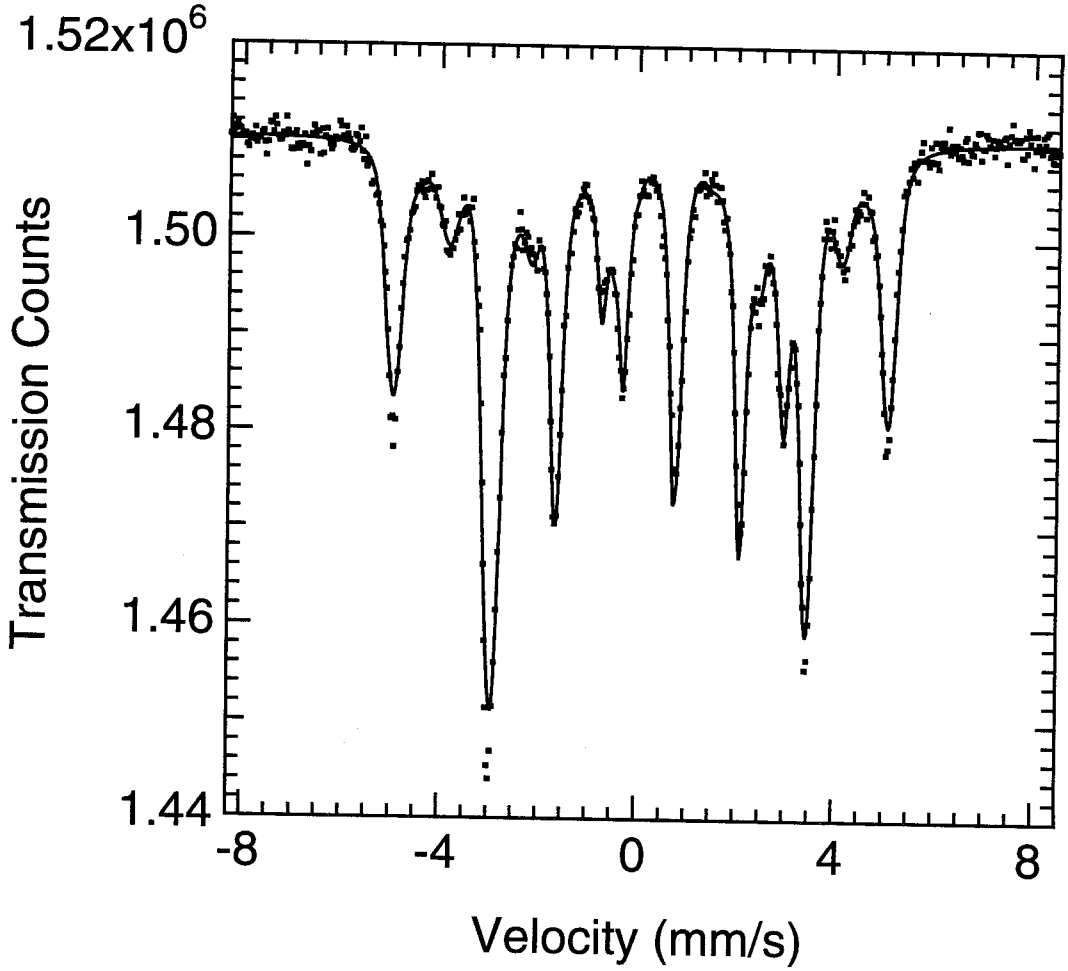

FIG. 1.12. Transmission Mössbauer spectrum from a well-ordered Fe_3Si sample (mechanically alloyed at 300 °C for 48 hours, then DSC-scanned to 600 °C at a rate of 20 °C / min). The dotted curve is the experimental spectrum while the solid one is the fitted spectrum.

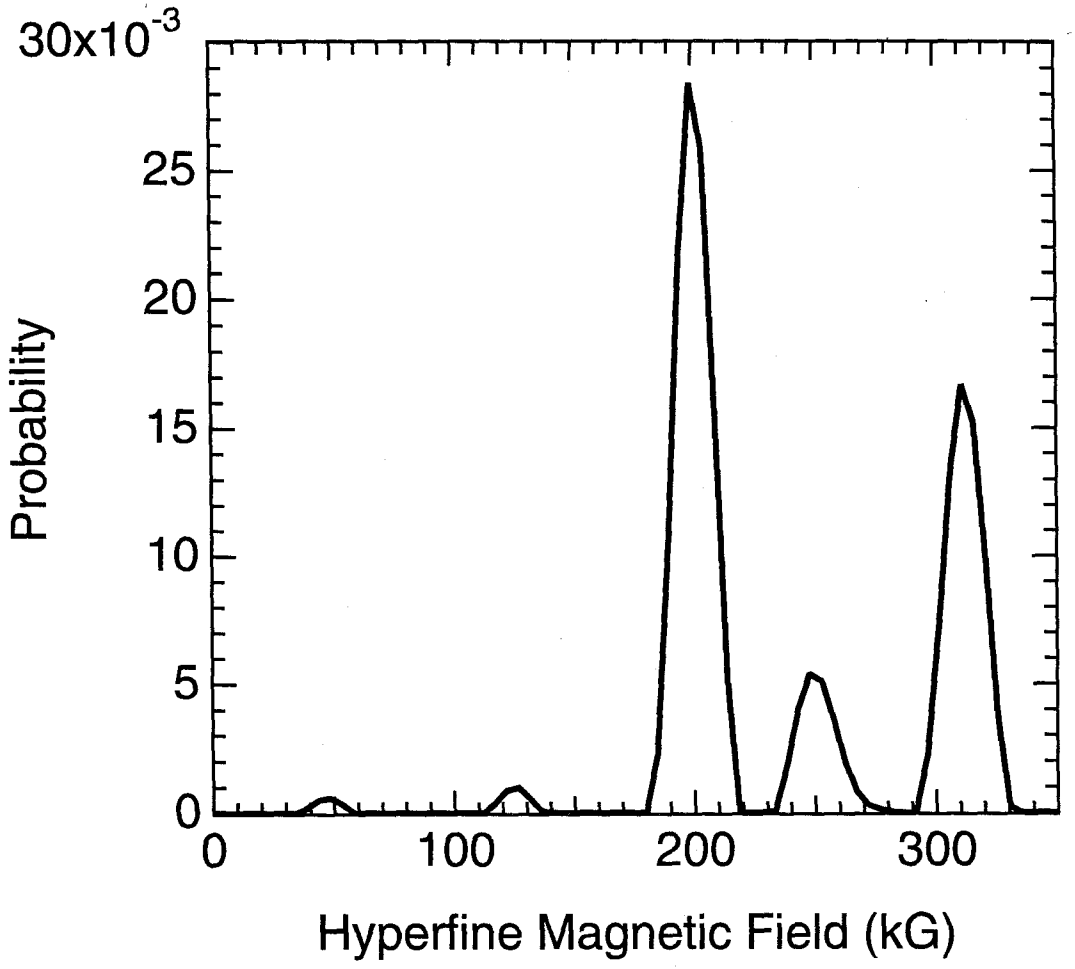

FIG. 1.13. Hyperfine magnetic field distribution extracted from the previous spectrum of Fe_3Si, using the method of Le Caër and Dubois. The peaks at about 200 KG and 310 KG signify DO_3 order of an Fe_3X alloy.

their first-nearest neighbor (1nn) shells, respectively [81-83]. Similarly, the peak at about 250 KG corresponds to Fe sites with 3 1nn Si atoms. The intensities of these peaks are termed P_0, P_4, P_3, respectively. While short range order parameters can be obtained from these intensities, chemical composition of Si, c, can also estimated [63, Sec. 3.3]. In short, the following equation is found for sub-stoichiometric $Fe_{1-c}X_c$ alloys:

$$\frac{P_4}{P_3} = \frac{1-2c}{8c-2} \quad . \tag{1.11}$$

The chemical composition for the sample shown in Fig. 1.13 was estimated by this method to be about Fe-23.86 at.% Si. It is not surprising to see a little more than 1 at.% Fe contamination, since the sample was ball milled with steel vial and balls for 48 hours at 300 °C. Since Mössbauer spectrometry is very sensitive to local chemical environment, it can provide information about chemical heterogeneities in nanocrystalline materials. For example, it can be used to detect chemical unmixing or the presence of multiple phases (such as Fe oxides).

1.3.4 Differential Scanning Calorimetry

Differential Scanning Calorimetry (DSC) is a technique to measure thermal properties of materials, such as specific heat, C_p, and the stored enthalpy, ΔH. It can be used to find phase transitions and chemical reactions. Unlike a differential thermal analyzer (DTA), which uses a single furnace and measures the temperature difference developed between the sample and a reference material during a thermal event, DSC uses two furnaces and measures the differential heat flow required to keep the sample and a reference material at the same temperature. Fig. 1.14 shows schematically various thermal analysis systems (DTA and DSC) [84]. Besides the difference in method, a DSC system has a smaller furnace and is more accurate that a DTA system.

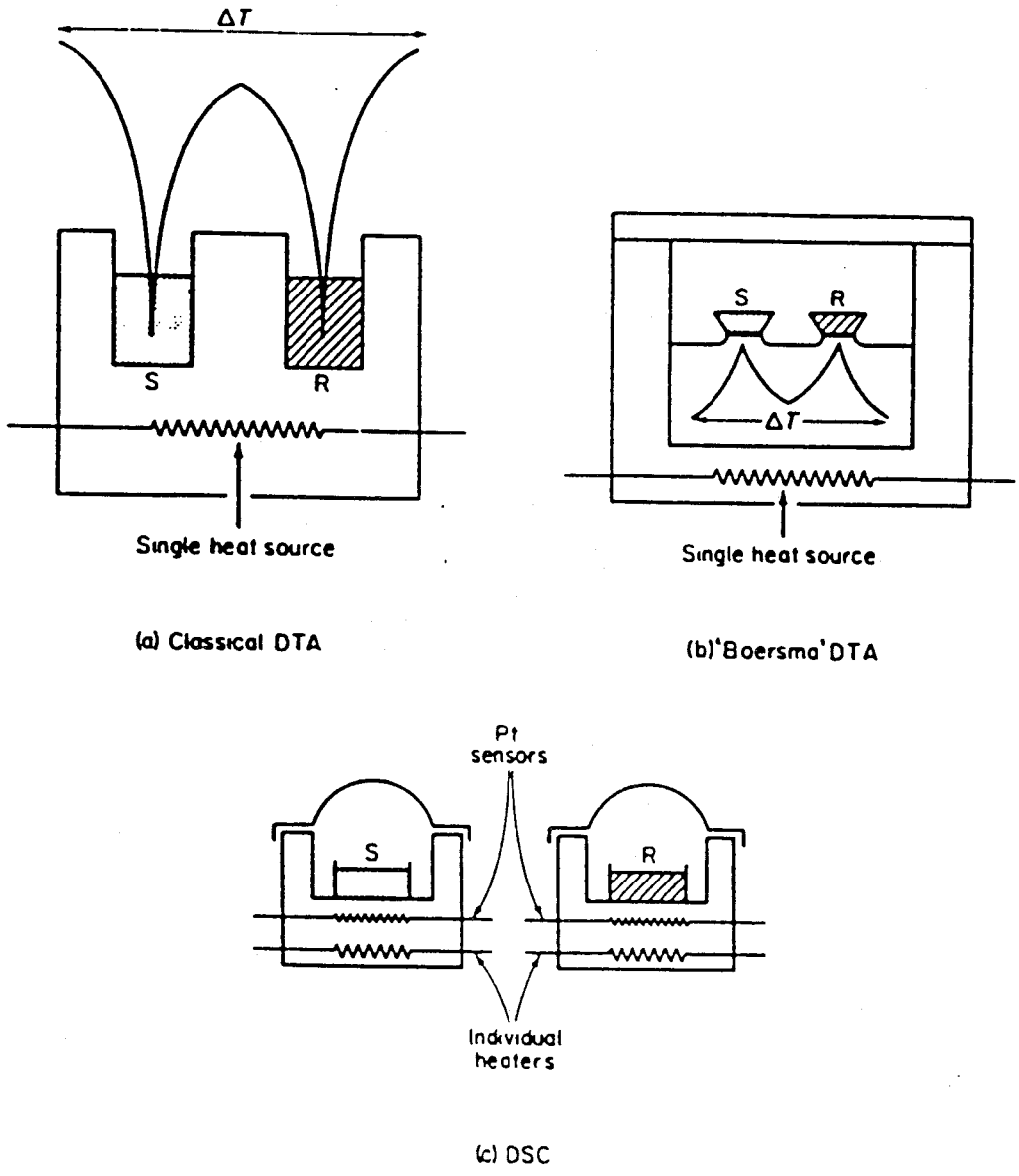

FIG. 1.14. Schematic drawing of various thermal analysis systems (DTA and DSC): (a) classical DTA, (b) "Boersma" DTA, (C) DSC.

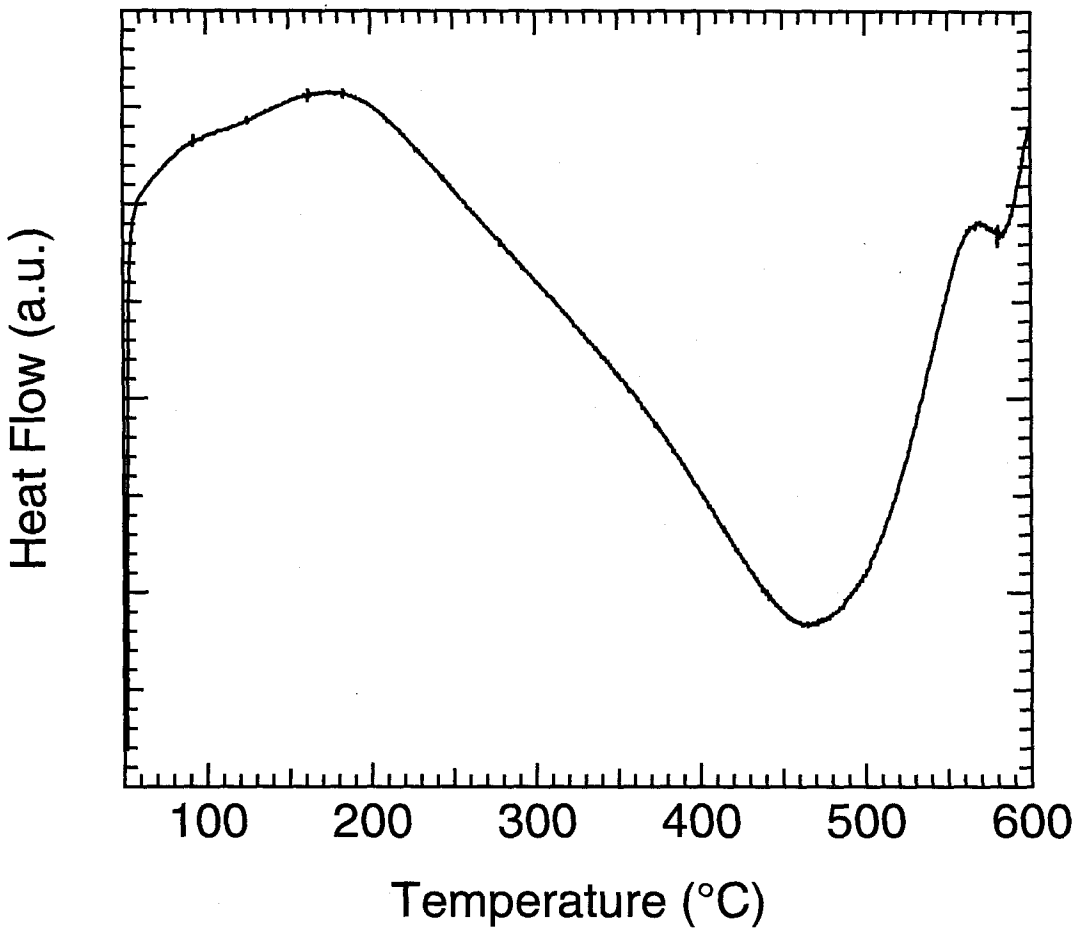

FIG. 1.15. DSC scan of a nanocrystalline Fe_3Si sample mechanically alloyed at 300 °C for 48 hours. The broad peak around 465 °C is due to grain growth, strain release, and DO_3 ordering.

Both a Perkin-Elmer DSC-4 and a DSC-7 were used in this study. Typically samples were scanned from 50 °C to 600 °C at a scan rate of 20 °C / minute, then were rapidly cooled to 50 °C. A typical DSC scan trace, taken from nanocrystalline Fe_3Si mechanically alloyed at 300 °C for 48 hours, is shown is Fig. 1.15. To access the nature of the broad peak around 465 °C, the same nanocrystalline Fe_3Si samples were scanned to various temperatures below and above the peak, and the microstructures of these samples were then characterized. The peak in Fig. 1.15 was found to originate from simultaneous grain growth, strain release, and DO_3 ordering of the original disordered nanocrystalline Fe_3Si sample.

The stored enthalpy, ΔH, can be obtained by integrating the corresponding peak of DSC scan after base-line correction. The later was typically achieved by measuring a subsequent DSC scan trace and subtracting this second scan from the first.

1.3.5 Other Techniques for Microstructural Characterization

Other experimental techniques were also employed to characterize nanocrystalline materials. A JEOL Superprobe 733 electron microprobe was used to measure chemical compositions and micron-scale chemical homogeneities. The microprobe data complemented energy-dispersive x-ray spectrometry (EDX) measurements of chemical composition. Energy filtered imaging was used for structural characterization and chemical analysis at spatial resolutions of less than 1 nm [85]. Small angle neutron scattering (SANS) can provide direct information about the composition profile around a grain boundary. Coupled with other experimental techniques, SANS provides information on the width, composition profile, and diffusiveness of grain boundaries in nanocrystalline materials. This information was used to access mechanisms of thermal instability against grain growth and phase separation, for example [86].

1.4 Properties and Applications of Nanocrystalline Materials

Unique properties of nanocrystalline materials are usually attributable to one or two microstructural features. Their small crystallite size can cause confinement, effects either in a quantum sense (as in exciton confinement in photonic semiconductors), or a classical sense (as in dislocation interactions in small crystallites). The second important microstructural feature of nanocrystalline materials is their large volume fraction of interfaces (grain boundaries or surfaces). For an average grain size of d and grain boundary width of Δ, the volume fraction of grain boundaries is approximately

$$\text{Interface Volume Fraction} \approx 1 - (1 - \frac{\Delta}{d})^3 \quad . \tag{1.12}$$

For grain boundary width of Δ = 0.5 nm and 1 nm (grain boundaries of 2 to 4 atomic planes wide), the volume fractions of grain boundaries as functions of d are shown in Fig. 1.16. The fraction of atoms associated with grain boundaries is substantial for nanocrystalline materials but negligible for conventional materials (grain size ~ 1 μm). This is expected to give large difference in physical and thermal properties of nanocrystalline materials compared with conventional materials.

Diffusivity

Grain boundaries form a network and thus provide short circuit diffusion paths for both self diffusion and solute diffusion. This effect is especially significant at high volume fractions of grain boundaries. Enhanced diffusivities in nanocrystalline materials have been reported [87,88]. For example, the diffusivity of Cu in nanocrystalline Au clusters was estimated to be about 9 orders of magnitude higher than in bulk polycrystalline Au [87]. Technologically, nanocrystalline materials may be useful when solids with high diffusivities are needed, as in sintering for example.

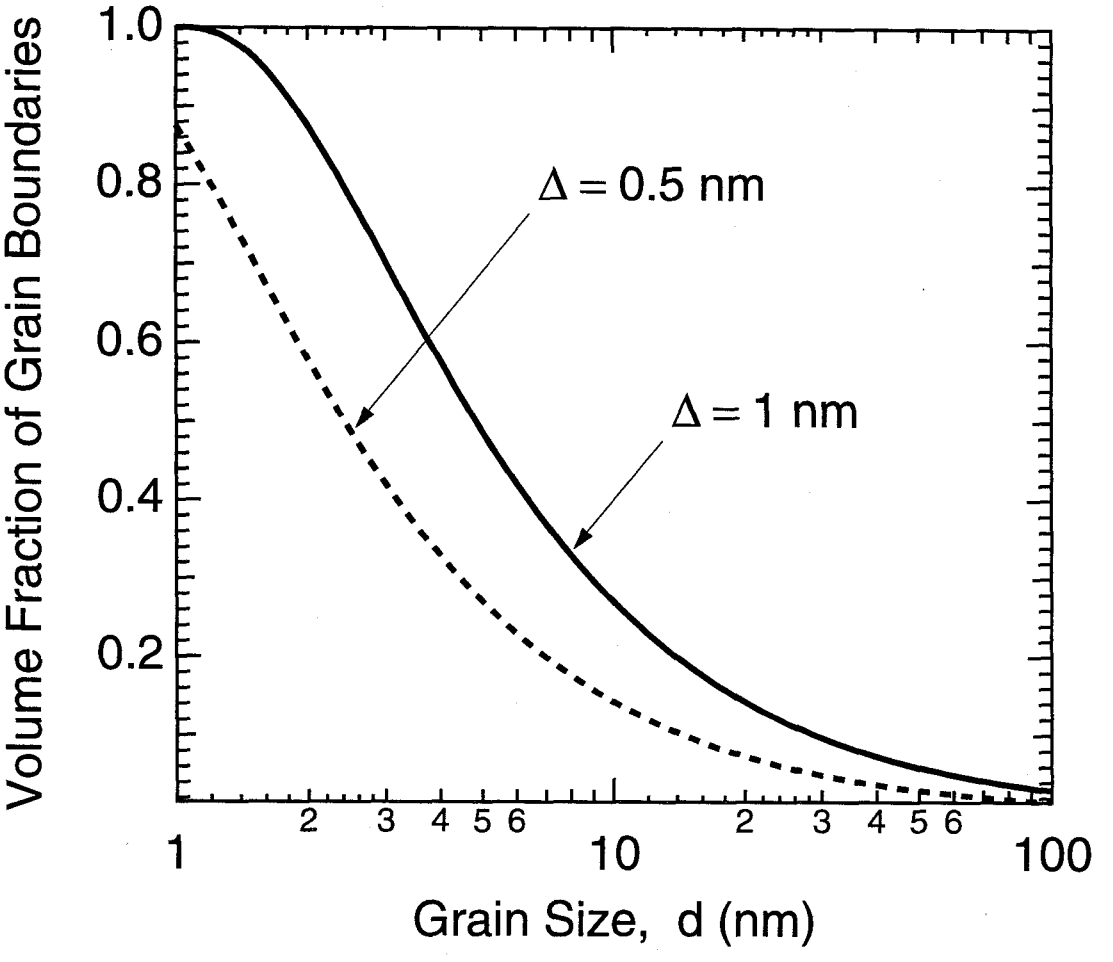

FIG. 1.16. Volume fraction of grain boundaries of nanocrystalline materials with average grain size of d and grain boundary width of Δ. Grain boundary widths of Δ = 0.5 nm and 1 nm correspond to grain boundaries of 2 to 4 atomic planes wide.

Nanocrystalline Metal Particle Catalysts

The large surface volume fraction of nanocrystalline particles make them excellent candidates for catalyzing chemical reactions. The activity of a solid catalyst is proportional to the specific surface area of the active component. There are two types of nanocrystalline metal particle catalyst: nanocrystalline metal particle homogenous catalysts comprising nanocrystalline metal particles suspended as in a liquid phase medium, and carrier nanocrystalline metal catalysts comprising nanocrystalline metal particles dispersed on the surface of oxides [56]. In the first type, nanocrystalline Ni particles (20 nm) were shown to be excellent liquid phase dehydration catalysts for 2-propanol [89]. As an example of the second type, the catalysts obtained by fixing nanocrystalline metal particles (1-10 nm) on a porous carrier such as alumina, silica, magnesia, titania or zeolite have a wide range of industrial applications [56].

One issue of concern for nanocrystalline particles as catalyst materials is the potential lack of durability because of their high surface activity and small particle sizes. In particular, chemical reactions typically require heat or high temperature to increase their rate. Nanocrystalline particle catalysts used in such conditions may be damaged by various surface reactions with the carrier or between particles. This can be solved by selecting a proper carrier, using mild reaction conditions, or by proper regulation of nanocrystalline particles. Nanocrystalline metal particles regulated by a dry process such as in-gas vapor deposition or gas phase chemical reaction have been involved in high temperature processing and can exhibit necessary durability if used under the right conditions [56].

Thermal Properties

Thermal properties substantially different from those of bulk materials have been reported for nanocrystalline materials. Nanocrystalline Fe and FeF_2 reportedly have lower

Debye temperatures [77,79]. Enhanced heat capacity were also observed for nanocrystalline materials [90,91] although it is believed that some of these early investigations could have been impaired by the presence of interstitial atoms in the nanocrystalline materials. Because atoms at interfaces (surfaces or grain boundaries) have higher energy and weaker chemical bonds, so the large fraction of atoms associated with interfaces in nanocrystalline materials does suggests a larger heat capacity for nanocrystalline materials. Our previous x-ray diffraction study [92] on nanocrystalline β–Sn of 7 nm average grain size prepared by inert gas condensation gave a lower Debye temperature of Θ_D = 133 K for nanocrystalline β–Sn compared with Θ_D = 161 K for bulk β–Sn. The large difference in Debye temperature between bulk and nanocrystalline β–Sn gives a large increase in vibrational entropy, 0.6 k_B / atom, for nanocrystalline β–Sn over that for bulk β–Sn. This larger vibrational entropy of nanocrystalline β–Sn will partially counteract the grain growth tendency provided by the enthalpy of the high density of interfaces. It will also help to stabilize nanocrystalline β–Sn against the β –> α phase transformation at 286 K.

Solid Solubility

In thermodynamic equilibrium, the solid solubility is controlled only by the chemical potential μ_A of solute A in solvent B. Nanocrystalline materials are far from thermodynamic equilibrium. Their solid solubility is controlled by both thermodynamic and kinetic factors. On the thermodynamic side, the chemical potential is expected to change as the solvent structure changes from bulk to nanocrystalline. The solid solubility is therefore expected to be different [2,93]. On the kinetic side, solute atoms are trapped due to rapid solidification processing from liquid or vapor phases. In mechanical alloying, the strong atomic mixing caused by the external driving forces overcomes the slow

diffusion caused by the thermodynamic driving force. This results in strong mixing of the various elements of the alloy. The extended solid solubility in nanocrystalline alloys prepared by mechanical alloying is one of the topics studied in my thesis research. Details are given in later chapters. In short, the extended solid solubility in nanocrystalline materials modifies the thermodynamic equilibrium phase diagrams substantially and can result in the appearance of new alloy phases.

Magnetic Properties

Finemet [63,94-97] is an excellent soft magnetic material that exhibits simultaneous high saturation magnetic flux density B and high permeability μ. It is a nanocrystalline Fe-Si-B-Cu-Nb alloy prepared by rapid quenching to an amorphous state followed by partial crystallization upon annealing. Its soft magnetic properties are attributed to the dependence of the magneto-crystalline anisotropy on the grain size as described by the random anisotropy model. In large grains, the magnetic microstructure consists of ferromagnetic domains separated by domain walls. The magnetization in each domain follows the local easy magnetic direction and the magnetic coercive field is determined by the magneto-crystalline anisotropy of the crystal. For nanocrystalline materials, however, each grain may be smaller than the width of a domain wall. The magnetic moments do not align along the easy magnetic direction of each crystallite. The effective magneto-crystalline anisotropy constant can be taken as average over the randomly distributed anisotropy of each grain within the ferromagnetic exchange correlation length scale. The effective anisotropy constant is drastically smaller for nanocrystalline materials, giving excellent soft magnetic properties, i.e., low coercivity and high permeability. Uniform grain size, random texture, and small strain all help to improve the soft magnetic properties. Finemet should be useful

in services in many kinds of magnetic devices such as saturable reactors, choke coils, and transformers.

Another magnetic property, giant magnetoresistance (GMR), has also been observed in multilayered $Ni_{80}Fe_{20}$-Ag thin films with nanocrystalline grains (2 to 4 nm) [98] and other similar layered thin films [99]. The small grain sizes in the films minimize the effects of crystal and shape anisotropy, allowing local antiparallel alignment of the magnetic moment between adjacent layers. With large changes in resistance at low fields, these GMR materials can have important technical applications, for example, as magnetoresistive heads for high density magnetic recording.

Nanocrystalline barium ferrite powder is an excellent candidate for a high density magnetic recording medium [56]. Nanocrystalline barium ferrite particles produced by glass crystallization are hexagonal plate crystals of 53 nm in diameter and 18 nm in height. They are easily magnetized in the direction perpendicular to their wide surface. When they align in such a way that their hexagonal plate surfaces are parallel to the plane of the base film, they constitute a magnetic recording medium for the vertical magnetization recording method, which allows much higher recording density than conventional methods of recording parallel to the surface of the recording medium. It is expected that these media can provide a recording capacity of 4 Mb on each side of a 3.5 inch floppy disk – 4 times the current capacity of conventional recording media [100].

Mechanical Properties

Compared with conventional bulk materials, consolidated nanocrystalline materials can retain both higher strength and better ductility. According to the Hall-Petch equation

$$\sigma_{ys} = \sigma_i + \frac{k_y}{\sqrt{d}} \qquad (1.13)$$

the yield strength of polycrystalline materials is larger for smaller grain size d due to grain-boundary strengthening (grain boundaries serve as barriers to the glide of dislocations). Experiments have confirmed the validity of the Hall-Petch relation for consolidated nanocrystalline materials, and high strengths have been reported. As an example, the yield strength in compression tests of an Fe-28Al-2Cr alloy is 0.27 GPa for bulk material, but 2.1 GPa for shock wave consolidated nanocrystalline material of 80 nm grain size, an improvement by a factor of 8 [101]. While the bulk sample failed at a true strain of 0.3, the consolidated nanocrystalline sample did not fail even at a true plastic strain of 1.4. The ductility was improved by at least 5 times for the consolidated nanocrystalline sample. In addition, Karch *et al.* [102] have reported increased formability in nanophase CaF_2 and TiO_2 foils at 80 and 180 °C respectively, while Hahn *et al.* [103] have reported 60% ductility in 99% dense TiO_2 at 600 °C under far-field compression loading. Coble and other diffusive creep mechanisms have often been used to explain these trends in ductility [104,105]. The increased diffusional creep rate originates from the small grain size and increased grain boundary diffusivity. The higher strength and better ductility of nanocrystalline materials make them good candidates for structural applications.

In summary, nanocrystalline materials have many novel or enhanced properties when compared conventional large grained materials of the same chemical composition. They look attractive for many technical applications.

References

1. P. Duwez, R. H. Willens, and W. Klement Jr., J. Appl. Phys. **31**, 1136 (1960).
2. H. Gleiter, Prog. Mater. Sci. **33**, 223 (1989).
3. R. Birringer, Mater. Sci. Eng. **A. 117**, 33 (1989).
4. H. Gleiter, J. Appl. Cryst. **24**, 79 (1991).
5. F. H. Froes and C. Suryanarayana, JOM, 12 (June 1989).
6. R. W. Siegel, Annu. Rev. Mater. Sci. **21**, 559 (1991).
7. H. Gleiter, Nanostruct. Mater. **6**, 3 (1995).
8. C. C. Ahn and L. B. Hong, "Ballistic Consolidation of Nanophase Sn Prepared by Inert Gas Condensation", submitted to Nanostructured Mater., 1994.
9. J. S. Benjamin, Metall. Trans. **1**, 2943 (1970).
10. J. S. Benjamin and T. S. Volin, Metall. Trans. **5**, 1929 (1974).
11. J. S. Benjamin, Scientific American **234**, 40 (1976).
12. P. S. Gilman and J. S. Benjamin, Ann. Rev. Mater. Sci. **13**, 279 (1983).
13. R. Sundaresan and F. H. Froes, JOM, 22 (August 1987).
14. C. C. Koch, O. B. Cavin, C. G. McKamey, and J. O. Scarbrough, Appl. Phys. Lett. **43**, 1017 (1983).
15. R. B. Schwarz, R. R. Petrich, and C. K. Saw, J. Non-Cryst. Solids **76**, 281 (1985).
16. E. Hellstern and L. Schultz, Appl. Phys. Lett. **48**, 124 (1986).
17. R. B. Schwarz, Mater. Sci. Eng. **97**, 71 (1988).
18. K. Suzuki, J. Non-Cryst. Sol. **112**, 23 (1989).
19. L. Schultz, Phil. Mag. B **61**, 453 (1990).
20. A. R. Yavari and P. Desré, Mater. Sci. Eng. **A134**, 1315 (1991).
21. M. A. Morris and D. G. Morris, J. Mater. Sci. **26**, 4687 (1991).
22. Y. Chen, M. Bibole, R. Le Hazif and G. Martin, Phys. Rev. B **48**, 14 (1993).

23. Y. Chakk, S. Berger, B. Z. Weiss and E. Brook-Levinson, Acta metall. mater. **42**, 3679 (1994).

24. M. Abdellaoui and E. Gaffet, J. All. Comp. **209**, 351 (1994).

25. E. Hellstern, H. J. Fecht, Z. Fu, and W. L .Johnson, J. Mater. Res. **4**, 1292 (1989).

26. H. J. Fecht, E. Hellstern, Z. Fu, and W. L .Johnson, Adv. Powder Metall. **1-2**, 111 (1989).

27. B. Fultz, G. LeCaër, and P. Matteazzi, J. Mater. Res. **4**, 1450 (1989).

28. H. J. Fecht, E. Hellstern, Z. Fu, and W. L .Johnson, Metall. Trans. **21A**, 2333 (1990).

29. E. Hellstern, H. J. Fecht, Z. Fu and W.L. Johnson, J. Appl. Phys. **65**, 305 (1989).

30. J. S. C. Jang and C. C. Koch, J. Mater. Res. **5**, 325 (1990).

31. H. Bakker, L. M. Di and D.M.R. Lo Cascio, Solid State Phenomena **23-24**, 253 (1992).

32. H. Bakker, G. F. Zhou and H. Yang, Prog. Mater Sci. (1995) in the press.

33. R. W. Cahn, Diffusion in Ordered Alloys, B. Fultz, R. W. Cahn and D. Gupta Eds (Warrendale, TMS, 1993) p.125.

34. H. Schröpf, C. Kuhrt, E. Arzt and L. Schultz, Scripta metall. mater. **30**, 1569 (1994).

35. S. Gialanella, Intermetallics (1994), to be published.

36. S. Begin-Colin, G. Le Caër, A. Mocellin and M. Zandona, Phil. Mag. Lett. **69**, 1 (1994).

37. S. Begin-Colin, G. Le Caër, M. Zandona, E. Bouzy and B. Malaman, J. All. Comp. (1995) in press.

38. C. C. Koch and M. S. Kim, J. de Physique C **8**, 573 (1985).

39. E. Hellstern, L. Schultz, R. Bormann, and D. Lee, Appl. Phys. Lett. **53**, 1399 (1988).

40. C. C. Koch, Annual Rev. Mater. Sci. 121 (1989).

41. A. Calka and A. P. Radlinski, Scripta Metall. **23**, 1497 (1989).

42. C. Suryanarayana and F. Froes, J. Mater. Res. **5**, 1880 (1990).

43. C. Suryanarayana and R. Sundaresan, Mater. Sci. Eng. A **131**, 237 (1991).

44. K. Uenishi, K. F. Kobayashi, K. N. Ishihara, and P. H. Shingu, Mater. Sci. Eng. A **134**, 1342 (1991).

45. M. V. Zdujic, K. F. Kobayashi, and P. H. Shingu, J. Mater. Sci. **26**, 5502 (1991).

46. D. K. Mukhopadhyay, C. Suryanarayana, and F. H. Froes, Scripta Metall. Mater. **30**, 133 (1994).

47. G. Veltl, B. Scholz, and H.-D. Kunze, Mater. Sci. Eng. A **134**, 1410 (1991).

48. K. Sakurai, Y. Yamada, C. H. Lee, T. Fukunaga, and U. Mizatuni, Mater. Sci. Eng. A **134**, 1414 (1991).

49. C. Bansal, Z.Q. Gao, L. B. Hong, and B. Fultz, J. Appl. Phys.**76**, 5961 (1994).

50. L. B. Hong, C. Bansal, and B. Fultz, NanoStructured Materials **4**, 949 (1994).

51. L. B. Hong and B. Fultz, "Two-Phase Coexistence in Fe-Ni Alloys Prepared by Ball Milling at Two Intensities", submitted to Acta Metall. Mater., 1995.

52. J. Eckert, J. C. Holzer, and W. L. Johnson, J. Appl. Phys. **73**, 131 (1993).

53. J. Eckert, J. C. Holzer, C. E. Krill III, and W. L. Johnson, J. Appl. Phys. **73**, 2794 (1993).

54. J. Eckert, J. C. Holzer, C. E. Krill III, and W. L. Johnson, J. Mater. Res. **7**, 1980 (1992).

55. W. A. Baeslack III and F. H. Froes, JOM, 13 (March 1995).

56. N. Ichinose, Y. Ozaki, and S. Kashu, Superfine Particle Technology (Springer-Verlag, London, 1991).

57. R. L. Bickerdike et al., Internat. J. Rapid Solidification **1**, 305 (1984-85).

58. D. Tench and J. White, Met. Trans. A **15A**, 2039 (1984).

59. T. R. Anatharaman and C. Suryanarayana, Rapidly Solidified Metals – A Technological Overview (Aedermannsdorf, Switxerland: Trans Tech Publ., 1987).

60. W. L. Johnson, Prog. Mater. Sci. **30**, 81 (1986).

61. M. Jain, Ph. D. dissertation, California Institute of Technology, 1995.

62. L. H. Schwartz and J. B. Cohen, Diffraction from Materials (Springer-Verlag, Berlin, 1987) p. 224.

63. Z. Q Gao, Ph. D. dissertation, California Institute of Technology, 1994.

64. B. Fultz and J. Howe, Transmission Electron Microscopy and Diffractometry of Materials.

65. H. Ouyang, Ph. D. dissertation, California Institute of Technology, 1992.

66. G. K. Williamson and W. H. Hall, Acta Metall. **1**, 22 (1953).

67. H. P. Klug and L. E. Alexander, X-Ray Diffraction Procedures (Wiley-Interscience, New York, 1974) p. 664.

68. P. Scherrer, Gött. Nachr. **2**, 98 (1918).

69. H. P. Klug and L. E. Alexander, X-Ray Diffraction Procedures (Wiley-Interscience, New York, 1974) p. 656.

70. H. Ouyang, B. Fultz, and H. Kuwano, in Nanophases and Nanocrystalline Structures, R. D. Shull and J. M. Sanchez, eds., (TMS, Warrendale, 1994) p. 95.

71. B. Fultz, H. Kuwano, and H. Ouyang, J. Appl. Phys. 76, 5691 (1994).

72. J. B. Nelson and D. P. Riley, Proc. Phys. Soc. (London) **57**, 160 (1945).

73. H. P. Klug and L. E. Alexander, X-Ray Diffraction Procedures (Wiley-Interscience, New York, 1974) p. 594.

74. Editor U. Gonser, Mössbauer Spectroscopy (Springer-Verlag, New York, Heidelberg Berlin, 1975).

75. Editor Richard L. Cohen, Applications of Mössbauer Spectroscopy Vol. 1 (Academic Press, New York, 1976).

76. Editor Leopold May, An Introduction to Mössbauer Spectroscopy (Plenum Press, New York-London, 1971).

77. U. Herr, J. Jing, R. Birringer, U. Gonser, and H. Gleiter, Appl. Phys. Lett. **50**, 472 (1987).

78. S. Ramasamy, J. Jiang, H. Gleiter, R. Birringer, and U. Gonser, Solid State Commun. **74**, 851 (1990).

79. J. Jiang, S. Ramasamy, R. Birringer, U. Gonser, and H. Gleiter, Solid State Commun. **80**, 525 (1991).

80. G. Le Caër and J. M. Dubois, J. Phys. **E12**, 1083 (1979).

81. B. Fultz, "Chemical Systematics of Iron-57 Hyperfine Magnetic Field Distributions in Iron Alloys", in Mössbauer Spectroscopy Applied to Magnetism and Materials Science, G. J. Long and F. Grandjean, eds., (Plenum Press, New York, 1993) p.1.

82. B. Fultz and Z. Q. Gao, Nucl. Instr. and Methods in Phys. Res. B **76**, 115 (1993).

83. B. Fultz, Z. Q. Gao, H. H. Hamdeh, and S. A. Oliver, Phys. Rev. B **49**, 6312(1994).

84. Thermal Analysis Newsletter No. 9 (Perkin-Elmer Co., Norwalk, 1970).

85. C. C. Ahn, L. Hong, J. Eckert, B. Fultz, and W. L. Johnson, Energy Filtered Imaging of Nanophase Materials, Proc. 50th Annual Electron Microscopy Society of America, G. W. Bailey, J. Bentley, and J. A. Small Eds (Boston, 1992) p. 1196.

86. B. Fultz, C. C. Ahn, S. Spooner, L. B. Hong, J. Eckert, and W. L. Johnson, "Thermal Stability of Nanophase Fe-Cu Alloys Prepared by Mechanical Alloying", to be submitted (1995).

87. H. Morri, M. Komatsu, K. Takeda, and H. Fujita, Phil. Mag. Let. **63**, 173 (1991).

88. S. Schumacher, R. Birringer, R. Strauss, and H. Gleiter, Acta Metall. **37**, 2485 (1989).

89. Noda, Shinoda, and Saitou, Nihon Kagakukaishi, 1017 (1984); 472 (1987).

90. E. Hellstern, H. J. Fecht, Z. Fu and W. L. Johnson, J. Appl. Phys. **65**, 305 (1989).

91. J. Rupp and R. Birringer, Phys. Rev. B **36**, 7888 (1987).

92. L. B. Hong, C. C. Ahn, and B. Fultz, "The Debye Temperature of Nanocrystalline β-Sn Measured by X-ray Diffraction", J. Mater. Res. (1995).

93. Y. Abe and W. L. Johnson, J. Jpn. Soc. Powder and Powder Metall. **40**, 272 (1993).

94. Y. Yoshiozawa, S. Oguma, K. Yamauchi, J. Appl. Phys. **64**, 6044 (1988).

95. Y. Yoshizawa, K. Yamauchi, Mater. Sci. and Eng. **A133**, 176 (1991).

96. G. Hampel, A. Pundt, and J. Hesse, J. Phys.: Condens. Matter. **4**, 3195 (1992).

97. G. Herzer, Mat. Sci. and Eng. **A133**, 1 (1991).

98. T. L. Hylton, K. R. Coffey, M. A. Parker, and J. K. Howard, Science **261**, 1021 (1993).

99. K. R. Coffey, T. L. Hylton, M. A. Parker, and J. K. Howard, Appl. Phys. Lett. **63**, 1579 (1993).

100. Imamura, Koike, and Suzuki, Toshiba Review **40**, 1111 (1985).

101. M. Jain and T. Christman, Acta Metall. Mater. **42**, 1901 (1994).

102. J. Karch, R. Birringer and H. Gleiter, Nature **330**, 10 (1987).

103. H. Hahn and R. S. Averbach, Nanostruct. Mater. **1**, 95 (1992).

104. R. L. Coble, J. Appl. Phys. **34**, 1679 (1963).

105. M. F. Ashby and R. A. Verrall, Acta Metall. **21**, 149 (1973).

Chapter 2. Phase Transformations, Driven Alloys, and Monte Carlo Simulations

2.1 Phase Transformations: Thermodynamics and Kinetics

A phase is a state of matter that is homogeneous and distinct from other states. When a system changes its state from one phase to another, it is said to undergo a phase transformation. Comparing the phases before and after a transformation, there are three types of phase transformations [1]: (1) change in structure, (2) change in composition, and (3) change in degree of order.

Examples of a change in structure alone include solid state amorphization and devitrification, phase transformations between amorphous and crystalline solids. Other examples are melting, martensitic and massive transformations. Spinodal decomposition or phase separation from supersaturated solid solutions belong to the second category, change in composition alone. A change in degree of order alone occurs in β-brass (CuZn), for example. Below a critical temperature, T_c, Cu atoms have a strong tendency to have Zn atoms as their nearest neighbors on the bcc lattice. This is the B2 phase. Above T_c, all atoms are randomly arranged over large regions, forming the A2 phase. Upon slow cooling from high temperature to room temperature, the alloy changes from the A2 phase to the B2 phase, while keeping the lattice structure and composition unchanged. This type of phase transformation is also called a disorder –> order transformation, or ordering.

Most transformations in alloys are combinations of two or more of the three basic types. Supersaturated Fe_3Zn solid solution prepared by ball milling undergoes phase separation into bcc Fe and hcp Zn upon high temperature annealing. This is a combination of (1) and (2). In our mechanical alloying experiments, the transformations are typically

combinations of (1) and (2), sometimes combinations of all three (Fe + Sn –> ordered Fe_3Sn). The transformations the as-milled alloys undergo upon annealing are also typically combinations of the three types. The disorder –> order transformations or spinodal decomposition studied in our Monte Carlo simulations are (3) or (2) alone, respectively. In the following, we will focus on disorder –> order transformations of binary alloys.

At constant temperature and low pressure, the Helmholtz free energy, F, determines the stabilities of various alloy phases. The global minimum of F gives the thermodynamic equilibrium state of the system while a local minimum gives a metastable state. These states can be a single phase or a mixture of several coexisting phases. The Helmholtz free energy of a hypothetical system is given in Fig. 2.1. State f is the equilibrium state and i is a metastable state. State s may be at the saddle point of a multi-dimensional free energy curve, and is a unstable state. If the system is initially in a state other than f, statistical mechanics says that the system will undergo a phase transformation and eventually reach its thermodynamic equilibrium state f. Knowing the free energy, we can always employ statistical mechanics to predict the final state of a phase transformation.

However, statistical mechanics does not provide kinetic paths of phase transformations, or equivalently, what nonequilibrium states a nonequilibrium system must pass through before reaching its final thermodynamic equilibrium state. There are cases, such as driven alloys, where free energy is not easily obtainable or not clearly defined. We need features of kinetics that are beyond statistical mechanics to find the steady states as well as the kinetics of the phase transformations.

To study pseudostable states or transient states, we also need kinetics rather than statistical mechanics. The pseudostable state [2] was proposed recently as a name for states at a saddle point of a free energy function, where

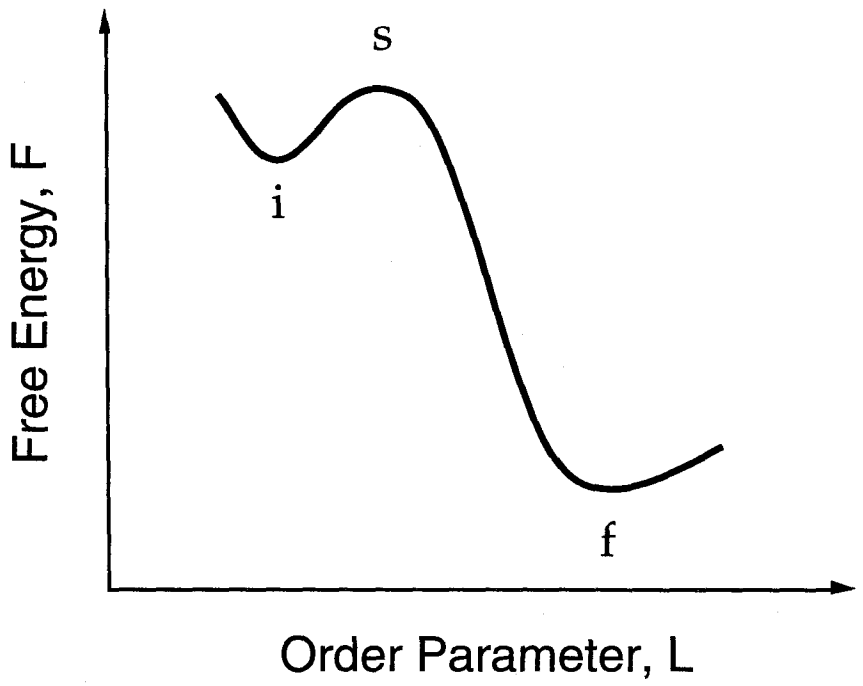

FIG. 2.1. Free energy curve of a system with equilibrium state f, metastable state i, and a saddle point s.

$$\frac{\partial F}{\partial \xi_i} = 0 \text{ for all state variables } \xi_i, \text{ and} \tag{2.1}$$

$$\text{the eigenvalues of } M_{ij} = \frac{\partial F}{\partial \xi_i \xi_j} \text{ have mixed signs.} \tag{2.2}$$

At this state, there is no thermodynamic driving force for ordering, and ordering should be slow when the state variables of the system are near those of the saddle point because

$$\frac{d\xi_i}{dt} = \sum_j (\gamma_{ij} \frac{\partial F}{\partial \xi_j}) \quad . \tag{2.3}$$

Therefore the pseudostable state is relatively long-lived, but it should disappear before equilibrium is eventually attained. In this sense, it is a transient state.

However, the concept of transient state is much more general than the concept of a pseudostable state, that is, it need be at a saddle point. As its name suggests, a transient state is a kinetic phenomenon and should disappear before the steady state or equilibrium state is attained. To study the appearance of transient states, we use a model system whose free energy is illustrated in Fig. 2.2. The free energy at stable state f, the initial unstable state i, and transient state t are F_i, F_f, and F_t, respectively. Because state i has very high free energy and is highly unstable, the system will undergo a phase transformation to reduce its free energy, and will eventually reach state f according to thermodynamic statistical mechanics. However, how will the system travel from i to f? Will it pass through state t? If the free energy difference $\Delta F_{fi} \sim \Delta F_{ti} >> \Delta F_{ft}$, then going from i to t can also reduce the free energy, and the thermodynamic preference for state f over state t is very weak. It is plausible that the system might pass through state t on its way to state f, that is, state t can appear transiently. State t can appear alone (for example, the transient DO_3 ordering of Fe_3Ge in Chapter 7), or appear together with the state f (see Chapter 4 for examples). In either case, the transient state formation is due to kinetics instead of

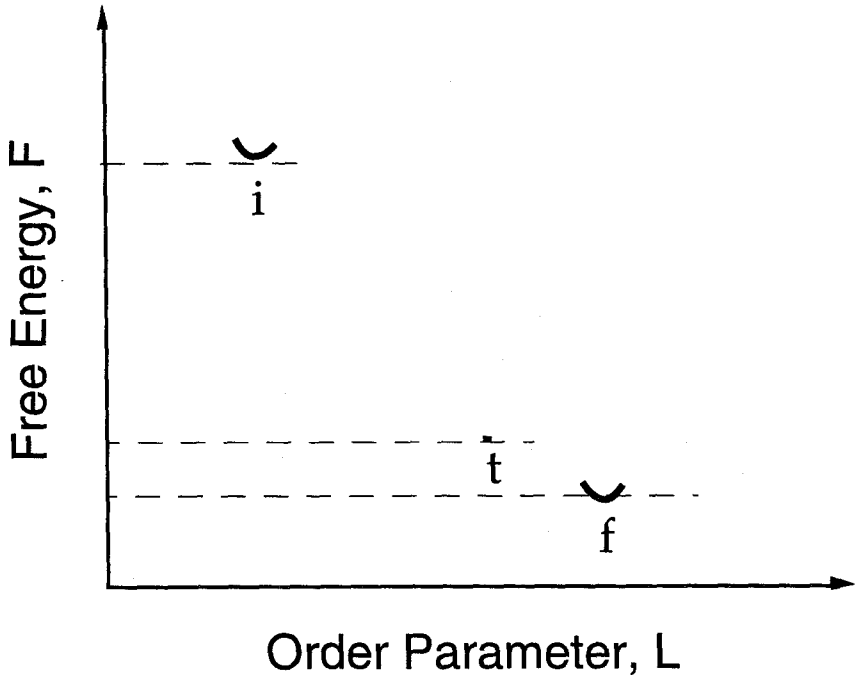

FIG. 2.2. Free energy of a system with equilibrium state f, metastable state i, and a transient state t.

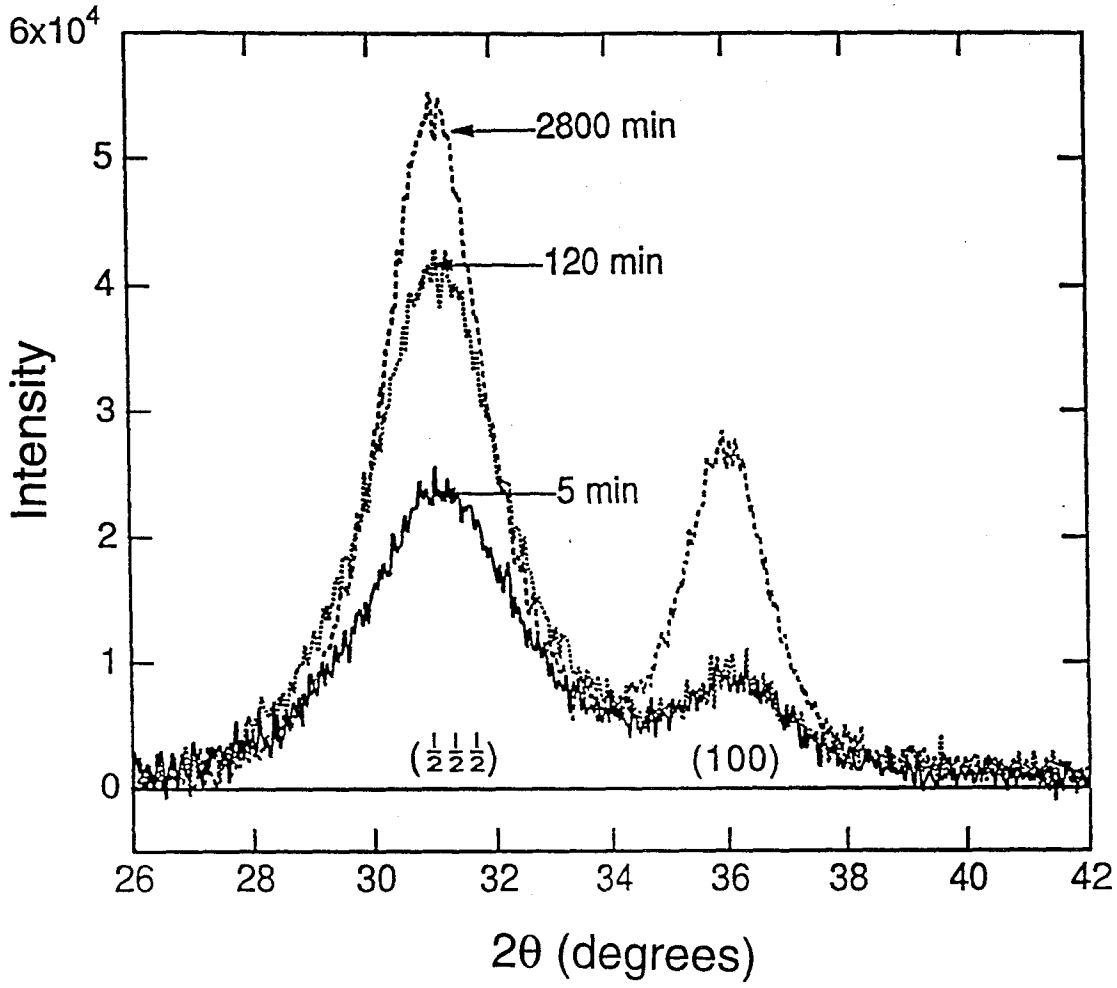

FIG. 2.3. Growth of superlattice diffraction peaks in an initially piston-anvil quenched Fe_3Al sample upon annealing at 300 °C for various times. There is transient B32 order between 5 min and 120 min annealing, seen by the growth of the $(\frac{1}{2}\frac{1}{2}\frac{1}{2})$ diffraction while the (100) remains unchanged [3].

thermodynamics. How strongly the transient state can form also depends on kinetic factors. For example, if state t forms on a much smaller spatial or time scale than state f, then the transient formation state t can be very strong (such as transient B2 ordering in disorder –> phase separation in Section 4.2.3). Even in the opposite situation, however, a transient state can still form (see also Section 4.2.3). Also we might expect that a transient state can form more strongly for smaller ΔF_{fi}. There is experimental evidence of transient ordering. Figure 2.3 shows transient B32 order in a piston-anvil quenched Fe_3Al sample upon annealing at 300 °C [3], while Fig. 7.5 shows transient DO_3 order in a ball milled Fe_3Ge sample upon annealing at 350 °C.

If the energy difference ΔF_{fi} is so small that some external driving force can alter its sign (as in a "driven alloy") , then the relative stability of states f and t can be switched. Also if the external driving force can spread the free energy into a broad distribution, and cause the energy bands associated with states f and t to overlap, then both state f and state t can co-exist. These new concepts appear frequently in my thesis work.

To study the kinetics of ordering, there are three approaches: the theoretical analytical approach, computer simulation, and experimental research. I used all three, but only the first two are described in this chapter. My theoretical study used two different approaches. Onsager kinetic rate equations are based on the control of kinetics by the thermodynamic free energy. The rate of change of an order parameter, L, is given as [4]

$$\frac{dL}{dt} = -\frac{l}{kT}\frac{\partial F}{\partial L} \quad , \tag{2.4}$$

where l is the mobility coefficient that depends on the kinetic mechanism. This approach is employed in the treatment of ordering kinetics of driven alloys in section 3.3.

My second approach to theoretical studies of kinetics is based on activated state rate theory, and includes the Master Equation Method (MEM) [5-9] and Path Probability

Method (PPM) [10-13]. As in Fig. 2.1, the system must surmount a free energy barrier between the initial state i and saddle point s in order to go from state i to final state f. Subscripts i, f and superscript * are conventionally used to denote free energies at states i, f, and s, respectively. The free energy barrier is

$$\Delta F = F^* - F_i = (E^* - E_i) - T(S^* - S_i) \quad . \tag{2.5}$$

Then, the probability of success for an attempt to transfer from i to f is

$$P = \exp\left(\frac{-\Delta F}{kT}\right) = \exp\left(\frac{E_i - E^*}{kT}\right)\exp\left(\frac{S^* - S_i}{k}\right) \quad . \tag{2.6}$$

In a study of ordering kinetics, the transformation occurs step by step, which is typically an atom jump. For an attempt frequency ν, the atom jump frequency is

$$\omega = \nu \exp\left(\frac{E_i - E^*}{kT}\right)\exp\left(\frac{S^* - S_i}{k}\right) \quad . \tag{2.7}$$

The entropy change during one atom movement could be small and virtually the same for all possible atom jumps. The attempt frequency, ν, and the saddle point energy, E^*, are both taken to be constant for all the jumps. These constant contributions to the jump frequency are typically set to 1 without loss of generality, then

$$\omega \propto \exp\left(\frac{E_i}{kT}\right) \quad . \tag{2.8}$$

This equation has been widely used in analytical kinetic theories such as PPM and MEM as well as in computer simulations of kinetics.

While my computer simulations will be described in detail later in this chapter, the Master Equation approach is reviewed briefly here. The Master Equation for alloy ordering kinetics with only one order parameter can be written as

$$\frac{d\mathbf{P}_i}{dt} = \sum_{i'} \left(\omega_{i'}^{i} \mathbf{P}_{i'} - \omega_{i}^{i'} \mathbf{P}_i \right) \quad . \tag{2.9}$$

Here the state of order is represented by the vector **P** (or a matrix for alloys with multiple order parameters), whose components represent the probabilities of the various possible states of order. Using activated state rate theory, the transition probabilities between two states of order (i and i') are given by the matrix $\omega_i^{i'}$, each element of which takes the form of Eq. 2.8. The Master Equation approach in the Bragg-William approximation was employed in the Sec. 3.1 to study the ordering kinetics of driven alloys.

2.2 Driven Alloys

As discussed in the previous section, thermodynamics and statistical mechanics are the standard tools for understanding phase transformations in materials. States of thermodynamic equilibrium are expected when atom movements are consistent with activated state rate theory. There are, however, a number of examples where some atom movements in alloys or semiconductors are not expected to be understood by activated state rate theory alone: (1) alloys subjected to high energy ball milling [14], a widely used technique to synthesize far-from-equilibrium alloys; (2) intermetallics in superalloys under cyclic fatigue, which can cause γ' precipitates in slip bands to undergo sustained shearing and redissolution [15]; (3) alloys under high energy ion bombardment (irradiation) [16], such as $FeZr_2$ in Zircalloy used as a cladding material in pressurized water nuclear reactors. These alloys are sustained in nonequilibrium states by permanent (continuous) external driving, such as nuclear collisions, shearing, fracturing, and welding. For simplicity, they are called "driven alloys" or "driven systems".

Due to external driving, some atom movements in driven alloys occur with a greater element of randomness than expected from the Boltzmann factors of activated state rate theory. These "forced" or "ballistic" atom movements tend to move atoms out of local environments characteristic of their thermodynamic distribution. Acting in parallel are the

usual thermal movements, which tend to restore these thermodynamic environments. Because both kinetic processes are Markovian, a steady state, which is unique at given conditions, will be achieved eventually [17]. This steady state is termed a "dynamical steady state" to distinguish it from the steady state of thermodynamic equilibrium.

Nonequilibrium or dynamical (kinetic) phase transformations [18] between dynamical steady states of driven systems have been of interest in a large variety of fields [19] besides materials science [20], such as physical chemistry [18,21] and electrical engineering [22]. Unlike thermodynamic phase transformations, the conventional Helmholtz or Gibbs free energy is not as useful for understanding dynamical phase transformations because it does not take into account the external driving. In particular, we can not minimize a free energy to obtain the steady state of a driven alloy.

To model these dynamical phase transformations, G. Martin et al. proposed a model of driven systems that is amenable to study by analytical methods and computer simulations [23-36,37-39]. In this model, the ballistic atom movements are assumed to occur at random (at an infinite temperature), and therefore are completely insensitive to the local chemical preferences of an atom. Meanwhile, the thermal atom movements follow conventional activated state rate theory. Kinetic events sample all outcomes with equal probability. While this model is an oversimplification of the processes that occur in high-energy ball milling and ion beam bombardment, it does include an essential difference between driven systems and thermodynamic systems. In fact, Martin and Bellon's early work [23,31,32] on dynamic ordering with this model (ballistic diffusion / Lyapunov functional) has found qualitative agreement with the observed irradiation-induced inversion of the relative stability of two ordered phases (LRO and SRO) as well as the domain of bistability in irradiated Ni_4Mo [40].

Most of Martin and co-workers' studies of steady states of ordering used the Master Equation approach with the pair interchange mechanism (two neighboring A and B atoms exchange their positions directly without the help of vacancy, with an exchange frequency given by Eq. 2.8 in thermodynamic case). Their theories were developed along two lines. Along the first line, they sought to balance the diffusional flux of either type of atoms between the two sublattices so that the average concentration of atoms on each sublattice would remain constant and the steady states would be found [23,24,26,27,31,32,34-36]. This gave the relationships between order parameter, temperature, driving intensity, and interatomic potentials at steady states. In particular, dynamic critical temperature was obtained. The second line followed the thermodynamic treatment of a thermodynamic system, i.e., minimizing the thermodynamic free energy in various approximations to obtain the thermodynamic equilibrium states. Much work was devoted to constructing and elucidating the properties of a "stochastic potential", which is the analogy for a driven alloy of the free energy for a thermodynamic alloy [23,24,32,35]. We review this stochastic potential approach here.

In thermodynamic equilibrium, statistical mechanics gives the probability of a state i with energy E_i as

$$P_i = \frac{\exp(-\beta E_i)}{Z} \quad , \tag{2.10}$$

with $\beta = 1 / kT$ and Z the partition function, which is the normalization constant. Suppose E and the free energy F are functions of a single order parameter L. Then the probability of observing a given value of L is:

$$P(L) = \frac{\exp(-\beta F(L))}{Z} \quad . \tag{2.11}$$

From Eq. 2.11, the respective stability of two states characterized by L1 and L2 is estimated from their respective probabilities: $\frac{P(L1)}{P(L2)}$, i.e., from the difference of their free

energies. In driven alloys, the conventional free energy becomes less meaningful and can not be used in the same way. However, from the same principle, we can build an alternative "free energy", the stochastic potential, which can be readily used to compare relative stability of various states of the driven alloy in the same manner.

To illustrate how to build the stochastic potential, we choose a simple case: B2 (or checkerboard) ordering in an bcc (or square) alloy with AB stoichiometry. The order parameter L is given by N, the number of A atoms on one of the two sublattice. At steady state, N is constant, that is:

$$P(N-1)\omega_{N-1/N} - P(N)\omega_{N/N-1} = P(N)\omega_{N/N+1} - P(N+1)\omega_{N+1/N} \qquad (2.12)$$

according to the Master Equation (Eq. 2.9). $\omega_{N-1/N}$ is the transition rate from state N-1 to state N.

In the absence of forcing, i.e., in the thermodynamic case, there exists "detailed balance" of kinetics between states N-1 and N:

$$P(N-1)\omega_{N-1/N} - P(N)\omega_{N/N-1} = 0 \quad \text{or} \quad \frac{P(N-1)}{P(N)} = \frac{\omega_{N-1/N}}{\omega_{N/N-1}} \quad . \qquad (2.13)$$

By iteration, this gives

$$\frac{P(N)}{P(N_0)} = \prod_{N0+1}^{N} \frac{\omega_{N-1/N}}{\omega_{N/N-1}} \quad . \qquad (2.14)$$

Calculating ω's with the activated state rate theory in the Bragg-Williams approximation and minimizing P(N) with respect to N gives the same steady state order parameter, that is obtained when the thermodynamic free energy in the Bragg-Williams approximation itself is minimized.

In the presence of driving, the ω's have an additional contribution from the driving, ω_f, as in Eqs. 3.6 and 3.18. Equation 2.13 still holds at steady state, as does Eq. 2.14, but now we need to use new ω's. Equation 2.14 becomes

$$\frac{P(N)}{P(N_0)} = \prod_{N0+1}^{N} \frac{\omega_{N-1/N} + \omega_{N-1/N\_f}}{\omega_{N/N-1} + \omega_{N/N-1\_f}} \tag{2.15}$$

$$= \exp\left(\Omega(\Phi(N) - \Phi(N_0))\right) \tag{2.16}$$

with $$\Omega[\Phi(N) - \Phi(N_0)] = \sum_{n=N_0+1}^{N} \ln\left(\frac{\omega_{N-1/N} + \omega_{N-1/N\_f}}{\omega_{N/N-1} + \omega_{N/N-1\_f}}\right) . \tag{2.17}$$

By comparison with Eqs. 2.10 and 2.11, Ω is the stochastic potential, the counterpart in the driven alloy to the free energy in the thermodynamic alloy. However, Ω is not so easily obtainable as the right-hand side of Eq. 2.15, and often requires numerical calculation.

Theoretically, the minimum of the stochastic potential gives the dynamical steady state of a driven system. Relationships between various parameters and external driving intensity, as well as the dynamical critical temperature, can be obtained. As in the first (kinetic) approach, this stochastic potential is also sensitive to features of the kinetic mechanism. For example, a dependence of the dynamical critical temperature on the details of replacement collision sequences was found previously [23,24,27]. As always for approximate kinetic theories, however, the stochastic potential is also sensitive to the nature of the approximation (point or pair, for example).

It is widely known that driven alloys have very different properties from thermodynamic alloys without driving; dynamical phase transformations are substantially different from thermodynamic ones. As early as in 1943, Evgene Wigner predicted a decreased lifetime for structural materials experiencing fast neutron bombardment in the

just-invented nuclear reactor [41]. The irradiation damage phenomena of driven alloys became known as "Wigner's disease" when observed later on. More recently, Martin and Hong et al. showed that in comparison to alloy kinetics based on activated state rate theory, with ballistic jumps the kinetics and the final steady states of driven systems can be altered substantially [23-39].

2.3 Monte Carlo Simulations

Experiment and theory had been the only two approaches to doing science until only a few decades ago. Now with the surge of computing power and the rapid development of computer algorithms, computer simulation has quickly become a third approach complementary to the first two traditional approaches.

The reasons are twofold. First of all, computer simulation yields *exact* information, apart from statistical fluctuations, on *model* systems which are characterized precisely. Meanwhile, analytical kinetic theories are rarely solvable exactly. Even the thermodynamic Ising model [42,43], the simplest model for ordering of binary alloys, can be solved exactly only in one [43] and two dimensions [44,45], not in three dimensions [46]. Analyses in two and three dimensions typically require various approximations [47-50]. It is often necessary to employ computer simulations to check the validity of the approximations made in the analytical treatment of a model. Similarly, experiments are rarely precisely characterized, leading to controversies on the intrinsic nature of the observed phenomena. This can pose problems for comparisons between experiment and theory. Being exact and precisely characterized, computer simulations can serve to bridge the gap between experiment and theory.

Secondly, model systems studied by computer simulations can be designed arbitrarily so much richer phenomena can be observed. In contrast, the choice of systems

studied by experiment are typically very limited. For example, alloy ordering studies can take arbitrary atom interaction potentials in simulations, but experiments have to take whatever the real alloys possess. Searches for particular phenomenon, such as transient B32 order in binary alloys, consequently proves much easier in simulations than in experiments. Computer simulation has its own merits as a third approach to scientific study.

There are many computer simulation methods and applications in statistical physics and condensed matter physics [51-53]. Monte Carlo simulation refers to a class of computer simulation methods based on "random sampling". It has been applied to a large variety of fields, including ordering transitions. In this thesis, Monte Carlo simulations have been used to study ordering transitions and spinodal decomposition of binary alloys. While results and discussion will be presented in the following two chapters, details of the simulation method itself are given in the following.

Monte Carlo simulations were performed for equiatomic binary bcc and square alloys with periodic boundary conditions. The typical lattice had $N = 32 \times 32 \times 32 \times 2 = 65\ 536$ sites for bcc alloys or $N = 256 \times 256 = 65\ 536$ sites for square alloys, but larger lattices of 262 144 or 524 288 sites were also used. All sites of the lattice were occupied by either A or B atoms, except for one site left unoccupied as a vacancy for use in the vacancy mechanism.

For bcc alloys, we considered only the first and second nearest neighbor (1nn and 2nn) pairwise interactions between the two species of atoms, A and B. The i^{th} ($i = 1$ or 2) nearest neighbor pairwise exchange potential V_i is defined as:

$$V_i \equiv V_{AAi} + V_{BBi} - 2\,V_{ABi} \quad , \tag{2.18}$$

where V_{MNi} (M, N = A or B) is the i^{th} nearest neighbor M-N pair potential in units of k_BT. For convenience, the ratio of 2nn and 1nn pair potentials, ν, is also defined:

$$v \equiv \frac{V_2}{V_1} \quad . \tag{2.19}$$

For square alloys, we considered only the 1nn pairwise interactions, and define the interchange potential V similarly:

$$V \equiv \frac{V_{AA} + V_{BB} - 2V_{AB}}{2} \quad . \tag{2.20}$$

Please note that the factor of 2 difference between Eqs. 2.18 and 2.20 to follow different conventions.

The intensity parameter of external driving, f, is defined as:

$$f \equiv \text{fraction of ballistic jumps} \equiv \frac{\text{number of ballistic jumps}}{\text{total number of jumps}} \quad . \tag{2.21}$$

f was the intensity parameter fixed during the simulation.

Each kinetic step occurred with a vacancy mechanism [54,55], modified to include ballistic atom movements. The vacancy mechanism provides a richness of kinetic features that are not available with the pair interchange mechanism, which was also explored but not covered in this thesis. The vacancy mechanism can offer new ways by which the mechanism of atom movements can affect the dynamical steady state of the alloy [24, 37-39]. Especially at low temperatures, the vacancy mechanism exhibits subtleties of behavior that cannot be included in analytical theories based on approximations with small cluster variables. The present Monte Carlo simulation work examined how the strong diffusional correlation factors unique to the vacancy mechanism [37-39,54-59] affect the phase boundaries between disordered and various ordered phases at different temperatures, T, fractions of ballistic atom movements, f, and atom pair interaction potentials, V's.

In the vacancy mechanism, an atom moves only by exchanging its position with a neighboring vacancy. All z (z is the 1nn lattice coordination number, and z = 8 for bcc lattice and z = 4 for square lattice) nearest neighboring atoms of the vacancy compete to

exchange position with the vacancy. One Monte Carlo step is defined as the number of atom movements equal to the number of sites in the lattice. The number of Monte Carlo steps was found to be nearly proportional to the time elapsed [55], so we used Monte Carlo steps as a convenient time scale.

The vacancy algorithm was modified in the following way to include ballistic jumps. Before each movement, a random number, R, is chosen, where $0 \leq R < 1$. If $R < f$, the movement is determined to be ballistic. If so, all z neighboring atoms have an equal probability of exchanging positions with the vacancy, and one of them is chosen at random. Otherwise the movement is a thermal jump, and every neighboring atom has its own thermal jump frequency, ω_j. The thermal jump probabilities, $\{p_j\}$, are set by the competition among all z neighboring atoms:

$$p_j = \frac{\omega_j}{\sum_{j'=1}^{z} \omega_{j'}} \quad . \tag{2.22}$$

Using these thermal jump probabilities, $\{p_j\}$, as weights, the Monte Carlo algorithm then selects randomly one of the neighboring atoms to exchange positions with the vacancy.

The thermal jump frequencies, $\{\omega_j\}$, are calculated according to activated state rate theory as described above. We rewrite Eq. 2.8 as:

$$\omega_j = \exp\left(\frac{E_j}{k_B T}\right) \quad . \tag{2.23}$$

Remember that E_j is the initial state energy for the jumping atom (the j^{th} neighbor of the vacancy). It is determined only by the configurational environment of the j^{th} atom alone and is calculated by summing the energy needed to break all its chemical bonds with other atoms:

$$E_j = \sum_i \left(N_{AAi} V_{AAi} + N_{BBi} V_{BBi} + N_{ABi} V_{ABi} \right) \quad , \tag{2.24}$$

where N_{MNi} are the number of i^{th} nearest neighbor M-N bonds (i = 1 or 2; M, N = A or B) to our j^{th} atom. Note that E_j (Eq. 2.24) differs from V_i (Eq. 2.18) or V (Eq. 2.20) in significant ways. In particular, V_i (V) depends only on the sum of V_{AAi} and V_{BBi} when $V_{ABi} = 0$, whereas E_j depends on their individual values. When f = 0, the driven alloys revert to thermodynamic alloys (without driving), and the above vacancy mechanism is that of a thermodynamic transformation.

Finally, we note that our approach of fixing the fraction of ballistic jumps, f, may seem different from previous work that used a constant jump frequency for ballistic jumps [23-34]. For example, the thermal jump rate depends on the state of order in the alloy, so a constant ballistic jump rate may be more appropriate for determining the kinetics of the alloy. For determining the steady states of a given alloy, however, both methods must provide the same result, since both L and f are constant in steady state, and are set by temperature and the ballistic jump rate. In particular, we expect the steady-state critical temperature and the dynamical phase diagram to be the same with either approach.

2.4 Characterization of Simulated Alloys

All simulations started from an initially random arrangement of atoms (characteristic of a quench from $T = \infty$) unless otherwise specified. The simulated lattice was examined periodically to obtain the internal energy density e, average domain length scale <r>, Warren-Cowley SRO parameters $\{\alpha(r)\}$ [60], and the LRO parameters, L for square lattices and L_{B2}, L_{B32} for bcc lattices. The simulated lattice was also saved periodically for direct observation and further characterization.

Internal Energy Density e

The pair interaction potentials for all atom pairs in the alloy were summed. A subsequent normalization by the number of atoms gave the internal energy density e of the alloy. The entropy can be estimated by an approach based on the cluster variation method (CVM) [61-63], but entropy measurements were performed routinely in the present work. Although the internal energy is just part of the free energy, it still plays a significant role, especially at the low temperatures used in the present work and when there is a high degree of order in the alloy as in many steady state microstructures.

Average Domain Length Scale <r>

To determine a characteristic length of the ordered domains on square lattices, <r>, we calculated a real space autocorrelation function after the alloy was transformed as follows. First, an overlay mask for the perfect ordered structure was generated for all x- and y-coordinates (i and j, respectively) of the lattice. For i+j even, each site in the mask was +1; for i+j odd, the site was −1. The alloy itself was then transformed by first assigning a value of +1 to each alloy site occupied by an A-atom, and −1 to each site occupied by a B-atom. These numbers of ±1 for all sites in the alloy were then multiplied by the numbers for their corresponding sites (same (i, j)) of the mask. This generated the transformed alloy. (For alloys having a strong domain structure, the different domains were seen in the transformed alloy as regions of sites with a preponderance of either +1 or −1.) The autocorrelation function of the transformed alloy, A⊗A, was then calculated by the usual procedure:

$$A\otimes A(\mathbf{R}) = \sum_{i=1}^{256} \sum_{j=1}^{256} A(i, j) \times A(i+R_i, j+R_j) \quad . \tag{2.25}$$

The autocorrelation function, A⊗A(**R**), was calculated for various magnitudes |**R**| (where $|\mathbf{R}| = \sqrt{R_i^2+R_j^2}$), and then averaged over the x- and y-directions. We determined the first zero crossing on graphs of the averaged A⊗A versus |**R**|. This value of |**R**| at the first zero crossing was defined as the characteristic length of ordered domains for the ordered alloy, <r>.

In the case of spinodal decomposition on square lattices, phase separated domains were formed instead of ordered domains. The characteristic length of phase separated domains on square lattices was calculated similarly as for ordered domains, except that the alloy itself, with +1 for A atoms and -1 for B atoms, was used in autocorrelation function calculation (the mask was unnecessary).

SRO Parameters $\{\alpha(r)\}$

Information on local atom arrangement is provided by the Warren-Cowley short range order (SRO) parameters, $\{\alpha(r)\}$, which are defined [60]:

$$\alpha(r) \equiv 1 - \frac{p_A}{x_A} \equiv 1 - \frac{p_B}{x_B} \quad , \tag{2.26}$$

with p_A (p_B) the probabilities of finding an A (B) atom as a r-th neighbor of a B (A) atom and x_A (x_B) the concentration of A (B) atoms. During simulations, $\{\alpha(r)\}$ were computed by counting the numbers of all rnn A-B pairs N_{ABr} (r = 1,2):

$$\alpha(r) = 1 - \frac{4N_{AB1}}{z_r N} \quad , \tag{2.27}$$

where z_r is the lattice coordination number for the r-th shell. Specifically,

$$\alpha(1) = 1 - \frac{N_{AB1}}{N} \quad , \qquad \alpha(2) = 1 - \frac{N_{AB2}}{N} \quad , \tag{2.28a,b}$$

for square lattices. $\alpha(1) = \alpha(2) = 0$ for the disordered state, and $\alpha(1) = -\alpha(2) = -1$ for perfect order.

LRO Parameters

To characterize the structural evolution during phase transformations, long range order (LRO) parameters (L_{B32}, L_{B2}, and L_{umx} for B32 order, B2 order, and the unmixed state of bcc alloys, or L for checkerboard ordering of square alloys) were calculated with a simulated x-ray diffraction procedure [9,37-39], which provided kinematical diffraction intensities, $I(\mathbf{k})$, through three-dimensional (or two-dimensional for square alloys) Fourier transformation:

$$I(\mathbf{k}) = \left| \sum_{\text{all sites}} f_{at}(\mathbf{r}) \exp(-i\mathbf{k}\cdot\mathbf{r}) \right|^2 \quad , \tag{2.29}$$

where $f_{at}(\mathbf{r})$ is the atomic form factor for the atom at site $\mathbf{r}$, and $f_{at} = 1$ for A-atoms and $f_{at} = 0$ for B-atoms.

For bcc alloys, non–zero intensities of the superlattice peaks $(\frac{1}{2}\ \frac{1}{2}\ \frac{1}{2})$ and (100) measured the extent of B32 and B2 order, respectively, while the excess intensity of the transmitted beam (000) (minus the (000) intensity of the random alloy) measured the degree of unmixing. We defined LRO parameters, L_{B32}, L_{B2}, and L_{umx}, as the square root of the intensities of the $(\frac{1}{2}\ \frac{1}{2}\ \frac{1}{2})$, (100), and (000) peaks, respectively, after normalizing by the intensity of the fundamental (110) peak of the random alloy:

$$L_{B32} = \left(\frac{2\, I_{1/2\,1/2\,1/2}}{I_{110}} \right)^{1/2} \quad , \tag{2.30}$$

$$L_{B2} = \left(\frac{I_{100}}{I_{110}} \right)^{1/2} \quad , \tag{2.31}$$

$$L_{umx} = \left(\frac{I_{000}}{I_{110}} \right)^{1/2} \quad , \tag{2.32}$$

where all the peak intensities were obtained by summing the corresponding $I(\mathbf{k})$ over a cubical volume of edge length $\pi/(4a)$ (a is the lattice constant of the bcc lattice) around their centers in **k**-space.

For square alloys, the lowest order superlattice diffraction peak corresponding to the checkerboard ordered structure is $(\frac{1}{2}\ \frac{1}{2})$, while the lowest order fundamental peak is (10). The intensities of these peaks, $I_{1/21/2}$ and I_{10}, were obtained by integrating $I(\mathbf{k})$ over a square around their centers in k-space of edge length $\frac{2\pi}{16a}$. The LRO parameter, L, was then obtained from the intensities in a way similar to that for bcc alloys:

$$L = \left(\frac{I_{1/21/2}}{I_{10}}\right)^{1/2} \quad . \tag{2.33}$$

For our choices of scattering factor and normalization, all the order parameters, L_{B32}, L_{B2}, L_{umx}, and L, ranged from 0 and 1, with 1 corresponding to perfect B32 or B2 order, or complete unmixing of bcc alloys, or perfect checkerboard order of square alloys, respectively.

Our interest was in determining the steady states of the alloys, but the identification of steady states required monitoring their kinetic behavior. Steady states were identified when the LRO and SRO parameters did not change if the simulation proceeded further, except for expected fluctuations. To ensure that the steady state was attained, we typically waited for times that were a factor of ten longer than the time for which the steady state values of these order parameters were first detected. In several cases we confirmed that the steady states were indeed correct by starting the simulations with the alloys having perfect ordered structures of various types, and verifying that the same values of order parameters were eventually attained as for the cases of starting from disordered alloys.

References

1. Morris E. Fine, Introduction to Phase Transformations in Condensed Systems, (the Macmilan Company, New York, 1964), Chap. 1.
2. B. Fultz, Phil. Mag. B **67**, 253 (1993).
3. Z. Q. Gao and B. Fultz, Phil. Mag. B **67**, 787 (1993).
4. A. G. Khachaturyan, Prog. Mater. Sci. **22**, 1 (1975).
5. B. Fultz, Acta Metall. **37**, 823 (1989).
6. L. Anthony and B. Fultz, J. Mater. Res. **4**, 1132 (1989).
7. B. Fultz, J. Mater. Res. **5**, 1419 (1990).
8. B. Fultz, J. Mater. Res. **7**, 946 (1990).
9. L. Anthony and B. Fultz, J. Mater. Res. **9**, 348 (1994).
10. R. Kikuchi, Ann. Phys. **10**, 127 (1960). Prog. Theor. Phys. Suppl. **35**, 1 (1966).
11. R. Kikuchi and H. Sato, J. Chem. Phys. **51**, 161 (1969).
12. H. Sato and R. Kikuchi, Acta Metall. **24**, 797 (1976).
13. K. Gschwend, H. Sato, and R. Kikuchi, J. Chem. Phys. **69**, 5006 (1978).
14. See, for example: C. C. Koch, O. B. Kalvin, C. G. McKamey, and J. O. Scarbrough, Appl. Phys. Lett. **43**, 1017 (1983). R. B. Schwarz, R. Petrich, and C. Saw, J. Non-Cryst. Solids **76**, 281 (1985). J. Eckert, J. C. Holzer, C. E. Krill, III, and W. L. Johnson, J. Appl. Phys. **73**, 2794 (1993).
15. Y. Brechet, F. Louchet, C. Marchionni, and J. L. Verger-Gaugry, Phil. Mag. **56**, 353 (1987).
16. See, for example: K. C. Russell, Prog. Mater. Sci. **18**, 229 (1984). J. S. Williams, R. G. Elliman, W. L. Brown, and T. E. Seidel, Phys. Rev. Lett. **55**, 1482 (1985). H. A. Atwater, C. V. Thompson, and H. I. Smith, Phys. Rev. Lett. **60**, 112 (1988).

17. W. Feller, An Introduction to Probability Theory and Its Applications, Vol 1 (John Wiley, New York, 1957) Chapter 15.
18. F. Schlögl, Phys. Rep. 62, 267 (1980).
19. H. Haken, Advanced Synergetics (Springer, Berlin, 1983).
20. L. Kubin and G. Martin eds., Non Linear Phenonmena in Materials Science (Trans. Tech., Aedermannsdorf, 1988).
21. H. K. Janssen, Z. Phys. 270, 67 (1974).
22. R. Landauer, J. Appl. Phys. 33, 2209 (1962).
23. P. Bellon and G. Martin, Phys. Rev. B **38**, 2570 (1988).
24. P. Bellon and G. Martin, Phys. Rev. B **39**, 2403 (1989).
25. G. Martin, Phys. Rev. B **41**, 2279 (1990).
26. F. Haider, P. Bellon and G. Martin, Phys. Rev. B **42**, 8274 (1990).
27. E. Salomons, P. Bellon, F. Soisson, and G. Martin, Phys. Rev. B **45**, 4582 (1992).
28. P. Bellon, Phys. Rev. B **45**, 7517 (1992).
29. P. Bellon, F. Soisson, and G. Martin, in Diffusion in Ordered Alloys, B. Fultz, R. W. Cahn, and D. Gupta, eds. (TMS, Chicago, 1992).
30. F. Haider, in Ordering and Disordering in Alloys, edited by A. R. Yavari (Elsevier, Amsterdam, 1992.
31. G. Martin, Phys. Rev. B **30**, 1424 (1984).
32. P. Bellon and G. Martin, J-LESSC-MET **145**, 465 (1988).
33. Y. Grandjean, P. Bellon, and G. Martin, Phys. Rev. B **50**, 4228 (1994).
34. F. Soisson, P. Bellon, and G. Martin, J. Phys. IV 4, 183 (1994).
35. F. Soisson, P. Bellon, and G. Martin, Phys. Rev. B **46**, 11332 (1992).
36. Y. Grandjean, P. Bellon, and G. Martin, Phys. Rev. B **50**, 4228 (1994).
37. L. B. Hong, L. Anthony, and B. Fultz, J. Mater. Res. **10**, 126 (1995).
38. L. B. Hong and B. Fultz, Phys. Rev. B **51**, 2687 (1995).

39. L. B. Hong and B. Fultz, Phys. Rev. B **52**, (1995).

40. K. C. Russell, Prog. Mater. Sci. **18**, 229 (1984), Sec. 14.7.

41. E. P. Wigner, J. Appl. Phys. **17**, 857 (1946).

42. W. Lenz, Z. Physik **56, 778** (1920).

43. E. Ising, Z. Physik **31**, 253 (1925).

44. L. Onsager, Phys. Rev. **65**, 117 (1944).

45. M. Kac and J. C. Ward, Phys. Rev. **88**, 1332 (1952).

46. R. K. Pathria, Statistical Mechanics (Pregamon Press, Oxford, 1972) Chapter 12.

47. J. G. Kirkwood, J. Chem. Phys. **6**, 70 (1938).

48. H. A. Bethe and J. G. Kirkwood, J. Chem. Phys. **7**, 578 (1939).

49. C. Domb, Bull. Inst. Phys. London **19**, 36 (1968).

50. M. E. Fisher, Lectures in Theoretical Physics Vol. VII C (University of Colorado Press, 1965).

51. Editor K. Binder, Applications of the Monte Carlo Method in Statistical Physics (Springer-Verlag, Berlin, 1987).

52. K. Binder and D. W. Heermann, Monte Carlo Simulation in Statistical Physics: An Introduction (Springer-Verlag, Berlin, 1988).

53. Editor K. Binder, The Monte Carlo Method in Condensed Matter Physics (Springer-Verlag, Berlin, 1992).

54. B. Fultz, J. Chem. Phys. **87**, 1604 (1987).

55. H. Ouyang and B. Fultz, J. Appl. Phys. **66**, 4752 (1989).

56. J. R. Beeler, Jr. and J. A. Delaney, Phys. Rev. **130**, 962 (1963).

57. J. R. Beeler, Jr., Phys. Rev. A **138**, 1259 (1965).

58. B. Fultz, J. Chem. Phys. **88**, 3227 (1988).

59. T. F. Lindsey and B. Fultz, J. Appl. Phys. **75**, 1467 (1994).

60. B. E. Warren, X-Ray Diffraction, (Addison-Wesley, Reading, Massachusetts, 1969), Chap. 12.

61. A. G. Schlijper and B. Smit, J. Stat. Phys. **56**, 247 (1989).

62. A. G. Schlijper, A. R. D. van Bergen, and B. Smit, Phys. Rev.A **41**, 1175 (1990).

63. L. Anthony and B. Fultz, Diffusion in Ordered Alloys, B. Fultz, R.W. Cahn and D. Gupta eds. (Warrendale, TMS, 1993).

Chapter 3. Ordering Transformations of Driven Alloys on a Square Lattice

In this chapter, we studied effects of ballistic atom movements on ordering transformations of equiatomic binary alloys with 1nn effective pair interactions. First, we took the analytical Master Equation method in the Bragg-Williams (mean-field) approximation to study ordering transitions via both vacancy and pair interchange mechanisms, and we compared the results. Second, we performed Monte Carlo simulations of checkerboard ordering on square lattices [1]. In the third part, we used results from Monte Carlo simulations to inspire a simple but general analytical theory based on modified Onsager kinetic rate equations. While the Monte Carlo simulations were performed for the specific case of checkerboard ordering on square lattices, the theoretical analyses based on the Master Equation method and the modified Onsager kinetic rate equation are applicable to both checkerboard ordering on a square lattice and B2 ordering on a bcc lattice.

3.1 Master Equation Method in the Bragg-Williams Approximation

The lattice (either square or bcc) was divided into two sublattices, termed α and β sublattices, each with $\frac{N}{2}$ sites. Every atom on one sublattice has all its z first nearest neighbors (1nn) on the other sublattice. Suppose the concentration of atom species M (M = A, B, or V in the vacancy mechanism – not to be confused it with a potential) on sublattice δ ($\delta = \alpha$ or β) is C_M^{δ}. For AB stoichiometry, we have:

$$C_A^\alpha + C_A^\beta = 1, \qquad C_B^\alpha + C_B^\beta = 1 , \tag{3.1}$$

$$C_A^\alpha + C_B^\alpha = 1, \qquad C_A^\beta + C_B^\beta = 1 . \tag{3.2}$$

Equations 3.1 and 3.2 are valid also for the vacancy mechanism if we consider only a limited number of vacancies. With the constraints listed of Eqs. 3.1 and 3.2, there is only one free independent variable. We define the long range order parameter L:

$$L \equiv C_A^\alpha - C_A^\beta \equiv C_B^\beta - C_B^\alpha \quad . \tag{3.3}$$

Note that $-1 \le L \le 1$, with $L = \pm 1$ for perfect order, and $L = 0$ for disorder. We have:

$$C_A^\alpha = C_B^\beta = \frac{1 + L}{2} , \tag{3.4a}$$

$$C_A^\beta = C_B^\alpha = \frac{1 - L}{2} . \tag{3.4b}$$

3.1.1 Vacancy Mechanism

In vacancy mechanism, an atom can jump to a neighboring site on the other sublattice only if that site contains a vacancy. We assume that atom A and atom B are chemically equivalent ($V_{AA} = V_{BB}$ and $V_{AB} = V_{BA}$), so there is no preference of vacancies on either sublattice, i.e.,

$$C_V^\alpha = C_V^\beta \quad . \tag{3.5}$$

With Eq. 3.5, we will see that many of the results for the vacancy mechanism become similar to those of the pair interchange mechanism. We also assume that the saddle point energies for all jumps are the same, and are denoted by E^*.

The jump rates of A atoms from sublattice α to β and β to α in the point (Bragg-Williams) approximation are:

$$\Gamma_{\alpha A\beta} = \left(\frac{N}{2} C_A^{\alpha}\right) (z\, C_V^{\beta})\, (\omega_{\alpha A\beta} + \omega_f) \tag{3.6a}$$

and

$$\Gamma_{\beta A\alpha} = \left(\frac{N}{2} C_A^{\beta}\right) (z\, C_V^{\alpha})\, (\omega_{\beta A\alpha} + \omega_f) \tag{3.6b}$$

respectively. The first terms in Eqs. 3.6 are the familiar thermal rates. The ω's are Boltzmann factors for the thermal jumping frequencies, which we write without the factor $\frac{1}{kT}$ to show their form:

$$\omega_{\alpha A\beta} = \exp\left(-E^* + \left(V_{AA}\,(z-1)\,C_A^{\beta}\right) + \left(V_{AB}\,(z-1)\,C_B^{\beta}\right)\right) , \tag{3.7a}$$

$$\omega_{\beta A\alpha} = \exp\left(-E^* + \left(V_{AA}\,(z-1)\,C_A^{\alpha}\right) + \left(V_{AB}\,(z-1)\,C_B^{\alpha}\right)\right) . \tag{3.7b}$$

In writing Eqs. 3.7 we have used the facts that the A atom on α sublattice has all its first nearest neighbors on the β sublattice, and one neighbor is a vacancy. We define the average thermal jump rate for A atoms:

$$\langle\omega_A\rangle \equiv \sqrt{\omega_{\alpha A\beta} * \omega_{\beta A\alpha}} = \exp\left(-E^* + \frac{z-1}{2}\left(V_{AA} + V_{AB}\right)\right) . \tag{3.8}$$

The definition of f gives

$$\omega_f = \frac{f}{1-f}\langle\omega_A\rangle = \frac{f}{1-f}\langle\omega_B\rangle . \tag{3.9}$$

The steady state of the alloy is found by seeking the condition when the total jump rates of A atoms from one sublattice to the other is balanced by jumps in the reverse direction, with this condition the atom concentrations on both sublattice will be constant. This requires:

$$\Gamma_{\alpha A\beta} = \Gamma_{\beta A\alpha} \tag{3.10}$$

Combining Eqs. 3.1–3.9 into Eq. 3.10, we have:

$$(1 + L)\left(\exp(-\frac{z-1}{2} L (V_{AA} - V_{AB})) + \frac{f}{1-f}\right)$$

$$= (1 - L)\left(\exp(\frac{z-1}{2} L (V_{AA} - V_{AB})) + \frac{f}{1-f}\right) \quad , \tag{3.11}$$

and

$$L = \frac{\sinh\left(\frac{z-1}{2} L (V_{AA} - V_{AB})\right)}{\cosh\left(\frac{z-1}{2} L (V_{AA} - V_{AB})\right) + \frac{f}{1-f}} \quad . \tag{3.12}$$

When f = 0, we recover the familiar thermodynamic results for Eq. 3.12:

$$L = \tanh\left(\frac{LT_c^0}{T}\right) \quad , \tag{3.13}$$

and

$$T_c^0 = \frac{(z-1)(V_{AA} - V_{AB})}{2k} = \frac{(z-1)(V_{AA} + V_{BB} - 2V_{AB})}{4k} \quad . \tag{3.14}$$

When f ≠ 0, we recover the new results for Eq. 3.12. for driven alloys:

$$L = \frac{\sinh\left(\frac{LT_c^0}{T}\right)}{\cosh\left(\frac{LT_c^0}{T}\right) + \frac{f}{1-f}} \quad , \tag{3.15}$$

and

$$T_c^f = T_c^0 (1 - f) \quad . \tag{3.16}$$

Equation 3.15 is the general relationship among L, T, T_c^0 (i.e., the interatomic potential), and f at steady states for driven alloys. Equation 3.15 reduces to Eq. 3.13 without ballistic jumps (f = 0). Qualitatively, at constant f, larger values of order parameter L require lower temperatures T with a correspondingly larger thermodynamic driving force towards ordering. Some steady state L - T curves for constant f are calculated from Eq.

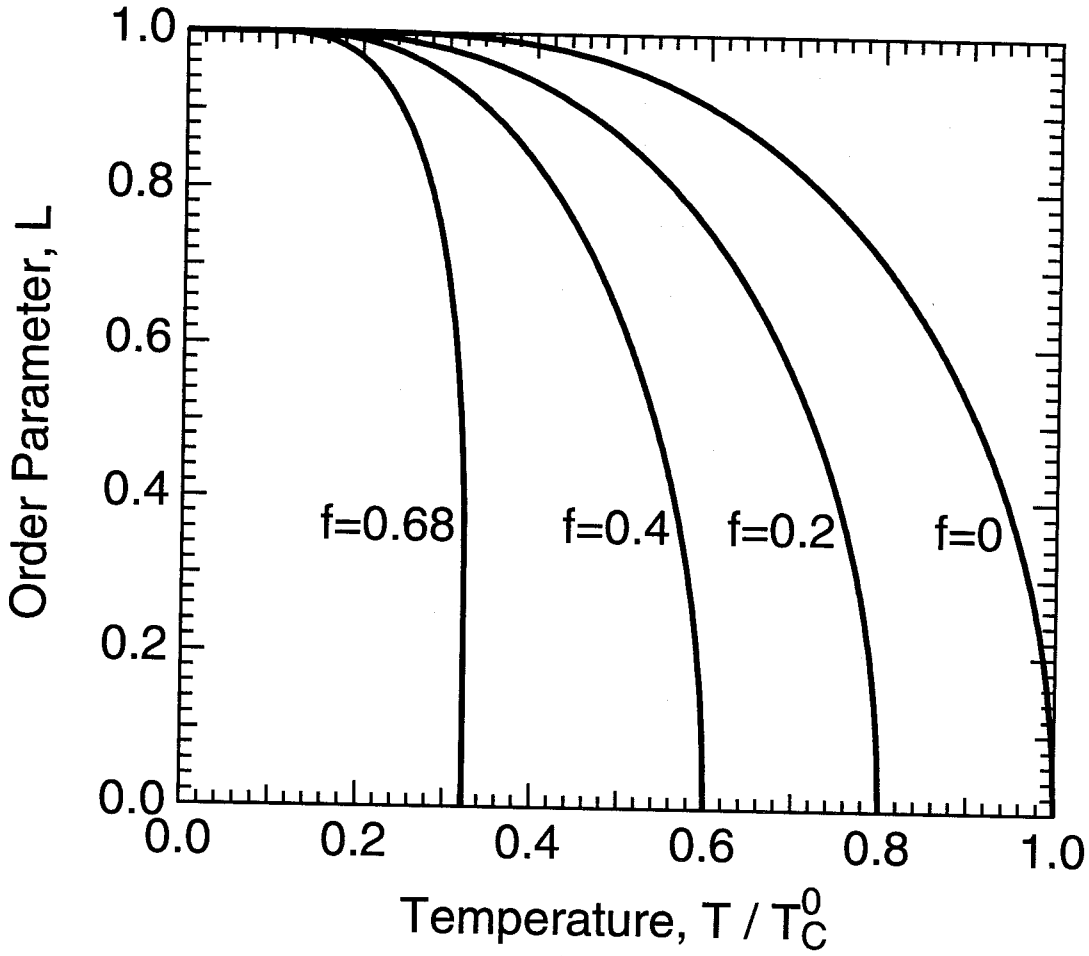

FIG. 3.1. The steady state LRO parameter, L, obtained with the vacancy mechanism in the Master Equation method in the point approximation (Section 3.1.1). Curves were obtained as functions of temperature T (in units of T_c^0) at constant f. Each curve is labeled with its value of f. Curves with $f < f^* = 0.68$ are second order phase transformations.

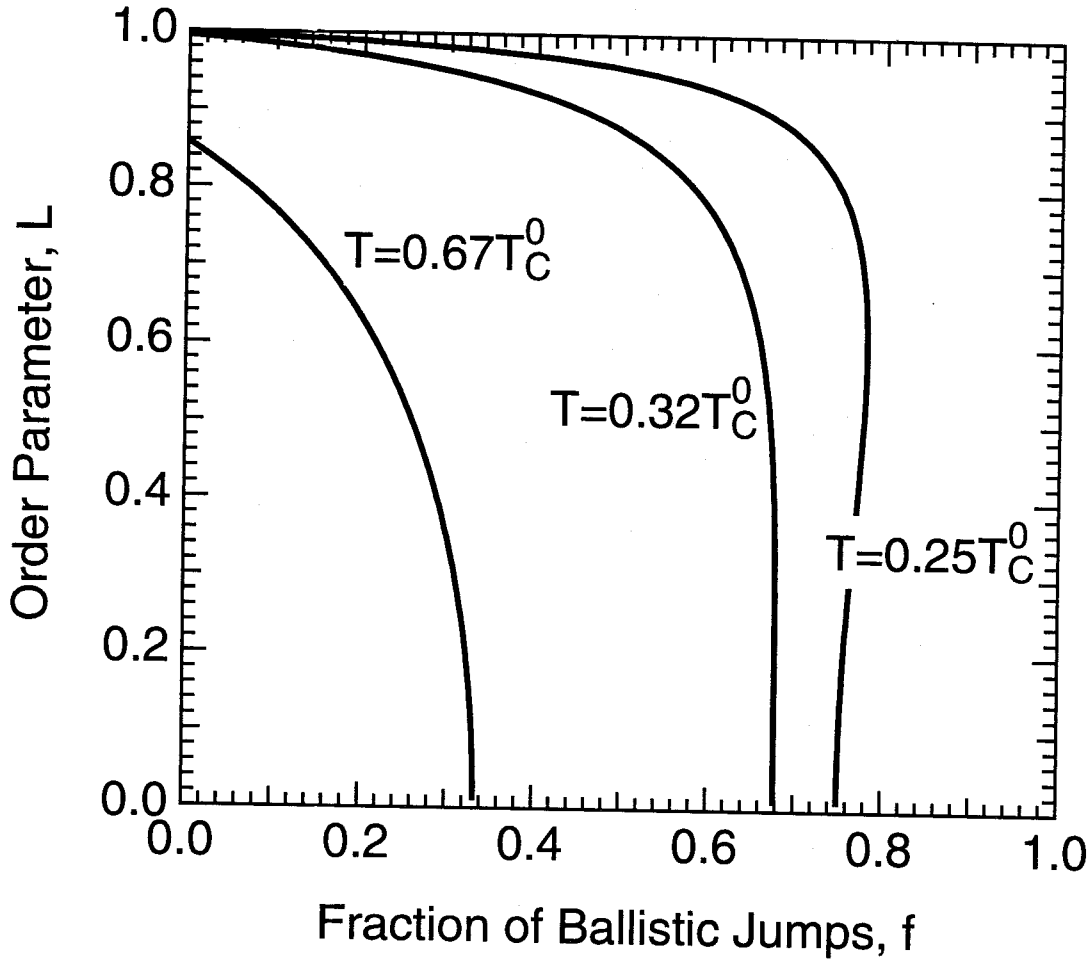

FIG. 3.2. The steady state LRO parameter, L, obtained with the vacancy mechanism in the Master Equation method in the point approximation (Section 3.1.1). Curves were obtained as functions of f at constant temperature T (in units of T_c^0). Each curve is labeled with its value of T. The curve with $T = 0.25\ T_c^0 < T^* = 0.32\ T_c^0$ is a first order phase transformation.

3.15 and are presented in Fig. 3.1. For f constant, but less than 0.68 (such as 0.2 and 0.4), the L - T curves all have the same shape as the thermodynamic curve. The ordering transformations are second order, but with critical temperatures that depend on f as by Eq. 3.16. When f is larger than 0.68 (such as 0.8), however, Eq. 3.15 has three solutions (one of them is unstable) at certain temperatures near the critical temperature, and the shape of the L - T curve is different. The ordering transformation becomes first order. The point where the transformation changes from second order to first order is called a tricritical point:, and occurs at the values of T and f denoted with an asterisk:

$$T^* = 0.32\, T_c^0 \qquad \text{and} \qquad f^* = 0.68 \quad . \tag{3.17}$$

Similarly, at constant T (and therefore constant thermodynamic driving force toward ordering), smaller values of L require larger f with a correspondingly larger external driving force for disordering. The steady state L - f curves for constant T are calculated from Eq. 3.15 and are presented in Fig. 3.2. For T constant and higher than 0.32 T_c^0 (such as 0.67 T_c^0), the L - f curves resemble those L - T curves with small f in Fig. 3.1 and the transformation is second order. On the other hand, the ordering transformation is first order for T lower than 0.32 T_c^0. Recall that $T^* = 0.32\, T_c^0$ is the tricritical temperature.

3.1.2 Pair Interchange Mechanism

In the pair interchange mechanism, two neighboring A and B atoms exchange their positions directly without the help of vacancy, with a frequency given by Eq. 2.8 in thermodynamic case. The exchange rate for all AB pairs of the α-β sublattice orientations to interchange to the β-α sublattice orientations is:

$$\Gamma_{AB}^{\alpha\beta} = \left(\frac{N}{2} C_A^{\alpha}\right) (z\, C_B^{\beta}) \left(\omega_{AB}^{\alpha\beta} + \omega_f\right) \quad . \tag{3.18a}$$

For the reverse interchange, it is:

$$\Gamma_{AB}^{\beta\alpha} = \left(\frac{N}{2} C_A^{\beta}\right) (z\, C_B^{\alpha}) (\omega_{AB}^{\beta\alpha} + \omega_f) \quad . \tag{3.18b}$$

Following the same line from Eq. 3.7 to Eq. 3.9 as in the previous section, we have:

$$\omega_{AB}^{\alpha\beta} = \exp\left(-E^* + (z-1)\,(V_{AA}\, C_A^{\beta} + V_{AB}\, C_B^{\beta}) + (z-1)\,(V_{BB}\, C_B^{\alpha} + V_{BA}\, C_A^{\alpha}) + V_{AB}\right) , \tag{3.19a}$$

$$\omega_{AB}^{\beta\alpha} = \exp\left(-E^* + (z-1)\,(V_{AA}\, C_A^{\alpha} + V_{AB}\, C_B^{\alpha}) + (z-1)\,(V_{BB}\, C_B^{\beta} + V_{BA}\, C_A^{\beta}) + V_{AB}\right) , \tag{3.19b}$$

$$\langle\omega_{AB}\rangle \equiv \sqrt{\omega_{AB}^{\alpha\beta} * \omega_{AB}^{\beta\alpha}} = \exp\left(-E^* + \frac{z-1}{2}(V_{AA} + V_{BB} + 2V_{AB}) + V_{AB}\right) , \tag{3.20}$$

$$\omega_f = \frac{f}{1-f} \langle\omega_{AB}\rangle \quad . \tag{3.21}$$

Balancing Eq. 3.18a and 3.18b gives:

$$(1+L)^2 \left(\exp\left(-\frac{z-1}{2} L\,(V_{AA} + V_{BB} - 2V_{AB})\right) + \frac{f}{1-f}\right)$$

$$= (1-L)^2 \left(\exp\left(\frac{z-1}{2} L\,(V_{AA} + V_{BB} - 2V_{AB})\right) + \frac{f}{1-f}\right) \quad , \tag{3.22}$$

and

$$\frac{2L}{1+L^2} = \frac{\sinh\left(\frac{z-1}{2} L\,(V_{AA} + V_{BB} - 2V_{AB})\right)}{\cosh\left(\frac{z-1}{2} L\,(V_{AA} + V_{BB} - 2V_{AB})\right) + \frac{f}{1-f}} \quad . \tag{3.23}$$

For the thermodynamic case (f = 0), the final results are:

$$\frac{2L}{1+L^2} = \tanh\left(\frac{2LT_c^0}{T}\right) \quad , \quad \text{or} \tag{3.24a}$$

$$L = \tanh\left(\frac{LT_c^0}{T}\right) \quad . \tag{3.24b}$$

Equation 3.24 is the same as Eq. 3.13 for the vacancy mechanism, with the altered critical temperature:

$$T_c^0 = \frac{(z-1)\,(V_{AA} + V_{BB} - 2V_{AB})}{4k} \quad . \tag{3.25}$$

With z – 1 instead of z, the critical temperature obtained here in Eq. 3.25 is slightly different from the critical temperature obtained by minimizing the thermodynamic free energy in the point approximation. We worked on AB 1nn pairs in our work, and this means we know some information on pairs. Therefore our approach differs from the spirit of the standard point approximation.

In general, with ballistic jumps (f > 0):

$$\frac{2L}{1+L^2} = \frac{\sinh\left(\frac{2LT_c^0}{T}\right)}{\cosh\left(\frac{2LT_c^0}{T}\right) + \frac{f}{1-f}} \quad , \tag{3.26}$$

and

$$T_c^f = T_c^0\,(1-f) \quad . \tag{3.27}$$

The general relationship among L, T, V's and f (Eqs. 3. 15 and 3.26) differs somewhat from one kinetic mechanism to the other, and this difference would be even greater were we to relax the condition of Eq. 3.5. This is typical for theoretical analyses of ordering kinetics; different details of the kinetic mechanism lead to different details in the results.

The tricritical point is also different. For the pair interchange mechanism it is:

$$T^* = 0.42\,T_c^0 \qquad \text{and} \qquad f^* = 0.58 \quad . \tag{3.28}$$

The tricritical point of Eq. 3.28 is to be compared with Eq. 3.17 for the vacancy mechanism. The steady state L - T curves at constant f and L - f curves at constant T are shown in Fig. 3.3 and Fig. 3.4, respectively.

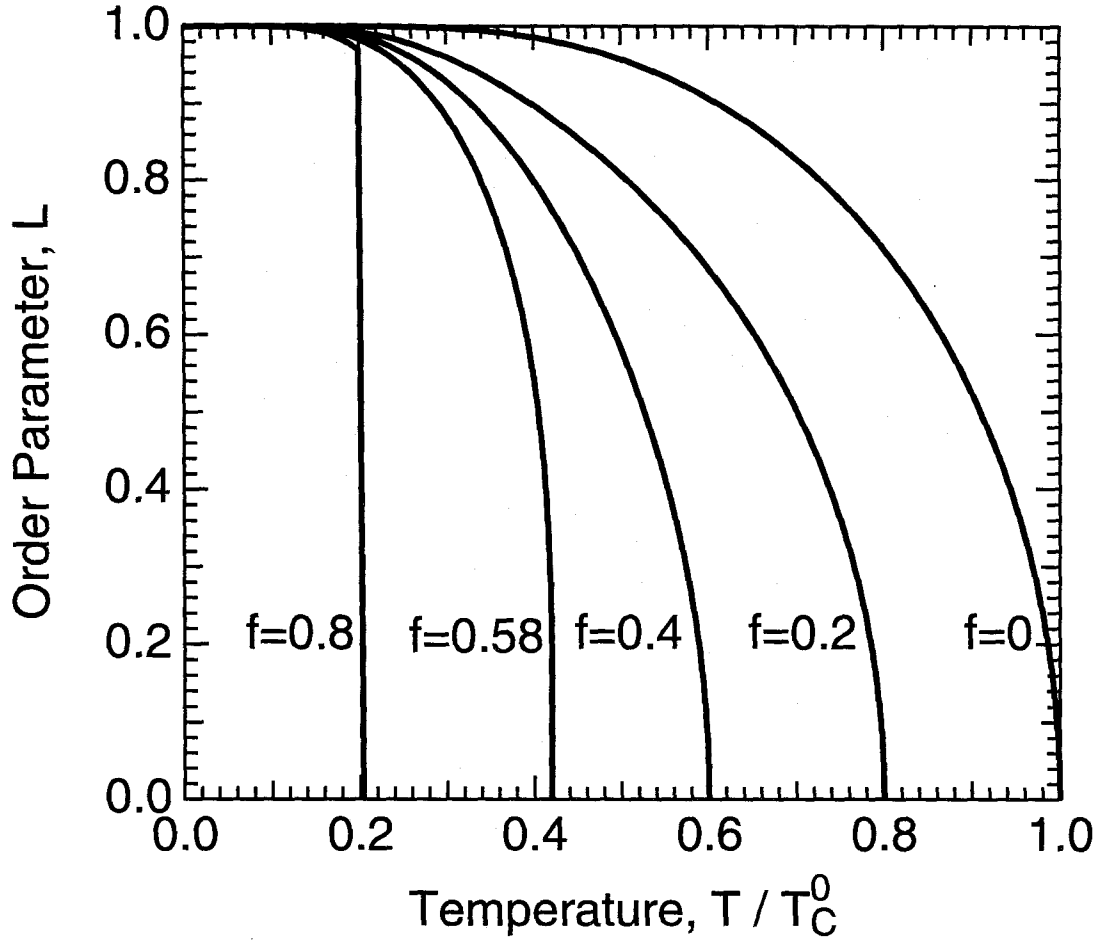

FIG. 3.3. The steady state LRO parameter, L, obtained with the pair interchange mechanism (Section 3.1.2), as functions of temperature T (in units of T_c^0) at constant f. Each curve is labeled with its value of f at its left side. Curves with $f < f^* = 0.58$ are second order phase transformations.

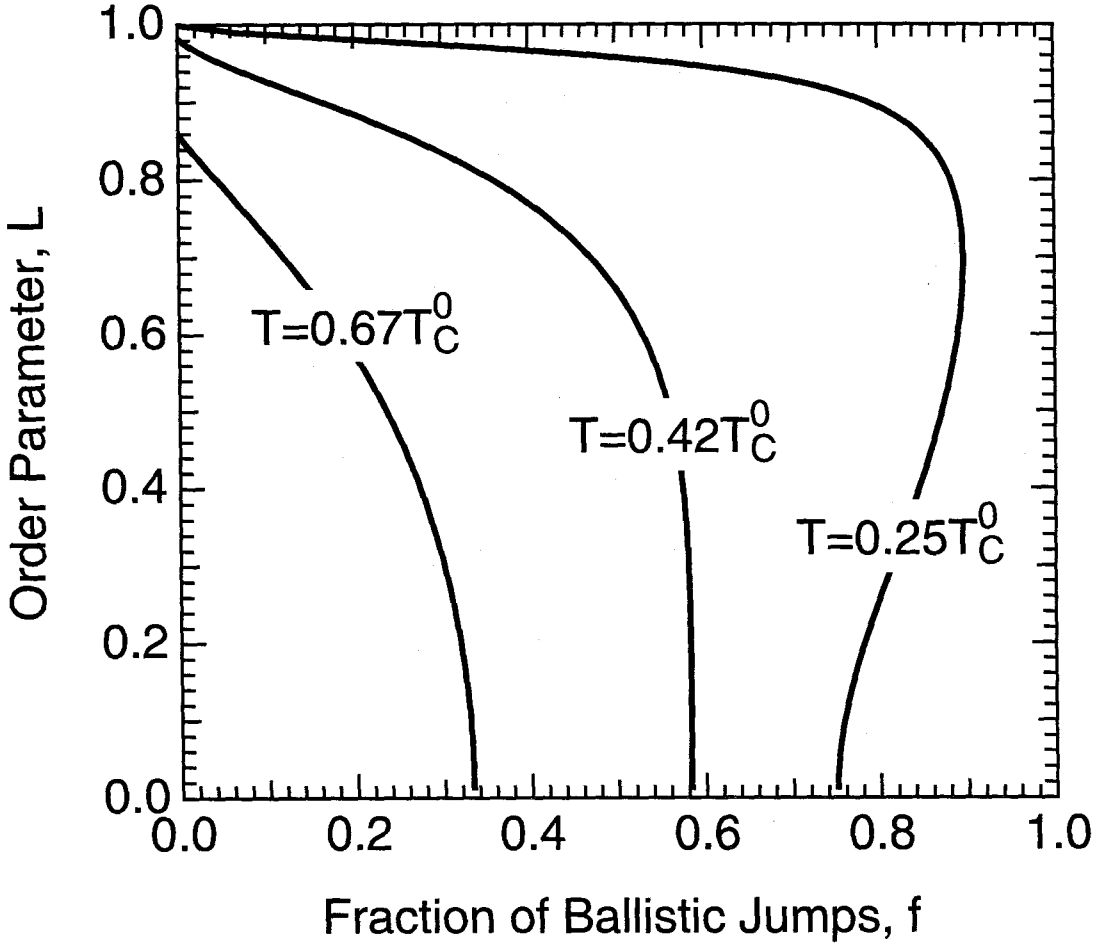

FIG. 3.4. The steady state LRO parameter, L, obtained with the pair interchange mechanism (Section 3.1.2), as functions of f at constant temperature T (in units of T_c^0). Each curve is labeled with its value of T. The curve with $T = 0.25\ T_c^0 < T^* = 0.42\ T_c^0$ is a first order phase transformation.

Although the steady states of the alloy, L versus T and f (and the values of T^* and f^*), are different for the vacancy and pair interchange mechanisms, the general physical phenomena are consistent. More significantly, both theories predict that ballistic jumps will cause a simple linear dilution of the critical temperature, and that the ordering transformation will become first order beyond a tricritical point. As a closing comment on the analytical treatments of ordering in the point approximation, we note that in the above treatment, each kinetic step (atom jump or atom pair interchange) has been taken independently. Any possible correlations among consecutive steps, which might be different for thermal jumps and ballistic jumps, are therefore ignored. We will see in later sections that this is a problem that leads to distorted results.

3.2 Monte Carlo Simulations

In this section, we present results from Monte Carlo simulations with a vacancy mechanism, with emphasis on how the strong diffusional correlation factors unique to the vacancy mechanism [1-8] affect the phase boundary between ordered and disordered phases at various temperatures, T, and fraction of ballistic atom movements, f. Our results suggest a simple but general picture of how the shape of a dynamical phase boundary can be affected by a combination of thermodynamic and kinetic effects.

The alloys studied are binary alloys of AB stoichiometry on square lattices. Only 1nn interactions were considered. We fixed $V_{AB} = 0$, and used $V_{AA} = V_{BB} > 0$ (so $V = V_{AA} = V_{BB}$), unless otherwise specified. The pairwise exchange potential, V, was defined in Section 2.3, Eq. 2.20. For thermodynamic alloys without ballistic atom movements (f = 0), it is known that the exact critical temperature for ordering is [9]:

$$T_c^0 = \frac{V}{0.88} \quad . \tag{3.29}$$

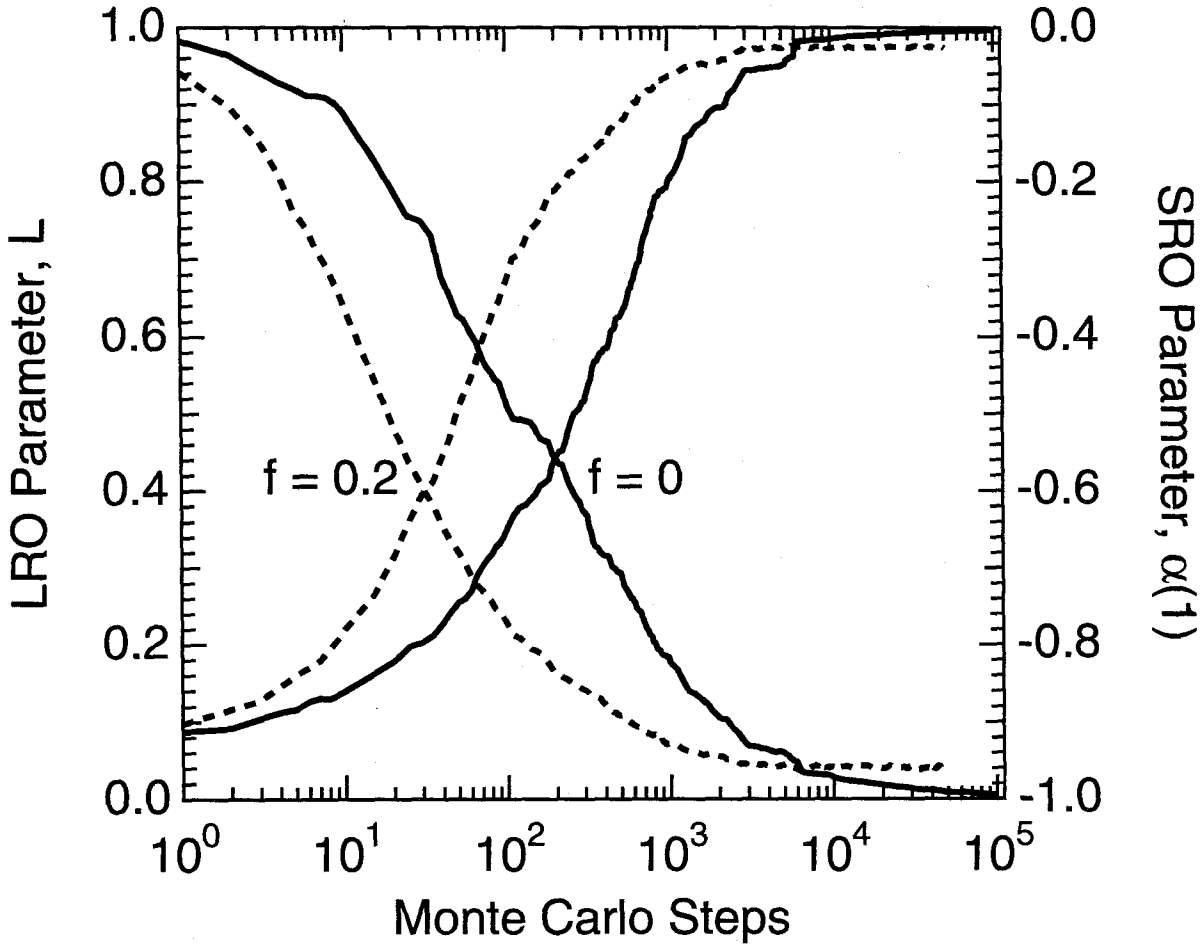

FIG. 3.5. Monte Carlo results with the vacancy mechanism for the time evolution of LRO parameter L (left axis) and SRO parameter $\alpha(1)$ (right axis) for an alloy with V = 2. Both f = 0 (solid curves) and f = 0.2 (dashed curves) were shown. The driven alloy (f = 0.2) had faster kinetics of ordering, but smaller steady state values of order parameters than did the thermodynamic alloy (f = 0).

(a) MCS = 0

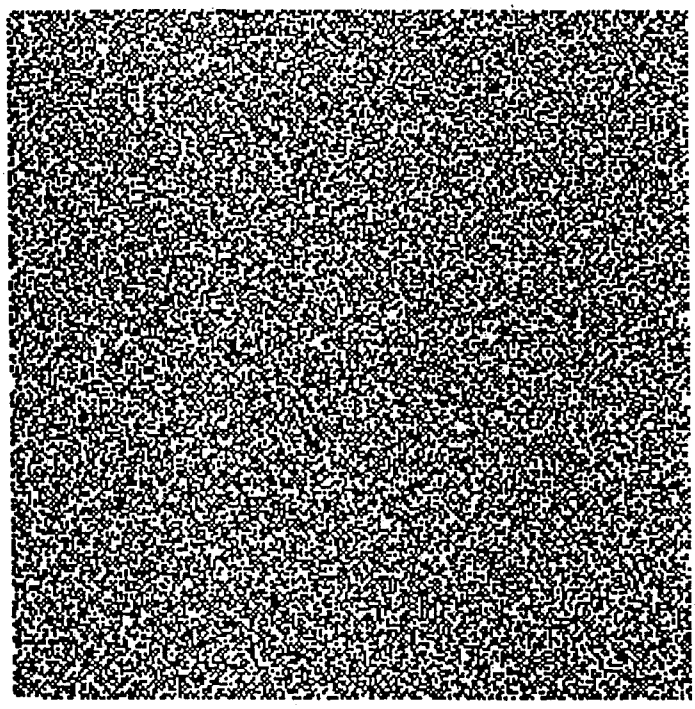

(b) MCS = 100

(c) MCS = 1000

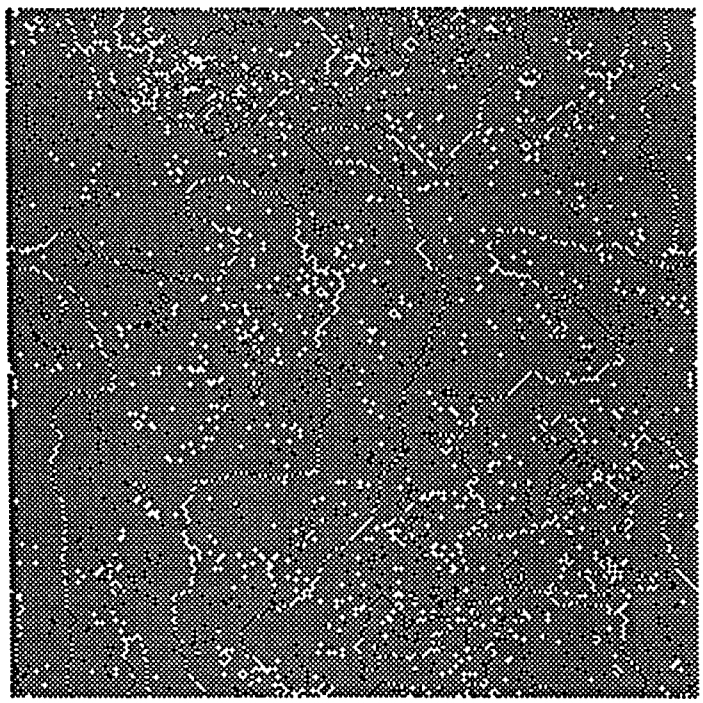

(d) MCS = 50000

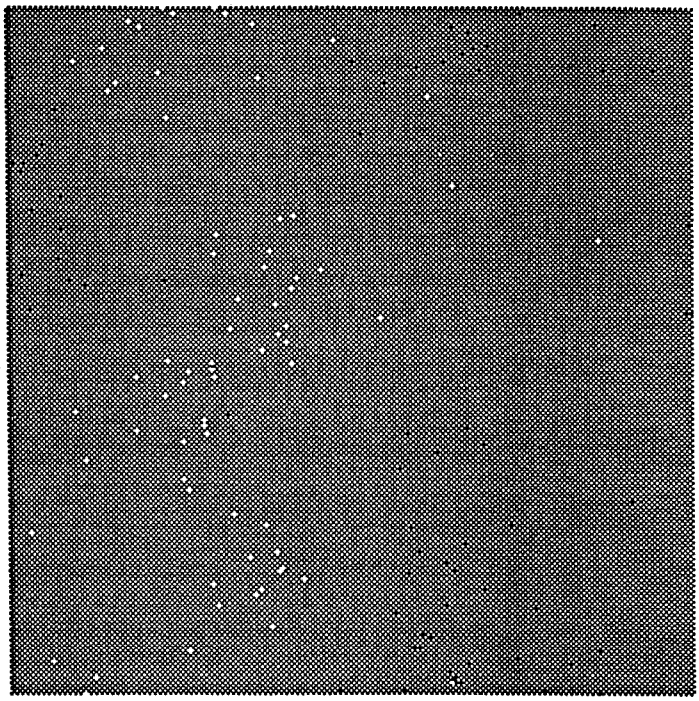

FIG. 3.6. Monte Carlo microstructures of the thermodynamic alloy shown in Fig. 3.5 (V = 2 and f = 0): (a) MCS = 0, (b) MCS = 100, (c) MCS = 1000, (d) MCS = 50000. A atoms are shown as black and B atoms as white.

(a) MCS = 20

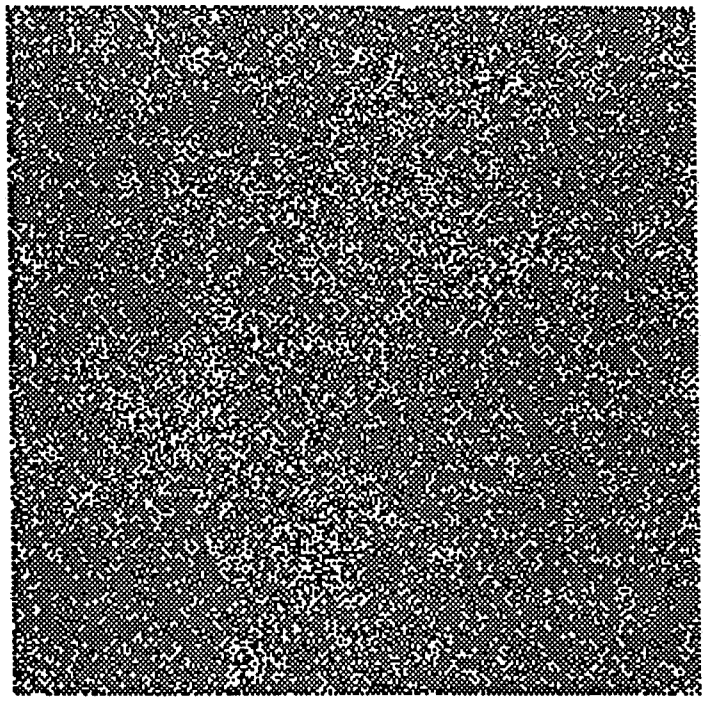

(b) MCS = 100

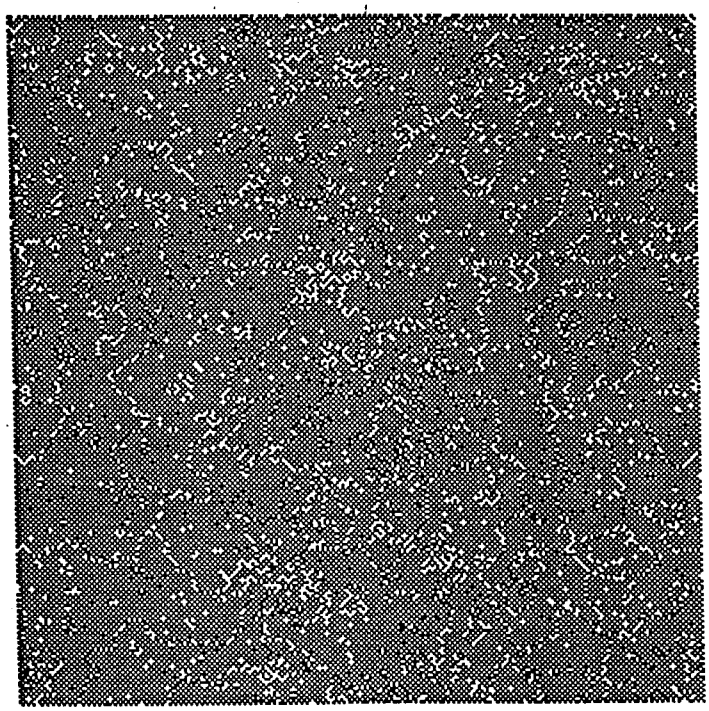

(c) MCS = 1000

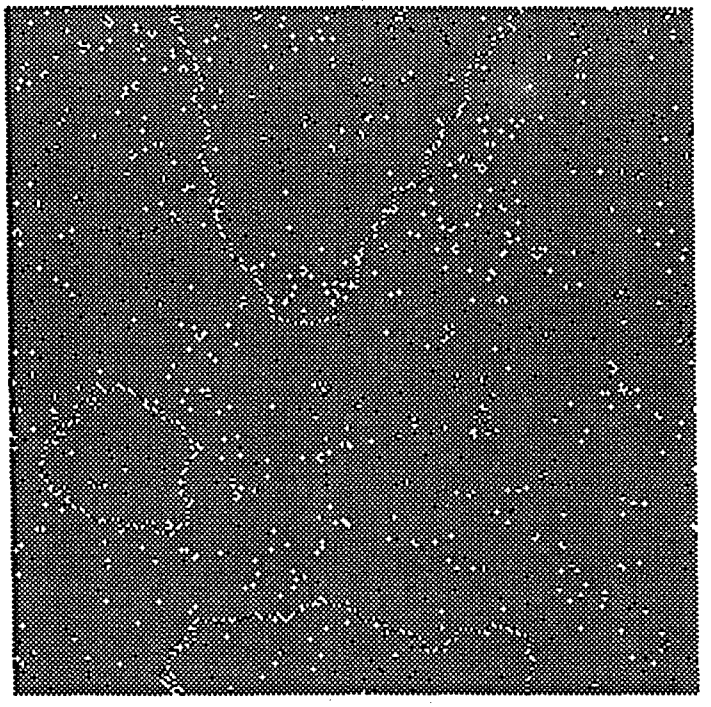

(d) MCS = 50000

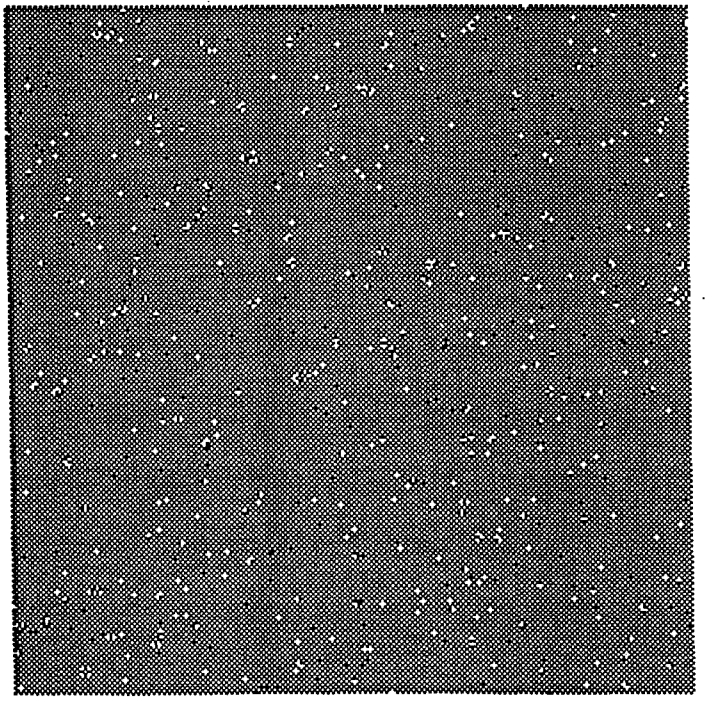

FIG. 3.7. Monte Carlo microstructures of the driven alloy shown in Fig. 3.5 (V = 2 and f = 0.2): (a) MCS = 20, (b) MCS = 100, (c) MCS = 1000, (d) MCS = 50000.

In this section we shall see how the critical temperature is altered by ballistic atom movements when $f \neq 0$.

Started from the disordered state (Fig. 3.6a), which can be obtained by rapid quenching from high temperature ($T = \infty$), the alloy developed short- and long- range order (SRO and LRO). Fig. 3.5 shows the time evolution (in Monte Carlo steps or MCS) of the LRO parameter L, and the SRO parameter $\alpha(1)$ for an alloy with $V = 2$ at $f = 0$ and $f = 0.2$. The actual states of the alloys during kinetic evolution are shown in Fig. 3.6 and Fig. 3.7, respectively. Checkerboard-ordered domains, antisite defects, antiphase domain boundaries, and other types of defects are clearly seen. In Fig. 3.5, the sharp increase of L and $\alpha(1)$ for $f = 0$ at about 6000 Monte Carlo steps is due to the annihilation of antiphase domain boundaries just before the final steady state (thermodynamic equilibrium state) was reached. While the general shapes of these two sets of curves are similar, there are noticeable differences. With ballistic jumps ($f = 0.2$), both L and $\alpha(1)$ evolved faster, but had smaller steady state values. Consistently, Figs. 3.7 show that with ballistic jumps, the ordered domains were larger and better-ordered at the beginning, but had more defects at the end compared with those for $f = 0$ in Figs. 3.6. In the early stages, ballistic jumps can actually speed up the ordering kinetics, even though they are random and tend to disorder the atom arrangements. Experimental observations have also shown that the overall atom mobility is enhanced by ballistic jumps (for example, see Ref. 23-25).

Although the kinetics is interesting, our work was devoted to determining the steady states of the alloys. To ensure that a steady state was attained, we typically waited for times that were a factor of ten longer than the time for which the steady state values of order parameters were first detected. The steady state order parameter can also be confirmed by starting the simulations from different initial states, and verifying that the same values of order parameters were eventually attained. Figure 3.8 shows one such

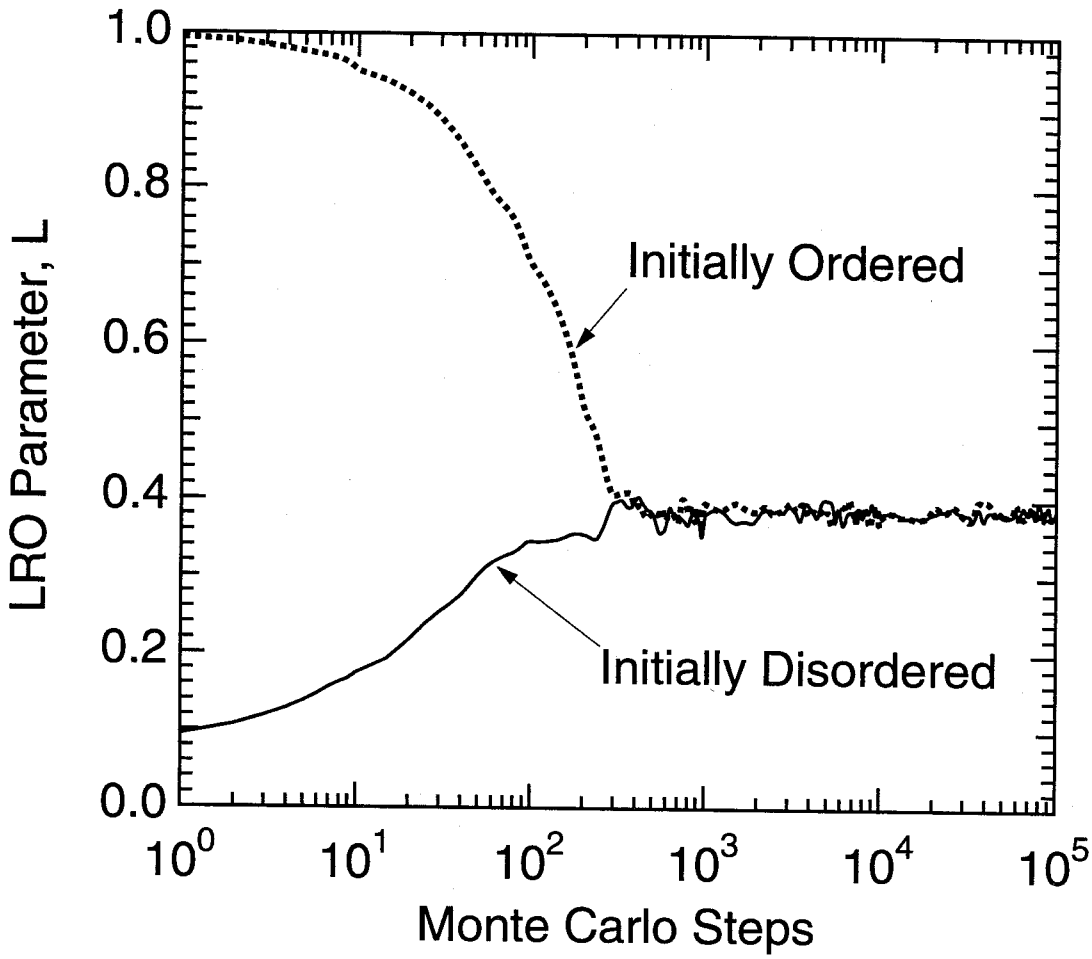

FIG. 3.8. Time evolution of the LRO parameter L for a driven alloy with V = 2 and f = 0.4. Monte Carlo simulations were started from two initial states: disordered (solid curve) and ordered (dashed curve). The same final steady state was reached in both case.

example, for an alloy with V = 2 and f = 0.4. Not only did L remain constant (except fluctuations) for a time of several hundred times longer than its first appearance, but L also reached the same value for both initially disordered and ordered states. These results confirm that the alloy indeed reached a unique steady state.

We performed a series of Monte Carlo simulations with variable V and fixed f. Typical results are presented in Fig. 3.9. For the thermodynamic case with f = 0, the critical temperature, T_c^0, was identified with the inflection point of the curve to be near $\frac{V}{kT}$ = 0.88, consistent with Eq. 3.29. There are many similarities between the L vs. V curves for f = 0 and for some cases of f > 0, although the ballistic atom movements tend to disorder the alloy and suppress the critical temperature. The critical temperatures, T_c^f, were determined for f > 0 either by identifying the inflection points of the L vs. V curves, or by locating the points where L had the same value as at T_c^0 when f = 0. Numbers obtained from both methods agreed well, and we do not distinguish them hereafter. On the other hand, the L vs. V curve for f = 0.55 has an almost flat and featureless shape, and is quite different from the curves for f = 0, 0.2, and 0.35. When f = 0.55, the largest value of L was no more than 0.2, even for temperatures as low as $\frac{V}{kT}$ = 100. Direct observations showed that the lattice had only small ordered domains and no long range ordering. Evidently there is no ordering transition at any temperature when f = 0.55.

We also performed a series of Monte Carlo simulations with variable f and fixed V. Figure 3.10 shows typical L vs. f curves for different V. Qualitatively, the shapes of these curves are reminiscent of curves of L vs. T. Again, by examining the inflection points of the curves, or by matching values of L to those on the curve for f = 0, critical values of f for the ordering transition, denoted f_c, were determined. For example, for $\frac{V}{kT}$ = 1.5 and 2, f_c = 0.275 and 0.355, respectively. Figure 3.10 shows that with reduced temperature, the

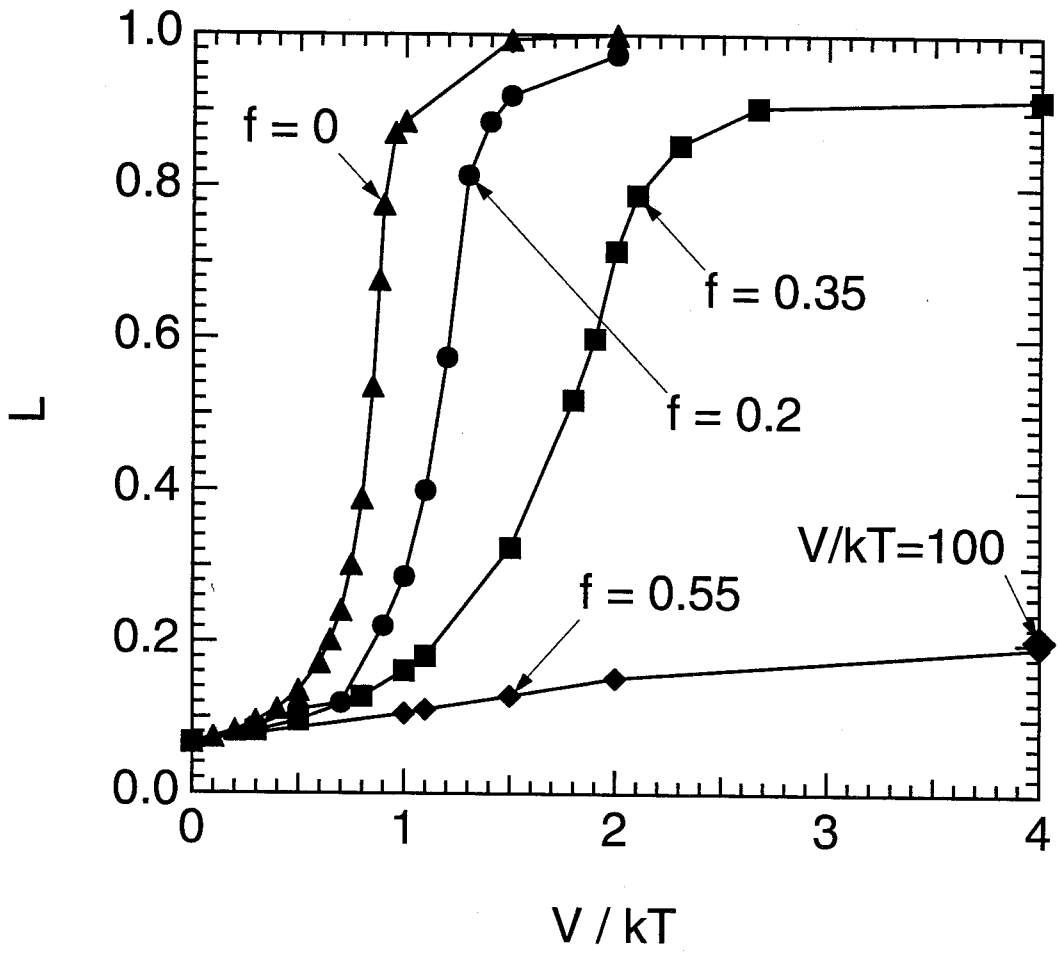

FIG. 3.9. Monte Carlo results for the steady state LRO parameter, L, as a function of V (i.e., inverse temperature) with f = 0 (triangles), f = 0.2 (circles), f = 0.35 (squares), and f = 0.55 (diamonds). The data point labeled with "$\frac{V}{kT} = 100$" was for f = 0.55 and V = 100.

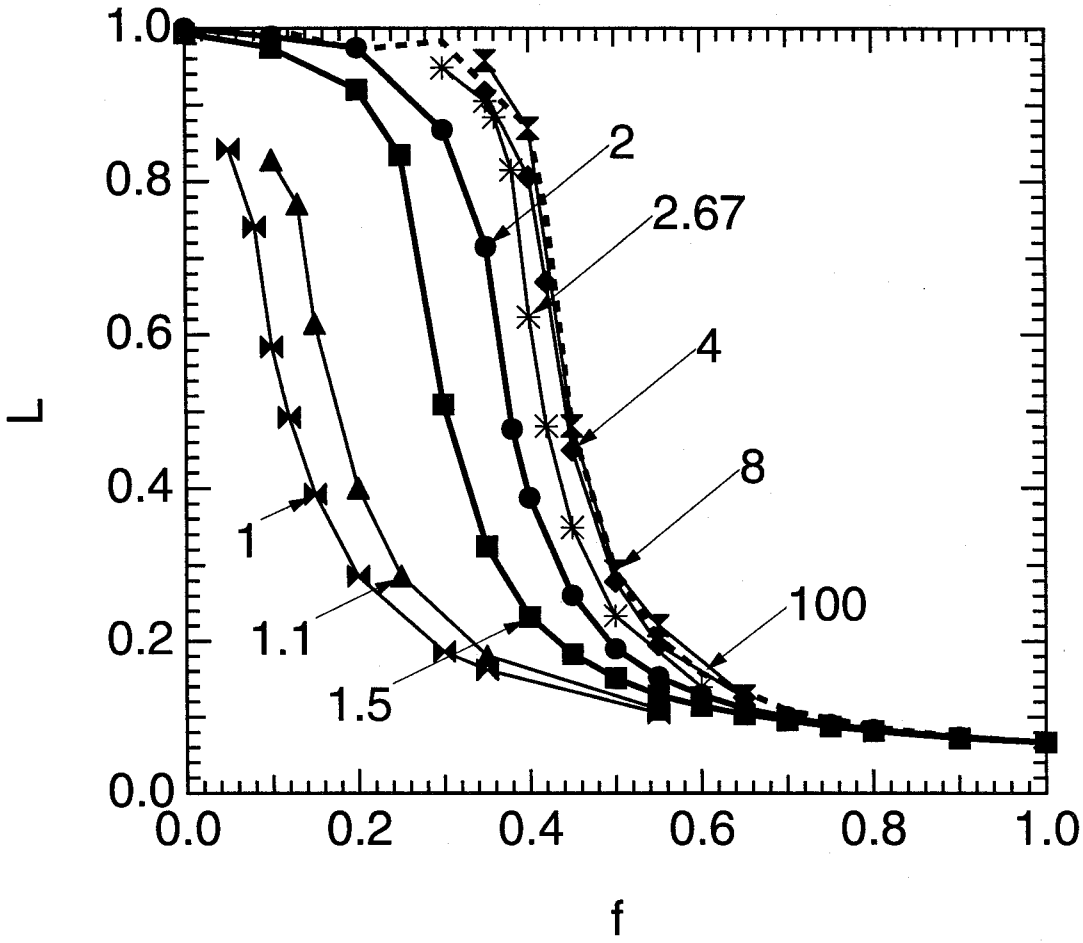

FIG. 3.10. Monte Carlo results for the steady state LRO parameter L as a function of f at various temperatures. Each curve is marked with its value of $\frac{V}{kT}$.

curves of L vs. f shift towards the right on Fig. 3.10, and converge toward the curve for $\frac{V}{kT}$ = 100. Accordingly, the critical fraction of ballistic atom movements f_c increases and approaches an ultimate limit f_c^0, as discussed below.

For ordered alloys at low values of T and f, there still remains the question of whether the ordered domains tend towards infinite length. This question cannot be answered rigorously with Monte Carlo simulations on finite systems, but we did perform some tests by extrapolation. The characteristic length of ordered domains, <r>, was calculated as described in Section 2.4, and Fig. 3.11a presents typical data on <r>, in units of the lattice constant, as a function of f at temperatures above T_c^f (or equivalently, for f > f_c). The two curves of <r> vs. f were obtained at fixed temperature, and so are labeled with their individual value of $\frac{V}{kT}$. As f approaches f_c from above, <r> increases rapidly and approaches a size comparable to the size of the lattice in the simulation. With analogy to a thermodynamic alloy, we might expect $\frac{1}{<r>}$ to decrease linearly with –f as f approaches f_c. Figure 3.11b presents curves of $\frac{1}{<r>}$ vs. f corresponding to the curves in Fig. 3.11a. The plateaus at $\frac{1}{<r>}$ = 0.33 and 0.25 correspond to integral changes in <r> from 3 to 4, and are not significant. For larger <r>, however, there seems to be a linear decrease of $\frac{1}{<r>}$ as f approaches f_c. Extrapolating the linear parts of both curves to $\frac{1}{<r>}$ = 0 gives f_c = 0.261 and 0.338 for $\frac{V}{kT}$ = 1.5 and 2, respectively. These values are reasonably close to those obtained from the curves of L vs. f in Fig. 3.10.

We compared the dynamical critical temperatures, T_c^f, that were determined from the data of L vs. V and from the data of L vs. f. The values of f_c from all curves in Fig. 3.10 are presented as solid circles in Fig. 3.12. The left axis of Fig. 3.12 is temperature, normalized by the thermodynamic critical temperature T_c^0 of Eq. 3.29. Also presented in Fig. 3.12 as open squares are some results from data of L vs. V. These two sets of data are in excellent agreement. Figure 3.12 is the T–f phase diagram of our driven alloy at the

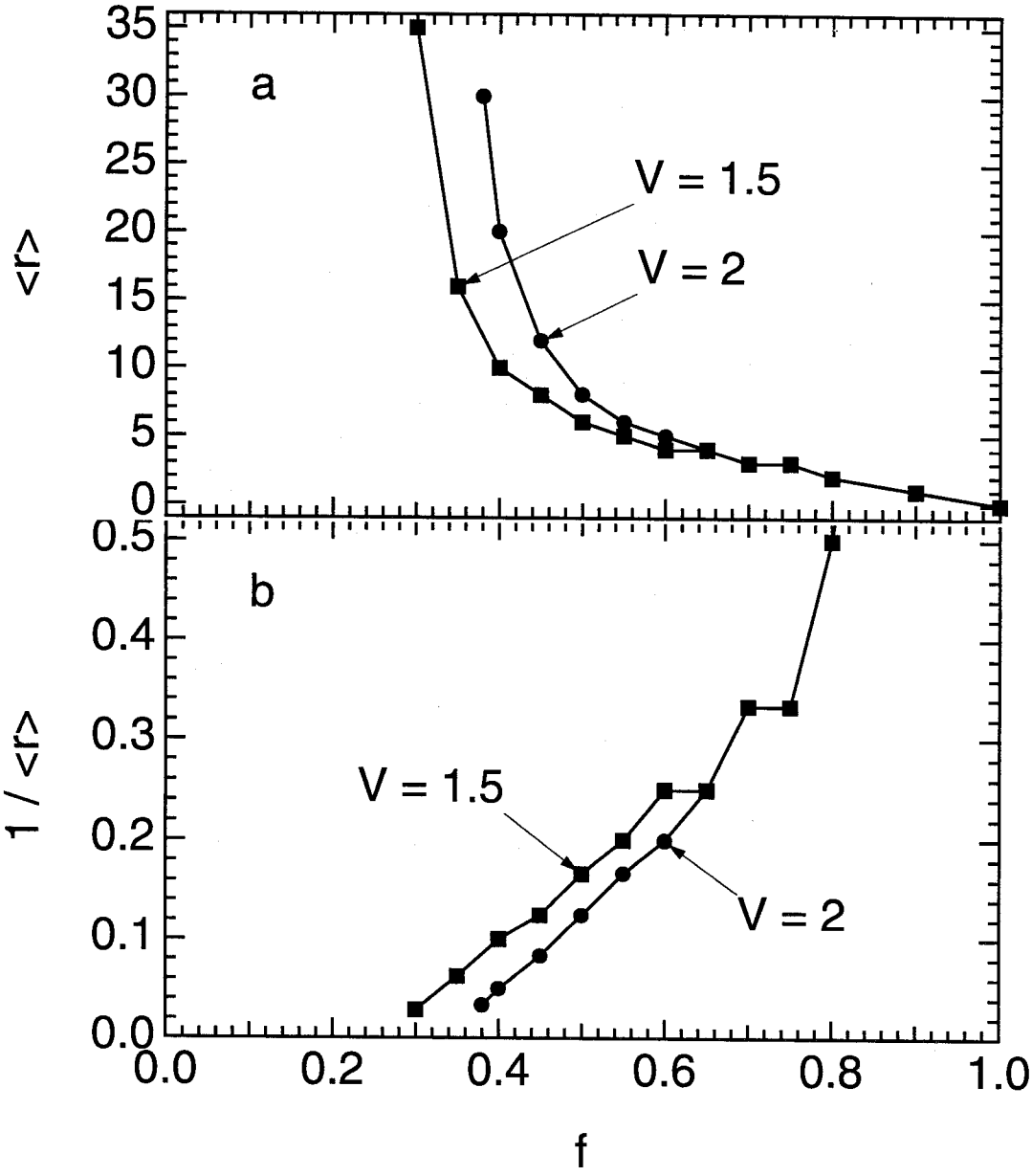

FIG. 3.11. Monte Carlo results for (a) the steady state average domain length scale <r>, and (b) its reciprocal $\frac{1}{<r>}$, as functions of f at V = 1.5 (squares) and V = 2 (circles), respectively.

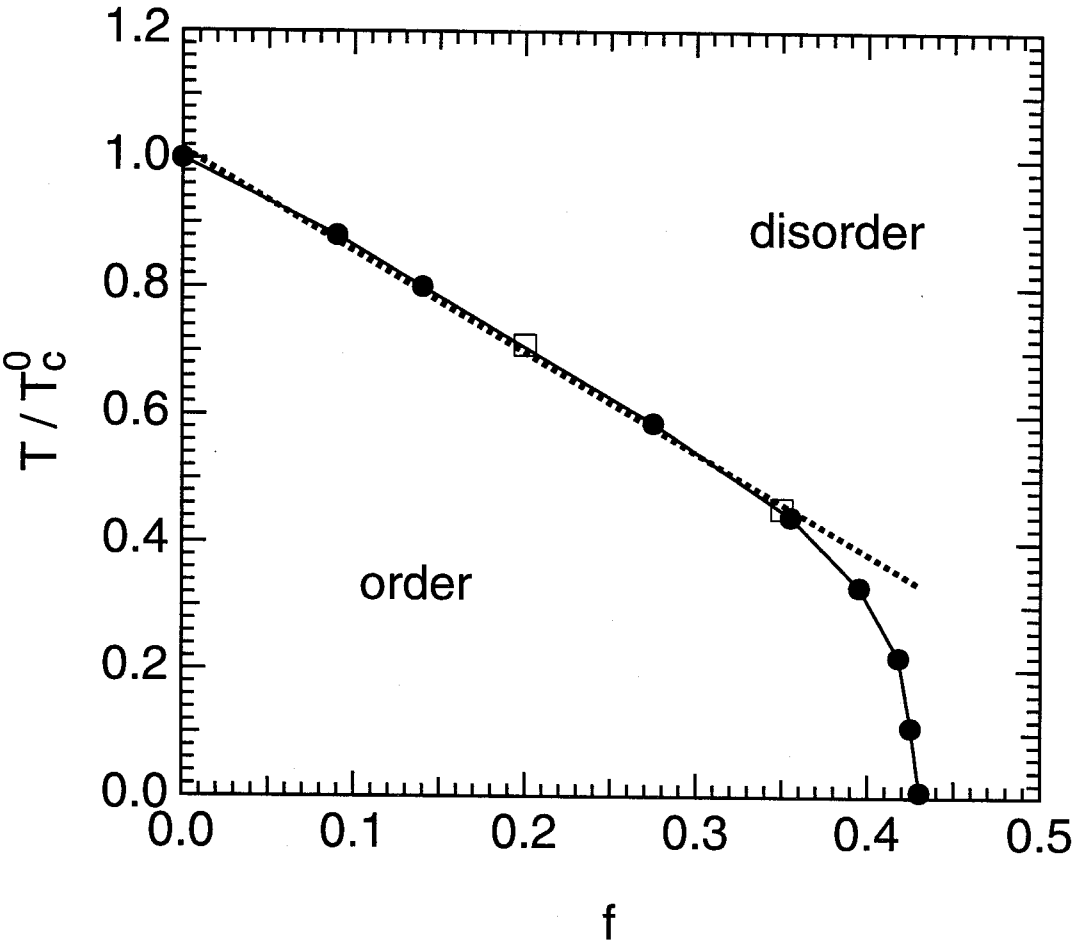

FIG. 3.12. Monte Carlo results for the T–f dynamical phase diagram for the ordering transition for symmetrical interatomic potentials ($V_{AA} = V_{BB}$). The phase boundary (solid curve) consists of the data points for T_c^f as a function of f. Circles were obtained from simulations with variable f at fixed V, while squares were from simulations with variable V at fixed f. The straight dashed line is a best fit to the linear part of the data.

steady states. The solid curve separates the regions of ordered and disordered phases. At f = 0, the dynamical phase diagram provides the thermodynamic critical temperature of Eq. 3.9. The ordered phase is stable for small values of T and f, whereas the disordered phase is stable for large values of T and f. Slightly below the phase boundary, the LRO is imperfect. Slightly above the phase boundary, there is significant SRO. This is typical of a second order phase transition, and the continuous curves of Figs. 3.9 and 3.10 do imply that the transition is of second order for all f.

The nearly linear part of the phase boundary in Fig. 3.12, between f = 0 and f = 0.36, was fit to a straight line with a slope of -1.58 ± 0.01:

$$T_c^f = (1 - 1.58f)\, T_c^0 \quad . \tag{3.30}$$

As f increased beyond this nearly linear region, T_c^f decreased dramatically. At f = 0.43, $T_c^f = 0.01\ T_c^0$. A logarithmic extrapolation to zero temperature of the dashed curve in Fig. 3.12 provides an ultimate fraction of ballistic atom movements, $f_c^0 = 0.43$, beyond which ordering does not occur at any temperature.

3.3 Modified Onsager Kinetic Analysis

Here we develop a simple but general analytical theory for the steady state of an ordering alloy in the presence of both ballistic and thermal atom movements. The approach is similar to that of Martin [10]. We use Onsager-type kinetic rate equations, suitably modified to include ballistic atom movements. Onsager-type kinetic rate equations allow us to neglect the details of atom movement mechanisms, thereby simplifying the problem. Nevertheless, this approach should be valid near the steady state of the alloy when $\frac{dL}{dt}$ is zero or nearly zero, which is appropriate for the problem of interpreting phase boundaries

between phases in steady states of the alloy. We write the time-dependence of the LRO parameter for the thermodynamic alloy (f = 0) as (Eq. 2.4):

$$\frac{dL}{dt} = -\frac{l}{kT}\frac{\partial F}{\partial L} \quad , \tag{3.31}$$

or equivalently,

$$\frac{dL}{dt} = -\frac{l}{kT}\frac{\partial E}{\partial L} + \frac{l}{k}\frac{\partial S}{\partial L} \quad , \tag{3.32}$$

where l is the mobility coefficient. F and E denote the Helmholtz free energy and enthalpy, respectively. At steady states, L does not change with time. Therefore,

$$T\frac{\partial S}{\partial L} = \frac{\partial E}{\partial L} \quad . \tag{3.33}$$

In a mean-field thermodynamic calculation (f = 0), the contributions to $\frac{\partial F}{\partial L}$ are:

$$\frac{\partial E}{\partial L} = \frac{N}{2} z L V \quad , \quad \text{and} \tag{3.34}$$

$$T\frac{\partial S}{\partial L} = Tk\frac{N}{2}\ln\left(\frac{1 - L}{1 + L}\right) \quad . \tag{3.35}$$

It is straightforward to take the mean-field thermodynamic expressions of Eqs. 3.34 and 3.35, substitute them into Eq. 3.33, and recover the mean-field critical temperature.

For a driven alloy having a fraction of ballistic atom movements, f, the fraction of thermal atom movements is 1 – f. For the thermal atom movements alone, Eq. 3.32 becomes:

$$\left(\frac{dL}{dt}\right)_{thermal} = -\frac{l}{k}(1-f)\left(\frac{1}{T}\frac{\partial E}{\partial L} - \frac{\partial S}{\partial L}\right) \quad . \tag{3.36}$$

Because the random ballistic atom movements are assumed to occur at infinite temperature, we have:

$$\left(\frac{dL}{dt}\right)_{ballistic} = -\frac{l'}{k} f\left(\frac{1}{\infty}\frac{\partial E}{\partial L} - \frac{\partial S}{\partial L}\right) \quad , \quad \text{or} \tag{3.37}$$

$$\left(\frac{dL}{dt}\right)_{ballistic} = \frac{l'}{k} f \frac{\partial S}{\partial L} \tag{3.38}$$

for the ballistic atom movements. Equation 3.38 is an entropy contribution. The enthalpy contribution is zero because the ballistic atom movements are independent of temperature and local environment.

It is important to note that the Onsager mobility constants in Eqs. 3.32 and 3.38 are different. As discussed in next section, we expect the thermal atom movements to be increasingly correlated at low temperatures, whereas the ballistic atom movements are not. We define ζ as the ratio of mobility coefficients for the ballistic and thermal atom movements:

$$\zeta \equiv \frac{l'}{l} \quad . \tag{3.39}$$

It was found from Fig. 3.5 and other studies with the vacancy mechanism [1,7,8,11-13] that the atom mobility was enhanced by ballistic atom movements, so we expect $l' > 1$ and $\zeta > 1$.

Combining Eqs. 3.36, 3.38, and 3.39, we can write a complete kinetic equation for the driven alloy:

$$\frac{dL}{dt} = -\frac{l}{kT}(1-f)\frac{\partial E}{\partial L} + \frac{l}{k}\left(1 + (\zeta - 1)f\right)\frac{\partial S}{\partial L} \quad . \tag{3.40}$$

To obtain the steady state value of L as a function of T and f, we set Eq. 3.40 equal to zero and obtain:

$$T\,\frac{1 + (\zeta - 1)f}{1 - f}\,\frac{\partial S}{\partial L} = \frac{\partial E}{\partial L} \quad . \tag{3.41}$$

Consider first the case when $\zeta = 1$, that is, the ballistic atom movements have the same mobility as the thermal atom movements. In this case Eq. 3.41 becomes:

$$\frac{T}{1-f}\frac{\partial S}{\partial L} = \frac{\partial E}{\partial L} \quad . \tag{3.42}$$

Upon comparison with Eq. 3.33, we see that the effective temperature, T^{ef}, of the driven alloy is rescaled with respect to the thermal temperature, T :

$$T^{ef} = \frac{T}{1-f} \quad . \tag{3.43}$$

Were Eq. 3.43 true, the dynamical critical temperature of ordering, T_c^f, would decrease linearly with the fraction of ballistic atom movements by simple dilution, becoming zero when f = 1:

$$T_c^f = (1-f)\,T_c^0 \quad . \tag{3.44}$$

This rescaling of temperature is a consequence of the ballistic atom movements being insensitive to the enthalpy driving force (Eq. 3.38). This reduction of T_c^f by a factor of 1 – f can be regarded as a dilution of the enthalpy driving force in the presence of the fraction, f, of ballistic atom movements. The same result was obtained previously in our mean-field kinetic analysis (Eqs. 3.16 and 3.27).

In general, however, mobility differences must be considered, and this provides a second means for the ballistic jumps to affect T_c^f. We expect $\zeta > 1$, and in fact ζ may be a function of T, f and L. From Eq. 3.41 we write:

$$T^{ef} = T\frac{1+(\zeta-1)f}{1-f} \quad , \quad \text{and} \tag{3.45}$$

$$T_c^f = \frac{1-f}{1+(\zeta-1)f}T_c^0 \quad . \tag{3.46}$$

There is no simple scaling of the critical temperature with f unless $\zeta(T, f, L)$ has a simple form. A precise estimate of ζ is not trivial, and we have not attempted to do so. On the other hand, we have used our Monte Carlo results for T_c^f (Fig. 3.12) to determine ζ.

3.4 Discussion

The analysis of Sections 2 and 4 relies on a single order parameter, L, to characterize the microstructure of the driven alloy. It is appropriate to ask if a single LRO parameter is adequate to characterize the microstructure of the driven alloys, or if the steady-state microstructures of alloys having the same value of L, but subjected to different combinations of T and f, may have different order parameters on short length scales. To address this concern, we compared both the LRO and SRO parameters for the steady states of alloys with various combinations of T and f. Figure 3.13 shows steady-state values of the SRO parameters $\alpha(1)$ and $\alpha(2)$ as functions of L for alloys with various combinations of T and f. The curves are nearly identical. Direct observation of the alloys also confirmed that alloys with the same steady-state values of L were very similar in appearance. The LRO parameter, L, seems a reasonable single parameter for specifying the steady state of order in our driven alloys.

We now use the analytical approach of Section 3.3 with its Onsager-type kinetic rate equation for L to interpret the Monte Carlo results of Figure 3.12. For $f \leq 0.36$ or $\frac{V}{kT} \leq 2$, Eq. 3.30 describes our data well. By comparing Eqs. 3.30 and 3.46, we obtain:

$$\zeta \equiv \frac{l'}{l} = \frac{1.58\ (1 - f)}{1 - 1.58f} \qquad (3.47)$$

According to Eq. 3.47, the mobility ratio ζ increases slightly as f increases. This can be confirmed by comparing the kinetics shown in Fig. 3.5. A much more dramatic increase in

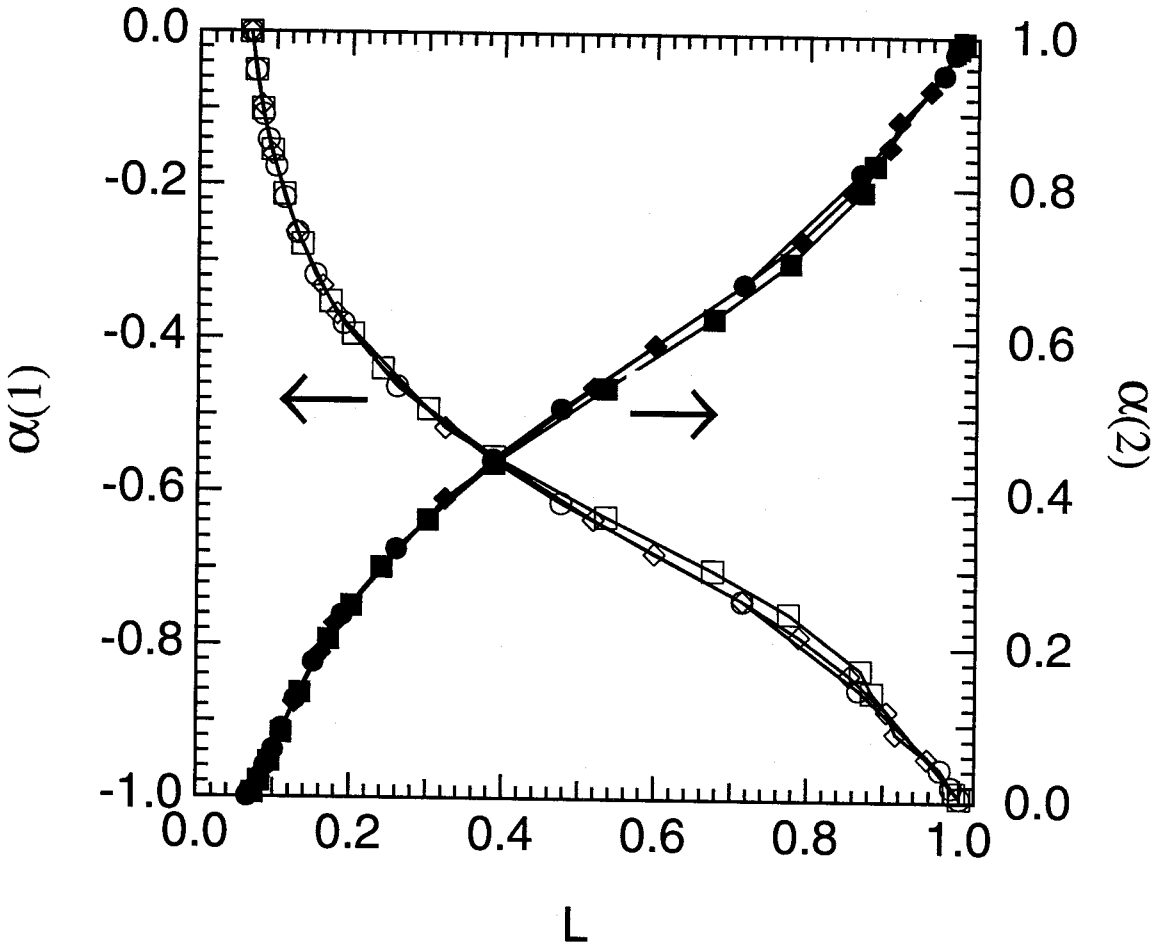

FIG. 3.13. Monte Carlo results for the SRO parameters, $\alpha(1)$ and $\alpha(2)$, vs. LRO parameter, L, for steady states of several alloys. $\alpha(1)$: Open marks against the left axis; $\alpha(2)$: solid marks against the right axis. Squares: thermodynamic alloys (f = 0) at various T; Diamonds: driven alloys at various T with fixed f = 0.35; Circles: driven alloys with various f at fixed $\frac{V}{kT} = 2$.

ζ occurs when $f > 0.36$ or $\frac{V}{kT} > 2$. These increases in ζ are not surprising for ordered alloys, however. At low temperatures (corresponding to large f on the phase boundary of Fig. 3.12) thermal diffusion in ordered alloys becomes highly correlated and inefficient, effectively suppressing l. For thermodynamic ordering transitions on a square lattice, there are dramatic changes in vacancy mobility when $\frac{V}{kT} > 2$ [4]. At these low temperatures, the vacancy becomes trapped in local regions from which it has insufficient thermal activation for escape. We found the same type of vacancy trapping in the present study. At the lowest temperatures, the vacancy moved cyclically between a set of sites until it was dislodged by a ballistic atom movement. This high degree of diffusional correlation suppresses strongly the effective thermal mobility coefficient, l. On the other hand, we do not expect the mobility coefficient for ballistic atom movements, l', to change with temperature. We therefore expect the mobility ratio, ζ, to increase with decreasing temperature, suppressing T_c^f dramatically when $\frac{V}{kT} > 2$.

To investigate further these effects of vacancy mobility, we performed some Monte Carlo simulations with asymmetrical chemical interaction potentials between A and B atoms ($V_{AA} \neq V_{BB}$), while maintaining the same thermodynamic pair exchange potential, V. It was established previously that diffusion coefficients, and therefore the effective mobility constants, will change when $V_{AA} \neq V_{BB}$ [4]. Figure 3.14 shows typical L vs. f curves for the same thermodynamic potential, $V = 2$, but for two different cases, one with $V_{AA} = V_{BB}$, and the other with $V_{AA} \neq V_{BB}$. Although the shapes of the curves are similar, the critical values of f are quite different: $f_c = 0.20$ for the asymmetrical case, while $f_c = 0.35$ for the symmetrical case. This cannot be a thermodynamic effect, since Eqs. 3.28 and 3.16

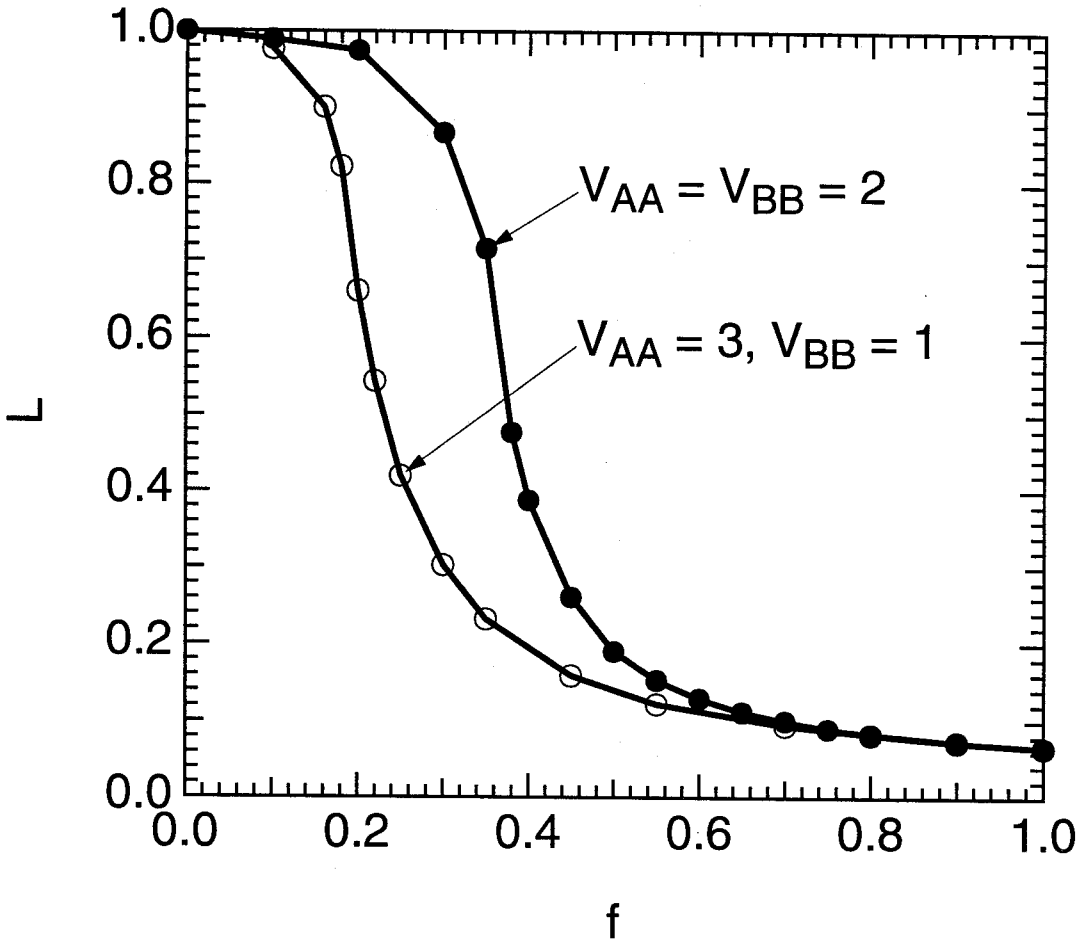

FIG. 3.14. Monte Carlo results for the steady state LRO parameter, L, as a function of f for alloys with the same thermodynamic exchange potential, V = 2. Solid circles: symmetrical case with $V_{AA} = V_{BB} = 2$. Open circles: asymmetrical case with $V_{AA} = 3$ and $V_{BB} = 1$.

depend only on V. The symmetry of the interatomic potentials must affect f_c through the mobility coefficients. Correlated thermal vacancy motion can explain this behavior. Vacancy trapping is controlled by the strongest interatomic potential [4], so in the approximately linear region of Fig. 3.12, we expect f_c to decrease by the factor of $\frac{2}{3}$ as V_{AA} increases from 2 to 3. This is approximately correct.

3.5 Summary

We performed a Monte Carlo study of steady states in alloys with thermal and ballistic atom movements. A vacancy mechanism was used for atom movements in equiatomic alloys on a square lattice. A T–f phase diagram for the order–disorder transition was constructed for alloys with symmetrical interatomic potentials ($V_{AA} = V_{BB}$). When $f < 0.36$, the dynamical critical temperature decreased by the factor $(1 - 1.58\ f)$ in the presence of a fraction of ballistic atom movements, f. For f greater than 0.36, but less than 0.43, the reduction of the critical temperature with f was much more rapid, and the critical temperature became zero at a critical value of f, $f_c^0 = 0.43$. An Onsager-type analytical theory was used to explain this behavior. The decrease in critical temperature with f occurred for two reasons. First, in the presence of ballistic atom movements, the enthalpy driving force for ordering, $-\frac{\partial E}{\partial L}$, is diluted by the factor $(1 - f)$. Second, the mobility coefficient for thermal atom movements becomes small at low temperatures, owing to a high degree of correlation in the vacancy diffusion mechanism. The ballistic atom movements are not subject to this correlation factor, and so are relatively more important at low temperatures, leading to a dramatic drop of T_c to zero near $f = 0.43$.

On the other hand, the kinetic Master Equation analysis in the point (Bragg-Williams) approximation with both vacancy and pair interchange mechanisms takes into consideration correctly only the first factor, the random nature of the ballistic jumps. The

second factor, the mobility enhancement by ballistic jumps, is ignored. This proves to be a problem leading to inaccurate results such as a simple dilution of the critical temperature by the ballistic jumps. It would be interesting to use Monte Carlo simulations to look for the tricritical point predicted by the kinetic Master Equation analyses in the point (Bragg-Williams) approximation. Our Monte Carlo work so far has shown no sign of any first order transition by Monte Carlo simulations across a broad range of temperature, but all the transformations observed in our studies were at relatively low values of f, below the critical point of $f^* = 0.68$ (or 0.58).

All the theories and Monte Carlo simulations predicted that if the external driving is strong enough (f is large enough), only the disordered state can exist at any temperature. The ordering tendency is completely suppressed even at low temperatures. In another work we found this is also true for systems with the tendency for phase separation.

References

1. L. B. Hong and B. Fultz, Phys. Rev. B **51**, 2687 (1995).
2. J. R. Beeler, Jr. and J. A. Delaney, Phys. Rev. **130**, 962 (1963).
3. J. R. Beeler, Jr., Phys. Rev. A **138**, 1259 (1965).
4. B. Fultz, J. Chem. Phys. **87**, 1604 (1987).
5. B. Fultz, J. Chem. Phys. **88**, 3227 (1988).
6. H. Ouyang and B. Fultz, J. Appl. Phys. **66**, 4752 (1989).
7. L. B. Hong, L. Anthony, and B. Fultz, J. Mater. Res. **10**, 126 (1995).
8. L. B. Hong and B. Fultz, Phys. Rev. B **52**, (1995).
9. L. Onsager, Phys. Rev. **65**, 117 (1944).
10. G. Martin, Phys. Rev. B **30**, 1424 (1984).
11. H. A. Atwater, C. V. Thompson, and H. I. Smith, Phys. Rev. Lett. **60**, 112 (1988).
12. H. A. Atwater and C. V. Thompson, Appl. Phys. Lett. **53**, 2155 (1988).
13. H. A. Atwater, C. V. Thompson, and H. I. Smith, J. Appl. Phys. **64**, 2337 (1988).

Chapter 4. Phase Diagrams of Driven bcc Alloys at Low Temperatures

Previous work has shown that ballistic atom movements can cause shifts in phase boundaries [3-10,13], such as suppression of the critical temperature for A2-B2 phase transitions [3-5,13], changes in the order of the transition [4-8], and other nonequilibrium microstructural features at steady states [9,10]. This chapter describes results of Monte Carlo simulations that were used to determine the steady states of equiatomic bcc driven alloys with first nearest neighbor (1nn) and second nearest neighbor (2nn) effective pair interactions (Section 2.3). Three phases are expected in these alloys at low temperature, depending on the relative strength of the 2nn and 2nn interactions: B2 order, B32 order, and chemically unmixed (denoted as "umx") bcc phases. Our simulations were performed near all three bcc phase boundaries so that we could obtain the phase diagrams of bcc driven alloys [12, 14]. We observed substantial amounts of transient order in distinct regions during disorder → order transformations, but these states vanished when the steady state was attained. One example was the transient formation of B2 order in a disorder –> B32 order transformation. Ballistic jumps, even just a small fraction, induced large changes in the transient states and steady states of order in the alloy. The phase diagram in the space spanned by V_1 and V_2 was determined for thermal atom movements alone, and in the presence of ballistic atom movements. With increasing temperature, the region of B32 phase receded against the adjacent regions of B2 order and unmixed states. With the presence of ballistic jumps, however, the opposite behavior was found. The region of B32 order encroached on the adjacent regions of B2 order and unmixed state. Furthermore, with ballistic jumps we found the development of B32/B2 or B32/umx two-phase regions. The shifts in phase boundaries are attributed to differences in how the internal energies of the different phases are affected by ballistic atom movements. Local fluctuations in the

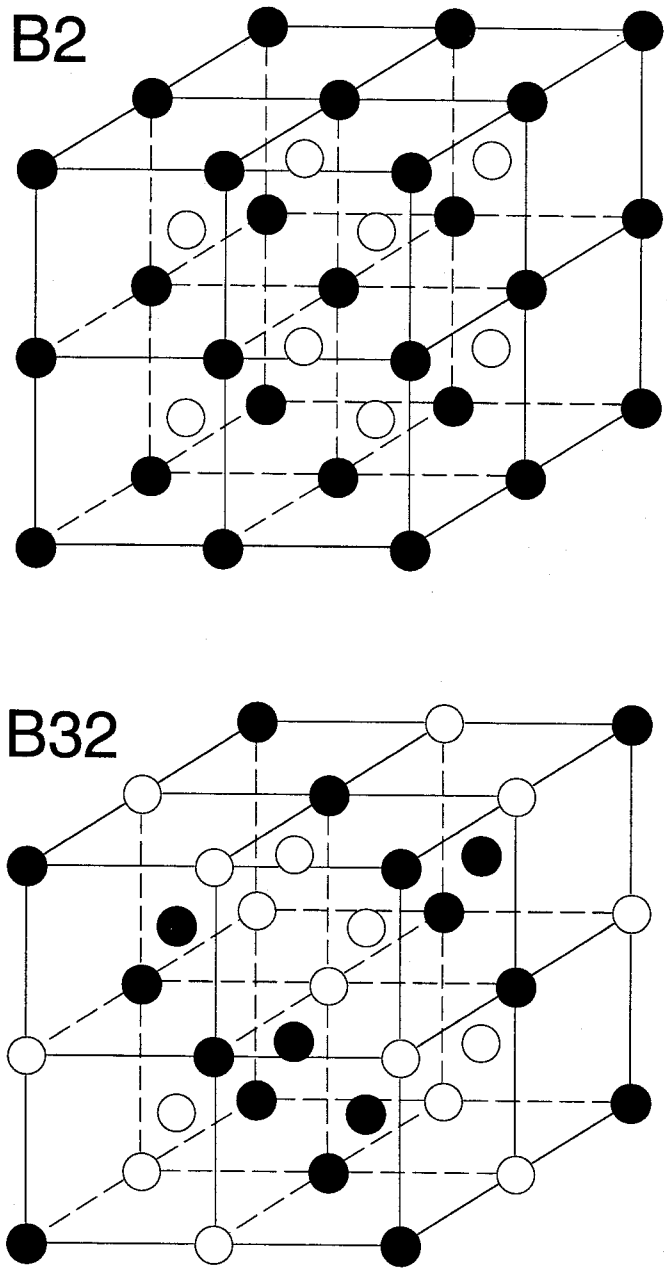

FIG. 4.1. The B2 (top) and B32 (bottom) ordered structures.

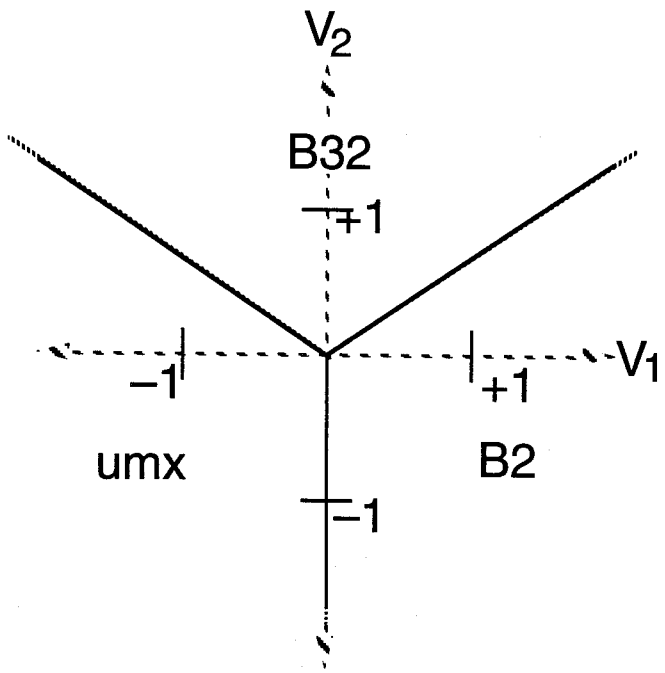

FIG. 4.2. Thermodynamic ground state phase diagram for equiatomic bcc alloys. The phase boundaries are solid straight lines with slopes of +2/3, –2/3, and ∞ ($V_1 = 0$ and $V_2 < 0$), respectively.

internal energy density in the presence of ballistic atom movements caused two-phase regions in the phase diagram.

4.1 Thermodynamic Ground States

Ground state (T = 0) structures of bcc binary alloys have been classified by Richards and Cahn [1] and Allen and Cahn [2]. For equiatomic AB alloys with 1nn and 2nn pair potentials, the ground state is either B2 order, B32 order, or an unmixed bcc alloy (denoted "umx"). The B2 and B32 ordered structures are shown in Fig. 4.1. In the B2 ordered structure, all A atoms take the corner sites of the bcc unit cells while all B atoms take the center sites. Every atom has 1nn neighbors of the opposite type and 2nn neighbors of the same type. The B32 ordered structure is a layered structure along the body diagonal direction of the bcc unit cell. Each atom has mixed 1nn neighbors and 2nn neighbors of the opposite type. In the unmixed state, A atoms are clustered together, as are B atoms. The thermodynamic ground state is the B2 ordered structure when $\nu < 2/3$ and $V_1 > 0$, the B32 ordered structure when $|\nu| > 2/3$ and $V_2 > 0$, and umx when $\nu > -2/3$ and $V_1 < 0$. The ground state phase diagram is shown in Fig. 4.2, with the phase boundaries shown as solid straight lines. The phase boundaries between B32/B2, B32/umx, and B2/umx are at $\nu_c = 2/3, -2/3$, and ∞ ($V_1 = 0$ and $V_2 < 0$), respectively.

It is straightforward to calculate the internal energy densities, i.e., free energy densities at T = 0, of these three possible ground states, E_{B2}, E_{B32}, E_{umx}. With respect to a disordered solid solution they are:

$$E_{B2} = -V_1 + \frac{3}{4}V_2 \quad , \tag{4.1}$$

$$E_{B32} = -\frac{3}{4}V_2 \quad , \tag{4.2}$$

$$E_{umx} = V_1 + \frac{3}{4}V_2 \quad . \tag{4.3}$$

Near a phase boundary, for example the B32/B2 phase boundary, the energy difference between the two phases is very small and the thermodynamic preference for one phase over the other is also weak. For this reason the unstable phase may form transiently during an ordering transformation, although it is not the thermodynamically stable phase.

Transient phase formation has been well documented in kinetic studies with the path probability method and Monte Carlo simulations, which reported that B2 order appeared transiently although the equilibrium state was B32 order when ν was slightly larger than 2/3 [18]. At low temperatures, especially when there is external driving, some defects will be expected and will contribute an additional energy term to Eqs. 4.1 to 4.3. Entropy will also play a role. It is very likely that these new contributions to the free energy will affect the phase diagram and the stable states, as well as the transient states. However, the systematic behavior is not intuitively obvious. Results are provided by our Monte Carlo simulations presented in next section.

4.2 Monte Carlo Simulations

From thermodynamic ground state analysis, the phase boundaries between the three ground state phase regions are at $\nu_c = \{+2/3, -2/3, \infty\}$. To study the effect of temperature and ballistic jumps on the phase diagrams and stable states, as well as transient states, most of our Monte Carlo simulations were on alloys near these three phase boundaries: {B32/B2, B32/umx, B2/umx}. Unless stated otherwise, these three regions of ν were obtained with pair potentials having approximate values: {($V_{AA1} = +1$, $V_{BB1} = +1$, $V_{AA2} \approx +1.32$, $V_{BB2} = 0$) , ($V_{AA1} = -1$, $V_{BB1} = -1$, $V_{AA2} \approx +1.32$, $V_{BB2} = 0$) , ($V_{AA1} \approx -0.06$, $V_{BB1} = 0$, $V_{AA2} = -1$, $V_{BB2} = -1$)}. For all simulations, $V_{AB1} = 0$ and $V_{AB2} = 0$.

4.2.1 B32 and B2 Phases

Figure 4.3 shows the evolution of L_{B2} and L_{B32} (Section 2.3) for an alloy with ν = 0.667, which is less than the critical ν_c of 0.6728 at this temperature. The alloy has B2 order at thermodynamic equilibrium, as shown by the thick curves labeled with f = 0. B32 order appears transiently before it vanishes completely at the steady state. Similarly Fig. 4.4 shows the evolution of L_{B2} and L_{B32} for an alloy with ν = 0.6735, slightly above ν_c. In the thermodynamic case (f = 0), again shown as thick curves labeled with f = 0, B32 order now is the equilibrium state while B2 order becomes transient. The transient B2 order is very strong at about 3000 MCS. A small fraction of ballistic jumps can also alter significantly the kinetics of the alloy. Figure 4.3 shows that when f changes from 0 to 0.01, both B2 order and B32 order start to develop at a much earlier stage as the ballistic jumps serve to enhance atom mobilities (Chapter 3). In Fig. 4.4, however, the same change of f only suppresses substantially the transient formation of B2 order, and suppresses slightly the final steady state B32 order, but does not switch the transient and steady state of order.

Transient B2 order has been observed previously [18] during disorder $\rightarrow$ B32 order phase transformations when B32 order was the thermodynamic equilibrium state. These transient B2 domains were a few lattice constants in diameter. Much larger regions with a high degree of order were found in the present study, especially when ν was near the boundary ν_c. As an example, Fig. 4.5 shows domain structures on two consecutive (100) planes at the time when the transient B2 order was a maximum. The simulations were performed for the case of chemically symmetric pair potentials (V_{AA}=V_{BB}) with ν slightly above the critical ν_c. The white region at the bottom is a well-ordered B2 domain, and the black region at the top is another B2 domain of the other variant. The pattern at the upper left and right is a well-ordered B32 domain. It is clear that the transient B2 order develops as distinct domains. Distinct domains were also found for cases of transient B32 order.

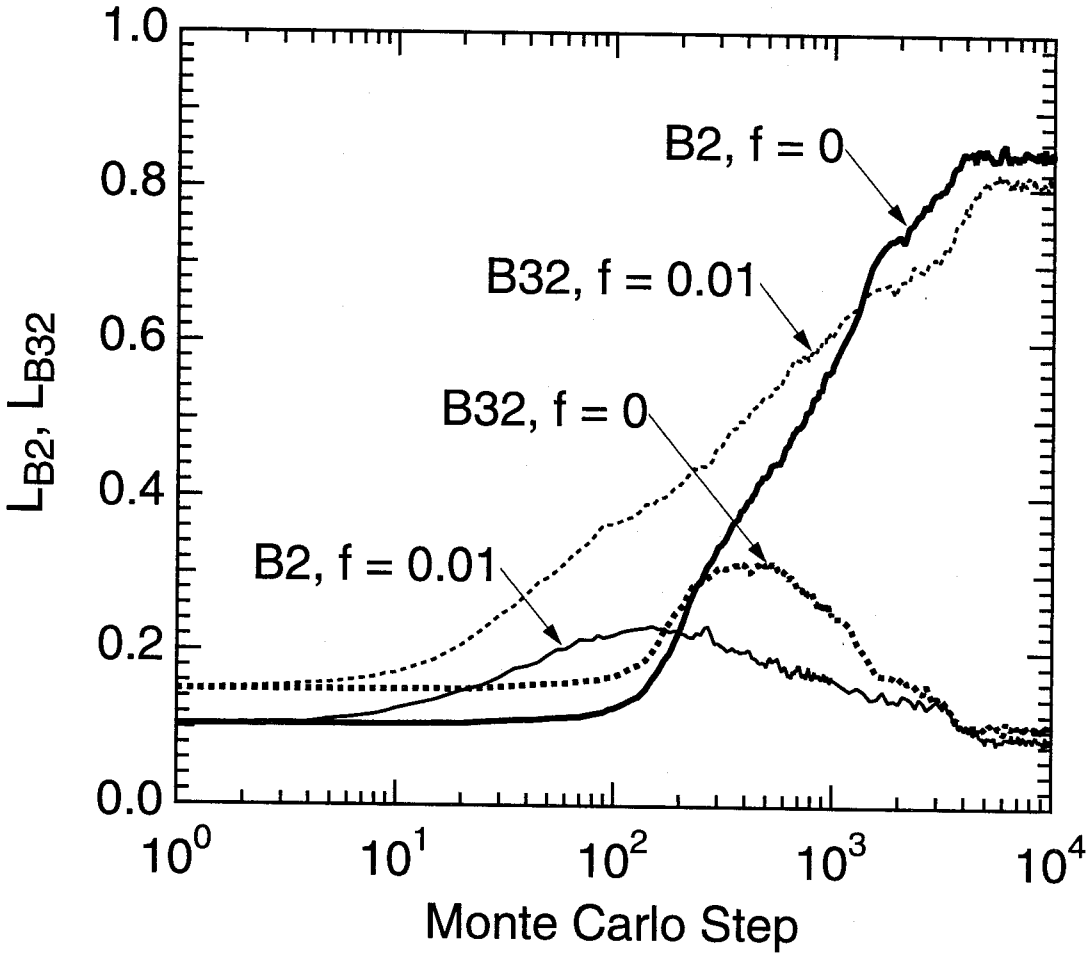

FIG. 4.3. The time dependence of B2 and B32 LRO parameters for an alloy with $\nu = V_{AA2}/2 = 0.6675$ ($< \nu_c$) and $V_{BB2} = 0$. B2 order, the thermodynamic stable state at f = 0, becomes transient state at f = 0.01. Solid curves: B2; dashed curves: B32. Thick curves: thermodynamic case with f = 0. Thin curves: with ballistic jumps, f = 0.01.

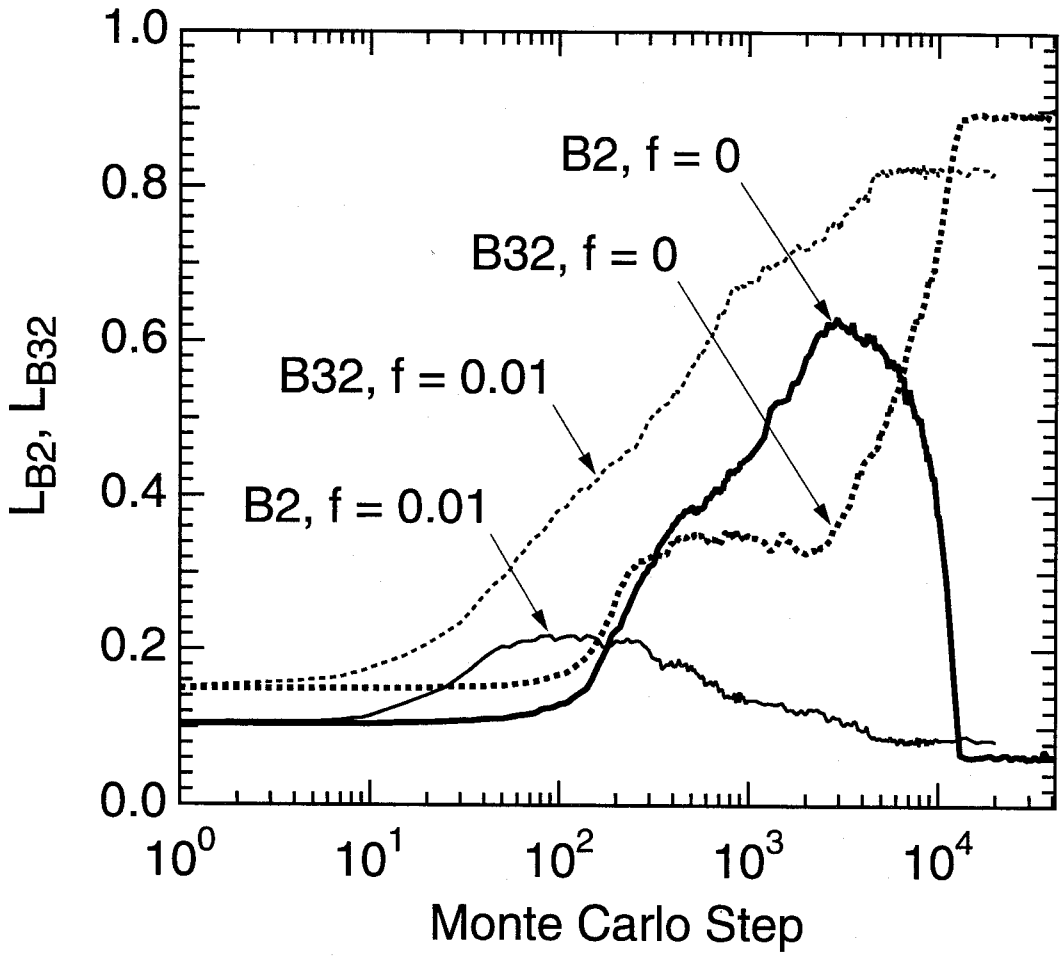

FIG. 4.4. The time dependence of B2 and B32 LRO parameters for an alloy with $\nu = V_{AA2}/2 = 0.6735$ ($> \nu_c$) and $V_{BB2} = 0$. The transient B2 order is suppressed strongly by ballistic jumps. Solid curves: B2; dashed curves: B32. Thick curves: thermodynamic case with f = 0. Thin curves: with ballistic jumps, f = 0.01.

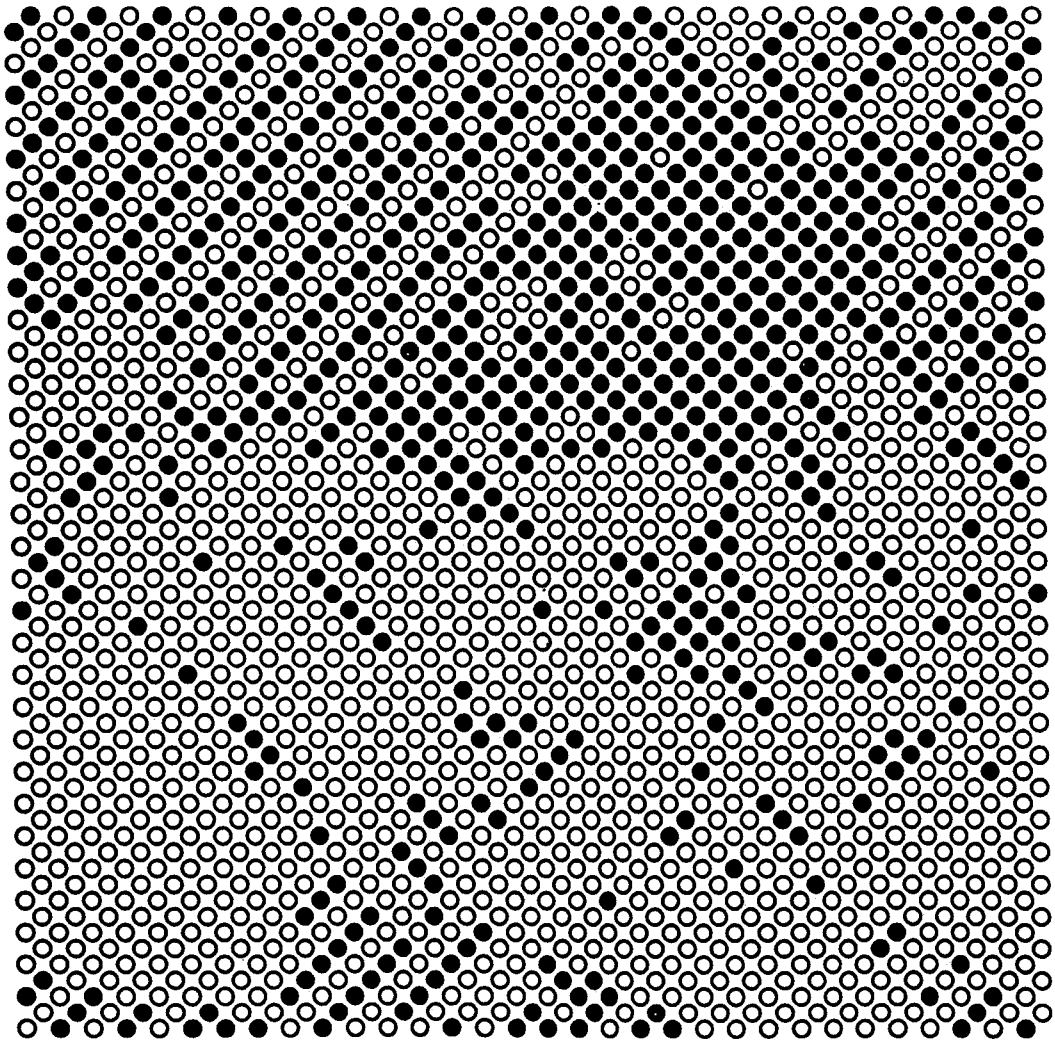

Figure 4.5. Snapshot of the alloy taken after 200 Monte Carlo steps in a simulation for the case of chemically symmetric pair potentials with $v = V_{AA2} = V_{BB2} = 0.6756$ and $f = 0$. Two consecutive (100) planes are shown; the center sites of the unit cell form a square lattice that interpenetrates the square lattice from the corner sites. The image was prepared by overlaying on the crystal a mask of B2 order of one domain variant. Atom occupancies consistent with this variant of B2 order are white, and those of the opposite variant are black. B2 order therefore appears as regions of black or white; B32 order as regions of diagonal stripes.

The difference between Figs. 4.3 and 4.4 suggests that ballistic jumps favor the development of B32 order over B2 order. To study systematically how the ballistic jumps change the steady state and transient state of order, a set of Monte Carlo runs with different values of f were performed for the same alloy with $\nu = V_{AA2}/2 = 0.66$. The steady state values attained by the order parameters L_{B32} and L_{B2} are presented as a function of f in Fig. 4.6a. The figure shows that at about f = 0.003, there is a switch of the steady state of order. That is, the ballistic jumps cause a change in the final steady state from B2 order to B32 order. Figure 4.6b presents the steady state internal energy density of the same alloys as a function of f. The internal energy density increases much faster with f in the B2 ordered state than in the B32 ordered state. This means the B32 ordered state gains much less energy from the presence of ballistic jumps than does the B2 ordered state. The B32 ordered state is favored over the B2 ordered state in the presence of ballistic jumps. A higher accumulation of internal energy density in the B2 ordered state is consistent with the drop in the internal energy at f = 0.003. Examination of the alloys showed that this was due to more antisite defects generated and sustained in the B2 ordered state that in the B32 ordered state.

In several cases we confirmed that the steady states were indeed steady states by starting the simulations with the alloys having perfect ordered structures of B2 or B32 order, and verifying that the same order parameters were eventually attained as for the cases of initially disordered alloys. The steady state is unique (as expected for a Markovian system [11]), and should be attained eventually for any initial states. One example is shown in Fig. 4.7, for an alloy with $V_{AA2}/2 = 0.66$ and f = 0.01. The transient states, however, did not form during the kinetic evolution of alloys that began with perfect order of their equilibrium type.

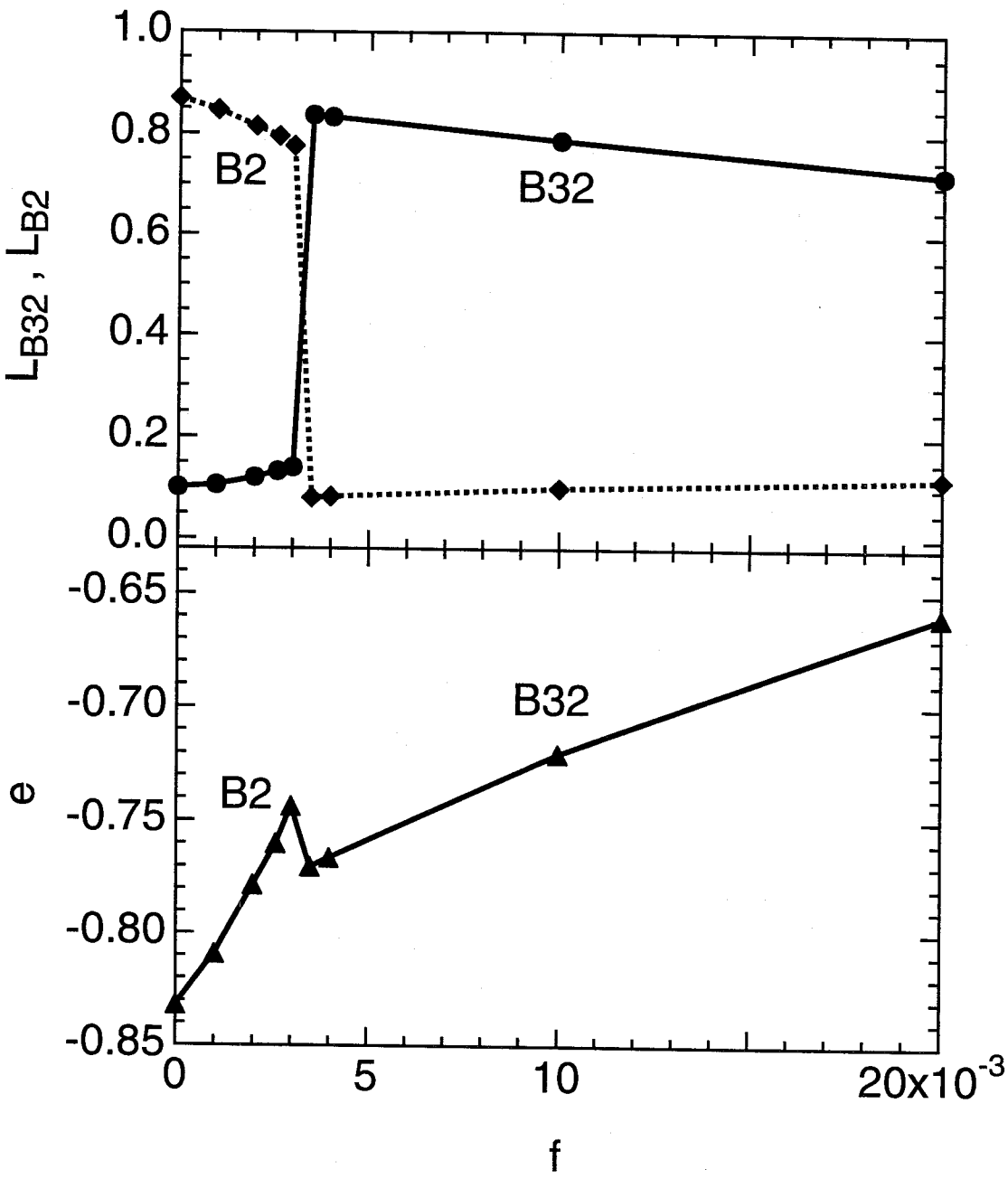

FIG. 4.6 (a) The steady state values of L_{B2} (diamonds) and L_{B32} (circles) during kinetic evolution with $\nu = V_{AA2}/2 = 0.66$ as functions of f. (b) The corresponding steady state internal energy per atom, e, as a function of f.

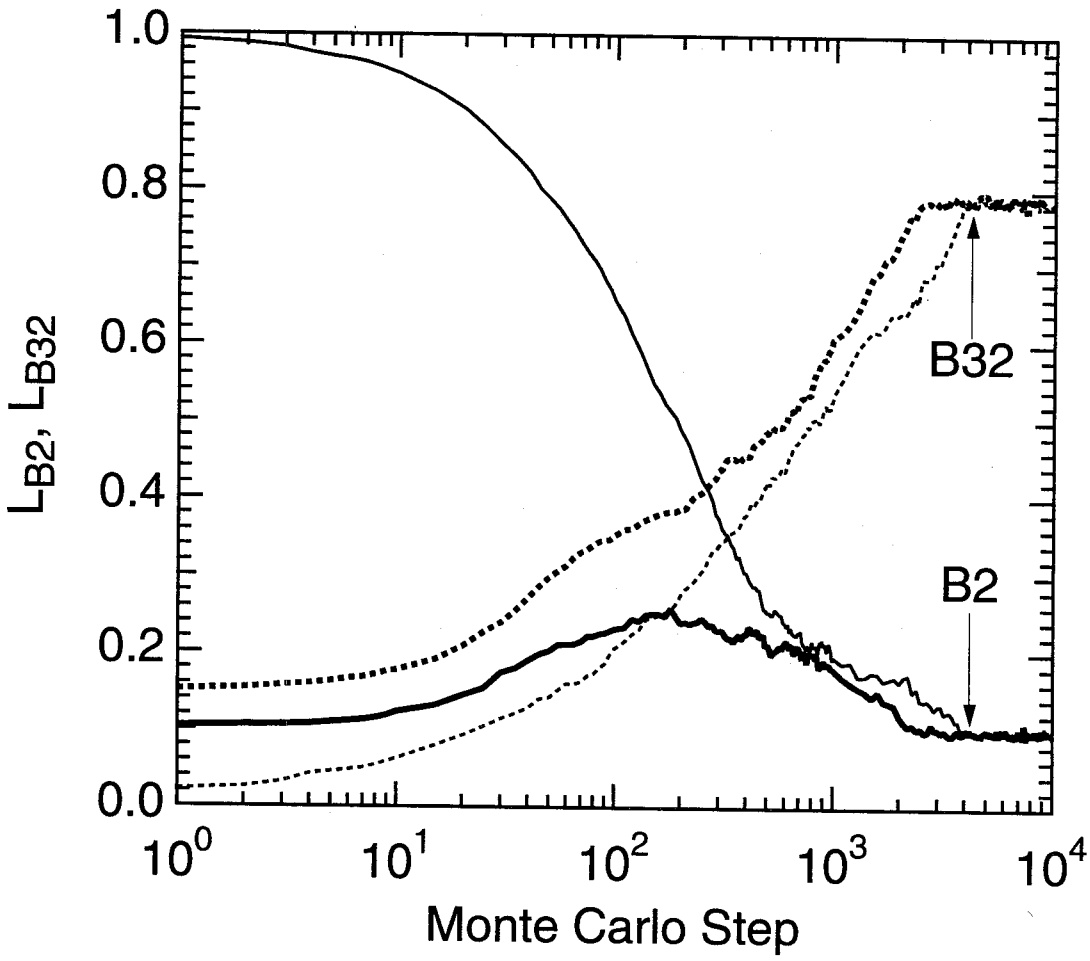

FIG. 4.7. The time dependence of B2 and B32 LRO parameters for an alloy with $\nu = V_{AA2}/2 = 0.66$, $V_{BB2} = 0$, and $f = 0.01$. Solid curves: B2; dashed curves: B32. Thick curves: initially disordered. Thin curves: initially perfect B2 order.

Results from many simulations like those of Figs. 4.3, 4.4, and 4.6 were used to compile the results presented in Fig. 4.8. This figure presents the maximum amounts, either transient or steady state, of the B2 and B32 LRO parameters as a function of ν for the case of chemically asymmetric pair potentials ($V_{AA2} = V_2$, $V_{BB2} = 0$). The thermodynamic case, without ballistic jumps, is the pair of thick curves for $f = 0$. As expected, the B2 phase is favored for small ν, and the B32 phase is favored for large ν. The crossover gives the thermodynamic phase boundary at this temperature, $\nu_c = 0.6728 \pm 0.0008$. However, even towards the left of Figure 4.8 where only the B2 phase is found in steady-state, the B32 phase appears transiently. The amount of this transient state increases with ν, and the B32 phase becomes the steady state structure above ν_c. The transient appearance of B2 order is stronger for alloys closer to the phase boundary ν_c, since the energy difference is smaller and therefore the thermodynamic preference of B32 order over B2 order is weaker. A complementary behavior of the transient B2 structure was found for the case when ν was decreased from values above ν_c.

The transition of stable B2 order to stable B32 order in the thermodynamic case of $f = 0$ is very sharp. No coexistence of the B2 and B32 structures was observed in steady state, except perhaps for the data point closest to the crossover, ν_c. Further study of this case would require a careful analysis of the finite sizes and times of our Monte Carlo simulations, however.

The curves with $f > 0$ in Fig. 4.8 show that very small fractions of ballistic jumps cause the crossover, ν_c (where $L_{B2} = L_{B32}$), to move strongly to lower values of ν. Alloys with ν between the new and the old values of ν_c have their steady state and transient state of order switched by the ballistic jumps, as shown in Fig. 4.3. Furthermore, when $f > 0$ and ν was near ν_c, a two-phase steady state was found, with domains of both B2 and B32 order. The locations of the domains of B2 and B32 order were not static, and the domain

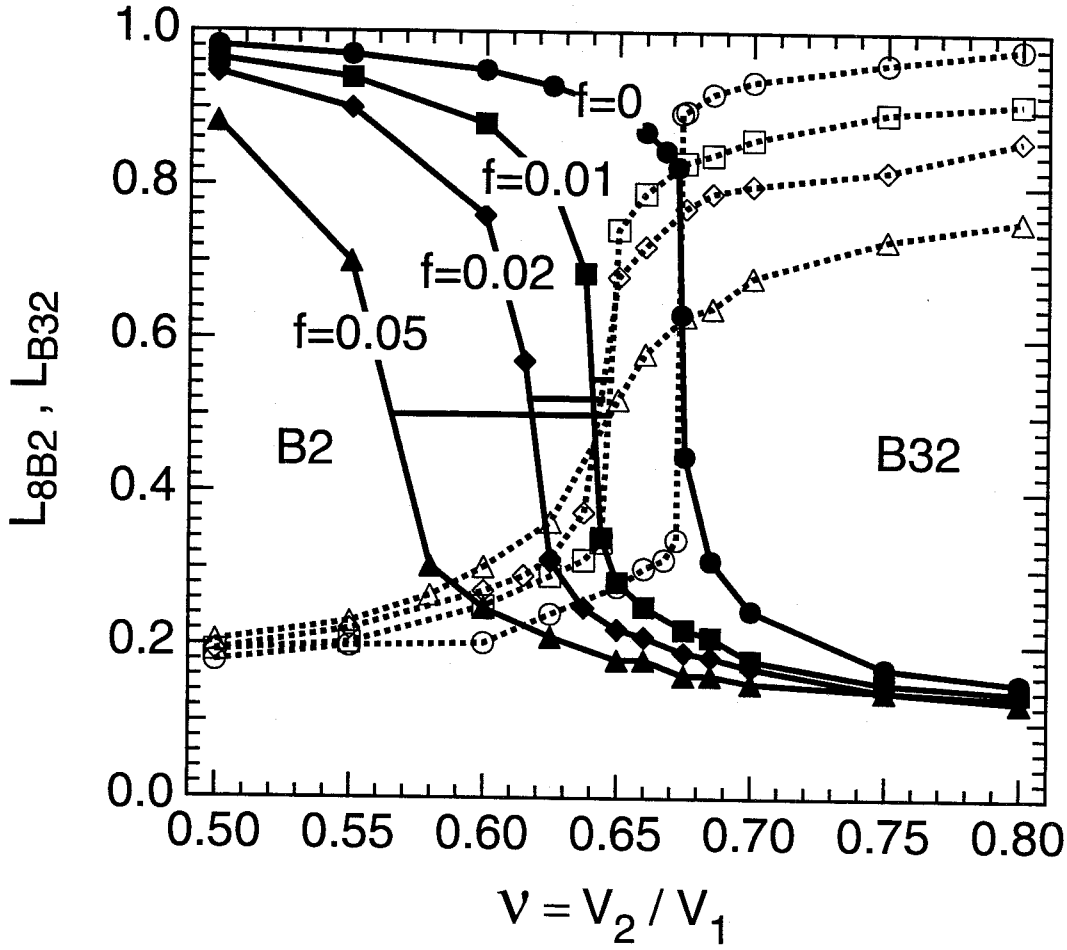

FIG. 4.8. Maximum B2 and B32 LRO parameters as functions of f and ν for the case of chemically asymmetric pair potentials with $\nu = V_{AA2}/2$ and $V_{BB2} = 0$. Solid markers and solid curves: B2; open markers and dashed curves: B32. Circles: f = 0; squares: f = 0.01; diamonds: f = 0.02; triangles: f = 0.05.

boundaries migrated with time. A similar phenomenon was also observed near the phase boundary between B32/umx states with $f > 0$, and will be described in the next section. Owing to the finite size of our simulations, the range in ν of this two-phase region could not be mapped precisely, but it spans approximately those values of ν between the steepest slopes of the pairs of curves in Fig. 4.8, where L_{B2} and L_{B32} are about 0.5. These regions of two-phase coexistence are marked by horizontal bands. Notice that while the two-phase regions move to lower values of ν with increasing f, most of the change occurs at the left edge; the B2 phase becomes especially unstable in the presence of the ballistic jumps for the case of chemically asymmetric 2nn pair potentials.

Finally, we examined some effects of the finite size of our Monte Carlo simulations. Using larger lattices with 524 288 sites, we found that the smallest values of L_{B2} and L_{B32} in Figure 4.4 decreased with increasing lattice size; an effect of the reduced importance of the diffuse scattering contribution to the superlattice peak intensities. Also affected were the values of the LRO parameters in cases where the sizes of the domains were comparable to the size of the alloy. Changing the size of the alloy did not have other effects of significance, however. In particular, the transient states, the steady states, and amount of shift of ν_c caused by ballistic jumps were largely unaffected by changing the size of the alloy.

4.2.2 B32 and unmixed Phases

The phenomena of transient and steady states, phase boundaries, and two-phase coexistence for the pair of B32/umx phases are very similar to those of the B32/B2 pair of phases presented in the last section. Perhaps the only qualitative difference is that one involves the unmixed state while the other the B2 phase. The presentation and discussions in this section will parallel those in the last section but with less detail.

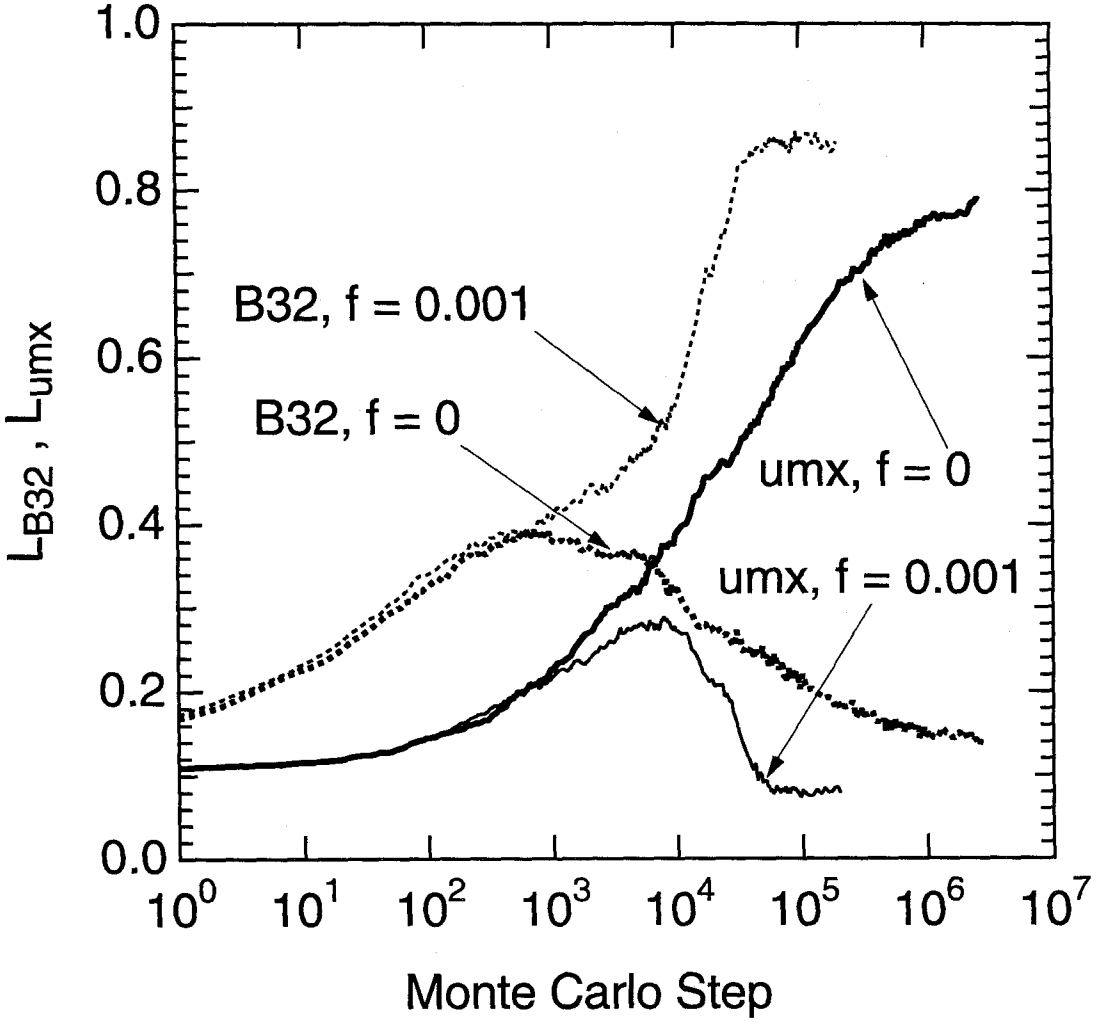

Figure 4.9 Time evolution of L_{umx} (solid) and L_{B32} (dashed) for $\nu = -V_{AA2}/2 = -0.66$ with f = 0 and 0.001, respectively.

Figure 4.9 presents the evolution of the order parameters L_{B32} and L_{umx} in an alloy with thermodynamic equilibrium as an unmixed state. The evolution of the order parameters for the thermodynamic case with $T > 0$ and $f = 0$ are shown by the thick curves. Kinetics allows the transient formation of B32 order, and for a brief time this transient B32 order is stronger than the state of unmixing. This is not surprising, since unmixing requires long-range diffusion, which is less expedient than the formation of B32 order [17-19]. Nevertheless, the state of the alloy after long times was the unmixed state, as expected in thermodynamic equilibrium. (As seen in Fig. 4.9 for $f = 0$, towards the end of our simulations the order parameter for the unmixed state, L_{umx} , was still evolving. The long times and large lattice sizes required to attain two large regions were difficulties in the present work, and some of our estimates of the steady state values of L_{umx} may be slightly low.)

Figure 4.9 also presents the evolution of order parameters in an alloy with the same effective pair potentials, but with a small fraction of ballistic jumps ($f = 0.001$). The early stages of ordering, which have large relaxation of internal energy, are unaffected by the presence of a small fraction of ballistic jumps. After about 10^4 Monte Carlo steps, however, the small fraction of ballistic jumps causes the two order parameters to be reversed in magnitude from their values for the thermodynamic case of $f = 0$. The ballistic jumps cause B32 order to be favored over the unmixed state.

A set of Monte Carlo runs with different values of f were performed for $\nu = -V_{AA2}/2 = -0.66$ as in Fig. 4.9. The steady state values attained by the order parameters L_{B32} and L_{umx} in these alloys are presented as a function of f in Fig. 4.10a. The figure shows that at about $f = 0.0003$, there is a crossover of the state of order where the ballistic jumps cause a change in the final state from an unmixed alloy to a B32 ordered alloy.

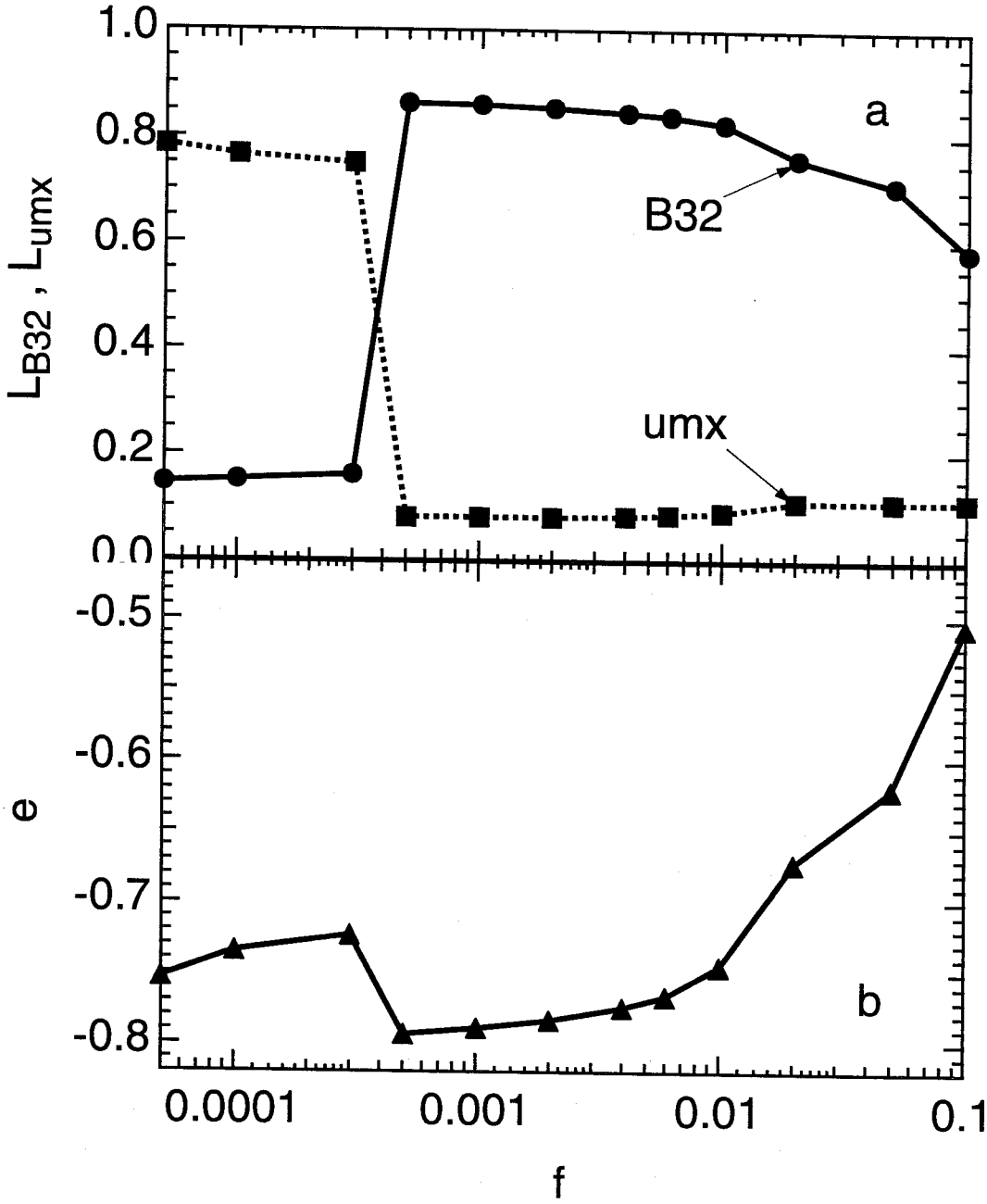

Figure 4.10 (a) The steady state values of L_{umx} (squares) and L_{B32} (circles) during kinetic evolution with $\nu = -V_{AA2}/2 = -0.66$ as functions of f. (b) The corresponding steady state internal energy per atom, e, as a function of f.

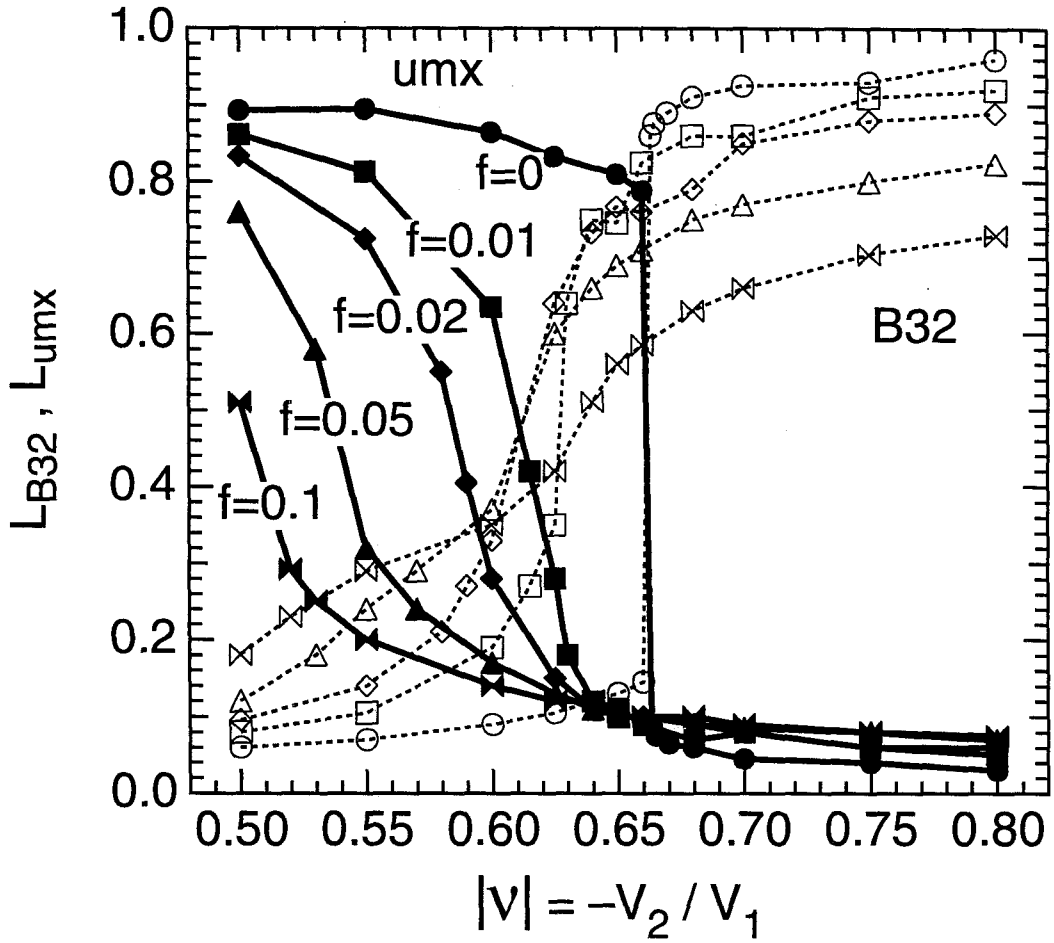

Figure 4.11. The steady state values of L_{umx} (solid) and L_{B32} (dashed) during kinetic evolution with f = {0, 0.01, 0.02, 0.05, 0.1} with markers {circles, squares, diamonds, triangles, bow ties}as functions of v.

Figure 4.10b presents the steady state internal energy density of the same alloys as a function of f. The internal energy density undergoes a distinct drop at f = 0.0003. This drop indicates that in the presence of ballistic jumps, the internal energy of the unmixed state is larger than that of the state of B32 order. Examination of the alloys showed that this was due in part to antisite defects, but the importance of an internal interface between A and B atoms in the unmixed alloy will be discussed in next section.

Figure 4.11 presents a compilation of all our results on the steady state values of the order parameters L_{B32} and L_{umx} for alloys of f = {0, 0.01, 0.02, 0.05, 0.10} for various ν near the B32/umx phase boundary. For the thermodynamic case of f = 0, we find that the phase boundary is sharp, and occurs at $\nu = -0.6632 \pm 0.0002$. We define ν_c as the crossover point of the two curves L_{B32} and L_{umx}. Notice that with increasing f, ν_c shifts to lower values of $|\nu|$, primarily because of the strong shift of L_{umx} with f.

Examination of selected planes of the alloy showed another important effect of ballistic atom movements on the state of order. The steady states of thermodynamic alloys (f = 0) were a state of pure B32 order or a pure unmixed state. For f > 0, however, the steady states of the alloy were heterogeneous, showing regions of B32 order in contact with unmixed regions. This phenomenon of two-phase coexisting due to ballistic jumps was also observed near the phase boundary between B32/B2 phases. Figure 4.12 shows a steady state of such an alloy. In steady state these regions did migrate with time, but they did not coarsen (at least coarsening was not observable for times of a factor of ten longer than the time required to achieve the steady state). The precise boundaries of this two-phase region were difficult to determine precisely, but they extend approximately between values of ν for which the curves of L_{B32} and L_{umx} were 0.5. With increasing f, this two phase region grew wider, primarily at the expense of the unmixed state. The domains in

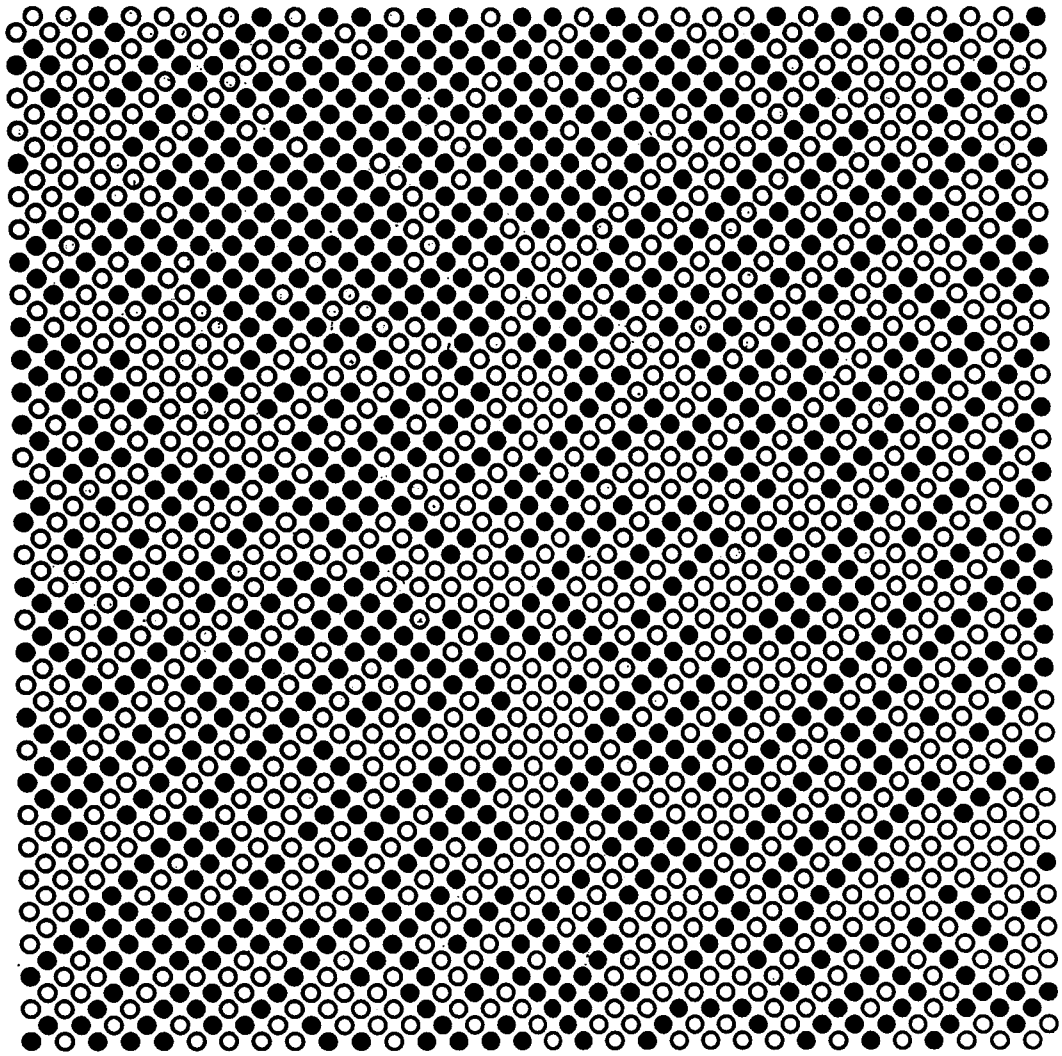

FIG. 4.12. Projection of two adjacent (200) planes of an alloy in steady state with $\nu = -0.6285$ and $f = 0.01$, showing two-phase coexistence. Corner and center atoms of standard cubic bcc unit cell are projected. A and B atoms are shown as black or white circles. Unmixed regions are found in the upper left as regions of black or white, whereas banded regions indicate B32 order. Order parameters of the alloy were $L_{B32} = 0.58$, $L_{umx} = 0.23$.

Fig. 4.12 are better described as B32 regions and unmixed regions with internal disorder, rather than fluctuations within a disordered alloy. The size of the ordered domains in steady state was found to decrease with increasing f. A fluctuation description is perhaps more appropriate for higher values of f.

4.2.3 B2 and Unmixed Phases

In the thermodynamic case with f = 0, the transient and steady state behavior of B2/umx phases was very similar to those of B32/B2 and B32/umx phases described in the previous sections. The thick curves in Fig. 4.13 are the time evolution of the order parameters L_{B2} and L_{umx} in a thermodynamic alloy with $V_{AA1} = -0.04$ and $V_{AA2} = V_{BB2} = -1$. While B2 order was the state of thermodynamic equilibrium, the unmixed state appeared transiently. Notice that the transient umx state was relatively long-lived (it was still slowly decaying at the end of our Monte Carlo simulation.) compared with those in Figs. 4.3, 4.4, and 4.7, and peaked at about 4000 MCS when B2 order was already very strong ($L_{B2} \approx 0.9$). The unmixed state is much more difficult to develop and grow than B2 order or B32 order because diffusion over a much larger spatial (and therefore time) scale is needed. The transient appearance of the umx state in this case shows that a smaller spatial or time scale is NOT a necessary condition for a state to appear transiently. A transient state can appear when its spatial or time scale is much larger, and it lives for a much longer time.

On the other hand, a much smaller spatial or time scale of the transient state can cause it to have a very strong appearance. The transient appearance of B2 order was typically very strong while the transient appearance of the unmixed state was much weaker. This difference was due to the very different spatial and time scales needed for formation and growth of B2 phase and unmixed state. Contrary to what was observed in last two

sections, however, neither the transient state nor the steady state was affected much by ballistic jumps. After extensive and systematic searching through the phase space, only in a very narrow range did we find such switch-over of the transient state and steady state by a relatively large fraction of ballistic jumps compared to those needed in B32/B2 or B32/umx phases. One example is given as thin curves in Fig. 4.13. Notice the large value of f (0.1) and the strong appearance of the transient B2 order. No two-phase region was found near the B2/umx phase boundary for any value of f.

The differences between the alloys near the B2/umx boundary compared to alloys near the B2/B32 and B32/umx boundaries were not surprising after a second thought, however. The results on B32/B2 phases in Section 4.2.1 and those on B32/umx phases in Section 4.2.2 have enormous similarities. For example, the curves in Figs. 4.8 and 4.11 are similar not only in shapes, but also in their degree of phase boundary shifts due to ballistic jumps. These similarities suggest that the B2 order and the umx state have similar responses to ballistic atom movements. Examination of the local atom arrangements in B2 and umx structures shows the opposite 1nn atomic environment but the same 2nn atomic environments. One structure can be considered as the mirror image of the other about the their phase boundary ($V_1 = 0$), although one domain boundary must exist in the unmixed state but need not in the B2 state. If an unmixed alloy and another B2 alloy are images of each other (i.e., same V_2 and opposite V_1) about the phase boundary, I suggest that the transient state and steady state will not be affected by the ballistic jumps in any way similar to B32/B2 or B32/umx phases because both alloys are expected to respond to the ballistic jumps in a similar way. The phase boundary will not be shifted by either temperature or ballistic jumps. These predictions were proved correct by our extensive Monte Carlo simulations, except very small deviation mainly due to the domain boundary in the unmixed state and its correlation with other defects. More discussions in term of partition function and some quantitative details are given in the next a few sections.

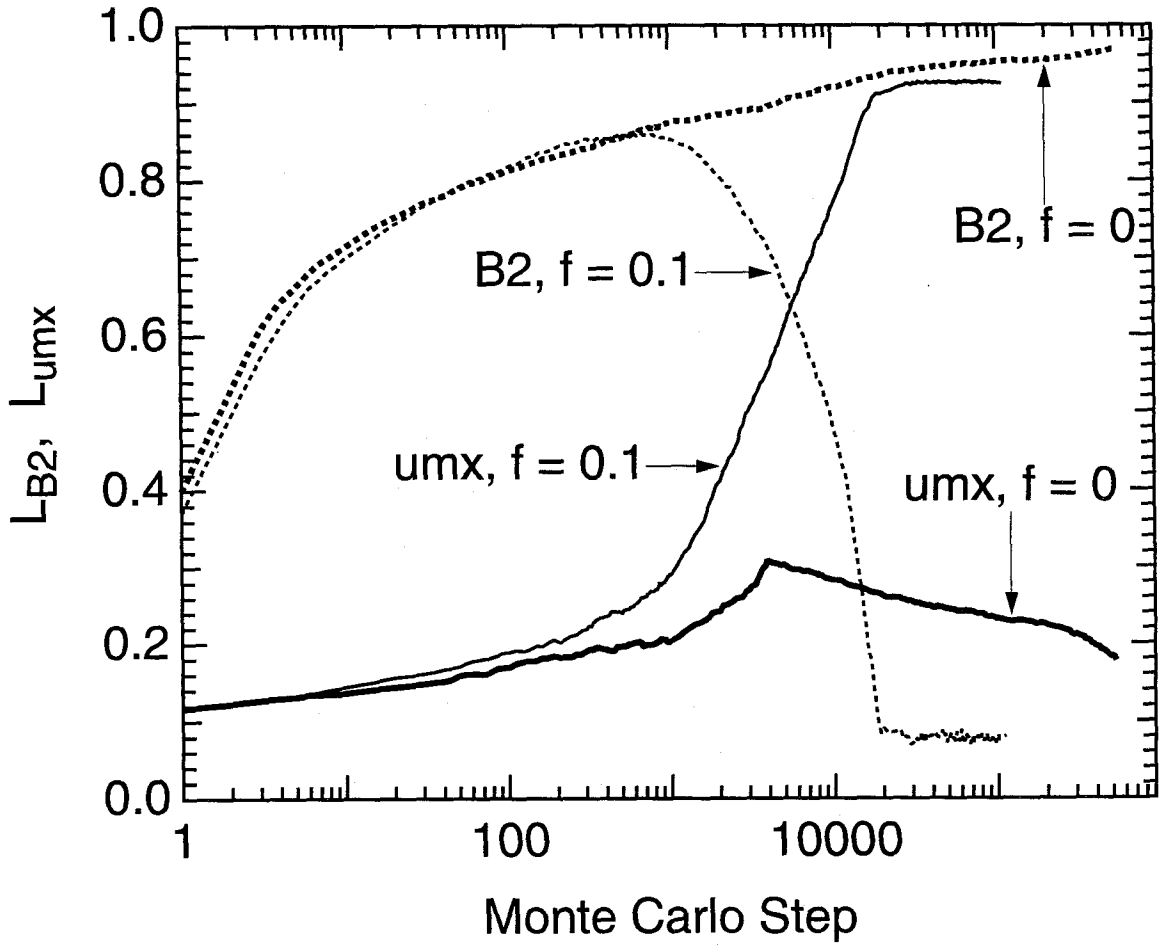

FIG. 4.13. Time evolution of L_{B2} (dashed) and L_{umx} (solid) for $1 / \nu = -V_{AA2}/2 = 0.02$ with f = 0 and 0.1, respectively.

4.3 Thermodynamic Partition Function and its Application to Low Temperature Phase Diagrams

Phase boundaries of thermodynamic phase diagrams are generally expected to change with temperature. To predict these changes analytically, we performed a low temperature expansion of the partition function for the B2, B32, and unmixed alloys [20]. The idea behind this expansion is to identify the sensitivity of the free energy to small amounts of disorder, as might be expected at very low temperatures. For the B2 and unmixed alloys, the partition function, Z, was evaluated with the following terms:

$$Z = \exp\left(-\frac{N\varepsilon_0}{kT}\right) + N\exp\left(-\frac{N\varepsilon_0}{kT}\right)\exp\left(-\frac{\delta\varepsilon_1}{kT}\right)$$

$$+ 4N\exp\left(-\frac{N\varepsilon_0}{kT}\right)\exp\left(-\frac{\delta\varepsilon_{2a}}{kT}\right) + 3N\exp\left(-\frac{N\varepsilon_0}{kT}\right)\exp\left(-\frac{\delta\varepsilon_{2b}}{kT}\right) \quad . \qquad (4.4)$$

The first term is the Boltzmann factor for the perfect crystal, and the second term is the Boltzmann factor for the perfect crystal with one antisite atom. The third term accounts for one pair of antisite defects that are separated by a 1nn distance. The atoms in this pair have one fewer 1nn pair than two separated antisite defects. On the bcc lattice these dimer defects have a degeneracy of 4N. The fourth term is for one pair of antisite defects separated by 2nn distances. Specific expressions for the energy differences $\{\delta\varepsilon\}$ are provided in Table 4.1. First neighbor pairs of antisite defects in the B32 structure required a slightly different treatment — the two antisite atoms could be located on sublattices of either like or unlike species.

Equation 4.4 was evaluated at the three phase boundaries: B2/B32 ($V_1 > 0$, $V_2 = 2/3V_1$), B32/umx ($V_1 < 0$, $V_2 = -2/3V_1$), B32/umx ($V_1 = 0$, $V_2 < 0$). The resulting free energy densities with respect to the disordered solid solution are:

TABLE 4.1. Terms of energy differences in low-temperature expansion of the partition function, Eq. 4.4.

$\varepsilon_0^{B2} = -V_1 + \frac{3}{4}V_2$	$\varepsilon_0^{B32} = -\frac{3}{4}V_2$	$\varepsilon_0^{umx} = V_1 + \frac{3}{4}V_2$
$\delta\varepsilon_1^{B2} = 4V_1 - 3V_2$	$\delta\varepsilon_1^{B32} = 3V_2$	$\delta\varepsilon_1^{umx} = -4V_1 - 3V_2$
$\delta\varepsilon_{2a}^{B2} = 7V_1 - 6V_2$	$\delta\varepsilon_{2ai}^{B32} = V_1 + 6V_2$; $\delta\varepsilon_{2aii}^{B32} = -V_1 + 6V_2$	$\delta\varepsilon_{2a}^{umx} = -7V_1 - 6V_2$
$\delta\varepsilon_{2b}^{B2} = 8V_1 - 5V_2$	$\delta\varepsilon_{2b}^{B32} = 5V_2$	$\delta\varepsilon_{2b}^{umx} = -8V_1 - 5V_2$

B2/B32 at ($V_{AA1} = V_{BB1} = \frac{V_1}{2}$, $V_{AA2} = V_2 = \frac{2}{3} V_1$, $V_1 > 0$):

$$F_{B2} = -\frac{V_1}{2} - kT\left(\exp(-\frac{2V_1}{kT}) + 4\exp(-\frac{3V_1}{kT}) + 3\exp(-\frac{14V_1}{3kT})\right) \quad , \tag{4.5}$$

$$F_{B32} = -\frac{V_1}{2} - kT\left(\exp(-\frac{2V_1}{kT}) + 2\exp(-\frac{3V_1}{kT}) + 2\exp(-\frac{5V_1}{kT}) + 3\exp(-\frac{10V_1}{3kT})\right) \quad , \tag{4.6}$$

B32/umx at ($V_{AA1} = V_{BB1} = \frac{V_1}{2}$, $V_{AA2} = V_2 = -\frac{2}{3} V_1$, $V_1 < 0$):

$$F_{umx} = \frac{V_1}{2} - kT\left(\exp(\frac{2V_1}{kT}) + 4\exp(\frac{3V_1}{kT}) + 3\exp(\frac{14V_1}{3kT})\right) \quad , \tag{4.7}$$

$$F_{B32} = \frac{V_1}{2} - kT\left(\exp(\frac{2V_1}{kT}) + 2\exp(\frac{3V_1}{kT}) + 2\exp(\frac{5V_1}{kT}) + 3\exp(\frac{10V_1}{3kT})\right) \quad , \tag{4.8}$$

B2/umx at ($V_1 = 0$, $V_{AA2} = V_{BB2} = \frac{V_2}{2} < 0$):

$$F_{umx} = \frac{3V_2}{4} - kT\left(\exp(\frac{3V_2}{kT}) + 4\exp(\frac{6V_2}{kT}) + 3\exp(\frac{5V_2}{kT})\right) \quad , \tag{4.9}$$

$$F_{B2} = \frac{3V_2}{4} - kT\left(\exp(\frac{3V_2}{kT}) + 4\exp(\frac{6V_2}{kT}) + 3\exp(\frac{5V_2}{kT})\right) \quad . \tag{4.10}$$

The presence of isolated antisite defects (the second term in Eq. 4.4) causes no shifts of phase boundaries. It is therefore reasonable to neglect larger numbers of isolated antisite defects when writing the partition function of Eq. 4.4, at least for the purpose of finding shifts of phase boundaries. We note that Eqs. 4.5 and 4.6 were obtained previously [21].

The low temperature free energy expressions of Eqs. 4.5-4.10 show that with increasing temperature, the B32/B2 and B32/umx phase boundaries shift by the same amounts. With increasing temperature, the B2 and unmixed phase regions encroach by the

same amount into the B32 region. On the other hand, the B2/umx phase boundary is unchanged with temperature, at least to our level of approximation. We therefore expect that at moderately low temperatures, the B2/umx phase boundary will shift much less with temperature than will the B32/B2 and B32/umx phase boundaries.

The shifts of phase boundaries caused by temperature predicted by the low temperature expansion of the partition function were compared to results from the Monte Carlo simulations. The directions and magnitudes of the shifts were qualitatively consistent for the two methods, as we now discuss. However, the comparison of these shifts of phase boundaries required careful consideration of finite size effects in the Monte Carlo simulations. In particular, the energy density of the unmixed state is affected strongly by the finite size of the lattice. While the ordered B2 and B32 phases become single domains in steady state, there must always be an interface between the regions of A-atoms and B-atoms in the unmixed state. The energy cost of this interface raises the internal energy density of the unmixed state with respect to the B2 and B32 states of order, causing these regions of ordered phase to encroach on the unmixed region of the phase diagram. To estimate this contribution to the internal energy, we prepared fully unmixed alloys on lattices of different sizes, with flat interfaces between the two species. We then determined the internal energy densities of these perfectly unmixed states. Using this excess energy density in a $T = 0$ ground state analysis of the B2/unmixed phase boundary, we found shifts of the phase boundary from the ideal $1/\nu = 0$ to $1/\nu = 0.0079$ and $1/\nu = 0.0333$ for lattices with 128 and 32 unit cells on their edges, respectively. (Notice that these changes in $1/\nu$ scale satisfactorily with the surface/volume ratio of the lattices, as expected.) For comparison, the B2/umx phase boundary determined by steady states of Monte Carlo simulations was at $1/\nu = 0.0322$ for lattices with 32 unit cells on their edges. Although the thermodynamic calculations of this section predict no shift of the B2/umx phase boundary, the observed shift is explained adequately by the interface excess energy density of the

unmixed state. The same finite size effect on the energy of the unmixed alloy affects the shift of the B32/umx phase boundary. In this case there are competing thermodynamic and finite size effects that provide opposing shifts of the position of the B32/umx boundary. Evidently the finite size effect of the surface excess energy density of the unmixed state is dominant, since the boundary shifts into the unmixed state with increasing temperature (and f = 0). For a lattice with 32 unit cells on an edge, Monte Carlo results gave $\nu_c = -0.6632 \pm 0.0002$. This loss of surface excess energy when the alloy transforms from the unmixed state to the B32 state is qualitatively consistent with the large change in internal energy seen in Fig. 4.10b at f = 0.0003. Finally, the B32/B2 phase boundary is not subject to any ambiguities from an internal interface. Monte Carlo simulations gave a B32/B2 phase boundary at $\nu_c = 0.6728 \pm 0.0008$. This shift from the thermodynamic ground state value of 2/3 was due solely to the temperature effect, since in steady state both phases were single domains without antiphase domain boundaries. Equations 4.5 and 4.6 provided the right sign for this shift, but the magnitude was low.

4.4 Phase Boundaries with Ballistic Jumps

Figure 4.14 shows how ballistic jumps cause shifts of phase boundaries and the formation of two phase regions between the B2, B32, and unmixed states. The results of Fig. 4.14 were obtained from the data of Figs. 4.8 and 4.11, and analogous results for the B2/umx boundary. The dashed lines in Fig. 4.14 are ν_c versus f. The values of ν_c, where the LRO parameters have equal values, were obtained by interpolation and are believed to be fairly accurate. The pairs of solid curves in Figs. 4.14a and 4.14c are approximate boundaries of the two phase regions, defined as the values of ν for which the order parameters were about 1/2 (see Figs. 4.8 and 4.11). Although these boundaries of the two-phase regions are semi-quantitative, they do show the right trend.

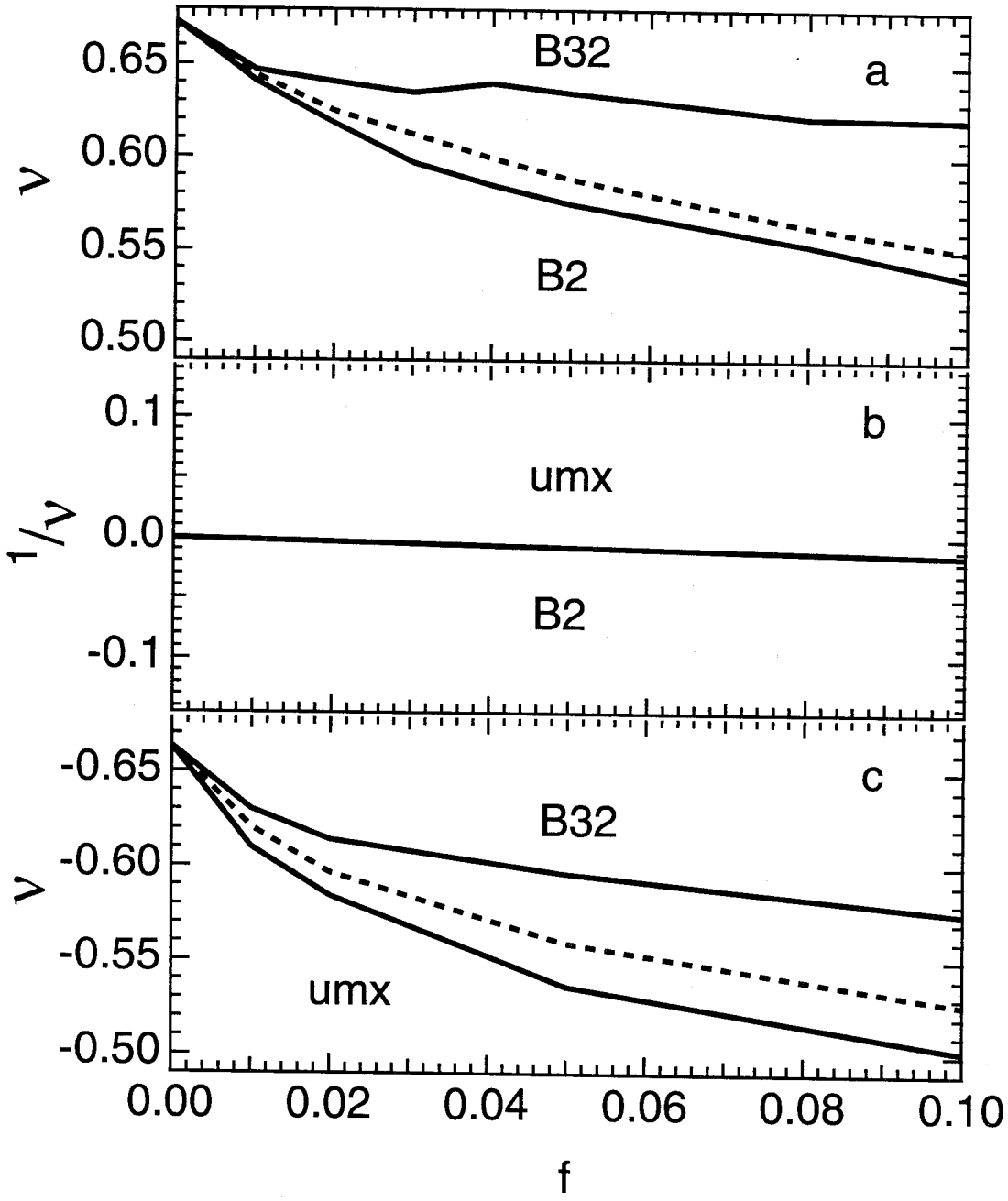

FIG. 4.14. The values of ν_c (dashed curve) and two-phase boundaries (solid curves) versus f for the pairs of phases: (a) B32/B2; (b) B2/umx; (c) B32/umx. The B2/umx boundary was shifted downwards by the amount $1/\nu = 0.03$ to account for the finite size effect in the Monte Carlo simulation.

The shifts of the phase boundaries with the fraction of ballistic jumps (Fig. 4.14) are much larger than the shifts with temperature, T. The effects of temperature are almost negligible on the scale of Fig. 4.14, as can be seen by comparing the data points at f = 0 to the ground state values of ν_c (which were +2/3, –2/3, ∞). This smaller effect of temperature is still found when the shifts of the phase boundaries are normalized by the average defect density in one of the phases, for example the B32 phase. We can monitor semiquantitatively the average defect density in the B32 phase in terms of 1 – L (see [22]). From Fig. 4.11 we see that for the thermodynamic case (f = 0) around $\nu = 0.7$, the value of 1 – L for the B32 phase changes from 0 at T = 0 to 1 – L ≈ 0.1 at the nominal T = 1 of the present simulations. From Fig. 4.11 we see that for a fraction of ballistic jumps of f = 0.05, around $\nu = 0.7$ there is a further change in 1 – L from about 0.1 to about 0.2. Approximately, then, the fraction of ballistic jumps of 0.05 serves to create about as much disorder as does temperature itself. With temperature, the B32/umx phase boundary changes from $\nu = -2/3$ to $\nu = -0.663$, a change of ν_c of only 0.003. On the other hand, with a fraction of ballistic jumps of f = 0.05, the change of ν_c is from –2/3 to –0.56, a much larger change of ν_c of 0.11. Although these numbers are imprecise, the shift of the phase boundary with ballistic jumps is much larger than expected if the change of ν_c were to scale with the defect concentration in the B32 phase in the same way as with temperature.

Since the energy cost of an isolated antisite defect is about the same in both the B32 and unmixed alloys, we must understand the shift in phase boundary with f as originating with a type of high-energy defect structure in the unmixed alloy, or a larger number of defects in the unmixed alloy. Observation of selected planes of the two phases showed that in steady state the predominant defect was the antisite defect, and there tended to be more of them in the unmixed alloy than in the B32 alloys. The presence of the same fraction of ballistic jumps sustains a greater number of antisite defects in the unmixed alloy than in an

alloy with B32 order. A greater number of antisite defects is also sustained in the B2 phase than in the B32 phase. The internal energies shown in Figs. 4.6 and 4.10 undergo a sharp change at the transition points. After accounting for finite-size effects of the Monte Carlo simulations, it is found that the changes in internal energy at both transitions, B2 –> B32 and umx –> B32, were approximately the same.

The detailed mechanism responsible for these different effects of ballistic jumps on antisite defect populations remains unclear, but it must depend on the detailed kinetics of atom movements. Here we propose [12,14] that differences in the diffusional correlation factors for vacancy diffusion in B32 phase and the unmixed state or B2 phase could be responsible for thermal jumps that are more effective in eliminating the defects created by the ballistic jumps in B32 phase than in the unmixed state or B2 phase. In the unmixed state with $V_{BB2} = 0$, the vacancy would tend to avoid some clustered domains [23]. Similarly in B2 (or checkerboard) ordered alloys at low temperatures, the vacancy will move most freely along antiphase domain boundaries (APDB's) or other regions of imperfect order in the alloy due to the strong diffusional correlation effects [24,25]. Therefore in both the unmixed state and the B2 phase, the vacancy was unable to spend sufficient time within some ordered or clustered domains to eliminate the antisite defects. On the other hand, the B32 phase allows the vacancy to move more freely through all the B32 domains by traveling along long channels of 1nn atoms of the like type. As a result of the larger diffusional correlation factors (promoting atomic diffusion) in the B32 phase than in the unmixed state or B2 phase, the thermal jumps can be more effective in eliminating the antisite and other defects induced by ballistic jumps in the B32 phase. Consistent with this explanation, we found that [12] near the B32/B2 phase boundary, there is a much smaller two-phase region, and a much smaller shift of the crossover, ν_c, with ballistic jumps in the chemically symmetric case than in the chemically asymmetric case ($V_{BB2} = 0$). This strong sensitivity of the phase boundaries to the chemical symmetry of the A-atom and B-atom

pair potentials is unlike that of any thermodynamic phase boundary, and is consistent with our kinetic explanation.

It is tempting to compare the effects of ballistic atom movements to the effects of temperature, and assign an elevated effective temperature to an alloy in the presence of ballistic atom movements. This elevated effective temperature would be the temperature at which a similar alloy without ballistic atom movements would have the same equilibrium density of antisite (or other) defects. Unfortunately, the B32 –> B2 transition that occurs with increased temperature does not occur with an increasing fraction of ballistic jumps; the opposite B2 –> B32 transition occurs instead. While this could possibly be explained by ballistic jumps causing a larger increase in effective temperature for the B2 than the B32 phase, we believe that using a different effective temperature for each phase causes the concept of effective temperature to lose some of its appeal. Another important limitation of the concept of an effective temperature arises because the relative populations of the different types of defects are generally expected to change with the fraction of ballistic jumps and with the particular phase. A single parameter of effective temperature is generally inadequate to account for the populations of all the different defect structures.

4.5 Two-phase Coexistence with Ballistic Jumps and Implications for Ball Milling of Nanocrystalline Alloys

The two-phase coexistence of both B32 order and B2 order (or unmixed state) in steady state near their crossover, ν_c , is an interesting and important feature of driven alloys. The two-phase regions grow with the fraction of ballistic jumps, f, and are shown as regions between the pairs of solid curves in Fig. 4.14a and Fig. 4.14c. While reminiscent of a two-phase region on a temperature-composition phase diagram, the origin

of this two-phase region must be quite different since there is no good parallel between the fraction of ballistic jumps and the composition.

We attribute the region of two-phase coexistence to local fluctuations in the fractions of ballistic jumps. If the ballistic jumps create locally some excess internal energy, statistical variations in the fraction of ballistic jumps will cause local variations in the internal energy. In the case of chemically asymmetric pair potentials, we expect those regions where the largest numbers of ballistic jumps have occurred will tend to be regions of B32 order. Since the ballistic jumps favor B32 order in the asymmetric case, we would not expect the two-phase region to encroach on the region of B32 stability above $\nu \approx 2/3$, but for $f > 0$ we would instead expect the two-phase region to grow into the B2 or unmixed region. This is seen in Figs. 4.8, 4.11, and 4.14. Since the ballistic jumps occur at random in a local region, the fluctuations in their numbers will be approximately the square root of their number in the regions, being proportionally smaller for more ballistic jumps. The fluctuations will occur over a smaller spatial scale when the fraction of ballistic jumps is larger. This is consistent with our observation that the sizes of the ordered domains in alloys of two-phase coexistence decreased with f, being only several lattice constants when f was about 0.1. We do not have sufficient data to quantify this effect, however.

It is also noteworthy that the case of chemically symmetric pair potentials with $V_{AA2} = V_{BB2}$ showed a much smaller B32/B2 two phase region. In the chemically symmetric case, the ballistic jumps contribute almost equally to the internal energies of the B2 and B32 structures, so fluctuations in the density of ballistic jumps are less likely to cause the B32 structure to be favored. We expect that there are, however, local structural differences induced by the ballistic jumps that tend to favor one structure over the other, but this smaller effect was not investigated in detail.

On the other hand, the phase boundary in Fig. 4.14b between B2/umx is very sharp. No two-phase microstructures of B2 phase plus unmixed state were observed in Monte Carlo simulations. This is as expected. Because both phases have similar stability with temperature and with f, local inhomogeneity in the internal energy density will not favor either the B2 phase or unmixed state.

The development of two-phase steady-states in driven systems has been noted previously, and interpreted with features of a stochastic potential [5,8]. The argument in the present paper, based on spatial variations in the internal energy density, is somewhat different. Analysis of such spatial variations requires a description of microstructure beyond the capability of practical analytical cluster approximations. In the present study, the A2, B2, B32, and unmixed structures were useful for providing a concrete example. The concept of spatial variations in the internal energy of a driven alloy is much broader than these particular B32/B2 and B32/umx examples, however, and may provide guidance in understanding how inhomogeneous defect densities may lead to two-phase steady-states. For example, mechanical alloying of Fe-Cu and Fe-Ni nanocrystalline alloys resulted in broad bcc/fcc two-phase regions, where bcc phases retained larger strain energy from ball milling than fcc phases. The spatial inhomogeneity of strain energy is also expected to be larger in bcc phases than in fcc phases, though no such measurement has been made. With analogy to B2/B32 two-phase, we would expect the bcc/fcc two-phase region to grow mainly into the bcc phase region with increasing ball milling intensity for reasons similar to those given here. This has actually been observed in experiments and will be presented in the next chapter.

4.6 Phase Diagrams of Driven Alloys at Low Temperatures

Figure 4.2 presents a ground state phase diagram for bcc alloys with 1nn and 2nn interactions [1,2]. Figures 4.15a and 4.15b are schematic phase diagrams that include the presence of a finite temperature (4.15a), and temperature plus ballistic jumps (4.15b). The effects of temperature on the boundaries between the B2, B32, and unmixed states are almost negligible on the scale of Fig. 4.15. A previous thermodynamic study of the B32/B2 phase boundary [21] seems consistent with our results.

The phase diagrams in Fig. 4.15a and 4.15b are our best efforts. Some of their features are more reliable than others. The A2 phase boundaries in Fig. 4.15a were obtained with only one point having mixed V_1 and V_2, but the straight lines between the axis intercepts are expected from mean field calculations. The size and detailed shape of the A2 region in Fig. 4.15b are semi-quantitative. Ballistic jumps cause an enlargement of the A2 region, drawn in Fig. 4.15b with estimates based on results from the two-dimensional square lattice [Chapter 3, 13]. A two-phase region might exist around the A2 phase, although it has not been reported for equiatomic alloys [7-9]. We performed a number of studies of alloys along the B2/B32 phase boundary at various values of V_1 from +2 to +8. These plots were similar to those of Fig. 4.8, and provided the values of ν_c and the B2 plus B32 two-phase boundaries in Fig. 4.15b. The B32 phase plus unmixed state two-phase region in Fig. 4.15b is drawn in analogy to the B32 plus B2 two-phase region. For the two-phase region of the B32 phase plus unmixed state, we have data only for one magnitude of V_1 (the data of Fig. 4.11), but these data are similar to those for the B32/B2 two-phase region. Although we examined many alloys along the B2/umx boundary, we did not find any two-phase region of the B2 phase plus unmixed state. We therefore did not include a B2 phase plus unmixed state two-phase region in Fig. 4.15b, although it might exist as a very narrow region.

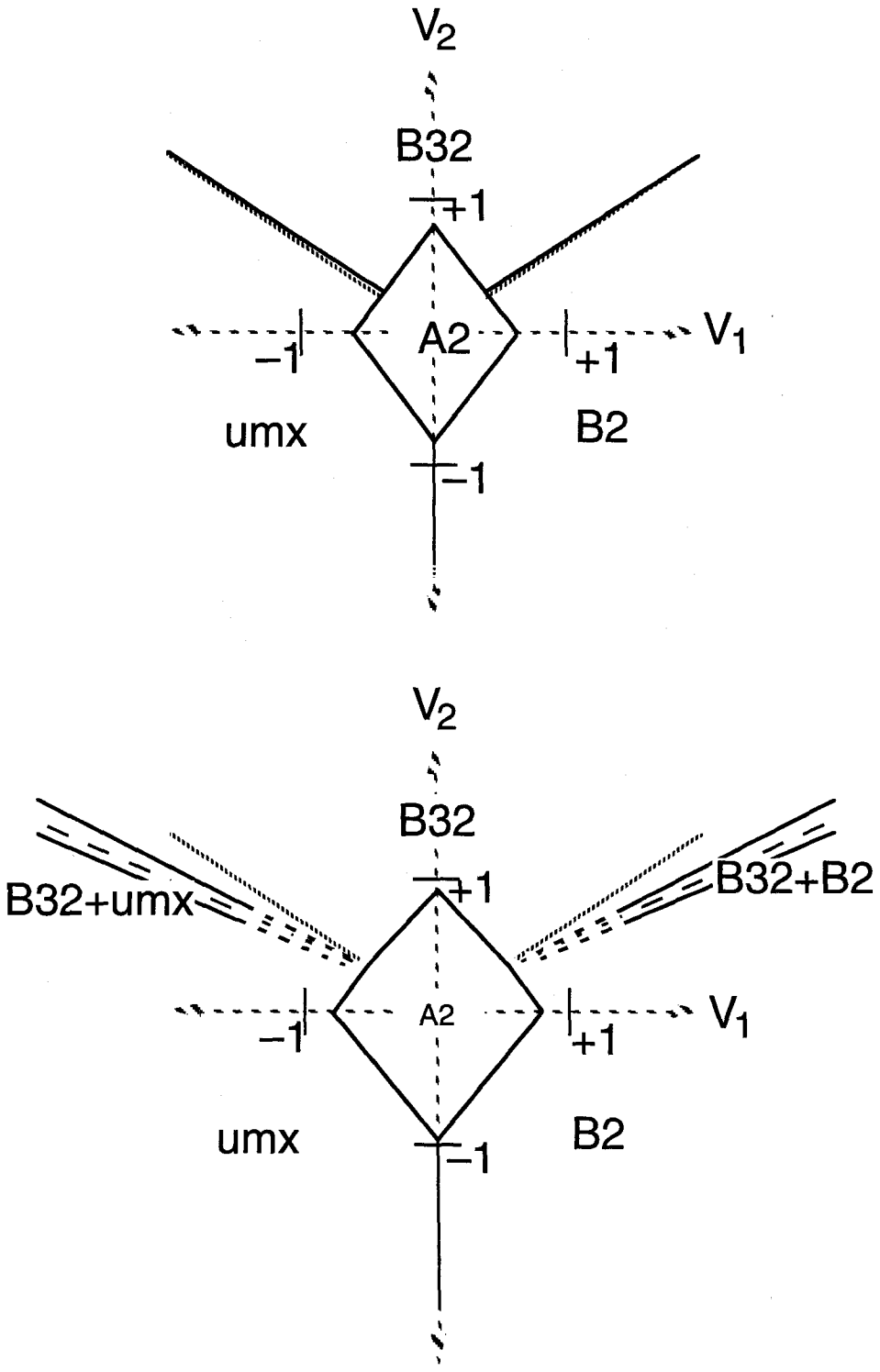

FIG. 4.15. Low temperature ($T \approx 1$) phase diagrams for the equiatomic bcc alloys: (a) without ballistic jumps ($f = 0$), (b) with ballistic jumps ($f \approx 0.1$). Dotted lines have slopes +2/3 and –2/3. For comparison, the thermodynamic ground state phase diagram is shown in Fig. 4.2.

4.7 Summary

We used Monte Carlo simulations to determine phase diagrams of equiatomic binary bcc alloys. Both thermal and ballistic atom movements occurred by means of a vacancy mechanism. Four phases exist on a bcc lattice with 1nn and 2nn interatomic potentials: B32 order, B2 order, an unmixed state of A- and B-rich regions, and a disordered A2 phase. The goal of our work was to measure and understand the shifts in the boundaries between the first three of these phases as a function of temperature and fraction of ballistic atom movements.

We found that near the phase boundaries of all three pairs of low temperature phases, B32/B2, B32/umx, and B2/umx, the phase out of the pair that is not the thermodynamic equilibrium state appeared transiently and vanished at the final steady states during A2 –> order or A2 –> decomposition transformations in the thermodynamic case. The transient phase formation was stronger for alloys closer to the phase boundary due to the weaker preference of one phase over the other. With just a very small fraction of ballistic jumps, this kinetic behavior was altered strongly. The transient state of order in the thermodynamic case either switched with the original steady state of order, or became a stable phase coexisting with the other phase. These changes of behavior were strongly related to the shifts of phase boundaries with ballistic jumps.

In thermodynamic alloys, with increasing temperature the phase boundaries involving the B32 phase receded under the growth of the regions of the B2 phase and the unmixed state. A low temperature expansion of the partition function showed that the higher energy for defect clusters in the B32 phase explained approximately the weak recession with temperature of the B32 phase boundaries. The opposite behavior was found in the presence of ballistic atom movements: there was a strong encroachment of the region of B32 phase into the regions of B2 phase and the unmixed state. The presence of ballistic

atom movements therefore cannot be considered as a simple increase of temperature. In the presence of ballistic atom movements there are evidently fewer defects in the B32 phase (which then has a lower internal energy) than in the B2 phase or the unmixed state. While the detailed reason for this difference remains unclear, it is expected to depend on the kinetic mechanism. We propose that it might be the differences in the diffusional correlation factors for vacancy diffusion. The phase boundary between the B2 order and the unmixed state shifted much less with temperature than did the boundaries involving the B32 phase.

Another important feature of the phase diagram in the presence of ballistic atom movements was the formation of two-phase regions between the B32 phase and the B2 phase, and between the B32 phase and the unmixed state. The width of these two-phase regions increased asymmetrically (mostly in the B2 or umx phase region) with increasing fraction of ballistic atom movements, and with decreasing temperature. This simulation result may provide useful theoretical guidance for mechanical alloying of nanocrystalline materials. We suggest that when the external driving causes heterogeneities in the enthalpy, the material may develop two-phase coexistence when the chemical free energies of the two phases are similar.

References

1. M. J. Richards and J. W. Cahn, Acta Metall. **19**, 1263 (1971).
2. S. M. Allen and J. W. Cahn, Acta Metall. **20**, 423 (1972).
3. G. Martin, Phys. Rev. B **30**, 1424 (1984).
4. P. Bellon and G. Martin, Phys. Rev. B **39**, 2403 (1989).
5. E. Salomons, P. Bellon, F. Soisson, and G. Martin, Phys. Rev. B **45**, 4582 (1992).
6. P. Bellon, Phys. Rev. B **45**, 7517 (1992).
7. F. Soisson, P. Bellon, and G. Martin, Phys. Rev. B **46**, 11332 (1992).
8. P. Bellon, F. Soisson, and G. Martin, in Diffusion in Ordered Alloys, B. Fultz, R. W. Cahn, and D. Gupta, eds. (TMS, Chicago, 1992).
9. P. Bellon and G. Martin, Phys. Rev. B **38**, 2570 (1988).
10. F. Haider, P. Bellon, and G. Martin, Phys. Rev. B **42**, 8274 (1990).
11. W. Feller, An Introduction to Probability Theory and Its Applications, Vol 1 (John Wiley, New York, 1957) Chapter 15.
12. L. B. Hong, L. Anthony, and B. Fultz, J. Mater. Res. **10**, 126 (1995).
13. L. B. Hong and B. Fultz, Phys. Rev. B **51**, 2687 (1995).
14. L. B. Hong and B. Fultz, Phys. Rev. B **52**, (1995).
15. G. Martin and P. Bellon in Statics and Dynamics of Alloy Phase Transformations, P. E. A. Turchi and A. Gonis, eds., (Plenum, New York, 1994).
16. G. Nicolis and I. Prigogine, Self-Organization in Nonequilibrium Systems (Wiley, New York, 1977).
17. L. Reinhard and P. E. A. Turchi, Phys. Rev. Lett. **72**, 120 (1994).
18. L. Anthony and B. Fultz, J. Mater. Res. **9**, 348 (1994).
19. L.-Q. Chen and A. G. Khachaturyan, Phys. Rev. B **44**, 4681 (1991), Scripta Metall. Mater. **25**, 61 (1991).

20. F. Ducastelle, Order and Phase Stability in Alloys, (North Holland, Amsterdam, 1991) Section 5.1.2.

21. M. Sluiter, P. Turchi, Z. Fu, and D. de Fontaine, Physica **148A**, 61 (1988).

22. In the Bragg-Williams analysis, recall that $L \equiv (R-W)2/N$, where R is the number of correctly-placed atoms on the sublattice of N/2 sites, and W is the number of wrongly-placed ones. Therefore: $1 - L = (R+W)2/N - (R-W)2/N = 4W/N$. The concentration of antisite defects, $c = (1 - L)/2$.

23. L. B. Hong and B. Fultz, unpublished results.

24. T. F. Lindsey and B. Fultz, J. Appl. Phys. **75**, 1467 (1994).

25. B. Fultz, J. Chem. Phys. **88**, 3227 (1988).

Chapter 5. Two-Phase Coexistence in Fe-Ni Nanocrystalline Alloys Prepared by Ball Milling at Two Intensities

5.1 Introduction

Ball milling is a common technique to synthesize materials far from thermodynamic equilibrium, such as nanocrystalline materials and amorphous materials (Section 1.2.2). The applicability of thermodynamics to materials synthesis by ball-milling is a subject of ongoing investigation. It is generally expected that the synthesis of new materials by ball milling depends on the thermochemistry of the alloy, and on the microstructural defects generated during ball milling. Some interpretations of the steady-state phases formed during milling have used model free energy calculations (of the "CALPHAD" style) with polymorphous constraints to restrict processes of chemical segregation [1,3-9]. The general preferences of Fe-Cu alloys for the bcc or fcc structure can be understood in this way [5-9]. For compositions from 20-40 % Cu, however, as-milled Fe-Cu alloys have a two-phase microstructure comprising bcc and fcc phases [5-13]. Such a two-phase coexistence cannot be predicted by a conventional free energy argument with a polymorphous constraint. For a specific composition and temperature, only one phase can have the lowest free energy. Furthermore, there is evidence from x-ray lattice parameter measurements that the atomic level mixing induced by ball milling also serves to homogenize the alloy chemistry, so the bcc and fcc phases may have similar chemical compositions [11,12].

For testing the validity of thermodynamic arguments it is useful to vary the chemical composition of the alloy, but control over the temperature [14-17] and milling intensity [18-22] may also be useful. In this chapter, we report our study on $Fe_{100-x}Ni_x$ alloys (x is the atomic percentage of Ni and varies from 0 to 50) ball milled at two different intensities.

Our interest was in understanding how milling intensity affected the region of two-phase (bcc plus fcc) coexistence that we found from about 13 to 30 at.% Ni. Model free energy calculations (with Thermo-Calc software) were performed for Fe-Ni alloys, and the general preference of the alloys for fcc or bcc structures was predicted from the calculated polymorphic transformation composition (the composition of the intersection of the bcc and fcc free energy curves, which was 28% at low temperature). With increased milling intensity, the region of two phase coexistence was found to expand asymmetrically into the bcc single phase region.

We propose a new explanation of this state of two-phase equilibrium by extending the polymorphic transformation concept to include defects in the alloy. It is not surprising that a higher average defect concentration can explain the loss of stability of the bcc phase with milling intensity. To explain two-phase coexistence, however, we consider heterogeneities in the defect concentration in the alloy. We propose that near the polymorphic transformation composition, the most defective bcc crystallites will transform into fcc crystallites, even if the chemical contribution to the free energy for the bcc phase is favorable. Owing to heterogeneities in the defect density in ball milled material, the free energy versus composition curves for both the fcc and bcc phases are no longer sharp lines, but are effectively smeared upwards in free energy. Using model free energy calculations, we show that the region of two-phase coexistence can be predicted if ball milling creates heterogeneities of 2 - 3 kJ/mole in the free energy of the bcc phase. We find that this defect enthalpy is consistent with the average heat release measured by differential scanning calorimetry. Our interpretation of the region of two-phase coexistence in ball-milled materials is essentially the same as that used for understanding Monte Carlo simulations of bcc alloys with thermal and ballistic atom movements [Chapter 4,23,24].

5.2 Experimental

Ball milling of $Fe_{100-x}Ni_x$ was performed with a Spex 8000 mixer / mill, for which some general information was provided in Section 1.2.2. Using four steel balls (two 10 mm, two 3 mm), the standard Spex 8000 mill provides a milling intensity that we denote as I_1. With I_1 the ball velocity has been reported to be about 3 m/s [25]. In a series of preliminary tests, we found that milling for 24 h at the I_1 intensity was more than sufficient time to reach a steady-state microstructure. For example, Fig. 5.1 presents the average grain sizes of both bcc and fcc phases of $Fe_{75}Ni_{25}$ alloy as functions of milling time at intensity I_1. No difference in grain size of either bcc phase or fcc phase was detected when the powders were ball milled for more than 18 hours (data for 48 hour milling are not shown in Fig. 5.1). This was also true for the phase fractions. To test further the effect of milling intensity on the steady-state microstructures of the powders, we modified the Spex mill to operate at a second milling intensity, lower than the standard one. We replaced the belt drive pulley on the shaker with a new one having an effective diameter $\sqrt{3}$ as large as the commercial pulley. This modification should reduce the kinetic energy of the balls to approximately one-third of the kinetic energy for intensity I_1. We denote this lower ball milling intensity as $I_{0.3}$. We found that 48 hours of continuous milling was sufficient for the powders to reach steady states with this lower intensity $I_{0.3}$; no differences in grain sizes or phase fractions were detected when the powders were milled for more than about 36 hours. Our interest in the present experiments was to study the steady-state microstructures produced by ball milling, not the kinetics of achieving them. All milling with intensity I_1 was performed for 24 h, and all milling with intensity $I_{0.3}$ was performed for 48 h.

During milling there was some tendency for the powders to become enriched with Fe from the vials and balls. Chemical analyses of several of the as-milled powders were performed by atomic emission spectrometry, where the powder was dissolved in acid

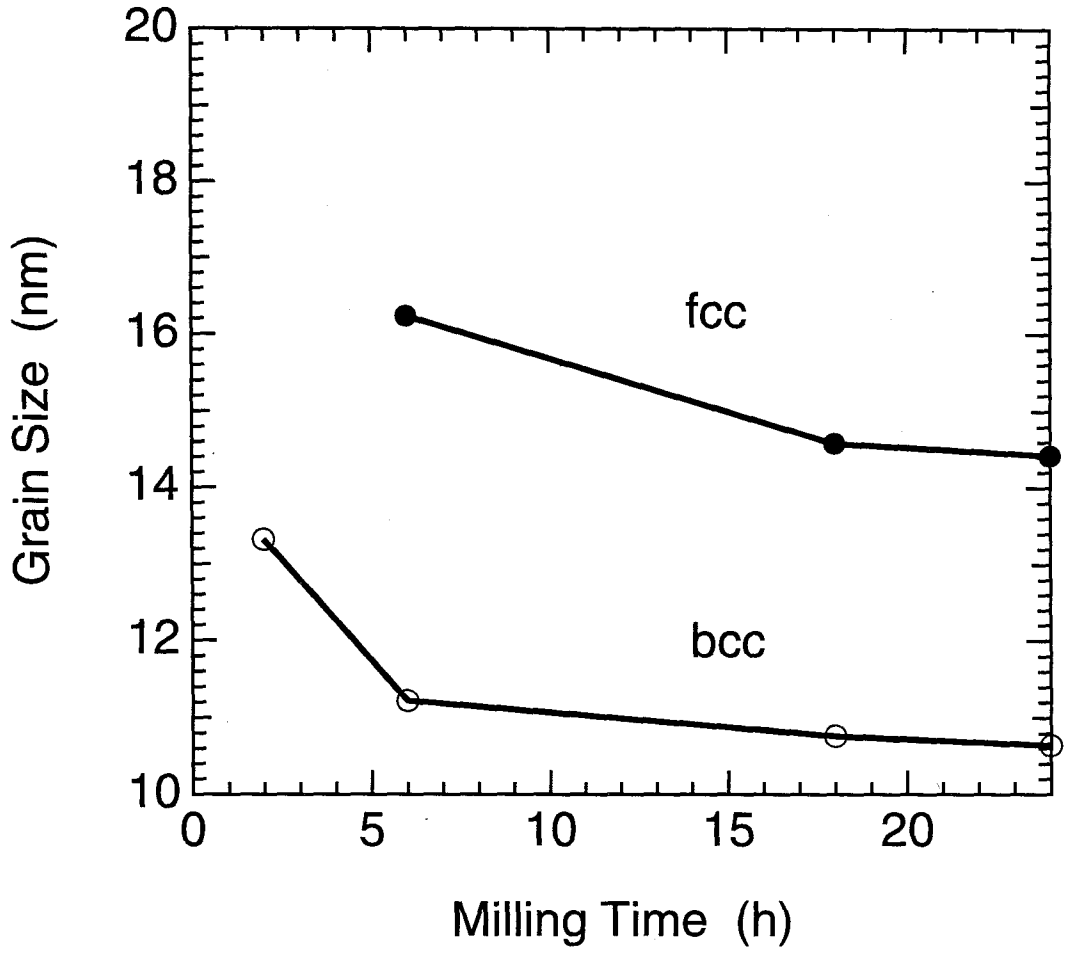

FIG. 5.1. Average grain sizes of the bcc and fcc phases of as-milled $Fe_{75}Ni_{25}$ alloys as functions of milling time at intensity I_1.

solution, introduced as an aerosol in an inductively-coupled plasma discharge, and the light emission analyzed by an optical spectrometer. We found that the powders milled at the higher intensity I_1 increased their Fe concentration more than did the samples milled at the $I_{0.3}$ intensity; typical changes in concentration were 3 at.% for I_1 and 0.2 at.% for $I_{0.3}$. The chemical concentrations given below were corrected for this Fe contamination.

5.3 Experimental Results

5.3.1 Phase Formation and Phase Fractions

Figure 5.2 presents x-ray diffraction patterns from powders of $Fe_{91}Ni_9$, $Fe_{77}Ni_{23}$, and $Fe_{63}Ni_{37}$ ball milled at I_1 for 24 hours. While the diffraction pattern from $Fe_{77}Ni_{23}$ has both bcc and fcc peaks, the $Fe_{91}Ni_9$ pattern has only bcc peaks and the $Fe_{63}Ni_{37}$ pattern has only fcc peaks. The bcc and fcc phase fractions were calculated according to Eqs. 1.4, and are plotted against the alloy Ni concentration, x, in Fig. 5.3. Compared to the boundaries from the equilibrium phase diagram at low temperatures, the bcc and fcc single phase regions are extended considerably. For example, at 60 °C the equilibrium two-phase region extends approximately from 2 % Ni to 71 % Ni [29]. We determined the compositional width of the two-phase region in the as-milled materials by extrapolation of the data in Fig. 5.3 to zero concentration of the phases, and found the boundaries to be at x $\approx$ 12 and 30 for I_1 and x $\approx$ 18 and 34 for $I_{0.3}$, respectively. Alternatively, a criterion of defining the phase boundary as a composition where the phase fraction fell below 5% gave x $\approx$ 16.5 and 29.5 for I_1, and x $\approx$ 24 and 33.5 for $I_{0.3}$. (This alternative criterion seemed to be more robust on the bcc side.) Both methods for determining the phase boundary give the same qualitative picture. Higher milling intensity shifts the phase boundaries asymmetrically towards the bcc region, with the bcc phase boundary being shifted most

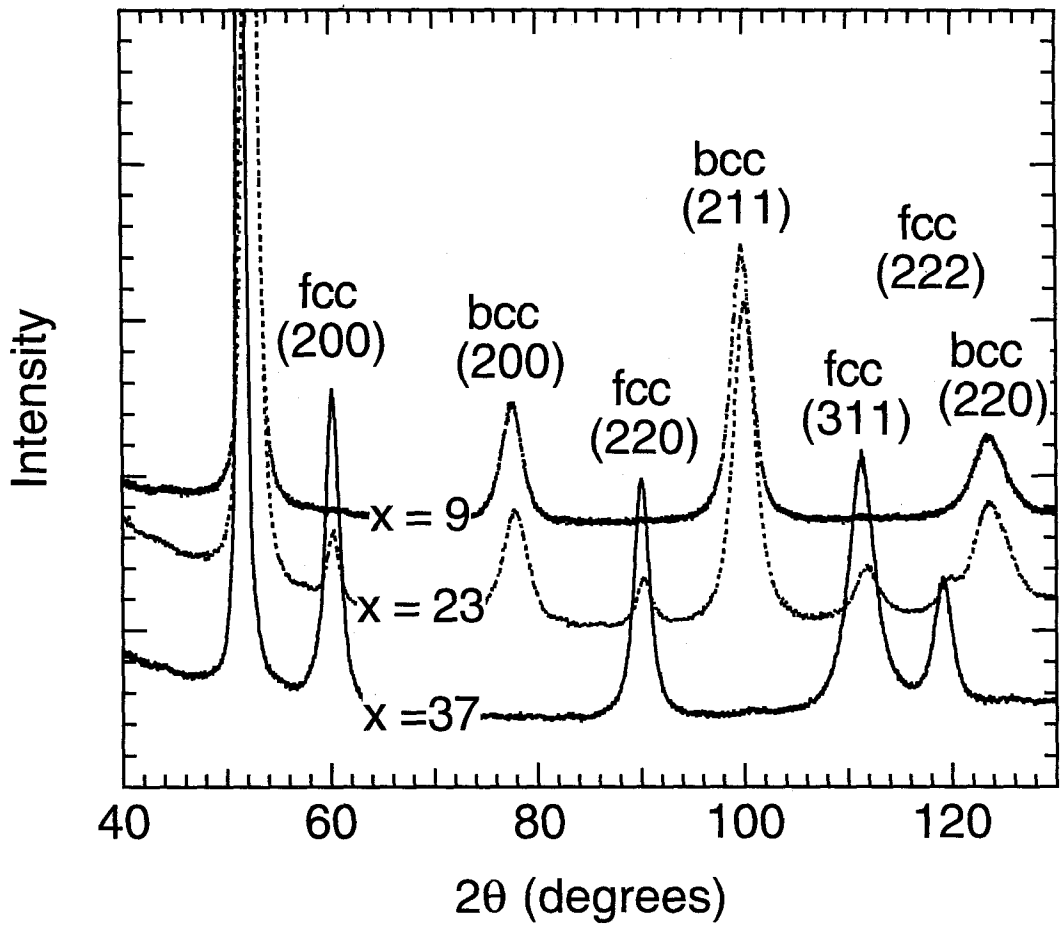

FIG. 5.2. X-ray diffraction patterns from as-milled $Fe_{100-x}Ni_x$ alloys with x = 9, 23, 37. Materials were milled for 24 h with intensity I_1, as described in text.

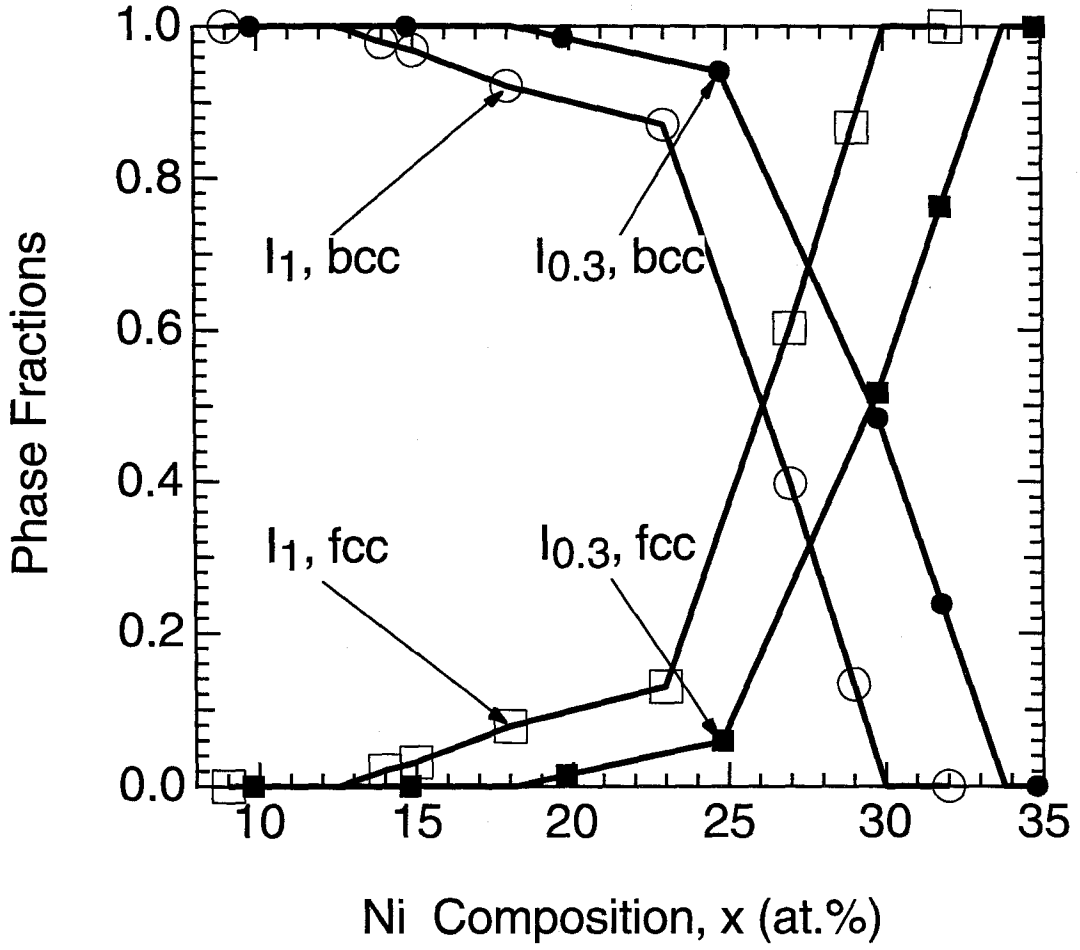

FIG. 5.3. Fractions of bcc and fcc phases in as-milled $Fe_{100-x}Ni_x$ alloys, determined by x-ray diffractometry. Alloys were milled for 24 h with intensity I_1, and for 48 h with intensity $I_{0.3}$.

strongly. Furthermore for any Ni concentration, the higher ball milling intensity, I_1, always results in less bcc phase than the lower milling intensity, $I_{0.3}$.

5.3.2 Chemical Analysis

For $Fe_{100-x}Ni_x$ alloys ball milled at I_1 for 24 hours, we observed pure (or predominantly pure) bcc phase for $x \leq 12$ and pure (or predominantly pure) fcc phase for $x \geq 30$. We therefore expect that ball milling extends the solubility of Ni in the bcc phase to at least 12 %, and the Fe solubility in the fcc phase is extended to at least 70 %. We have evidence, however, that in the two-phase region the chemical compositions of the individual bcc and fcc crystallites are extended even further. X-ray lattice parameter data are presented in Fig. 5.4. Figure 5.4 also includes results from the JCPDS index of bcc and fcc alloys, and other previously-reported data [30,31]. There is excellent agreement between the lattice parameter data from our bcc powders and from those reported previously, suggesting that the single-phase as-milled bcc powders do not have a significant mean strain. The data of Fig. 5.4 suggest a mean strain of about 0.1% for the Ni-rich single-phase fcc powders, however. In the two-phase region for Ni concentrations below 30 % Ni, the lattice parameters of the fcc phase decrease significantly below their values in single phase Fe-Ni. In the composition range of two-phase coexistence, the lattice parameters of as-milled Fe-Ni follow closely the lattice parameters of bulk Fe-Ni alloys of nearly the same chemical composition. The lattice parameters of the fcc phase in the two phase region are not characteristic of an alloy having a chemical composition of 30 % Ni, which marks the boundary of the fcc single phase region. Unfortunately, the lattice parameter of the bcc phase is rather insensitive to the chemical composition of the alloy, so the bcc lattice parameter data were not useful for checking the chemical composition of the bcc phase.

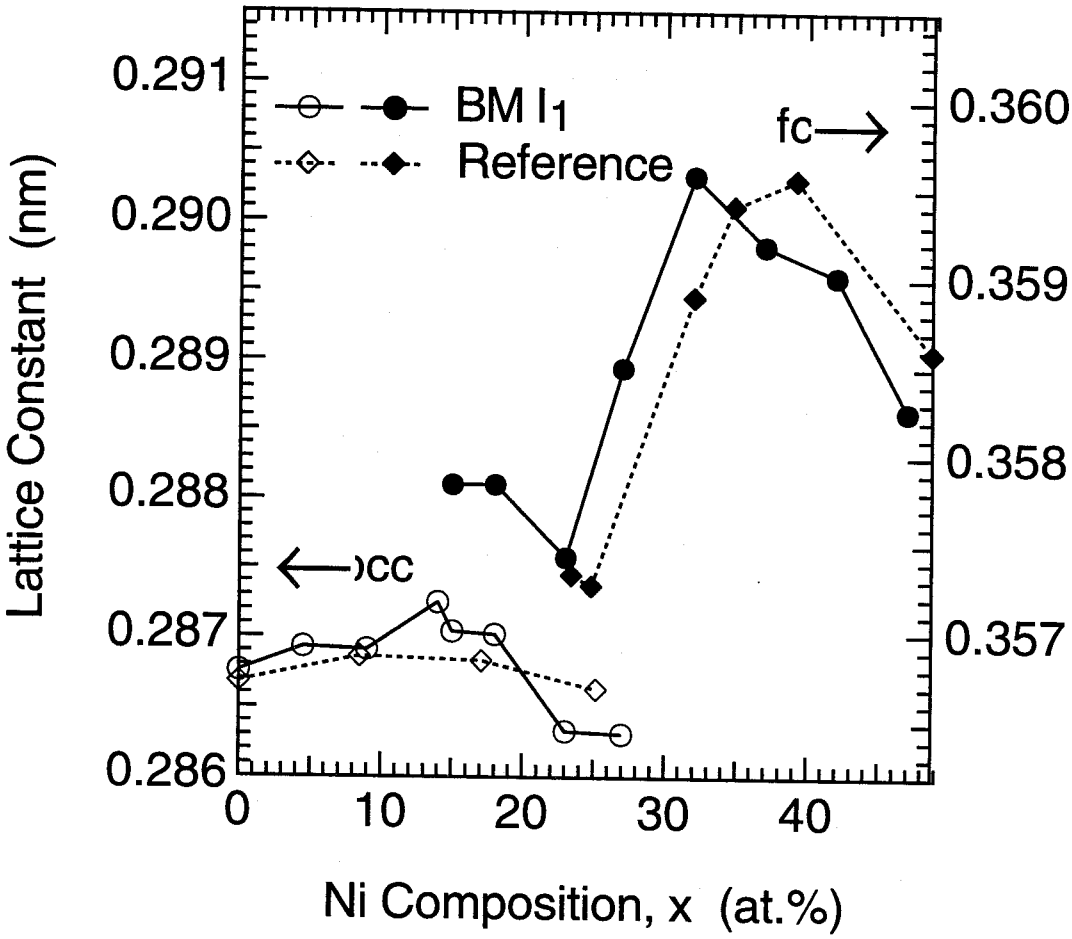

FIG. 5.4. Lattice parameters of bcc and fcc phases in as-milled $Fe_{100-x}Ni_x$ alloys. Data from Refs. [30,31] are also shown.

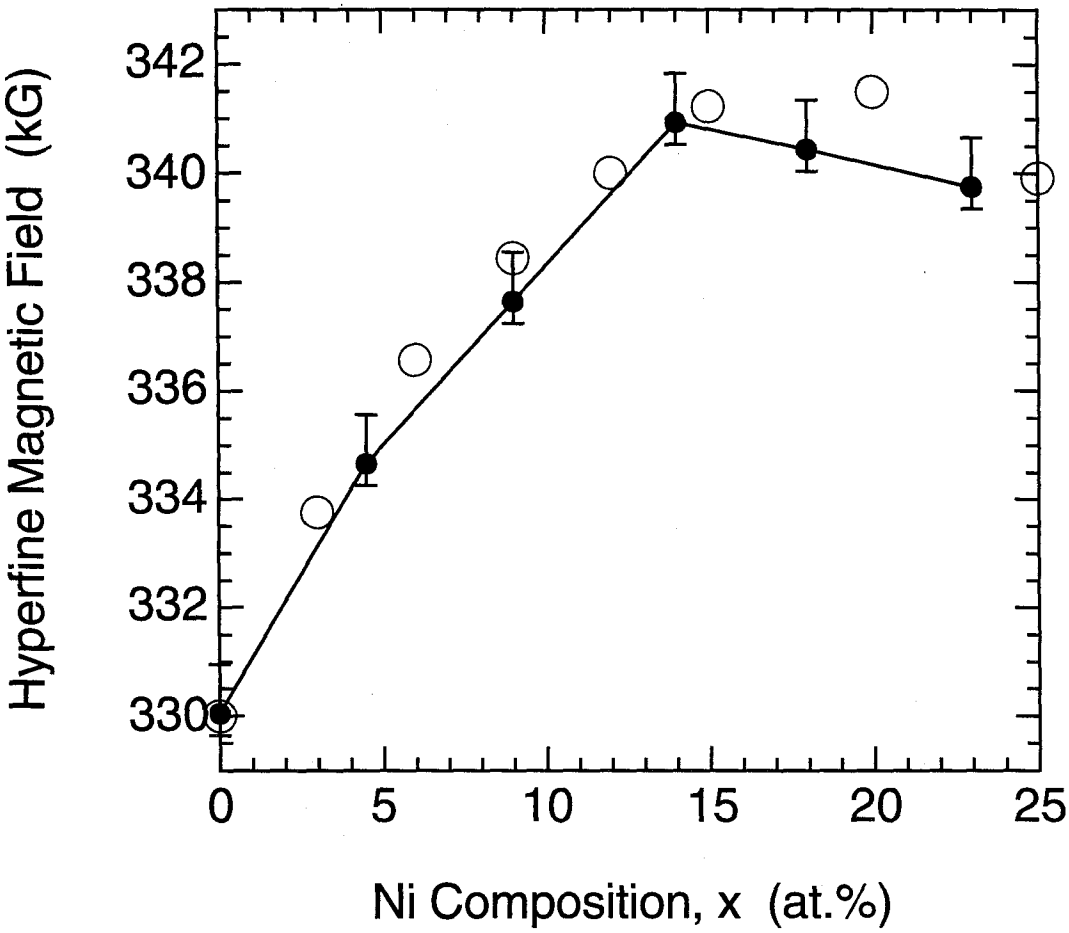

FIG. 5.5. ^{57}Fe hyperfine magnetic fields for the bcc phase of as-milled $Fe_{100-x}Ni_x$ alloys. Also shown are hyperfine magnetic fields from previous work [28], and data points from bulk bcc alloys obtained in the present study.

Average hyperfine magnetic fields obtained from Mössbauer spectrometry are presented in Fig. 5.5, together with some hyperfine magnetic fields reported previously for bcc Fe-Ni alloys [28], and data from our own bcc calibration samples. (These samples, with x = 15, 20, 25, were arc melted under an Ar atmosphere. The ingots were inverted and remelted four times, and filings taken from them were found to be pure bcc by x-ray diffraction.) At least to compositions of 12 % or so, these data show that the Ni concentration in the bcc phase of the as-milled powder is the same as the overall alloy composition. Unfortunately, for higher Ni concentrations the hyperfine magnetic field becomes insensitive to the Ni concentration in the bcc phase, and is not a useful measure of chemical composition. The measured hmf's are consistent with the x-ray result that the chemical composition the bcc phase is the same as the overall composition of the alloy.

5.3.3 Defect Enthalpy

The bcc (200) and fcc (220) peaks of x-ray diffraction are shown in Fig. 5.6 for the $Fe_{100-x}Ni_x$ powders ball milled with intensities I_1 and $I_{0.3}$. These peaks were normalized to give the same backgrounds and the same bcc (200) peak heights (Fig. 5.6a) or the same fcc (220) peak heights (Fig. 5.6b). Figures 5.6a and 5.6b show that the diffraction peak shapes for the bcc and fcc phases were little changed for the different compositions and milling conditions. These diffraction peaks have significant intensities in their tails, typical of a particle size distribution that includes some small crystallites. The average grain size and root-mean-squared strain are presented as functions of nickel composition in Figs. 5.7a and 5.7b, respectively. Within the capabilities of our peak analysis methods we do not find any differences in the grain size or RMS strain caused by milling intensity or by chemical composition differences. We do find, however, that the bcc phase has both smaller grains

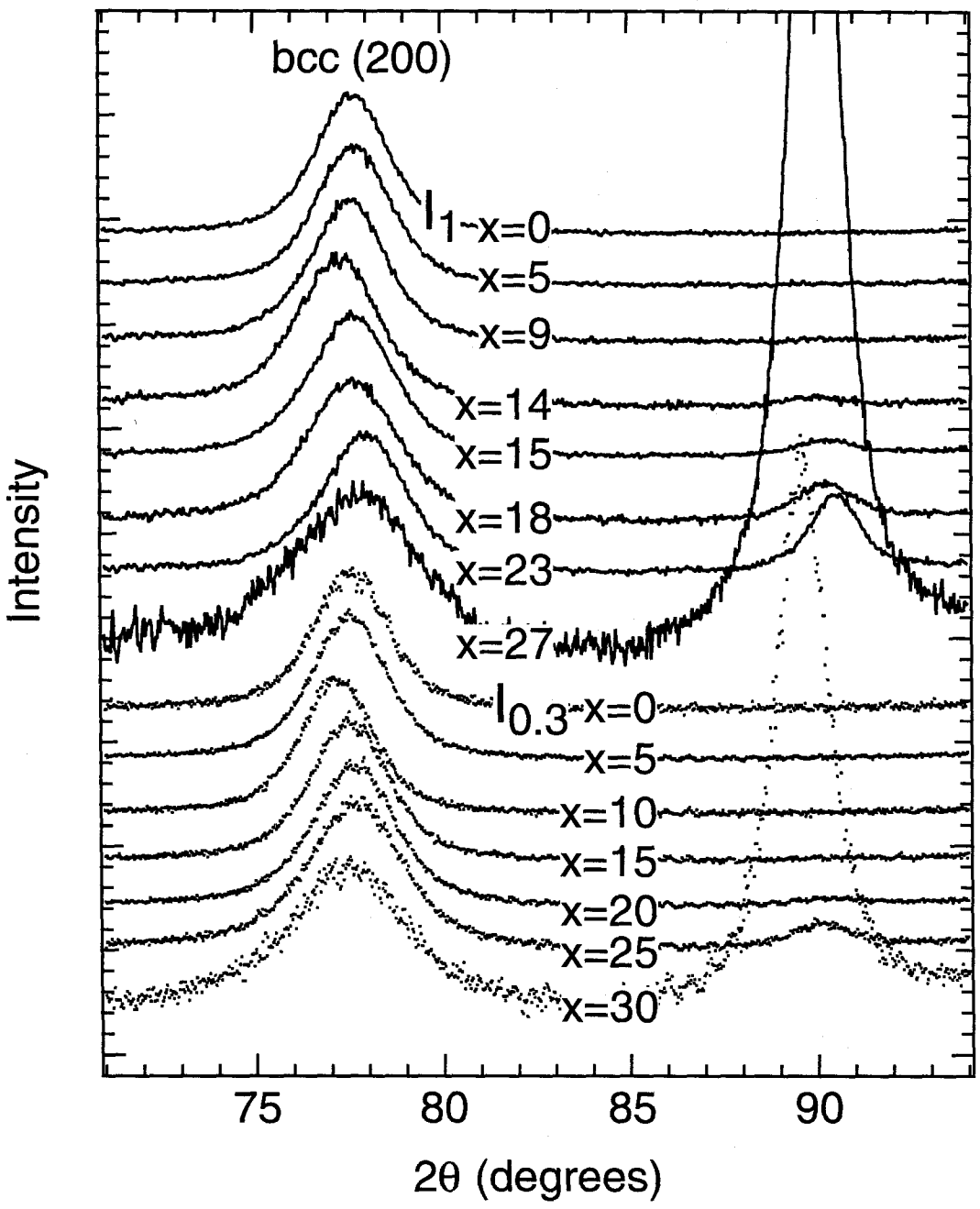

FIG. 5.6a. bcc (200) x-ray diffraction peaks. Peaks are presented with background corrections and normalized intensities.

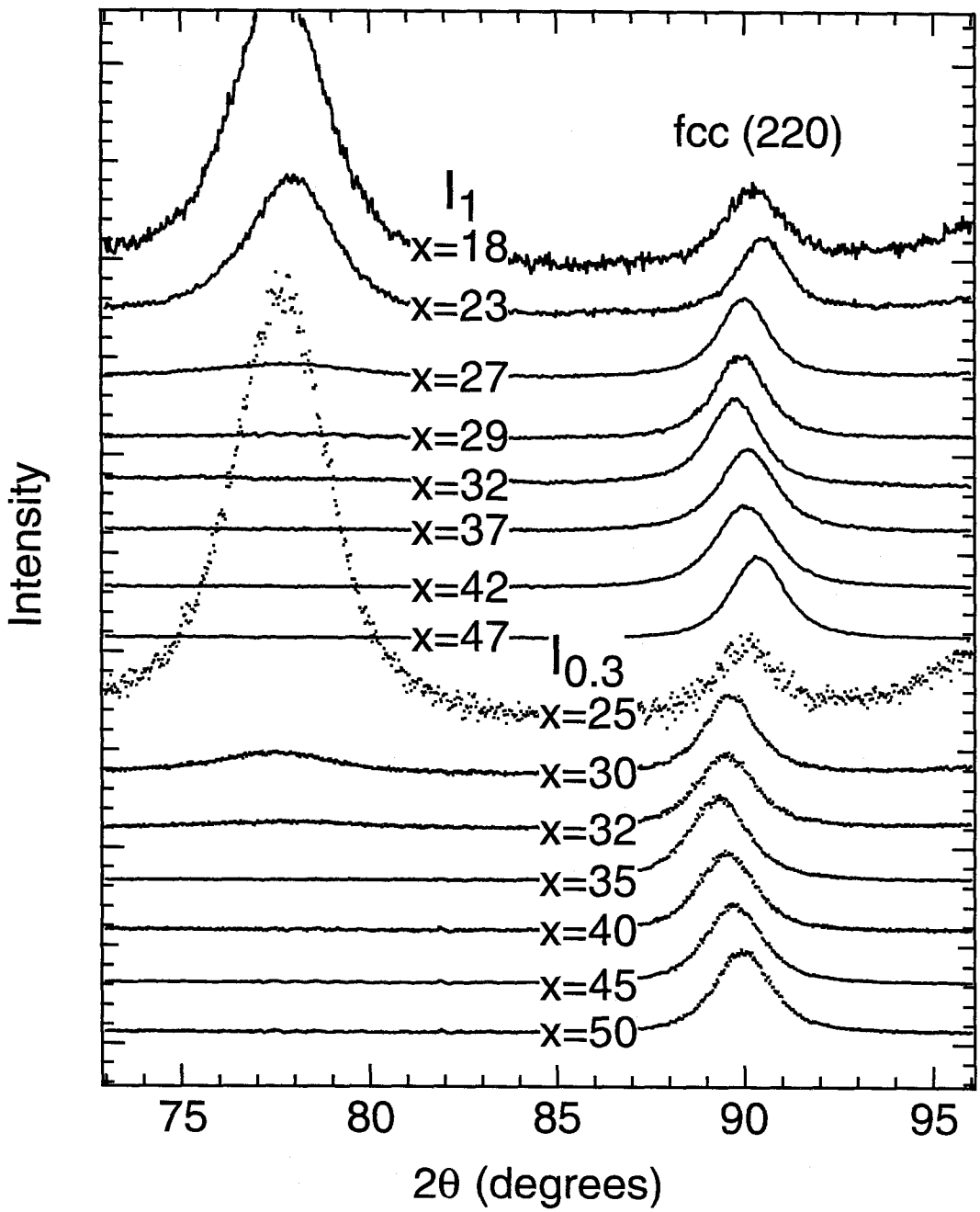

FIG. 5.6b. fcc (220) x-ray diffraction peaks. Peaks are presented with background corrections and normalized intensities.

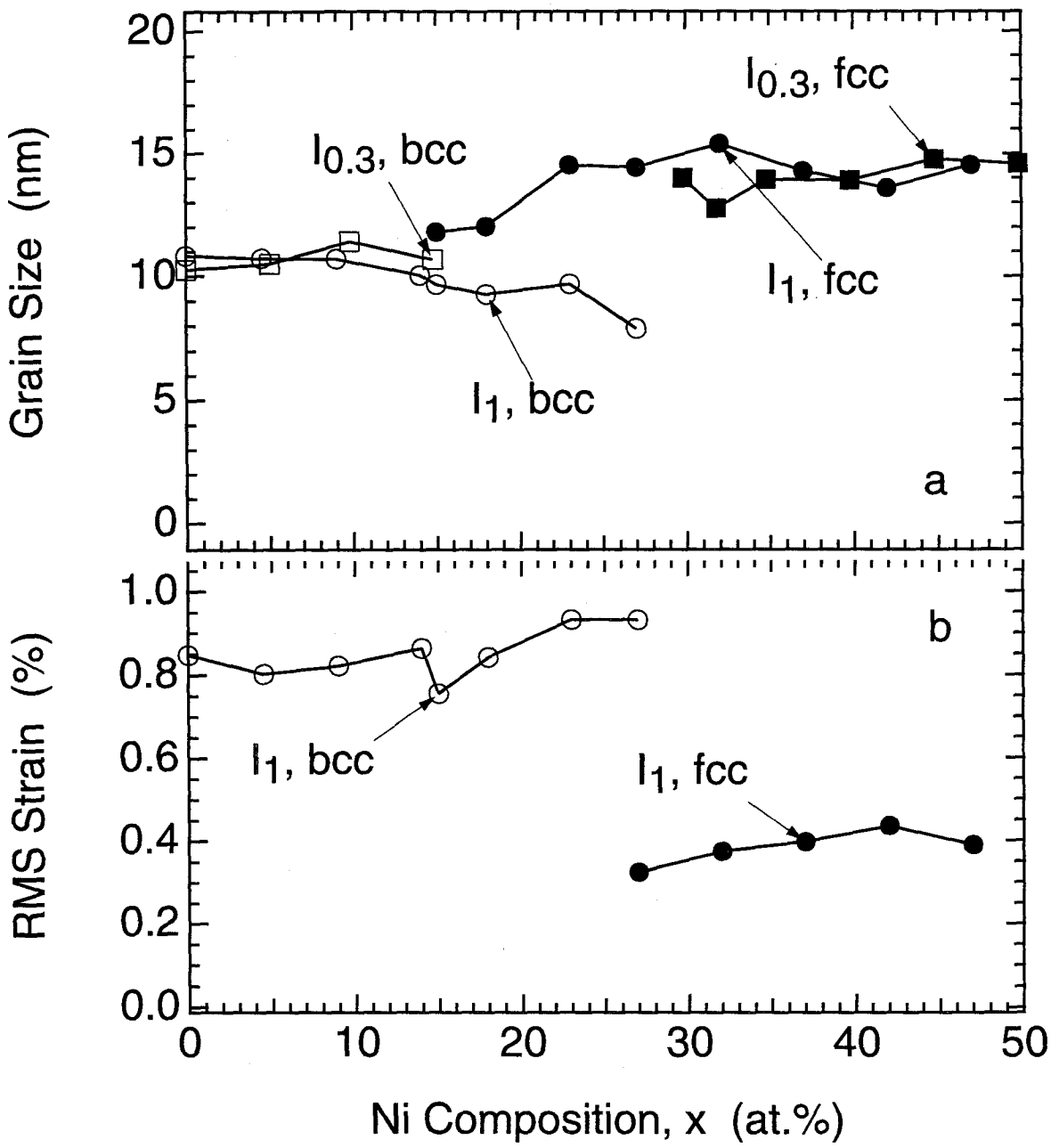

FIG. 5.7. X-ray diffractometry determination of grain size and root-mean-squared strain of the bcc and fcc phases of as-milled $Fe_{100-x}Ni_x$ alloys. (a) grain size determined by Scherrer broadening of (110) bcc and (111) fcc diffractions, and (b) root-mean-squared strain determined by the method of Williamson and Hall.

and a larger root-mean-squared strain than the fcc phase. This is not surprising and is consistent with previous studies [10,11].

The DSC traces presented in Fig. 5.8 are differences between the first and second scans of the sample up to 550 °C at a scan rate of 20 °C / minute. For all specimens we observed a broad exothermic peak that began at 130 °C. We also observed a second peak at about 400 °C for the bcc alloys and 520 °C for the fcc alloys. We performed x-ray diffraction measurements on the powders heated in the DSC to 550 °C. In none of the samples of pure bcc or fcc phase did we observe any transformation to the other phase after the DSC scans. We therefore interpret the measured heats as enthalpies of defect recovery. We also performed partial DSC scans to 300 °C, which is a temperature between the first and second broad peaks in Fig. 5.8. Figure 5.9 presents the x-ray diffraction patterns of the $Fe_{53}Ni_{47}$ alloy at its as-milled state, and after DSC scan up to 300 °C and 600 °C. X-ray peak analysis showed that the first DSC peak corresponded primarily to the relaxation of the root-mean-squared strain, whereas the second DSC peak corresponded to grain growth. Integrating the DSC traces such as those in Fig. 5.8 gave about 1.5 kJ/mole for the bcc alloys, and 0.5 kJ/mole for the fcc alloys. In both cases the integrated heat in the first peak was approximately the same as the integrated heat in the second peak. These numbers are only approximate, however. We hesitate to claim, for example, that the materials milled at the lower intensity showed a distinctly smaller heat evolution than those milled at the higher intensity, although this seems to be true. Unfortunately, in the composition range from $25 < x < 35$, the fcc phase undergoes a ferromagnetic Curie transition in the temperature range of our DSC measurements. We were therefore unable to extract reliable enthalpies of defect recovery for the two-phase alloys.

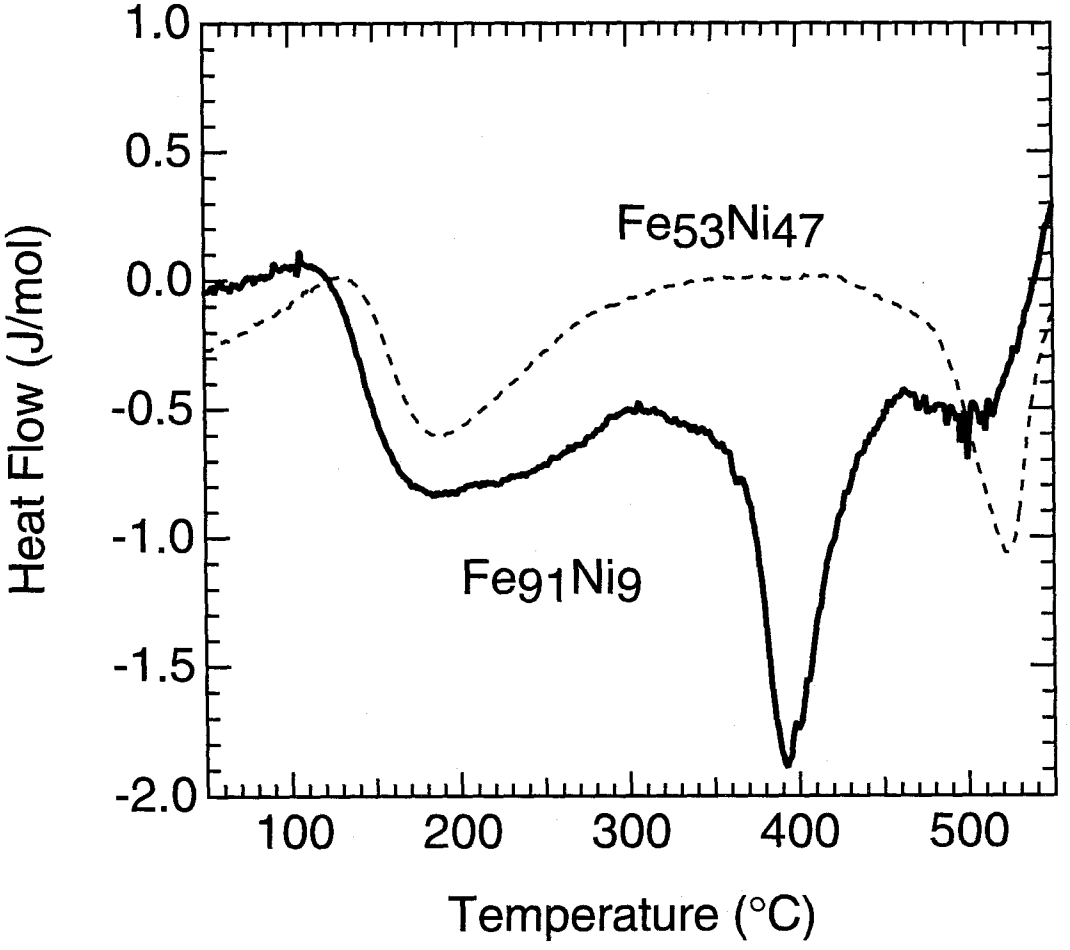

FIG. 5.8. DSC scans of $Fe_{91}Ni_9$ and $Fe_{53}Ni_{47}$ ball milled at intensity I_1 for 24 h, after subtracting their respective backgrounds obtained from subsequent scans.

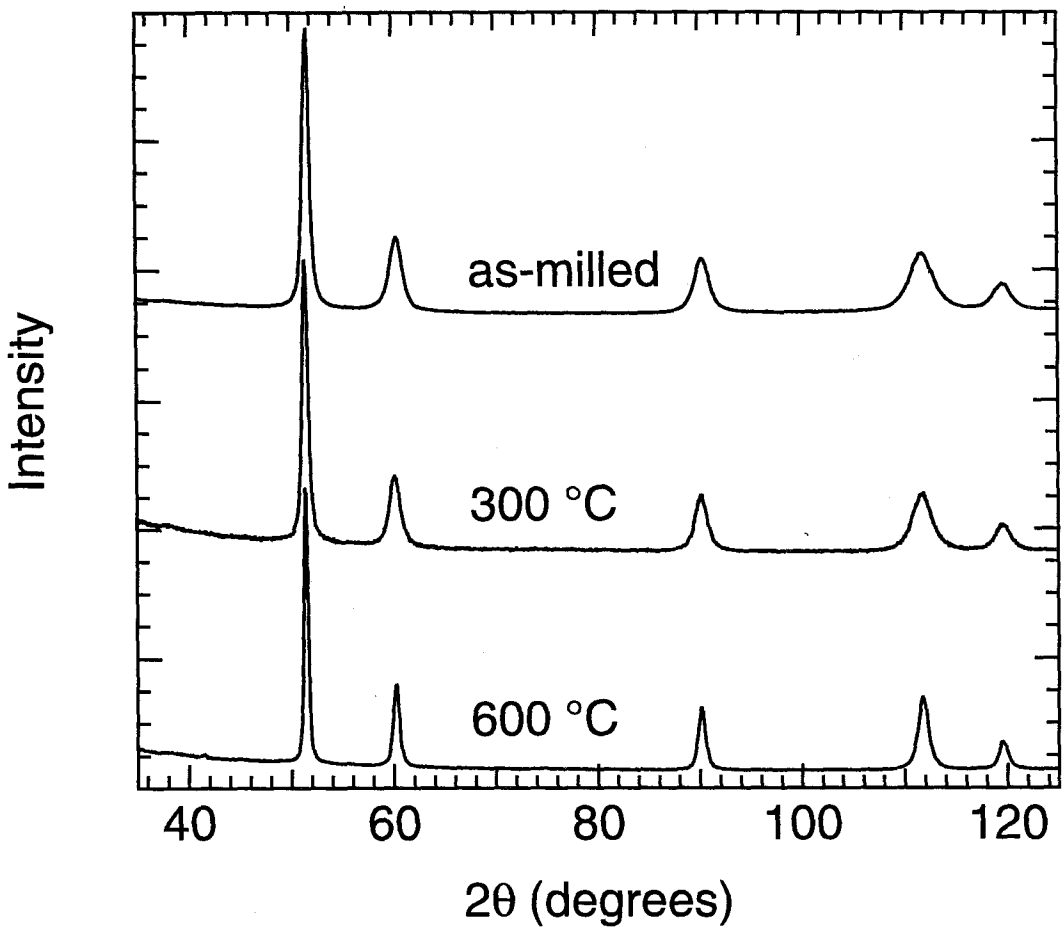

FIG. 5.9. X-ray diffraction patterns of $Fe_{53}Ni_{47}$ in its as-milled state and after annealing at a rate of 20 °C per minute up to various temperatures.

5.4 Discussion on Two-Phase Coexistence

For Fe-rich alloys, the as-milled alloy is fully bcc. For Ni-rich alloys, the as-milled alloy is fully fcc. At intermediate compositions, however, the as-milled alloys are two-phase mixtures of bcc and fcc phases. This two-phase region spans the range in Ni concentration, $18 < x < 34$, for the milling intensity $I_{0.3}$, and the broader composition range, $12 < x < 30$, for the intensity $I_{1.0}$. Recall that conventional thermodynamic explanations of two-phase coexistence rely on chemical segregation between the two phases. The minimum in free energy of a two-phase alloy, F_{tot}, is found by constructing a common tangent between the free energy curves of the two phases. The points of tangency mark the equilibrium compositions of the two phases for any alloy having a composition between these two compositions.

For several reasons we doubt that the two-phase coexistence found in our as-milled alloys can be understood with the conventional thermodynamic explanation. There is poor agreement between the phase fractions shown in Fig. 5.3 and the predictions with the lever rule and the Fe-Ni phase diagram for any assumed temperature. Even allowing for enhanced solid solubility in the bcc and fcc phases, the conventional argument is unsuccessful in predicting the trends of Fig. 5.3 — the lever rule predicts a linear change in phase fraction across the two-phase region, which is inconsistent with the skewed curves of Fig. 5.3.

Another reason we doubt the conventional thermodynamic explanation of two-phase coexistence is our evidence that through the two-phase region the compositions of the bcc and fcc phases are approximately the same. In particular, our data on lattice parameters show that in the two-phase region, the fcc phase has a chemical composition close to that of the alloy itself. It is difficult to determine a precise chemical composition of a phase from its lattice parameter, but the data of Fig. 5.4 suggest that the fcc phase is

enriched in Ni by perhaps only 3 % beyond the overall composition of the alloy. By conservation of solute, the bcc phase must also have nearly the composition of the alloy. Although not sufficient in themselves, our data on hyperfine magnetic fields are consistent with the bcc phase having the composition of the bulk alloy. Our data cannot show an absence of chemical segregation to much better than 3-4 %, but this accuracy is sufficient for what follows. A previous study of as-milled alloys of Fe-Cu suggested that both the bcc and fcc phases had nearly the same compositions [10], and we note that the elements Fe and Cu are less miscible than Fe and Ni.

Another peculiarity of the two-phase region is that it becomes broader as the milling intensity is increased. This is inconsistent with the general expectation that a higher ball milling intensity should promote solid solubility. Notice that the broadening of the two-phase region is asymmetrical; with higher milling intensity the fcc single-phase region grew slightly, but the bcc single-phase region shrank more.

5.5 Interpretations of Two Phase Coexistence

Using results from previous assessments of the Fe-Ni phase diagram implemented by the commercial software package Thermo-Calc [32,33], the Helmholtz free energy versus composition was calculated for bcc and fcc Fe-Ni alloys at various temperatures, $F_{bcc}(x,T)$ and $F_{fcc}(x,T)$. The dark curves in Fig. 5.10 are the calculations for F_{bcc} and F_{fcc} at 300 K. These results were obtained by extrapolation of higher temperature data, so their precise reliability is unknown. Nevertheless, it is interesting that the two curves cross at x = 28, which is quite close to the compositions where the as-milled alloys have equal fractions of the bcc and fcc phases ($x \approx 26$ and 30 in Fig. 5.3). This crossing of free energy curves defines the polymorphic transformation composition at the temperature of interest. (We assume this temperature is 300 K, but Thermo-Calc results show that the

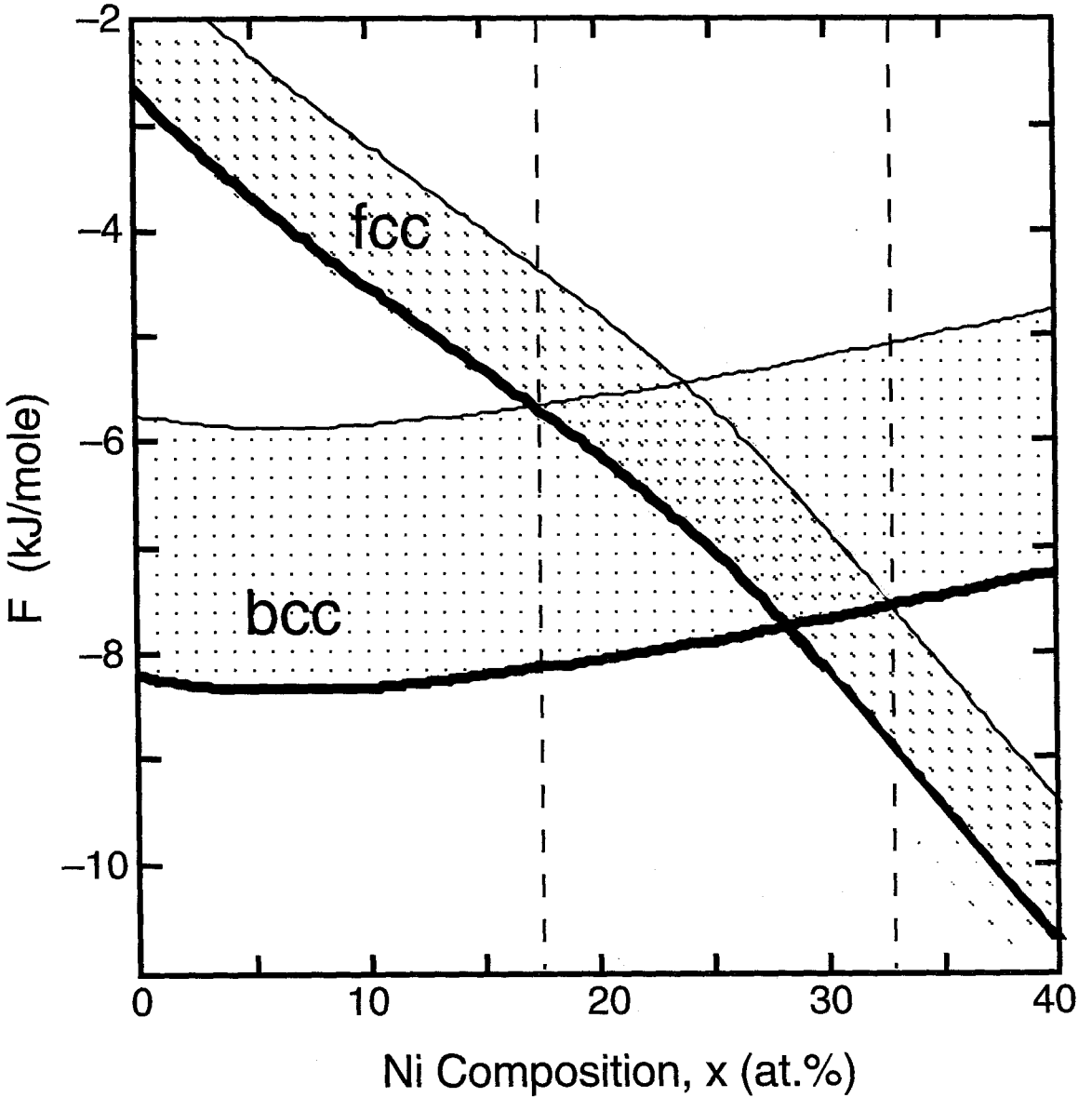

FIG. 5.10. Dark curves: Thermo-Calc calculations of the free energies of bcc and fcc Fe-Ni alloys at 300 K (reference states for Fe and Ni were their stable element reference states at 298 K and 1 atm). See text for description of bands above the dark curves.

polymorphic transformation composition does not vary strongly with temperature; it decreases by only 4 % Ni when the temperature is raised from 300 K to 500 K.) Polymorphic transformations involve a change in structure with no change in composition, so it is not surprising that the polymorphic transformation line is relevant for as-milled alloys. A similar argument was used previously for understanding extended solid solubility in Fe-Cu [5-12].

A simple crossing of free energy curves cannot explain two-phase coexistence, however. For compositions on either side of the crossing point of the two curves, the free energy is minimized by the existence of only one phase. We have considered modifications of the polymorphic transformation concept to explain two-phase coexistence in ball milled Fe-Ni. These modifications presume that the alloy has spatial heterogeneities involving: 1) composition, 2) temperature, 3) pressure, and 4) defect structures. In the present section we discuss in sequence the success of these ideas.

Compositional heterogeneities would allow the Ni-rich regions to be fcc, and Ni-poor regions to be bcc, based on the free energy curves $F_{fcc}(x,T')$ and $F_{bcc}(x,T')$. The problem with this argument is that rather large compositional heterogeneities are required to explain the data of Fig. 5.3. For example, in alloys with low Ni concentration this argument predicts that the fcc regions would have Ni enrichments of more than 15%, and our experimental results are inconsistent with such large chemical heterogeneities. A second problem with the concept of compositional heterogeneities is that we would expect the heterogeneities to be suppressed with higher milling intensity. With higher milling intensity, however, the composition range for two-phase coexistence grows larger, in contrast to this expectation.

The existence of thermal heterogeneities can cause two-phase coexistence if the polymorphic transformation composition has a strong temperature dependence. For the bcc

and fcc phases of Fe-Ni, however, Thermo-Calc calculations show that the polymorphic transformation line is nearly vertical (see also Fig. 7 in [34]). Since the polymorphic transformation composition changes little with temperature, temperature elevations of 500 K would be needed to obtain fcc phase in the Ni-poor alloys. The bcc phase could not be obtained in the Ni-rich alloys for any elevation of temperature.

Owing to the volume difference of 3 % between the bcc and fcc phases, pressure heterogeneities will affect strongly the thermodynamic stabilities of the bcc and fcc phases. Since the bulk moduli of both phases are high, high elastic energies can be achieved with modest internal strains. An elastic strain of 1% can increase the free energy of the bcc phase by several kJ/mole, so reasonable strains can cause large shifts of free energy curves. There is certainly a distribution of internal strains in the as-milled alloys, as shown by the data of Fig. 5.7b, and these internal strains are larger for the bcc phase than for the fcc phase. Since the bcc phase is also expected to have the larger elastic moduli, it has the larger distribution of elastic energy density. We believe that these localized strain distributions, which originate with dislocations and other defect structures, have major effects on the stability of individual bcc and fcc crystallites.

We also expect the stability of bcc or fcc crystallites to be affected by the high density of grain boundaries, which are capable of elevating bulk enthalpies by several kJ/mole [2]. The grain boundary energy cannot be understood easily as a property of one crystallite or another, but this is not necessary. Regions rich in small bcc crystallites, for example, will be expected to have a higher internal energy than will regions rich in larger fcc crystallites.

We do not know accurately the relative importance of grain boundaries and other defects in affecting the free energy, although the two peaks in the DSC traces, the strain recovery peak and the grain growth peak, have about equal areas. Similarly, our x-ray

lineshape analysis does not provide precise numbers for the grain sizes and the root-mean-squared strains. Nevertheless, we can state with confidence that the enthalpy measured by DSC scans of the bcc material (about 1.5 kJ/mol) is greater than that of the fcc material (about 0.5 kJ/mol), and the x-ray peaks from the bcc phase are broadened more strongly than the fcc peaks. Besides the larger defect enthalpy in the bcc phase, we have the following evidence that there is a larger distribution in defect enthalpy in the bcc phase. Dark field transmission electron microscopy studies of grain size distributions in ball-milled alloys have shown a broad distribution of crystallite sizes [26,27], and this is consistent with the tendency of diffraction peaks from ball milled materials to have Lorentzian shapes [35]. Our x-ray diffraction peaks were not accurately Lorentzian functions, but they did show strong intensities in their tails, and more so for the bcc alloys. The root-mean-squared strain measured for the bcc alloys, which was about twice as large as for the fcc alloys, originates from a large distribution of local interplanary spacing in the alloy.

With a distribution of grain sizes and a distribution of internal strains, we expect that different crystallites will be destabilized by different amounts. In what follows, we consider in a general sense the heterogeneities in free energies of the bcc and fcc phases in Fe-Ni alloys prepared by ball milling. The free energy is considered in the sense of a "coarse-grained" free energy, where the coarse graining encompasses several crystallites. The meaning of the internal energy is not a serious problem in principle, since we can add to the internal energy new contributions from defect density and grain size. The magnitude of the excess entropy induced by ball milling, however, is less clear. The simple approach is to ignore it, and we justify this as follows. Microstructural features such as dislocations and grain boundaries are often termed "non-thermodynamic", because their abundance in thermodynamic equilibrium is essentially negligible. This can be true only if they are responsible for a relatively minor increase in the entropy of the alloy, but a relatively large increase in enthalpy. To a first approximation, our picture of an increased free energy in

ball-milled materials reflects primarily an increase in the internal energy due to the microstructural defects created by milling.

To accommodate the spatial heterogeneities in coarse-grained free energy, we modify Fig. 5.10 by drawing a band above the calculated dark curves for F_{bcc} and F_{fcc}. The bands serve to indicate approximately the distribution of free energy that exists for the fcc and bcc regions of differing defect densities. Since the x-ray diffraction peak shapes do not depend on composition for either the bcc or fcc phases (Figs. 5.5, 5.7), we have represented the elevation of the free energy curves as equal vertical shifts at all compositions. The centers of the bands match the average enthalpy measured from DSC scans of bcc and fcc material. In milled materials we might expect upwards translations of the free energy bands that will contribute to the heat evolution measured in a DSC experiment. However, the lattice parameters of Fig. 5.4 agree reasonably well with those of bulk Fe-Ni alloys compiled by the JCPDS [30,31], indicating that there is no overall average strain in the material. It seems plausible that the bottoms of the free energy bands, associated with the least defective regions, are not altered significantly by ball milling.

During milling, we assume it is possible for a crystallite of one phase to transform into a crystallite of the other phase when the local coarse-grained free energy favors the transformation. (There may be a nucleation impediment to this transformation, but nucleation should be less of a problem when both phases are already present in the alloy, or when martensitic transformations can occur.) Such a transformation could occur if the chemical contribution to the free energy is not favorable, provided that the defect enthalpy is reduced significantly by the transformation. Such transformations of the more defective crystallites would be expected to occur in the composition range from $17 < x < 33$, where the free energy bands for the fcc and bcc phases overlap in Fig. 5.10. We have drawn vertical dashed lines in Fig. 5.10 to indicate the expected two-phase region. We expect that for compositions $x < 17$, the chemical preference for the bcc phase is too large to be

overcome by milling-induced defects. Similarly for x > 33, the defect density in the fcc phase is insufficient for fcc crystallites to be destabilized with respect to perfect bcc crystallites.

The overlap of the free energy bands in Fig. 5.10 can explain qualitatively the occurrence of two-phase coexistence in Fig. 5.3, but a little more detail is required to explain the asymmetrical phase fraction curves in Fig. 5.3 (i.e., the negative skewness for the fraction of fcc phase). We propose two reasons for this asymmetry. Differences in curvature of the Thermo-Calc free energy curves of the bcc and fcc phase (see Fig. 5.10) cause the bcc and fcc free energy bands to approach each other on the Fe-rich side of the polymorphic transformation composition. The increased overlap of these bands will extend the range of fcc phase to lower Ni concentrations. Our second proposed reason for the asymmetrical phase fraction curves in Fig. 5.3 involves asymmetrical distribution functions for the coarse-grained free energies of the fcc- and bcc-rich regions. Figure 5.11 shows the type of free energy distribution functions* that are needed to predict the skewness of the phase fraction data of Fig. 5.3. We have drawn a positive skewness of the distribution functions in Fig. 5.11, and a wider spread of the bcc free energy distribution function, $\rho_{bcc}(F,x,T=300K)$, compared to the fcc free energy distribution function, $\rho_{fcc}(F,x,T=300K)$. Each of the distribution functions has been normalized to unity:

$$1 = \int_{-\infty}^{\infty} \rho_{bcc}(F,x',T')\, dF \quad , \qquad 1 = \int_{-\infty}^{\infty} \rho_{fcc}(F,x',T')\, dF \quad . \tag{5.1}$$

A two-phase alloy need not have regions that fill all states in ρ_{bcc} and ρ_{fcc}, however. Instead, we expect that the states to be filled approximately to a maximum, F_F, defined* so that:

---

* For conventional thermodynamics as in Thermo-Calc calculations, the distribution functions in Fig. 8 would be Dirac delta functions whose positions change with composition.

* This argument runs parallel to the using a density of states function for electrons, $\rho(E)$, that is filled to a Fermi level, E_F, defined at low temperature as the energy that accounts for all electrons.

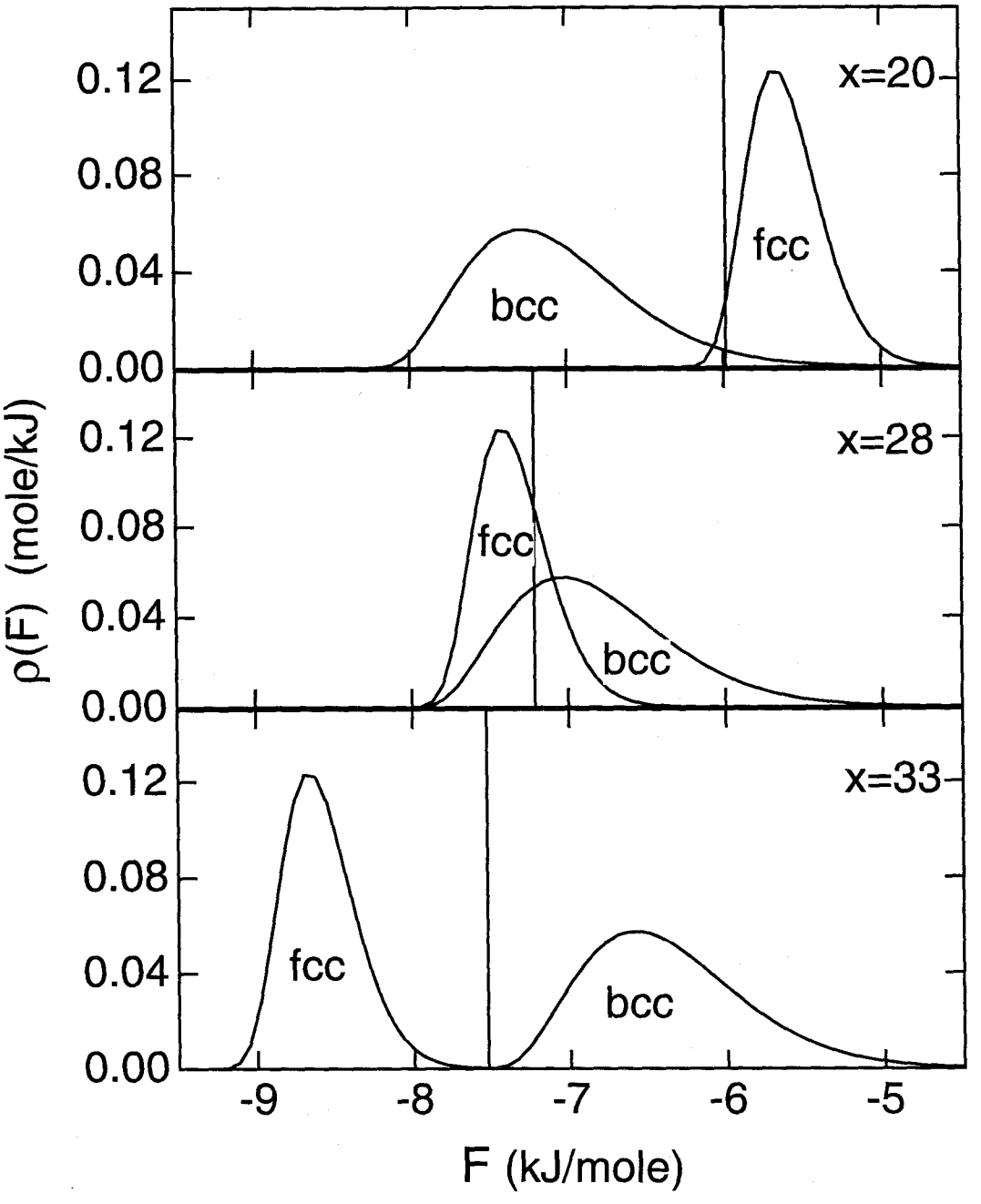

FIG. 5.11. Semi-quantitative distributions of free energy functions for bcc and fcc Fe-Ni alloys of three compositions at 300 K after ball milling. The lowest energies of each curve were obtained from the dark curves of Fig. 5.10 for compositions x = 20, 28, and 33, respectively.

$$1 = \int_{-\infty}^{F_F} \rho_{fcc}(F,x',T') + \rho_{bcc}(F,x',T') \; dF \quad . \tag{5.2}$$

Vertical lines mark the values of F_F for the three cases shown in Fig. 5.11. Note in particular that at the composition corresponding to the crossover of the free energy curves (x = 28), a greater fraction of fcc phase is expected than bcc phase. By shifting the bottoms of the distribution functions in Fig. 5.11 to coincide with the compositions provided by the Thermo-Calc free energy curves of Fig. 5.10, the asymmetry of the phase fraction data of Fig. 5.2 is predicted qualitatively.

The prediction of the asymmetrical phase fraction curves in Fig. 5.3 requires that $\rho_{bcc}(F,x',T')$ has a tail that extends to higher F than the tail of $\rho_{fcc}(F,x',T')$. With increased milling intensity, we expect this tail of $\rho_{bcc}(F,c',T')$ to extend to yet higher F. We can then understand how with increased milling intensity, the two-phase region should extend further into the region of low Ni concentration because F_F moves upwards to include relatively more of the fcc phase. The effect of milling intensity on the free energy distribution of the fcc phase, $\rho_{fcc}(F,c',T')$, is evidently less strong.

5.6 Comparison to Two-Phase Coexistence in Other Processings

Our interpretation of two-phase coexistence in as-milled Fe-Ni involves a larger distribution of the coarse-grained free energy for the bcc phase than the fcc phase. This interpretation is based on the bcc phase accumulating a higher density of defects and smaller grains during milling. This type of enthalpy buildup may be unique to ball milling, so it is interesting to compare the composition range for two-phase coexistence in ball

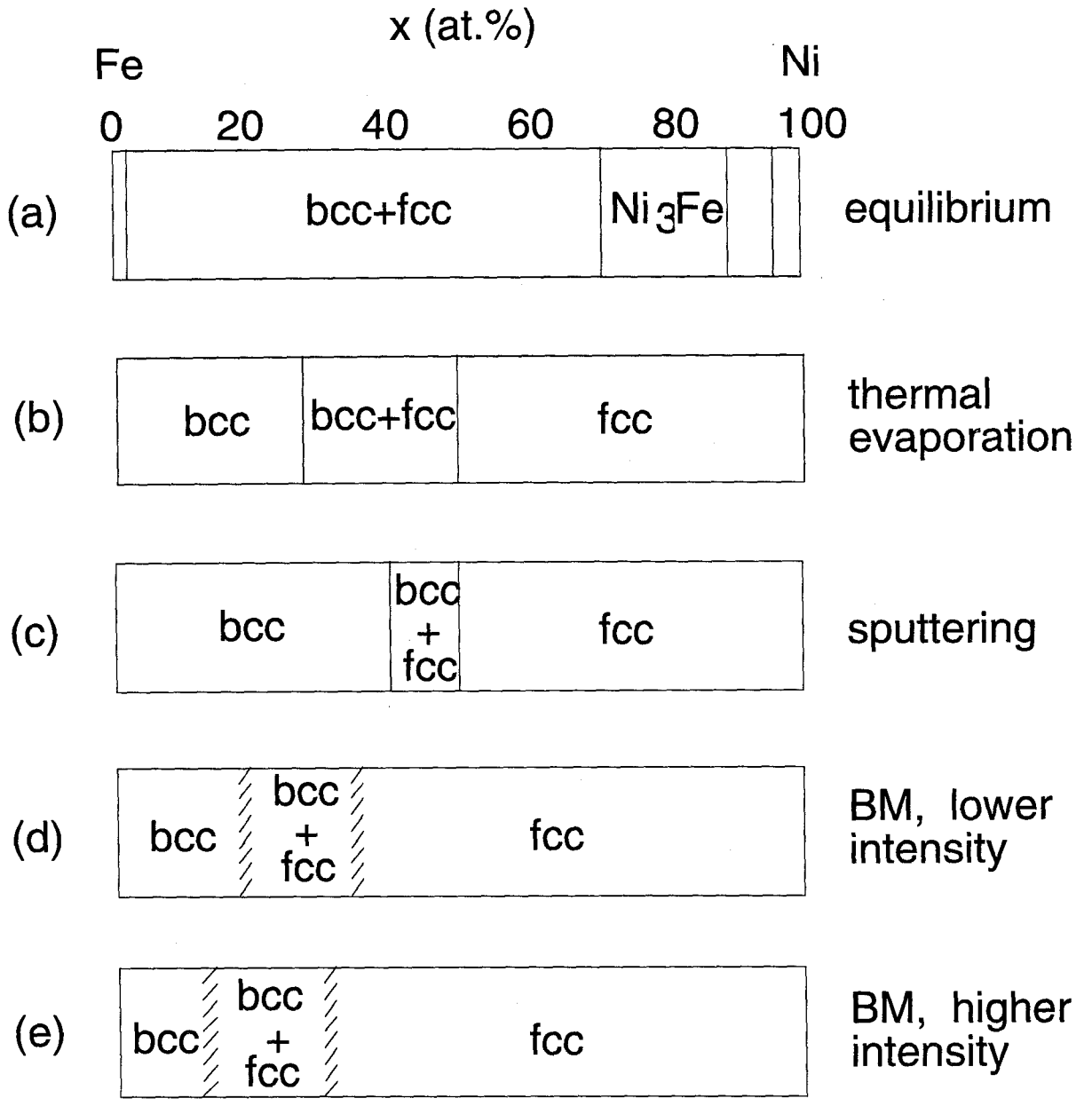

FIG. 5.12. Phase boundaries for Fe-Ni alloys processed by different methods: equilibrium [29], evaporation [36], sputtering [37], ball milling at intensity $I_{0.3}$, and ball milling at intensity I_1.

milled Fe-Ni alloys to the composition range for two-phase coexistence for other nonequilibrium processings. Figure 5.12 compares the phase boundaries of the bcc and fcc phases of Fe-Ni for five different types of processing. Thermodynamic equilibrium at room temperature shows a broad two-phase region, bounded on the right by $L1_2$ ordered Ni_3Fe, which is a sluggishly-ordering superstructure based on an fcc lattice. Thermal evaporation [36] and sputtering [37] produce alloys with a narrower range of two-phase coexistence, as expected. Note, however, that thermal evaporation and sputtering produce two-phase regions that are located more centrally in the two-phase region of the equilibrium diagram. In comparison, ball milling produces a two-phase region that is shifted to low Ni concentrations, and becomes more so with increased milling intensity. It seems that ball milling differs from the thin film preparation methods in that it produces a higher defect enthalpy in the bcc phase than the fcc phase. It would be interesting to compare the phase fractions across the two-phase regions for Fe-Ni alloys synthesized by thermal evaporation or sputtering.

5.7 Summary

We synthesized mechanically-alloyed $Fe_{100-x}Ni_x$ alloys over the range of x from 0 to 50. Our Spex mill was modified so that it could also operate at a significantly reduced milling intensity, and we compared the materials milled for long milling times with the normal and reduced intensities. We found that the composition ranges of the bcc and fcc single phase regions were greatly extended with respect to their equilibrium ranges. At the higher milling intensity, we found that the bcc phase was destabilized with respect to the fcc phase, and the two-phase region shifted to lower Ni concentrations. Lattice parameters measured by x-ray diffractometry, and hyperfine magnetic fields measured by Mössbauer spectrometry, indicated that the chemical compositions of the individual phases in the as-

milled alloys were the same as the overall composition of the alloy. We therefore expect the thermodynamic phase preference of as-milled Fe-Ni to be influenced by the polymorphic transformation line. In fact, the composition range for two-phase coexistence in as-milled Fe-Ni does enclose the polymorphic transformation composition.

In DSC scans, we measured enthalpies for defect recovery in the fcc and bcc alloys of about 0.5 and 1.5 kJ/mole, respectively. X-ray lineshape analysis showed that there was a large distribution in the internal strains of the as-milled crystallites. We found evidence for a distribution in the crystallite sizes, and a distribution in crystallite sizes in as-milled materials is generally expected. We propose that heterogeneities in the defect enthalpy of the fcc and (especially) the bcc phase will effectively broaden the free energy curves. We propose that the distribution in the defect enthalpies is responsible for the region of two-phase coexistence around the polymorphic transformation composition. Near the polymorphic transformation composition, the free energy curves of the bcc and fcc phase are not strongly separated, so it may be possible for highly defective bcc-rich regions to transform into fcc phase, even though the Ni concentration may be a bit below the polymorphic transformation composition. We can predict semiquantitatively the composition range of two-phase coexistence by broadening upwards the Thermo-Calc free energy curves by average amounts equal to the enthalpies measured in DSC scans for bcc and fcc alloys. The asymmetrical phase fraction curves can be understood by the differences in curvature of the bcc and fcc free energy curves, or by a high energy tail of the bcc free energy curve. If the bcc free energy curve broadens upwards with milling intensity more than does the fcc free energy curve, we can understand the shift with milling intensity of the composition range for two-phase coexistence.

References

1. R. B. Schwarz, R. R. Petrich, and C. K. Saw, J. Non-Cryst. Solids **76**, 281 (1985).
2. E. Hellstern, H. J. Fecht, Z. Fu, and W. L. Johnson, J. Mater. Res. **4**, 1292 (1989).
3. A. W. Weeber, P. I. Loeff, and H. Bakker, J. Less-Common Metals **145**, 293 (1988).
4. T. J. Tiainen and R. B. Schwarz, J. Less-Common Metals **140**, 99 (1988).
5. M. Oehring, T. Klassen, and R. Bormann, J. Mater. Res. **8**, 2819 (1993).
6. E. Ma, F. Brunner, and M. Atzmon, J. Phase Equil. **14**, 137 (1993).
7. E. Ma. M. Atzmon, and F. Pinkerton, J. Appl. Phys. **74**, 995 (1993).
8. A. R. Yavari, Phys. Rev. Lett. **70**, 3522 (1993).
9. E. Ma and M. Atzmon, Mater. Chem. Phys. **39**, 249 (1995).
10. J. Eckert, J. C. Holzer, and W. L. Johnson, J. Appl. Phys. **73**, 131 (1993).
11. J. Eckert, J. C. Holzer, C. E. Krill III, and W. L. Johnson, J. Appl. Phys. **73**, 2794 (1993).
12. J. Eckert, J. C. Holzer, C. E. Krill III, and W. L. Johnson, J. Mater. Res. **7**, 1980 (1992).
13. E. Gaffet, M. Harmelin, and F. Faudot, J. Alloys Compounds **194**, 23 (1993).
14. L. B. Hong, C. Bansal, and B. Fultz, NanoStructured Materials **4**, 949 (1994).
15. Y. Abe and W. L. Johnson, J. Jpn. Soc. Powder and Powder Metall. **40**, 272 (1993).
16. Z. Fu and W. L. Johnson, Nanostruct. Mater. **3**, 175 (1993).
17. K. Yamada and C. C. Koch, J. Mater. Res. **8**, 1317 (1993).
18. E. Gaffet, Mater. Sci. Eng. A **132**, 181 (1991).
19. E. Gaffet, Mater. Sci. Eng. A **135**, 291 (1991).
20. J. Eckert, L. Schultz, and E. Hellstern, J. Appl. Phys. **64**, 3224 (1988).
21. Y. Chen, M. Bibole, R. Le Hazif, and G. Martin, Phys. Rev.B **48**, 14 (1993).
22. C. Kuhrt and L. Schultz, J. Appl. Phys. **73**, 1975 (1993).

23. L. B. Hong, L. Anthony, and B. Fultz, J. Mater. Res. **10**, 126 (1995).

24. L. B. Hong and B. Fultz, "Phase Diagrams of bcc Alloys at Low Temperatures with Ballistic Atom Movements", Phys. Rev. B, in press, Sept. 1, 1995.

25. D. Basset, P. Matteazzi, and F. Miani, Mater. Sci. Eng. A **174**, 71 (1994); Mater. Sci. Eng. A **168**, 149 (1993).

26. H. Ouyang, B. Fultz, and H. Kuwano, in Nanophases and Nanocrystalline Structures, R. D. Shull and J. M. Sanchez, eds., (TMS, Warrendale, 1994) p. 95.

27. B. Fultz, H. Kuwano, and H. Ouyang, J. Appl. Phys. **76**, 5691 (1994).

28. B. Fultz and J. W. Morris, Jr., Phys. Rev. B **34**, 4480 (1986).

29. Editors T. B. Massalski, H. Okamoto, P. R. Subramanian, and L. Kacprzak, Binary Alloy Phase Diagrams, 2nd Ed., Vol. **2**, 1736 (ASM International, 1990).

30. Joint Committee on Powder Diffraction Standards, files 23-297 and 18-877, published by the International Center for Diffraction Data, 1993.

31. R. P. Reed and R. E. Schramm, J. Appl. Phys. **40**, 3453 (1969).

32. B. Sundman, B. Jansson and J.-O. Andersson: Calphad, **9**(2), 153-190 (1985).

33. Z. S. Xing, D. D.Gohil, A. T. Dinsdale and T. G. Chart, National Physics Laboratory, DMA (A) 103, London, 1985.

34. Y.-Y. Chuang, Y. A. Chang, R. Schmid, and J.-C. Lin, Metall. Trans. A **17**, 1361 (1986).

35. C. N. J. Wagner and M. S. Boldrick, Mater. Sci. Eng. A **133**, 26 (1991).

36. G. Dumpich, E. F. Wassermann, V. Manns, W. Keune, S. Murayama, and Y. Miyako, J. Magn. Magn. Mater. **67**, 55 (1987).

37. K. Sumiyama, M. Kadono, and Y. Nakamura, Trans. Jpn. Inst. Met. **24** (4), 190 (1983).

Chapter 6. Temperature Effects on Ball Milling of Ni_3Fe and Fe_3X (X = Si, Zn, Sn) Nanocrystalline Alloys

This chapter [1] describes studies of ball milling of Ni_3Fe and Fe_3X (X = Si, Zn, Sn) at temperatures from 23 °C to 300 °C. The average grain size, internal strain distribution, and thermal stability against grain growth and equilibrium phase formation of as-milled powders were measured and compared for different milling temperatures. The effect of milling temperature was little different from the role of temperature itself on the microstructure of nanocrystalline materials.

6.1 Introduction

During high energy ball milling, substantial structural disorder in the powder material is created during severe mechanical deformation. During and after milling the powder materials are not in a state of thermodynamic equilibrium, but a steady microstructural state is typically achieved after tens of hours of milling. High energy ball milling has been used to synthesize nonequilibrium materials such as metallic glasses [2-16], and more recently nanophase materials [13-21]. These nonequilibrium materials are unstable at low temperatures, and will usually form large grains of equilibrium crystalline phases when annealed at low temperatures of a few hundred degrees Celsius. The thermal stability of nanophase materials is important for both fundamental and technological reasons. It seems plausible that the control of temperature during the synthesis of nanophase materials can affect their subsequent thermal stability. A secondary goal of the present study of ball milling at elevated temperatures was to test if the thermal stability of the as-milled nanophase materials was affected by the temperature of milling. The primary goal of our present study was to find how the steady state grain size depends on the

temperature of ball-milling, and to identify alloy characteristics that may affect this temperature dependence.

Some work on ball milling at elevated temperatures [22-26] has been reported previously. The top of Table 6.1 summarizes the available steady state results on temperature dependent ball milling of Zr-Al [22, 23], and Ti-Cu [24, 25]. The average atomic strain of $Zr_{87.5}Al_{12.5}$ and pure Zr after ball milling at 300 °C was smaller than after milling at 23 °C. This is not surprising, as thermal relaxation is expected during milling at 300 °C. What is surprising, however, is that the reported grain sizes of $Zr_{87.5}Al_{12.5}$ and $Ti_{95}Cu_5$ after milling at 300 °C were *smaller* than after milling at 23 °C. This is in contradiction with results on elemental Zr [22, 23]. These currently available results are interesting, but not yet systematic. We therefore performed an investigation of the effect of temperature on the steady state microstructures achieved by ball milling, using alloys that form either intermetallic compounds or supersaturated solid solutions in thermodynamic equilibrium. We report results on the binary alloys Ni_3Fe and Fe_3X (X = Si, Zn, Sn). The thermodynamic equilibrium states of these alloys at low temperatures are $L1_2$ order, DO_3 order, or two-phase mixtures, as listed in the second column of Table 6.1.

TABLE 6.1. Steady States of Ball Milling at Different Temperatures

Alloy	Equilibrium State	Structure After Ball Milling	Ball Milling Temperature	Average Grain Size (Å)	Mean Square Strain (%)	DSC Peak Position (°C)	$\Delta\kappa$ $\times 10^{-3}$ Å^{-1}	Metallic Radius Difference (Å)
Previous Results [22-25]								
Pure Zr	A3 (hcp)	A3 (hcp)	23 °C	140	0.4		0.89	
			300 °C	160	0.3			
$Zr_{87.5}$-$Al_{12.5}$	2-phase	A3 (hcp)	23 °C	100	0.6	550	−6.7	0.16
			300 °C	60	0.2	525		
Ti_{95}-Cu_5	2-phase	A3 (hcp)	23 °C	160		360	−6.3	0.17
			300 °C	80		370		
Present Results								
Ni_3Fe	$L1_2$	fcc	23 °C	134	0.56	510	2.12	0
			200 °C	155	0.45			
			300 °C	187	0.36			
Fe_3Si	DO_3	bcc	23 °C	82	1.06	465	1.33	0.07
			300 °C	92	0.79			
Fe_3Zn	2-phase	bcc	23 °C	112	0.66	357	1.18	0.15
			200 °C	118	0.57			
			300 °C	129	0.51			
Fe_3Sn	2-phase	bcc	23 °C	61	0.765	365	0	0.22
			200 °C	61	0.762			

6.2 Experimental

Some general experimental procedures of ball milling were described in Section 1.2.2. Here we provide some additional details. The starting materials for ball milling were Ni_3Fe powders filed from ingots prepared by arc melting in an argon atmosphere, or mixtures of Fe and X elemental powders at an atomic ration of 3:1 (Section 1.2.2). Temperature-dependent ball milling was performed in a vibratory ball mill NEV-MA8 (Nisshin Giken, Japan), shown in Fig. 6.1. Cu gaskets were used to seal the vials to prevent gas contamination during ball milling. Chemical analysis indicated that oxygen contamination was less than 0.5 at.%, and contamination from Fe in the balls and vial was less than 0.5 at.% after 48 hours of milling [22-25]. For milling at room temperature (nominally 23 °C), the outside surface of the vial was cooled by flowing cold water. For high temperature milling, the vial was heated with an electrical resistance heater in contact with the vial. Temperatures of 200 °C and 300 °C were maintained by feedback control with a thermocouple mounted between the heater and the vial. After high temperature milling, the vial was quenched immediately into cold water to avoid possible grain growth or strain relaxation.

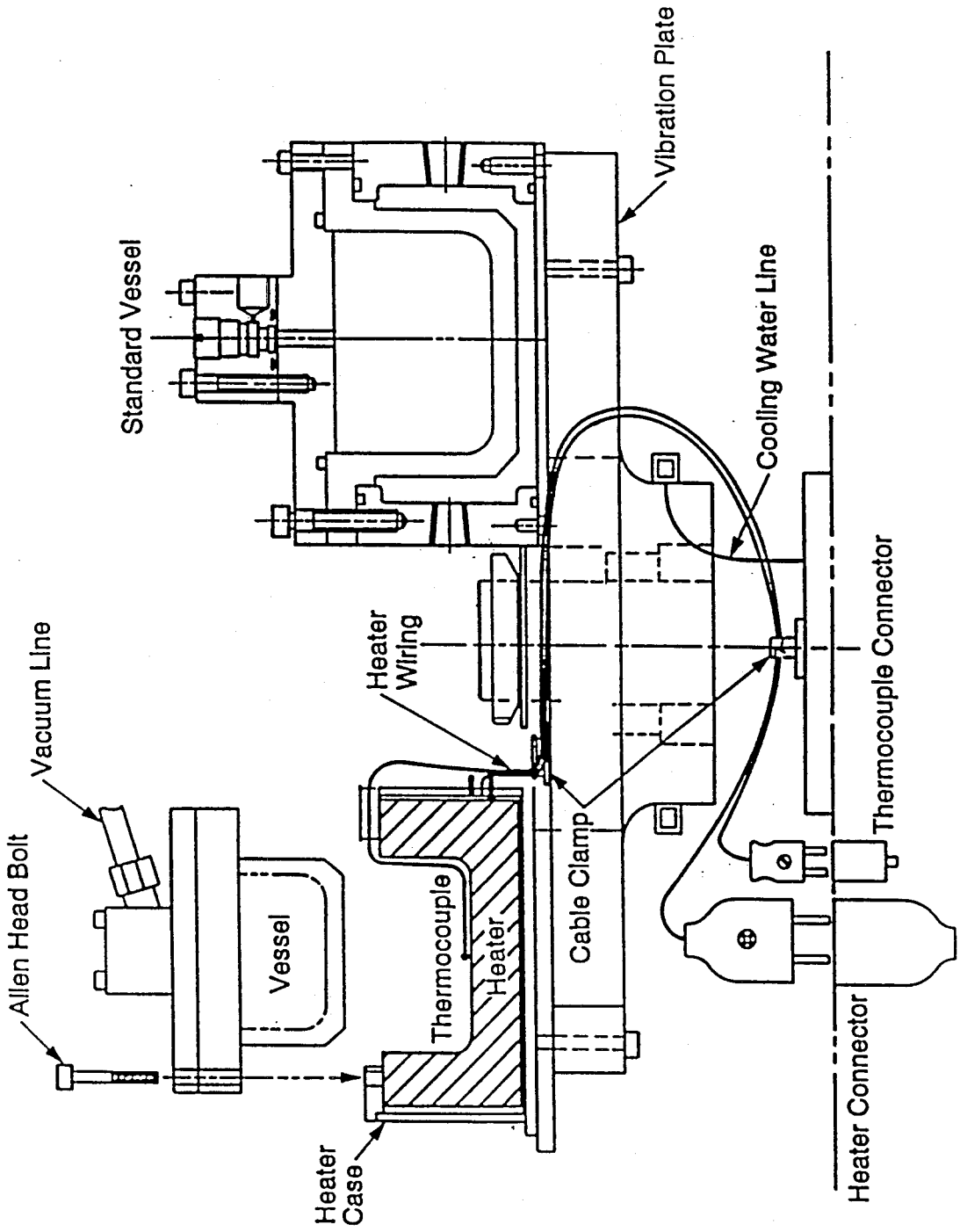

FIG. 6.1. Schematic drawing of the NEV-MA8 high temperature ball mill.

6.3 Results and Discussion

Crystal structure information is summarized in the third column in Table 6.1. After ball-milling at any of our temperatures, Ni_3Fe had the fcc structure while our Fe_3X (X = Si, Zn, Sn) alloys had the bcc structure. Figure 6.2 presents x-ray diffraction patterns of Ni_3Fe, measured after 48 hours milling at 23 °C, 200 °C and 300 °C. It can be seen that the diffraction peaks of Ni_3Fe are narrower after higher temperature ball milling. Figures 6.3a and 6.3b present the average grain sizes determined by Scherrer broadening of fcc (111) peaks and root-mean-squared (RMS) strains determined by the method of Williamson and Hall (Section 1.3.1) for Ni_3Fe milled for various times at 23 °C, 200 °C and 300 °C. Higher milling temperatures result in larger average grain sizes and smaller RMS strains. For all milling temperatures, we believe that 48 hours of milling time is more than sufficient to achieve a steady state of the alloy microstructure. All new data in Table 6.1 were obtained for samples ball milled for 48 hours.

We first present and discuss our results from Fe_3Zn. Figure 6.4 shows x-ray diffraction patterns of as-milled Fe_3Zn samples. The only difference visible among all three patterns is that the peaks are narrower after higher temperature ball milling, as for Ni_3Fe in Fig. 6.2. The as-milled samples were single-phase bcc at all milling temperatures, even though the thermodynamic equilibrium solubility of Zn in α-Fe is less than 2 at.%. We suspect that there was some clustering or inhomogeneous distribution (i.e., concentration fluctuation) of Zn atoms on the bcc lattice, because the hyperfine magnetic field (HMF) distributions shown in Fig. 6.5 of these Fe_3Zn alloys peaked around a large value of 310 kG in a distribution that was narrower than expected for a disordered solid solution [27]. However, we cannot prove this rigorously. We note also that bcc Fe-Zn alloys were reported previously for alloys prepared by sputtering [28] and cathodic pulverization [29], and these authors report some tendency for Zn clustering in more

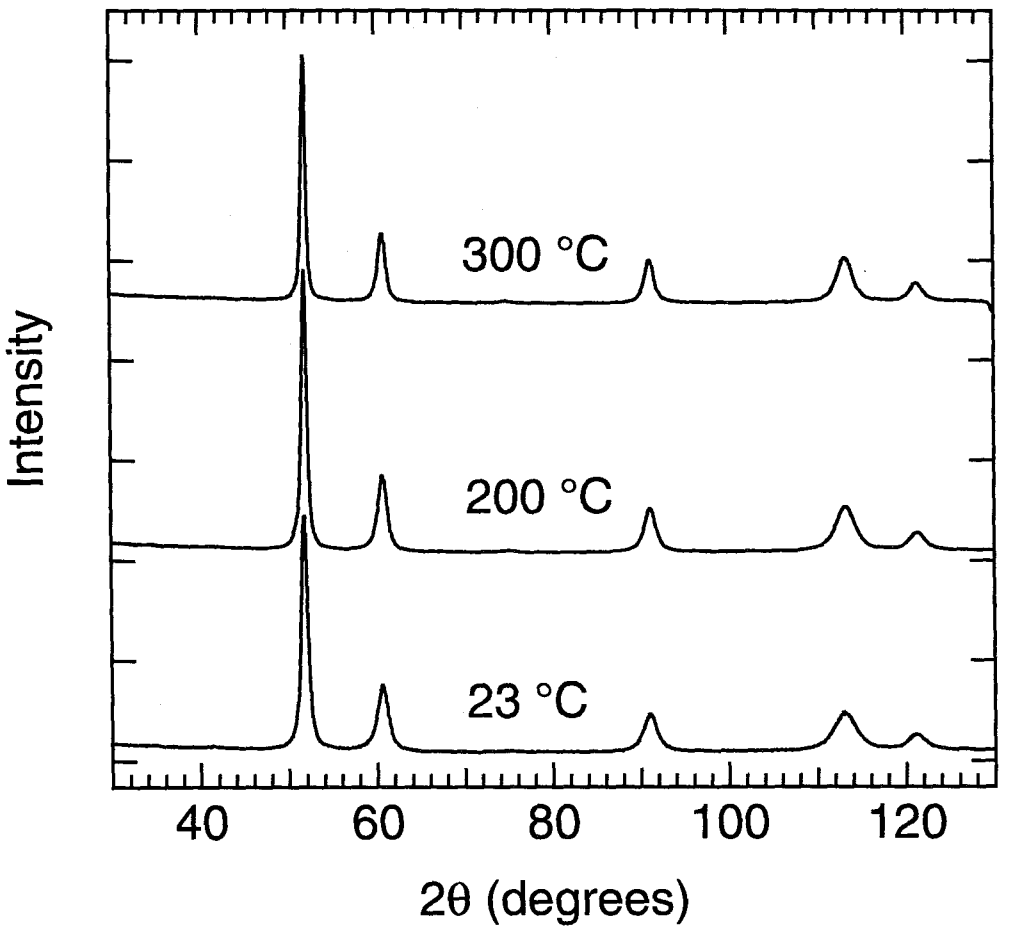

FIG. 6.2. X-ray diffraction patterns of Ni_3Fe after ball milling for 48 h at various temperatures.

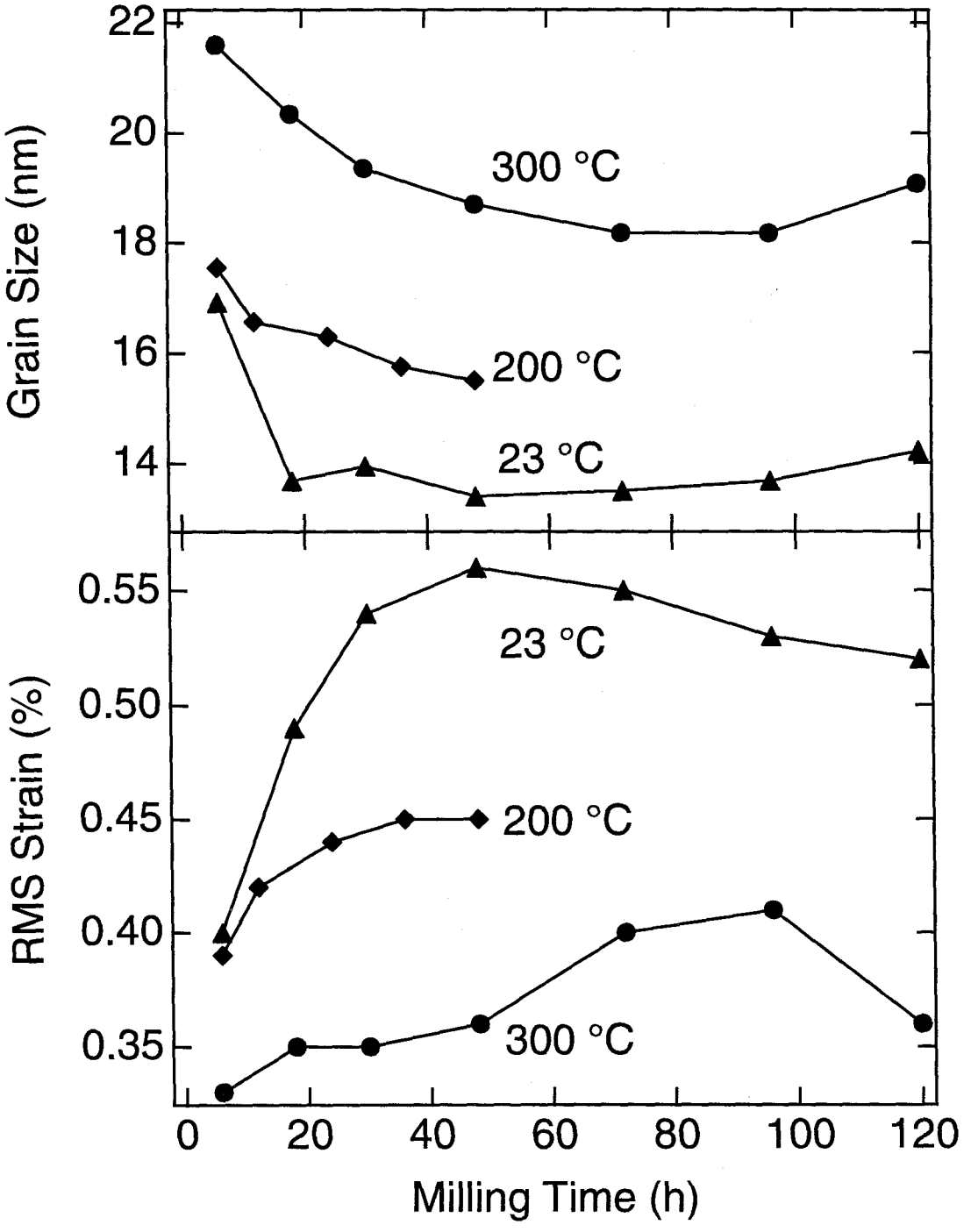

FIG. 6.3. (a) Average grain sizes, and (b) Root-mean-squared (RMS) strains of Ni_3Fe after ball milling for various times at the indicated temperatures.

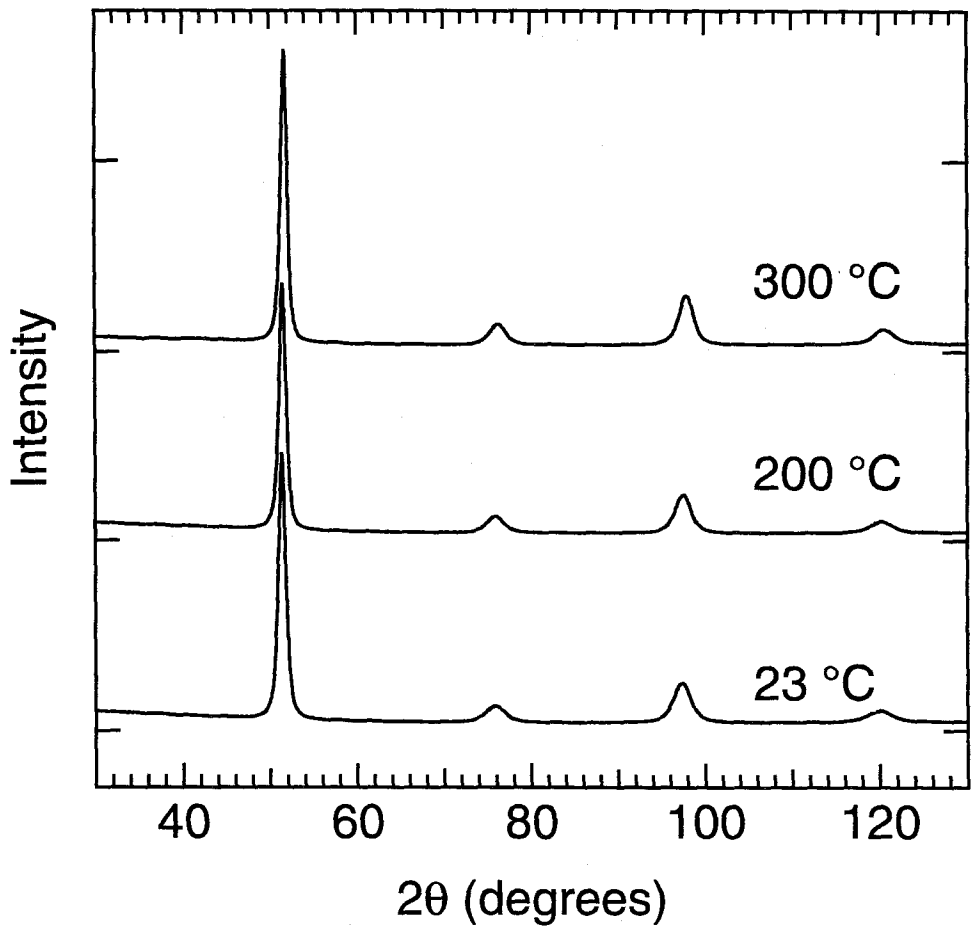

FIG. 6.4. X-ray diffraction patterns of Fe_3Zn after ball milling for 48 h at the indicated temperatures.

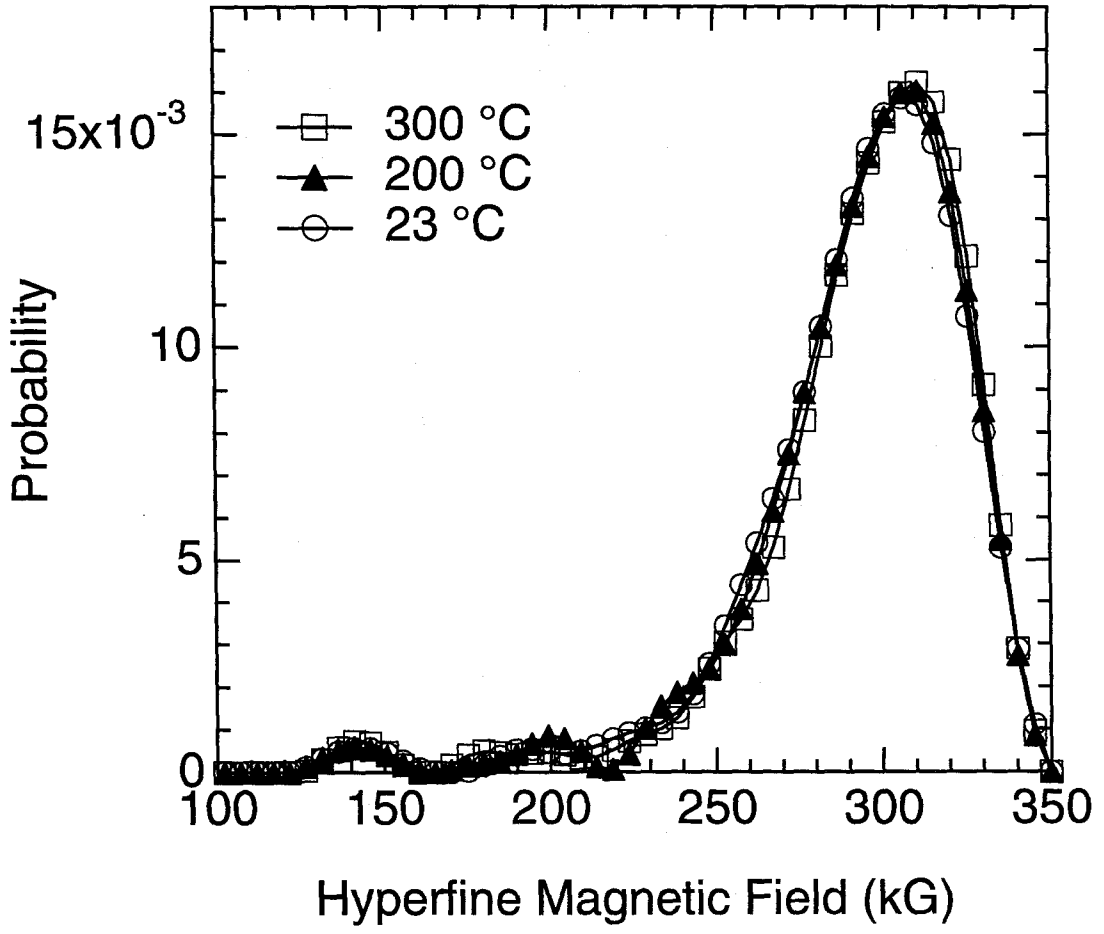

FIG. 6.5. Hyperfine magnetic field distributions of Fe_3Zn ball milled at 23 °C, 200 °C, and 300 °C for 48 hours

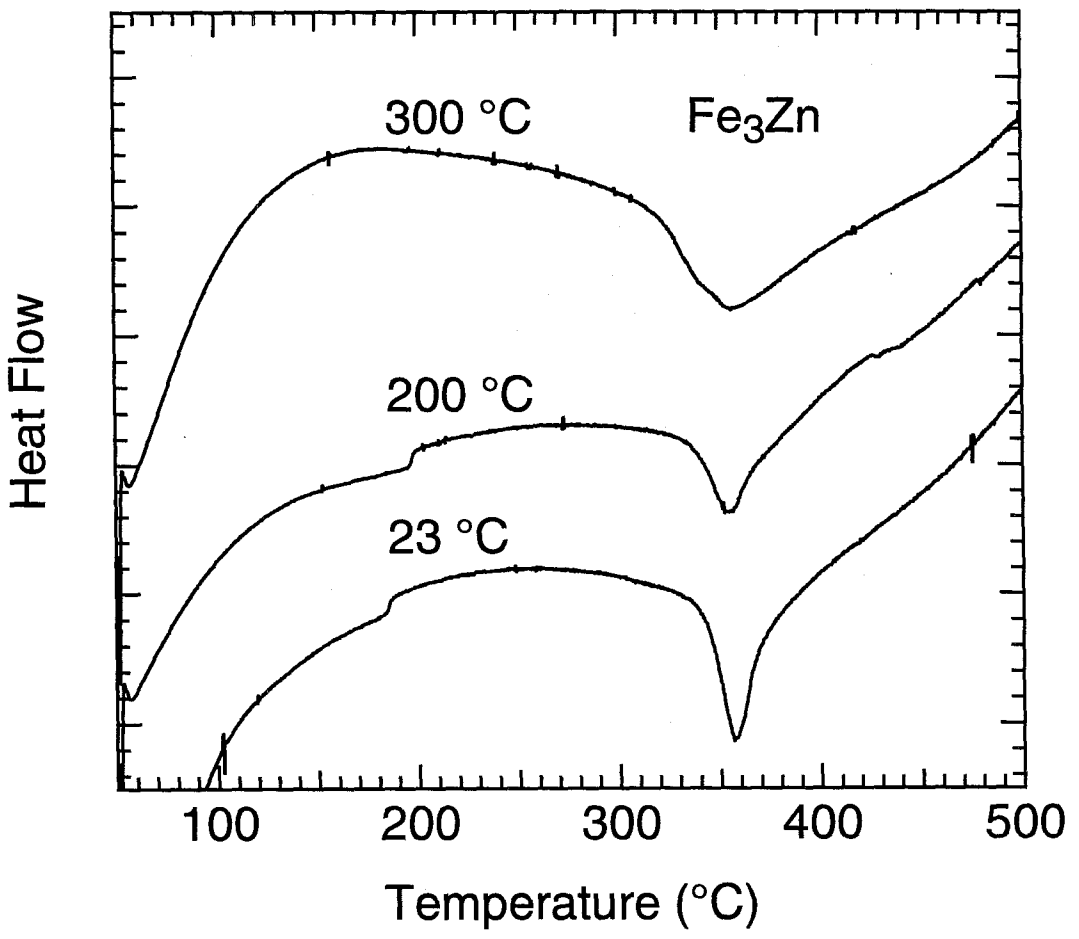

FIG. 6.6. DSC scans of Fe_3Zn after ball milling for 48 h at the indicated temperatures.

concentrated alloys. Also worth noticing in Fig. 6.5 is the similarity of all three HMF distributions, even though the samples were ball milled at different temperatures. Annealing of the as-milled Fe_3Zn materials for 1 hour at 300 °C causes phase separation and grain growth, regardless of the milling temperature. However, ball milling at 300 °C for 48 hours causes neither phase separation nor grain growth. In fact there was only a small difference in grain size between materials milled at 23 °C and 300 °C. Evidently ball milling, even at high temperature, suppresses the thermodynamic tendencies for both phase separation and normal grain growth, and results in single-phase disordered bcc nanocrystalline alloys.

The extreme similarity of the x-ray diffraction patterns in Fig. 6.2 and the HMF distributions in Fig. 6.5 suggests similar microstructures and therefore similar thermal stabilities for all three Fe_3Zn samples. Indeed, DSC scans of the 48 h ball milled samples of Fe_3Zn match each other very closely, as shown in Fig. 6.6. For all three milling temperatures, an exothermic peak is found at 357 °C. With x-ray diffractometry we determined that this peak originated from both phase separation and grain growth. The slight decrease of the depth of the peak with increasing ball milling temperature was attributed to larger grain size and smaller strain due to higher ball milling temperature. Otherwise perhaps surprisingly, the thermal stabilities of the as-milled Fe_3Zn materials were not measurably affected by the choice of milling temperature.

Similar results were obtained for Fe_3Si. Figure 1.15 shows the DSC scan of the Fe_3Si sample ball milled at 300 °C. The scan for the sample ball milled at 23 °C is not shown in Fig. 1.15, but is very similar. There is a broad exothermic peak at 465 °C. The as-milled Fe_3Si samples were annealed at a heating rate of 20 °C per minute up to various temperatures, 170 °C, 400 °C, 450 °C, 500 °C, 550 °C, 600 °C, and then were rapidly cooled to room temperature. The annealed samples were then characterized by x-ray

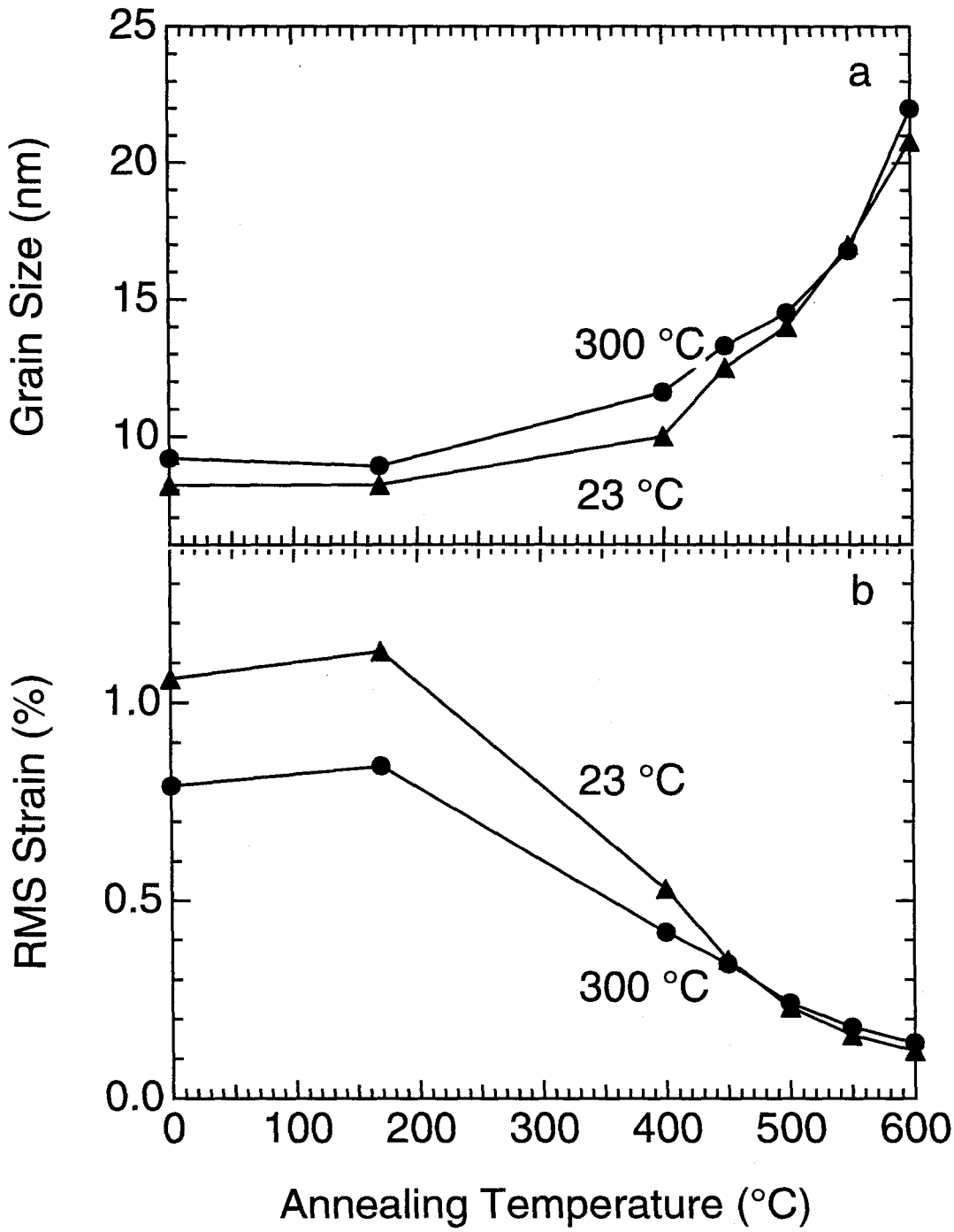

FIG. 6.7. (a) Average grain size, and (b) Root-mean-squared (RMS) strain of Fe_3Si ball milled at 23 °C or 300 °C (labels) for 48 h and annealed at a heating rate of 20 °C per minute up to a maximum temperature given on the x-axis.

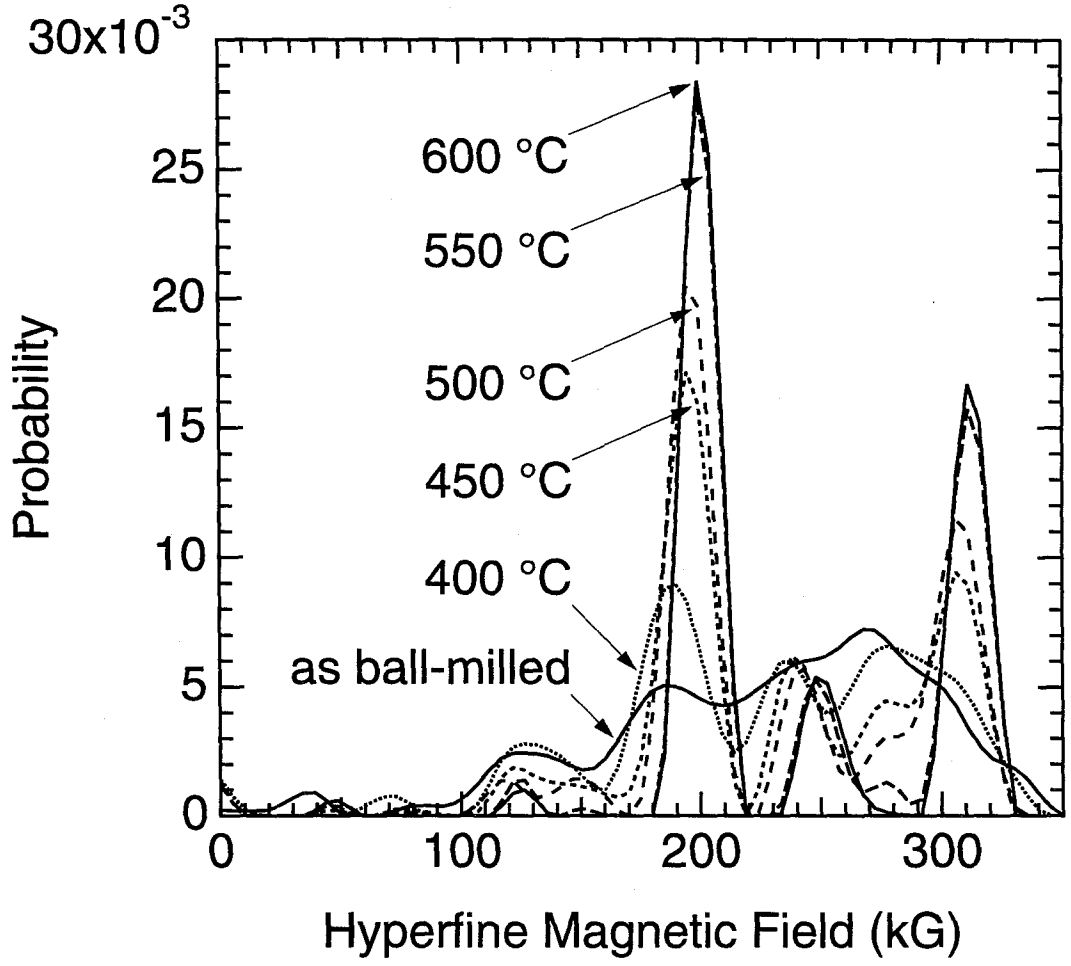

FIG. 6.8. Hyperfine magnetic field distributions of Fe_3Si ball milled at 300 °C for 48 hours and annealed at a rate of 20 °C per minute up to the indicated temperatures. The peaks at about 200 KG and 310 KG signify DO_3 order of an Fe_3X alloy.

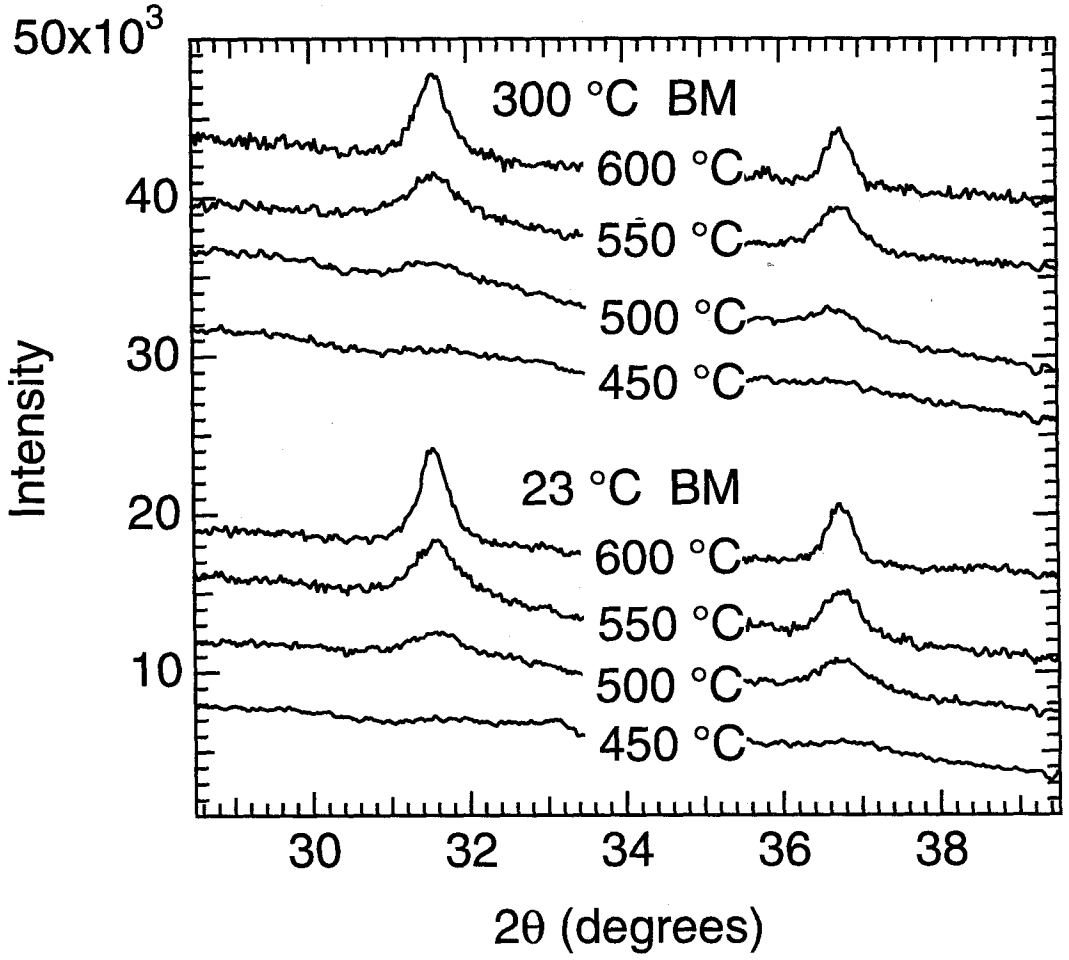

FIG. 6.9. X-ray diffraction patterns of Fe_3Si ball milled at 300 °C for 48 hours and annealed at a rate of 20 °C per minute up to various temperatures. Only $(\frac{1}{2}\frac{1}{2}\frac{1}{2})$ (≈ 31.6 °C) and (100) (≈ 36.7 °C) superlattice peaks (normalized by the fundamental (110) peak intensity) for DO_3 order are shown.

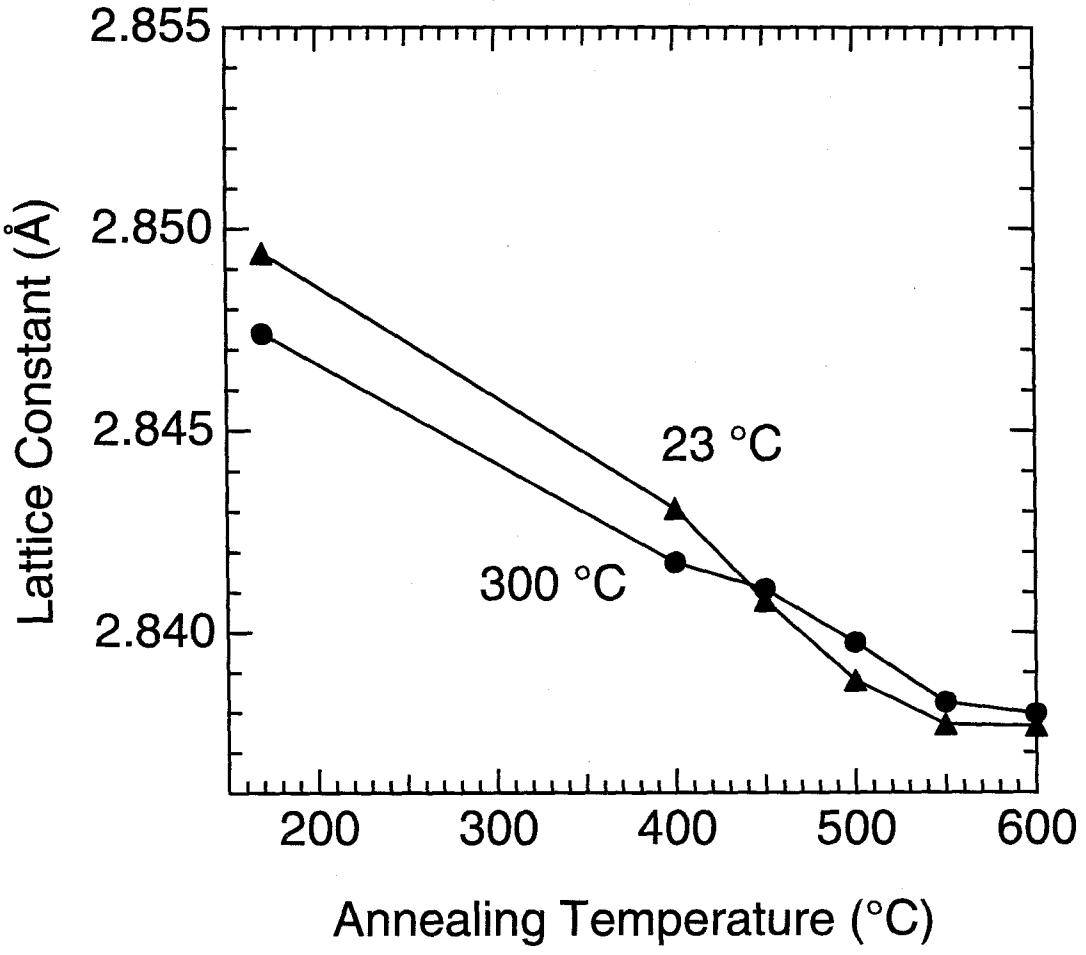

FIG. 6.10. Lattice parameter of Fe_3Si ball milled at 23 °C or 300 °C (labels) for 48 h and annealed at a heating rate of 20 °C per minute up to a maximum temperature given on the x-axis.

diffractometry and Mössbauer spectrometry. The average grain sizes and root-mean-squared strains measured from the x-ray diffraction patterns are presented as functions of the ultimate annealing temperature in Figs. 6.7a and 6.7b, respectively. Substantial grain growth was found only after heating to 400 °C for both samples, while most strain release occurred between 170°C and 500 °C. Both grain growth and strain release contributed to the broad exothermic DSC peak at 465 °C, but there was little difference in the thermal stability against grain growth or strain release between samples ball milled at 23 °C or 300 °C.

Both x-ray diffraction patterns and Mössbauer spectra of the annealed samples ball milled at both temperatures showed that substantial DO_3 ordering also occurred between 400 °C and 600 °C, and this also contributed to the DSC peak. One of the Mössbauer spectra is shown in Fig. 1.12, and the hyperfine magnetic field (HMF) distributions extracted from all Mössbauer spectra are shown in Fig. 6.8. The two peaks near 200 kG and 310 kG grew with increasing annealing temperature. They had a ratio close to 2:1 after heating to 600 °C, signifying DO_3 order of Fe_3X alloys. From this HMF distribution, we determined in Section 1.3.3 that the actual chemical composition of this sample was Fe-23.9 at.%. The extra one percent of Fe was due to contamination from the milling tools. At lower temperatures (200 °C, 100 °C, 23 °C, etc.), the amount of Fe contamination is expected to be smaller. The (1/2 1/2 1/2) and (100) superlattice peaks of DO_3 order in Fe_3X alloys were also observed to develop after heating to 450 °C, and are shown in Fig. 6.9. They grew with increasing annealing temperature, and reached an intensity ratio (after appropriate corrections described in Section 1.3.1) close to 2:1 at 600 °C. (However, the intensity ratios were quite different from 2:1 for other temperatures, especially 500 °C and 550 °C, indicating partial B2-like DO_3 order at these temperatures. It is a transient state as it quickly gave way to perfect DO_3 order with 2:1 peak intensity ratio upon heating to 600 °C. See Chapter 2 for more information on transient states, and Chapter 7 for another

experimental example of transient state of order) Consistent with DO_3 ordering as well as strain release, the lattice parameters measured from x-ray diffraction patterns also decreased substantially after heating in the DSC to temperatures between 170 °C and 550 °C, as shown in Fig. 6.10. None of grain growth, strain release, DO_3 ordering, or decrease of lattice parameters show any obvious difference between Fe_3Si ball milled at 23 °C and 300 °C. That is, the temperature of milling had little effect on the thermal stability of as-milled Fe_3Si samples.

We found many similarities in the results of elevated temperature ball milling of Ni_3Fe, Fe_3Zn, Fe_3Si, and Fe_3Sn. X-ray diffractometry, transmission electron microscopy, and Mössbauer spectrometry all showed no difference except grain size and strain among alloys ball milled at different temperatures. A strong exothermic peak was found in all DSC traces, although it was weaker in the case of Ni_3Fe. For all alloys we confirmed by x-ray diffractometry (from materials run to temperatures below and above the exotherm) that this exotherm marked the simultaneous occurrence of grain growth, strain release, and the development of the equilibrium phases listed in Table 6.1. The temperatures of the exotherms were nearly identical for materials milled at either 23 °C or 300 °C, and these temperatures are listed in Table 6.1. For all alloys studied here, the grain size after ball milling for 48 h was larger for materials milled at the higher temperatures. The average grain sizes as functions of ball milling temperature are shown in Fig. 6.11. It was also found that the root-mean-squared strain was always smaller after high temperature milling, consistent with previous work [22-25]. We expect that the role of temperature during milling is to increase atomic diffusivity, which promotes both grain growth and strain relaxation. The systematics is not simple, however, since the low temperature DSC exotherms of Fe_3Sn and Fe_3Zn indicate high atom mobilities at low temperatures, but these two alloys are relatively stable against grain growth during high temperature milling.

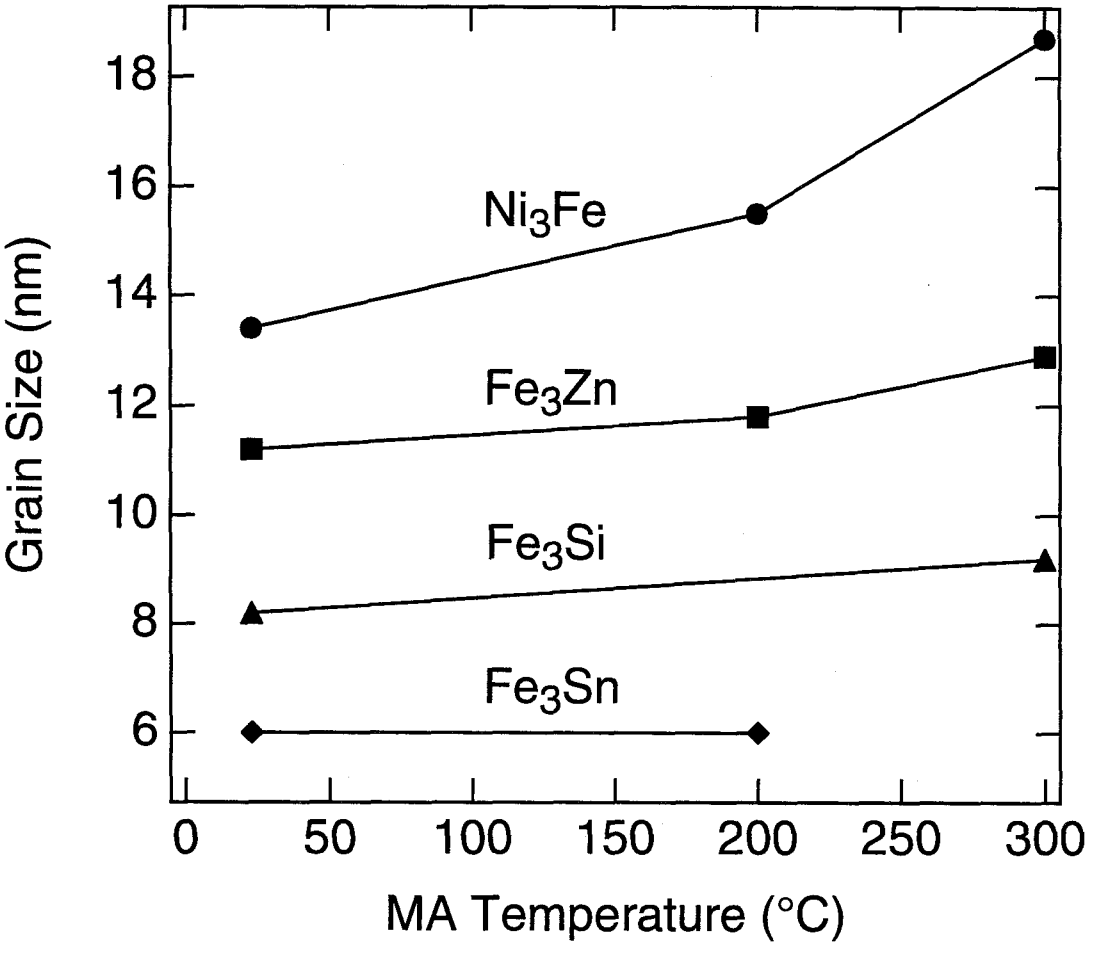

FIG. 6.11. Average grain sizes as functions of ball milling temperature for Ni_3Fe and Fe_3X (X = Si, Zn, Sn) nanocrystalline alloys

Among the alloys listed in Table 6.1, there are distinct differences in the effect of milling temperature on the as-milled grain size. There was slight increase of grain size with ball milling temperature for most of the alloys. We tentatively choose to parameterize the sensitivity of grain size to milling temperature by using the difference in curvature of the grains in samples milled at 23 °C and 300 °C. We define a temperature sensitivity parameter, $\Delta\kappa$, as:

$$\Delta\kappa \equiv \frac{1}{d_{RT}} - \frac{1}{d_{HT}} \quad , \tag{6.1}$$

where $1/d_{RT}$ is an averaged grain curvature of the alloy milled at 23 °C (d_{RT} is the grain size), and $1/d_{HT}$ is an averaged grain curvature of the alloy milled at 300 °C. There is nothing fundamental about the choice of 23 °C and 300 °C for determining the effect of temperature on grain growth, and our definition of $\Delta\kappa$ was determined largely by our ability to perform systematic experiments.

For the alloys in the present study, we found that the temperature sensitivity parameter, $\Delta\kappa$, correlated rather well with the difference in metallic radius of the two components in the alloy, $|r_{Fe} - r_X|$. Both $\Delta\kappa$ and $|r_{Fe} - r_X|$ are listed in the right-hand columns of Table 6.1.* The temperature sensitivity parameter, $\Delta\kappa$, decreases with the difference in metallic radius. It seems that for alloys with larger differences in metallic radius, the thermal tendencies for grain growth become less effective in competing with the grain reduction that is driven by milling. In a pair of "unsuccessful" experiments, we found that when the difference in metallic radius is even larger, it was impossible to make an alloy of the two components (Fe_3In) or the resulting alloy was amorphous (Fe_3Hf). We noticed that the previous results on Ti-Cu and Zr-Al do not agree with the trend reported here. We tried to repeat the Zr-Al experiment but had little success due to various problems such as adherence of materials to the milling tools.

---

* For our three bcc alloys, the root-mean-squared strain also correlates with the difference in metallic radius.

6.4 Summary

Ball milling of Ni_3Fe and Fe_3X (X = Si, Zn, Sn) was performed at temperatures from 23 °C to 300 °C. In all alloys, the root-mean-squared strain in the material was lower for the materials milled at higher temperatures. In the alloys studied in the present work, the grain size was larger for materials milled at higher temperatures. Perhaps surprisingly, it was found that the different milling temperatures had no effect on the subsequent thermal stability of the materials against grain growth, strain release, and equilibrium phase formation, which occurred nearly simultaneously when the materials were heated to temperatures of 350 to 550 °C. For the different alloys, however, their as-milled grain sizes had different sensitivities to the milling temperature. The temperature sensitivity seems to decrease for larger differences in the metallic radii of the elements in the alloy.

References

1. L. B. Hong, C. Bansal, and B. Fultz, Nanostructured Materials **4**, 949 (1994).
2. C. C. Koch, O. B. Cavin, C. G. McKamey, and J. O. Scarbrough, Appl. Phys. Lett. **43**, 1017 (1983).
3. R. B. Schwarz, R. R. Petrich, and C. K. Saw, J. Non-Cryst. Solids **76**, 281 (1985).
4. E. Hellstern and L. Schultz, Appl. Phys. Lett. **48**, 124 (1986).
5. R. B. Schwarz, Mater. Sci. Eng. **97**, 71 (1988)
6. K. Suzuki, J. Non-Cryst. Sol. **112**, 23 (1989)
7. L. Schultz, Phil. Mag. B **61**, 453 (1990)
8. A. R. Yavari and P. Desré, Mater. Sci. Eng. **A134**, 1315 (1991)
9. M. A. Morris and D. G. Morris, J. Mater. Sci. **26**, 4687 (1991)
10. Y. Chen, M. Bibole, R. Le Hazif and G. Martin, Phys. Rev. B **48**, 14 (1993)
11. Y. Chakk, S. Berger, B. Z. Weiss and E. Brook-Levinson, Acta metall. mater. **42**, 3679 (1994)
12. M. Abdellaoui and E. Gaffet, J. All. Comp. **209**, 351 (1994)
13. E. Hellstern, H. J. Fecht, Z. Fu, and W. L .Johnson, J. Mater. Res. **4**, 1292 (1989)
14. H. J. Fecht, E. Hellstern, Z. Fu, and W. L .Johnson, Adv. Powder Metall. **1-2**, 111 (1989)
15. B. Fultz, G. LeCaër, and P. Matteazzi, J. Mater. Res. **4**, 1450 (1989)
16. H. J. Fecht, E. Hellstern, Z. Fu, and W. L .Johnson, Metall. Trans. **21A**, 2333 (1990)
17. E. Hellstern, H. J. Fecht, Z. Fu and W. L. Johnson, J. Appl. Phys. **65**, 305 (1989).
18. H. J. Fecht, G. Han, Z. Fu and W. L. Johnson, J. Appl. Phys. **67**, 1774 (1990).
19. H. Kuwano, H. Ouyang and B. Fultz, Nanostructured Materials **1**, 143 (1992).

20 J. Eckert, J. C. Holzer, C. E. Krill III, and W. L. Johnson, J. Mater. Res. **7**, 1980 (1992); J. Appl. Phys. **73**, 2794 (1993); **131** (1993)..

21. Z. Q. Gao and B. Fultz, Nanostructured Materials **2**, 231 (1993).

22. Z. Fu and W. L. Johnson, Nanostructured Materials **3**, 175 (1993).

23. Z. Fu, Ph. D. dissertation, California Institute of Technology, 1993.

24. Y. R. Abe and W. L. Johnson, J. Jpn. Soc. Powder and Powder Metall **40**, 272 (1993).

25. Y. R. Abe, Ph. D. dissertation, California Institute of Technology, 1993.

26. K. Yamada and C. C. Koch, J. Mater. Res. **8**, 1317 (1993).

27. B. Fultz, Chapter 1 in Mössbauer Spectroscopy Applied to Magnetism and Materials Science Vol. I, G. J. Long and Fernande Grandjean, eds., (Plenum Press, New York, 1993) pp. 1-31.

28. A. Laggoun, A. Hauet, and J. Teillet, Hyperfine Interact. **54**, 825 (1990).

29. A. Hauet, A. Laggoun, and J. Teillet, Mater. Sci. Eng. A **148**, 123 (1991).

Chapter 7. Extended Solid Solubility in Ball Milled Fe_3X (X = Al, As, Ge, In, Sb, Si, Sn, Zn) Nanocrystalline Alloys

7.1 Introduction

It is well-established that high energy ball milling can be used to synthesize alloy phases with extended solid solubilities. References [1-14], for example, include reports of extended solid solubilities, although solubility was not always the main topic of study. A systematic study of extended solid solubility promoted by mechanical alloying is best performed with similar solutes under identical experimental conditions. This chapter is such a study of extended solubility in bcc Fe of the main group (IIB, IIIB, IVB, and VB) solutes Al, As, Ge, In, Sb, Si, Sn, Zn [15]. X-ray diffractometry was our main technique for determining if the as-milled alloys were bcc, ordered bcc, or if they comprised a mixture of equilibrium compounds. Mössbauer spectrometry was employed and proved useful for obtaining information on local chemistry and short-range order in the bcc phase.

We show that the systematics of phase formation in the as-milled phases can be explained with the first two Hume-Rothery rules [26-28]. We implement these two rules with a Darken-Gurry plot of electronegativity versus metallic radius [28,29]. Mechanical alloying extends the compositional range of bcc solid solubility from the typical 5% for alloys in thermodynamic equilibrium, to 25% in the as-milled nanocrystalline alloys of the present study. Annealing of the as-milled Fe_3Ge and Fe_3Sn leads to transient appearance of DO_3 order and B2 order before the alloys develop equilibrium phases. The transient ordered phase found in annealed Fe_3Ge was much more stable than that in Fe_3Sn, perhaps because of the better match of the metallic radii between Fe and Ge.

There has been recent interest in transient phase formation during the thermal annealing of nonequilibrium alloys. When the transient states occur far from

thermodynamic equilibrium, transient state formation is best understood by kinetic, rather than thermodynamic arguments [16-20, Chapter 4]. In cases where the equilibrium phases form by nucleation and growth, however, thermodynamic explanations with an assumption of suppressed nucleation may be appropriate [21-23]. We have been studying experimentally the kinetic transients in ordered phases [24], including powders prepared by mechanical alloying [25]. Here transient order in Fe_3Ge and Fe_3Sn was observed upon annealing. We interpret the transient states of DO_3 and B2 order as an expedient mechanism to reduce free energy before the formation of the equilibrium phases.

7.2 Experimental Results

In our study of extended solid solubility in this chapter, Fe contamination was a concern. Chemical compositions and micron-scale chemical homogeneities were checked using a JEOL Superprobe 733 electron microprobe. Iron contamination from the milling media was significant only for the Fe_3Si alloys, which gained about 2 at.% Fe. This is a little bit more that the 1 at.% Fe gained in the temperature-dependent ball milling experiments presented in last chapter, perhaps due to the much higher ball milling intensity in the study.

X-ray diffraction patterns from the as-milled alloys prepared in this work are presented in Fig. 7.1. The as-milled alloys of Fe_3Al, Fe_3Ge, Fe_3Si, Fe_3Zn were almost entirely the bcc phase. The alloys of Fe_3As and Fe_3Sb contained some bcc phase, although with the presence of a second phase we cannot be sure that the stoichiometry of the bcc phase was Fe_3X. In the last chapter, we decided results of a study on bcc Fe_3Zn nanocrystalline alloys obtained by high and room temperature ball milling [13, Chapter 6].

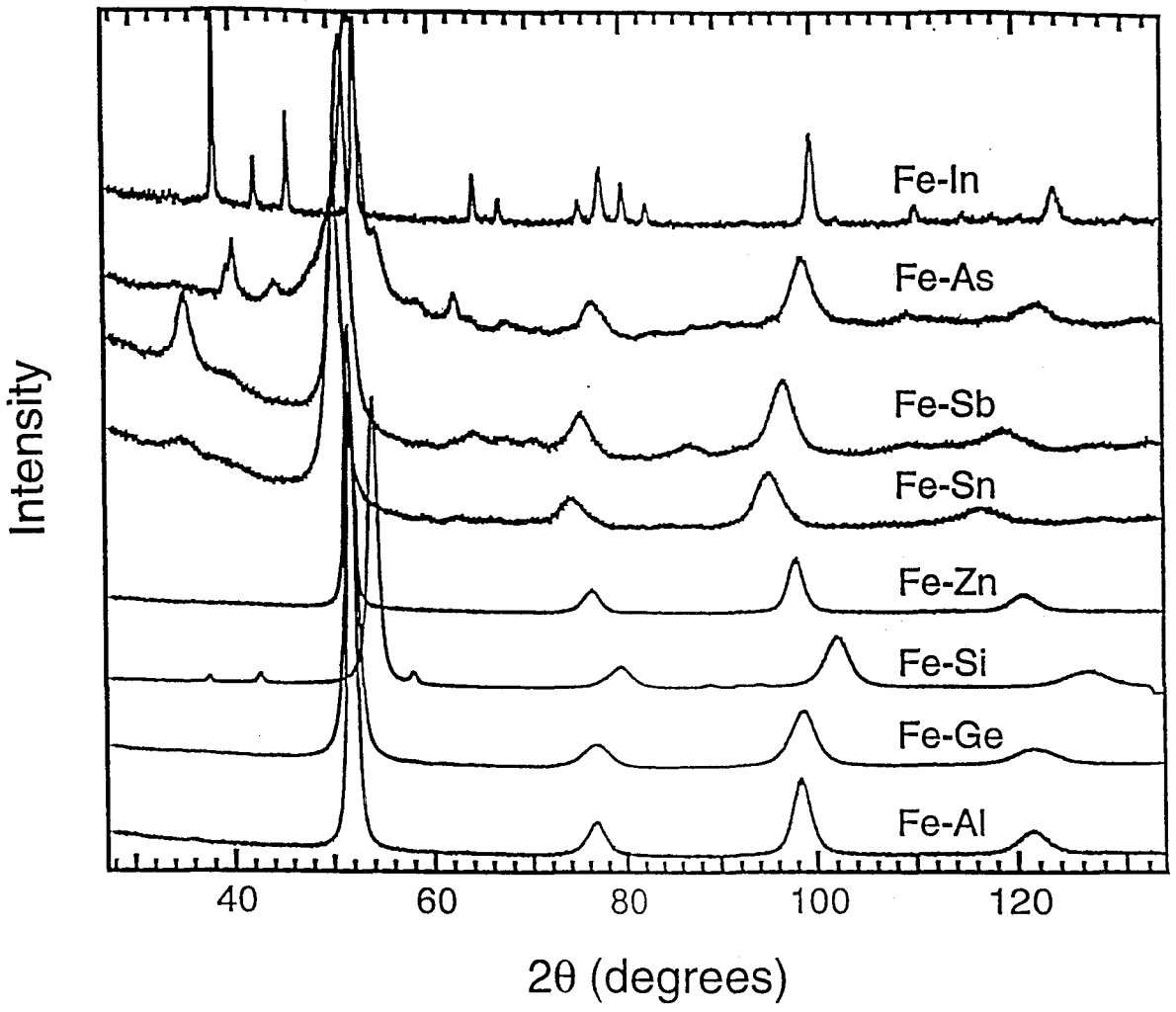

FIG. 7.1. X-ray diffraction patterns from as-milled powders of Fe-X powders mixed in 3:1 stoichiometry. Milling time in the Spex mill was 24 hours, except for Fe-Ge (16h) and Fe-As (50 h). The Fe-Si powders were milled in tungsten carbide vials, so small peaks from the milling media are seen.

TABLE 7.1. X-Ray Measurements on bcc Phase of As-Milled Powders

Alloy	lattice constant (nm)	grain size (nm)	strain
Fe_3Al	0.291	11.7	0.70%
Fe_3As	0.290	8.4	1.02%
Fe_3Sb	0.295	6.0	0.80 %
Fe_3Sn	0.298	6.0	0.78 %
Fe_3Zn	0.292	13.3	0.62 %
Fe_3Si	0.285	9.6	1.10%
Fe_3Ge	0.290	8.4	1.10%

We note also that bcc Fe-Zn alloys prepared by sputtering [30] and cathodic pulverization [31] were reported previously, and these authors report some tendency for Zn clustering in more concentrated alloys.

Table 7.1 presents results from the analysis of x-ray diffraction peaks from the bcc phases. The lattice parameters were obtained by the Nelson-Riley extrapolation method with the (110), (200), (211), and (220) diffractions. The grain sizes in Table 7.1 were obtained by a Scherrer analysis of the (110) diffraction peaks, and the root-mean-squared strains from the (110), (200), (211), and (220) diffractions by the method of Williamson and Hall (Section 1.3.1). From Table 7.1, all the bcc phases are nanocrystalline alloys.

In as-milled Fe_3As and Fe_3Sb, the B8 (NiAs) intermetallic phase was found along with the bcc phase. In spite of our best efforts, the Fe-In powders did not form an alloy. Although there were problems with adhesion of In to the walls of the vial, the experimental configuration should have allowed for some alloying of the Fe and In powders. We also milled Fe-In with surfactants such as hexane, but again no alloy was formed. We note that Fe-Sb alloys prepared by sputtering were found to be amorphous [32,33].

Figure 7.2 shows x-ray diffraction patterns for Fe_3Sn in the as-milled condition, and after annealing. A bcc phase is not the equilibrium phase according to the phase diagram [34], which shows a two-phase region below 600 °C and a hexagonal phase intermetallic compound at higher temperatures (750-880 °C). Nasu et al. [35] used Mössbauer spectrometry to infer the formation of a bcc Fe-Sn solid solution by mechanical alloying. The presence of B2 order has been reported in splat-quenched Fe_3Sn [36].

Besides the fundamental diffractions of the disordered bcc phase, the x-ray diffraction pattern of Fe_3Sn had a (100) superlattice diffraction characteristic of B2 order at $2\theta = 35°$. We were concerned that this diffraction could have originated from another intermetallic phase, however. The hexagonal B8 (NiAs) structure is such a candidate,

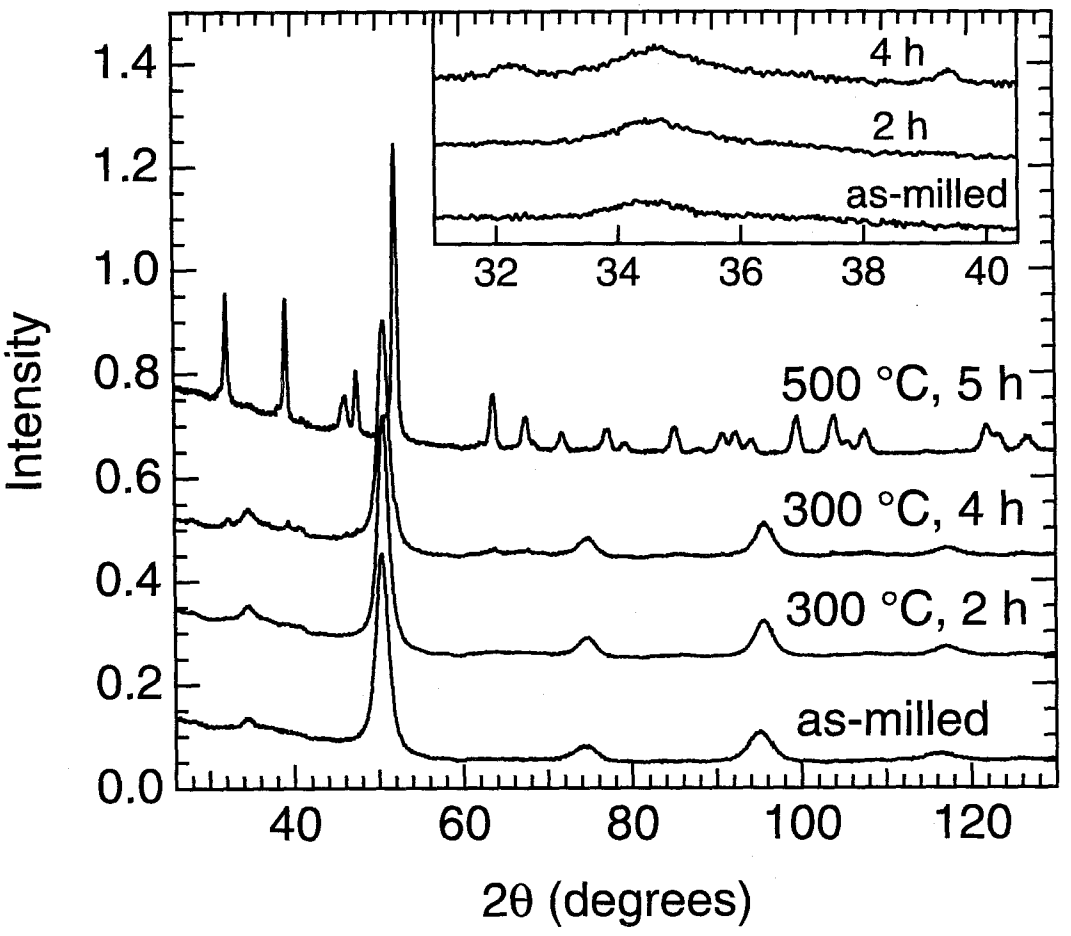

FIG. 7.2. X-ray diffraction patterns from Fe_3Sn powder in the as-milled state, after annealing at 300 °C for 2 h, after annealing at 300 °C for 4 hours, and after annealing at 500 °C for 5 hours. Inset is an enlargement of the region near the (100) superlattice diffraction of the three lower diffraction patterns.

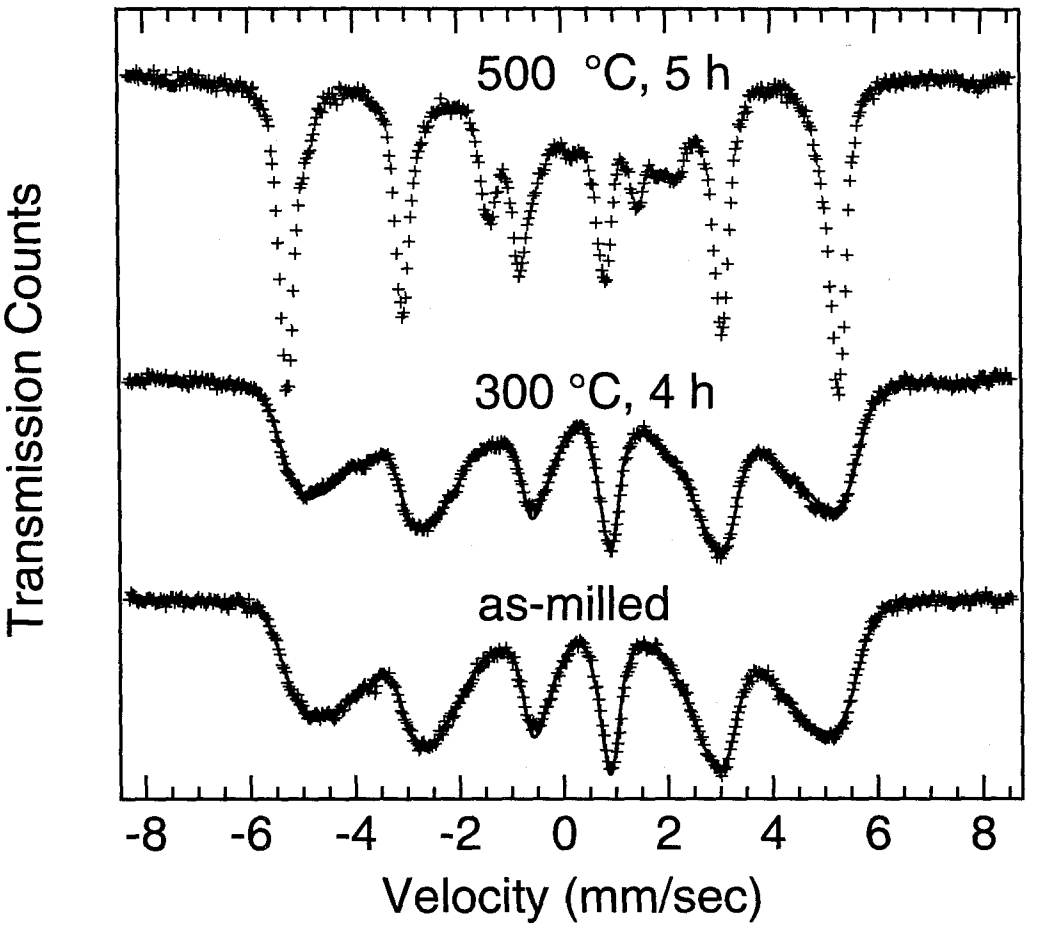

FIG. 7.3. Mössbauer spectra from Fe_3Sn powder in the as-milled state, after annealing at 300 °C for 4 hours, and after annealing at 500 °C for 5 hours.

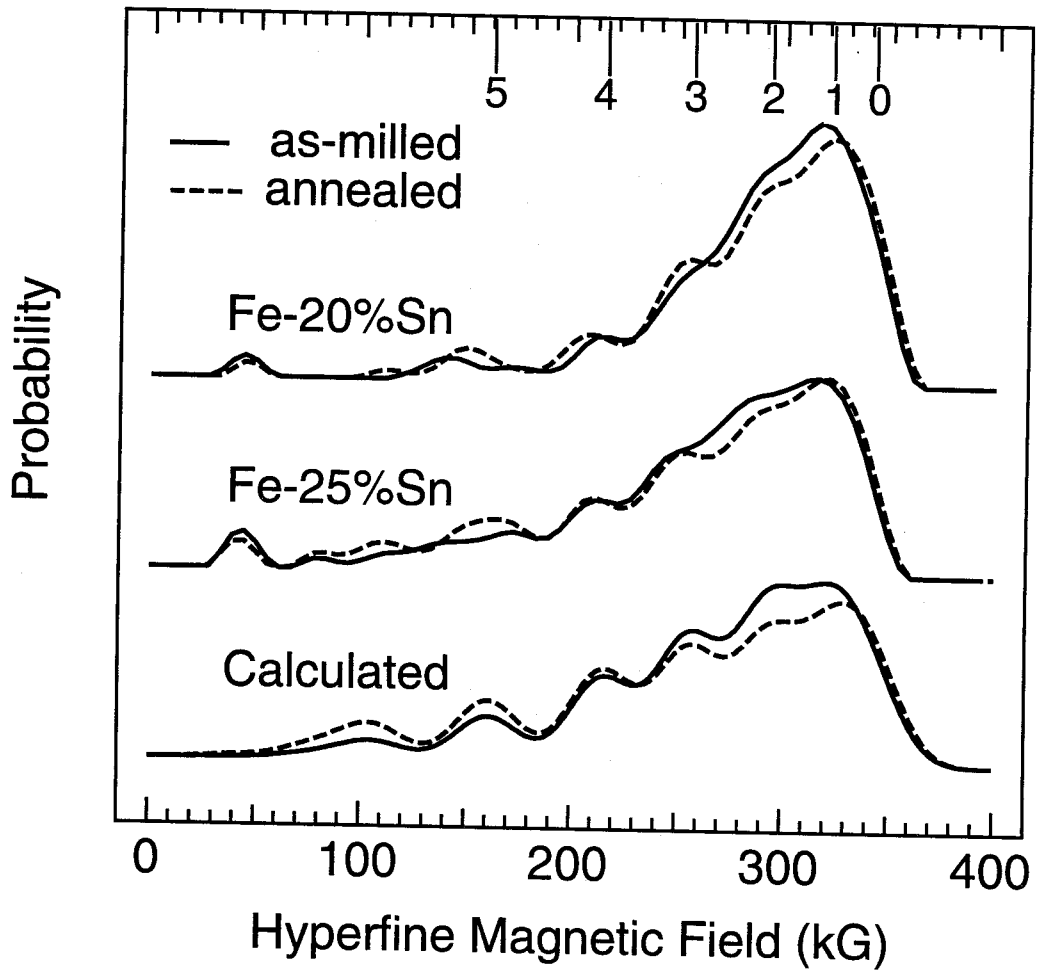

FIG. 7.4. Hyperfine magnetic field (HMF) distributions (probability of HMF). Top two pairs of distributions are from experimental data such as shown in Fig. 7.2. Top pair is from $Fe_{80}Sn_{20}$ alloy in its as-milled state (solid curve), and after annealing at 300 °C for 20 hours (dashed curve). Middle pair is from $Fe_{75}Sn_{25}$ alloy in its as-milled state (solid curve) and after annealing at 300 °C for 4 hours (dashed curve). Lower pair was calculated as described in the text for states of partial B2 order determined from x-ray diffractometry: L=0.36 (solid curve), and L=0.49 (dashed curve).

although with increasing transition metal concentration this structure goes continuously to the $B8_2$ (Ni_2In type) [26]. The γ phase of composition $Fe_{13}Sn_{10}$ has this $B8_2$ structure [37]. In the present work we used mechanical alloying to prepare an alloy of $Fe_{13}Sn_{10}$ stoichiometry, and we found a $B8_2$ (Ni_2In type) structure for the as-milled alloy. Although the (101) diffraction for the $B8_2$ structure coincides with the (100) reflection of the B2 structure, other diffractions of the $B8_2$ structure were not observed in the as-milled Fe_3Sn. We are confident that the observed diffraction pattern of the as-milled Fe_3Sn indicated B2 order in the alloy. The same result was obtained on ball milling of Fe_3Sn at elevated temperatures as described in Chapter 6. As-milled $Fe_{80}Sn_{20}$ and $Fe_{85}Sn_{15}$ also had diffraction patterns characteristic of a B2 structure, but their (100) diffractions were weaker. We also believe that there is some B2 order in the bcc phase of the as-milled Fe-Sb alloy, since the peak at $2\theta = 35°$ is so much stronger than expected from the B8 phase alone.

The amount of B2 order in Fe_3Sn increased upon annealing at low temperatures, as shown in the inset of Fig. 7.2. The intensity of the (100) superlattice peak increases from 3.9 percent of the fundamental (110) peak for the as-milled sample, to 6.5 percent after annealing at 300 °C for two hours. By calculating the intensities of (100) superlattice diffractions for various degrees of order in the Fe_3Sn (including multiplicity, Lorentz-polarization, and form factor corrections [38]), we found this change corresponded to an increase in the Bragg-Williams LRO parameter, L, from 0.35 to nearly 0.50 (where 0.50 is the highest possible degree of order for the Fe_3Sn stoichiometry). Upon further annealing there is the growth of the equilibrium hexagonal B35 FeSn phase plus bcc α-Fe, as seen by the new diffraction peaks from the sample annealed for 4 hours. The diffraction pattern for a sample annealed at 500 °C for 5 hours (Fig. 7.2) shows the final phase separation into α-Fe and B35 FeSn, consistent with the phase diagram [34].

The presence of B2 order in the as-milled material, and its increase upon annealing, was also confirmed by measurements of Mössbauer spectra and HMF distributions (Figs. 7.3 and 7.4). A nonmagnetic solute atom such as Sn will reduce the HMF at a neighboring ^{57}Fe atom, and the HMF distribution can be used to obtain the distribution of solute neighbors about ^{57}Fe atoms [39]. Such assignments of peaks in the HMF distribution to ^{57}Fe atoms with different numbers of first-neighbor solute atoms were shown to be very similar for the alloys Fe_3Al, Fe_3Si, Fe_3Ge, and Fe_3Ga [40]. We make similar assignments here for Fe_3Sn, since the ^{57}Fe HMF perturbations caused by Sn neighbors are expected to be like those of other non-magnetic solutes [39]. Our assignments are shown as numbers at the top of Fig. 7.4. To help check these assignments, and to interpret the changes in these solute neighborhoods upon B2 ordering, a Monte Carlo simulation was performed as described in Chapter 2. The only difference from Chapter 2 and Chapter 4 is that we simulated an AB_3 alloy (instead of an AB alloy) of 65,536 atoms with first neighbor pair potentials of $V_{AA} = V_{BB} = 1.5$ kT and $V_{AB} = 0$. For simulated alloys having values of L = 0.36 and 0.49, we determined the distribution of the number of A-atoms in the first nearest neighbor shell of the B-atoms by finding all B-atoms and counting their neighbors. Simulated HMF distributions were then obtained by superposing Gaussian functions centered at the HMFs determined experimentally for each of the nine possible nearest neighbor configurations (B atoms with 0 to 8 A-neighbors), but with amplitudes determined from these computed nearest neighbor distributions. These simulated HMF distributions are presented as the lower pair of curves in Fig. 7.4. They should correspond approximately to the top two pairs of curves in Fig. 7.4, which are the experimentally determined HMF distributions for $Fe_{75}Sn_{25}$ and $Fe_{80}Sn_{20}$ as-milled, and after annealing at 300 °C for 2 h. There is good qualitative agreement between the simulated and experimental HMF distributions. In both the simulated and the experimental HMF distributions, the probabilities of Fe atoms having 1 or 2 solute neighbors decrease upon

B2 ordering, whereas the probabilities increase for Fe atoms having 4, 5 or 6 solute neighbors. We tried to perform a more detailed analysis in which we assumed that the Sn concentration in the alloy was inhomogeneous with Sn-rich and Sn-poor regions in the bcc phase. These assumptions did improve the agreement between the calculated and the experimental HMF distributions, but we are not confident that the systematics of the HMF distributions in concentrated Fe-Sn alloys are sufficiently well understood to justify such detailed interpretations.

7.3 Extended Solid Solubility

The most important Hume-Rothery rule for solid solubility is the size factor rule [27], which states that good solubility (5 at.% at modest temperatures) requires that the metallic radii of the solute atom and matrix atom differ by less than 15 %. Figure 7.6 shows the metallic radii [26,43] of the solutes in the present study. Approximate boundaries are drawn to show the phases of our as-milled Fe_3X alloys. These phases correlate reasonably well to the metallic radius of the solute atom, although the as-milled Fe_3As did contain a significant amount of intermetallic second phase. The 15% rule seems reasonably successful for the alloys in the present study prepared by ball milling, although here we are considering a much larger solubility, 25%, than the 5% that is typically used to define good solubility.

The second Hume-Rothery rule states that for good solubility, the electronegativity difference between the two elements should not be too large, typically within a range of ±0.4. This second rule was combined with the first rule by Darken and Gurry [28,29] in constructions such as that of Fig. 7.7. Figure 7.7 is a parametric plot of the Pauling electronegativity [44] versus the metallic radius [26,43]. The ellipse on the plot, centered about Fe, spans a horizontal range in metallic radius of ±15%, and a vertical range in

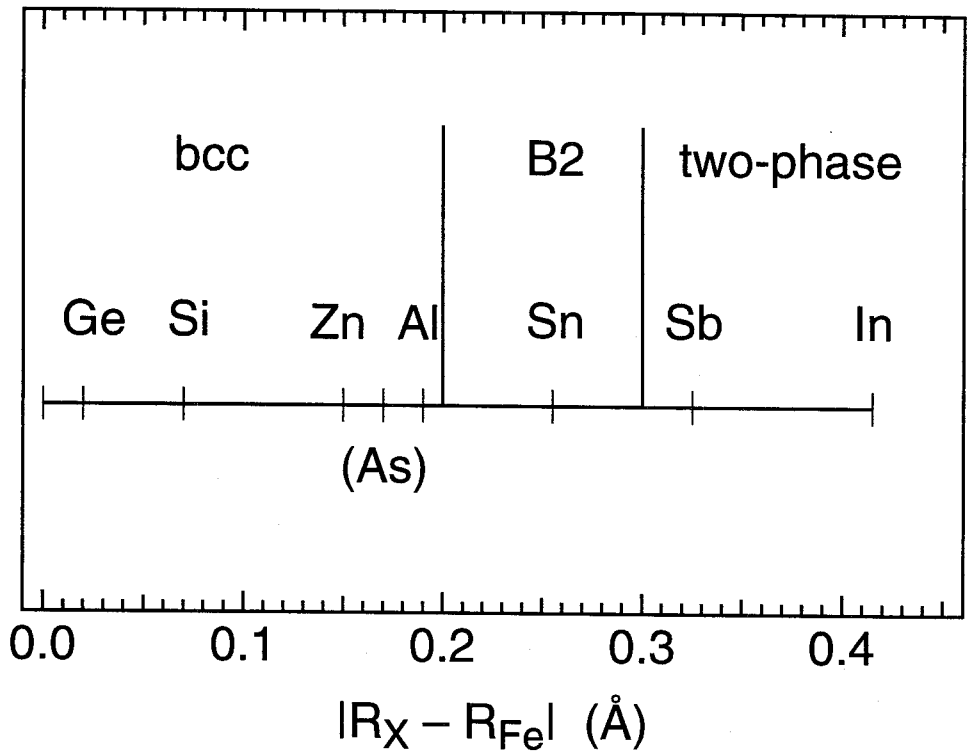

FIG. 7.5. Difference between the metallic radius of Fe and the radii of the solutes used in the present study, with approximate boundaries of the as-milled phases.

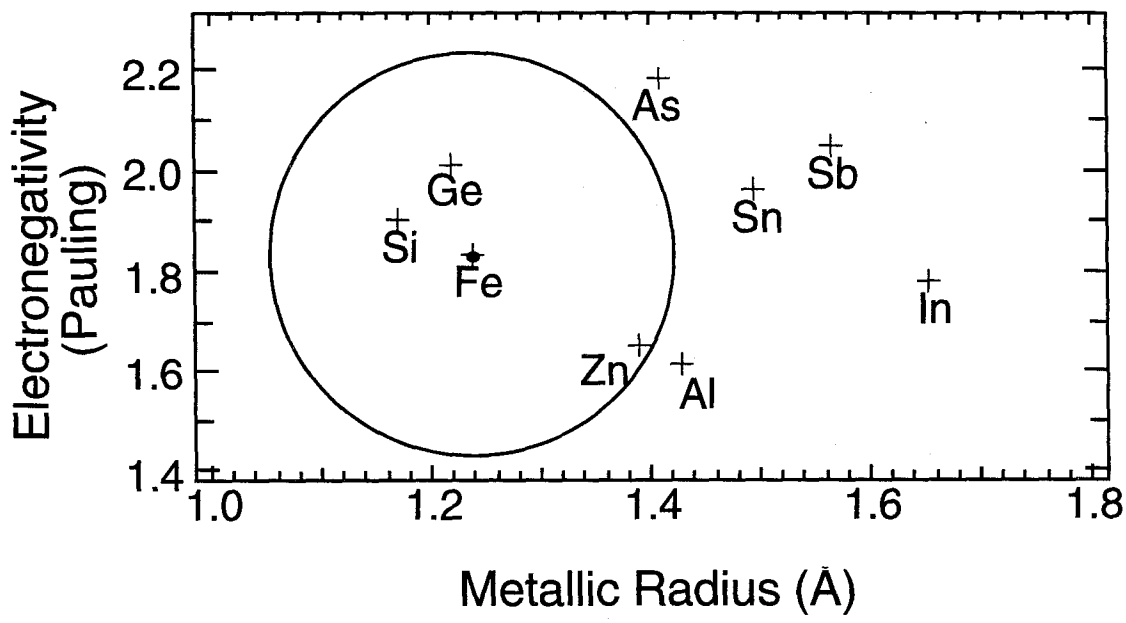

FIG. 7.6. Darken-Gurry plot for various solutes in Fe. Ellipse was drawn around Fe with a range in electronegativity of ±0.4, and a range of ±15% in metallic radius.

electronegativity of ±0.4. (For the present plot, we scaled the axes so that the ellipse became a circle.) In the present study we found that all Fe_3X alloys containing solutes inside the ellipse were bcc solid solutions after milling. Alloys of Al and As are near the edge of the ellipse, but Fe_3Al was a bcc solid solution after milling, whereas Fe_3As included a significant amount of B8 phase. It is interesting that both the electronegativity axis and the size axis of the ellipse, which are useful for predicting 5% thermodynamic solubility, are reasonable axes for predicting 25% solubility in alloys prepared with a Spex mill.

The small crystallite sizes of the alloys (Table 7.1), could promote a grain boundary segregation of solute atoms. Our x-ray diffractometry measurements were not sensitive to such grain boundary segregation, but the ^{57}Fe Mössbauer spectra are sensitive to changes in local solute concentrations in the bcc phase. The problem is how to obtain an accurate solute concentration in the bcc phase from the measured ^{57}Fe HMF distributions. Such interpretations are well-established for the solutes Al, Ge, and Si [40]. There was no indication of any strong loss of these solutes from the bcc phase, although the loss of a few percent is certainly possible. The analysis of Fe_3Sn, as shown in Fig. 7.4, was also accomplished successfully by assuming a solute concentration of 25 %. The HMF distribution of Fe_3Zn certainly did show a loss of Zn from the neighborhoods of ^{57}Fe atoms, and this could be caused by the segregation of Zn atoms to grain boundaries (or a segregation of Zn atoms within the bcc grains). The Mössbauer spectra from the two-phase alloys Fe_3As and Fe_3Sb were less easy to interpret, but the narrowness of their HMF distributions at high fields implies some solute loss from the bcc phase. This implies a chemical heterogeneity in these alloys, which in turn could be related to the formation of the B8 intermetallic phase.

7.4 Transient Ordering in Fe_3Ge and Fe_3Sn upon Annealing

The as-milled Fe_3Ge was single-phase bcc. Upon annealing at 350 °C, the formation of transient $D0_3$ order was observed. This is seen clearly in the x-ray diffraction patterns presented in Fig. 7.5a, where the formation of the superlattice peaks of the (1/2 1/2 1/2) and (100) families indicate that a high degree of $D0_3$ order had formed after annealing. The $D0_3$ ordered structure is shown in Fig. 7.5b. There was no formation of the equilibrium phases in this material after annealing at 350 °C for 4 h or 300 °C for 24 h, although the equilibrium phases were found after annealing at 500 °C for 1 h. Mössbauer spectra of the annealed Fe_3Ge (at 350 °C) were consistent with the evolution of chemical environments characteristic of the $D0_3$ structure, as reported previously for sputtered films of bcc Fe_3Ge [41,42].

The B2 structure was found in as-milled Fe_3Sn. We suspect that the bcc phases in Fe_3As and Fe_3Sb also have partial B2 order, but interpretations of the x-ray and Mössbauer data were impaired by the contributions from the B8 phase in these alloys. The B2 structure comprises two interpenetrating simple cubic lattices, which provide for good packing of large and small atoms. Although the B2 structure is not an equilibrium phase for Fe-Sn, the large size difference between Fe and Sn atoms may promote B2 order in as-milled Fe_3Sn. We suggest that the lower symmetry equilibrium $B8_2$ and B35 phases of Fe-Sn develop a high defect enthalpy during milling, and are destabilized with respect to the higher symmetry B2 structure. We note that the B2 structure is an equilibrium high temperature phase for Fe_3Al and Fe_3Si, although ball milling disorders these alloys into the bcc phase.

When the as-milled Fe_3Sn powder is annealed at 300 °C, there is the eventual formation of a two-phase microstructure of bcc α-Fe plus hexagonal B35 FeSn. In the early stages of thermal annealing, however, the imperfect B2 structure of the as-milled

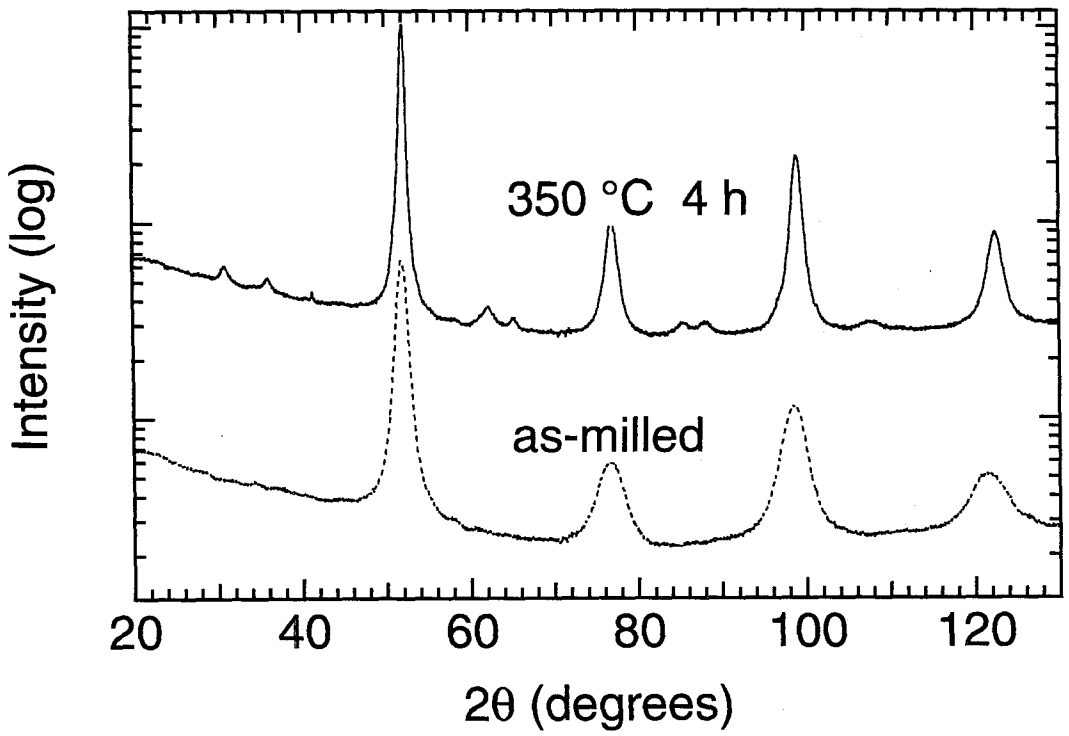

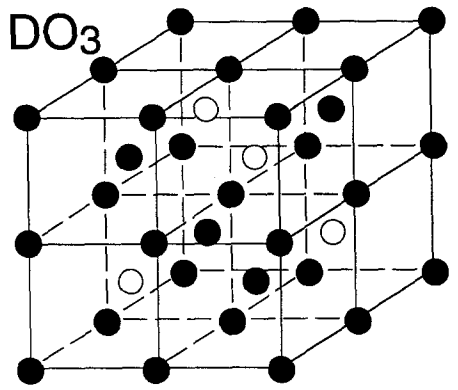

FIG. 7.7. (a) (top) X-ray diffraction patterns from Fe_3Ge alloys as-milled for 24 h, and after the as-milled powder was annealed for 4 h at 350 °C. (b) (bottom) The DO_3 ordered structure.

powder becomes more ordered, eventually achieving nearly perfect order for the Fe_3Sn stoichiometry. This transient ordering may occur for the same reasons that have been discussed theoretically [16-23]. The growth of B2 order should allow for some free energy reduction in the alloy. The formation of equilibrium phases would reduce the free energy by an even greater amount, but this requires many more atom movements to form critical nuclei and allow them to grow. It may be kinetically expedient, therefore, for the alloy to develop a transient state of B2 order before the equilibrium phases are formed. The same argument applies to the formation of transient DO_3 order in Fe_3Ge. The DO_3 structure in Fe_3Ge was more stable against the formation of equilibrium phases than was the B2 structure in Fe_3Sn. We note that the distance on the Darken-Gurry plot (Fig. 7.7) between Fe and Sn is larger than the distance between Fe and Ge. Perhaps there is a tendency of transient phases to be more long-lived when this distance is not so large.

7.5 Summary

We used mechanical alloying to prepare several alloys of the Fe_3X composition, where the solutes, X = Al, As, Ge, In, Sb, Si, Sn, Zn, were all from groups IIB, IIIB, IVB, and VB of the periodic table. The trends in the as-milled phases largely followed the metallic radius of the solute atoms; for solutes with metallic radii increasingly different from that of Fe, a bcc solid solution (Ge, Si, Al, Zn), gives way to B2 order of the bcc Fe alloy (Sn) plus some intermetallic compound formation (As, Sb), and finally no bcc-based Fe alloy was observed for the largest solute (In). Even better predictions of bcc solid solubility were obtained with a modified Darken-Gurry plot of electronegativity versus metallic radius. The Hume-Rothery rules for 5% solubility in equilibrium alloys seem to translate to a 25% solubility for powders prepared by mechanical alloying.

Thermal stabilities of the as-milled bcc Fe_3Ge and B2 Fe_3Sn were tested. Transient $D0_3$ order in Fe_3Ge and transient B2 order in Fe_3Sn evolved before the nucleation of equilibrium intermetallics. The transient $D0_3$ order in Fe_3Ge was much more stable than the transient B2 order in Fe_3Sn, however.

References

1. C. C. Koch and M. S. Kim, J. de Physique C **8**, 573 (1985).
2. E. Hellstern, L. Schultz, R. Bormann, and D. Lee, Appl. Phys. Lett. **53**, 1399 (1988).
3. C. C. Koch, Annual Rev. Mater. Sci. **19**, 121 (1989).
4. E. Hellstern, H. J. Fecht, Z. Fu, and W. L. Johnson, J. Mater. Res. **4**, 1292 (1989).
5. H. J. Fecht, E. Hellstern, Z. Fu, and W. L. Johnson, Adv. Powder Metall. **1-2**, 111 (1989).
6. B. Fultz, G. LeCaër and P. Matteazzi, J. Mater. Res. **4**, 1450 (1989).
7. A. Calka and A. P. Radlinski, Scripta Metall. **23**, 1497 (1989).
8. C. Suryanarayana and F. Froes, J. Mater. Res. **5**, 1880 (1990).
9. C. Suryanarayana and R. Sundaresan, Mater. Sci. Eng. A **131**, 237 (1991).
10. K. Uenishi, K. F. Kobayashi, K. N. Ishihara, and P. H. Shingu, Mater. Sci. Eng. A **134**, 1342 (1991).
11. M. V. Zdujic, K. F. Kobayashi, and P. H. Shingu, J. Mater. Sci. **26**, 5502 (1991).
12. D. K. Mukhopadhyay, C. Suryanarayana, and F. H. Froes, Scripta Metall. Mater. **30**, 133 (1994).
13. L. B. Hong, C. Bansal, and B. Fultz, NanoStructured Materials **4**, 949 (1994).
14. L. B. Hong and B. Fultz, submitted to Acta Metall. Mater., 1995.
15. C. Bansal, Z.Q. Gao, L. B. Hong, and B. Fultz, J. Appl. Phys.**76**, 5961 (1994).
16. L. Anthony and B. Fultz, J. Mater. Res. **4**, 1132 (1989).
17. B. Fultz, Philos. Mag. B **67**, 253 (1993).
18. L. Anthony and B. Fultz, J. Mater. Res. **9**, 348 (1994).
19. L. B. Hong, L. Anthony, and B. Fultz, J. Mater. Res. **10**, 126 (1995).
20. L. B. Hong and B. Fultz, Phys. Rev. B **52**, (1995).
21. W. A. Soffa and D. E. Laughlin, Acta Metall. **37**, 3019 (1989).

22. L.-Q. Chen and A. G. Khachaturyan, Phy. Rev. B **44**, 4681 (1991).

23. L. Reinhard and P. E. A. Turchi, Phys. Rev. Lett. **72**, 121 (1994).

24. Z. Q. Gao and B. Fultz, Philos. Mag. B **67**, 787 (1993).

25. Z. Gao and B. Fultz, Nanostructured Materials **2**, 231 (1993).

26. W. Hume-Rothery and G. V. Raynor, The Structure of Metals and Alloys (Institute of Metals, London, 1962).

27. A. Cottrell, Introduction to the Theory of Metals (Institute of Metals, London, 1988).

28. K. A. Geschneider, Jr., in Theory of Alloy Phase Formation, L. H. Bennett, ed. (TMS, Warrendale, 1980) p. 1.

29. L. S. Darken and R. W. Gurry, Physical Chemistry of Metals (McGraw-Hill, New York, 1953) p. 74.

30. A. Laggoun, A. Hauet, and J. Teillet, Hyperfine Interact. **54**, 825 (1990).

31. A. Hauet, A. Laggoun, and J. Teillet, Mater. Sci. Eng. A **148**, 123 (1991).

32. C. L. Chien, G. Xiao, and K. M. Unruh, Phys. Rev. B **32**, 5582 (1985).

33. G. Xiao and C. L. Chien, Hyperfine Interact. **27**, 377 (1986).

34. T. B. Massalski, Binary Alloy Phase Diagrams (ASM, Metals Park, Ohio, 1986).

35. S.Nasu, S. Imaoka, S. Morimoto, H. Tanimoto, B. Huang, T. Tanaka, J. Kuyama, K. N. Ishihara, and P. H. Shingu, Materials Science Forum **88-90**, 569 (1992).

36. V. K. Singh, M. Singh and S. Bhan, Phys. Stat. Sol. **74**, K115 (1982).

37. M. Asanama, J. Phy. Soc. Japan **17**, 300 (1962).

38. H. M. Rietveld, Acta Cryst. **20**, 508 (1966).

39. Brent Fultz, Chapter 1 in Mössbauer Spectroscopy Applied to Magnetism and Materials Science Vol. I, G. J. Long and Fernande Grandjean, eds., (Plenum Press, New York, 1993) p. 1-31.

40. B. Fultz, Z-Q. Gao, H. H. Hamdeh, and S. A. Oliver, Phys. Rev. B **49**, 6312 (1994).

41. H. H. Hamdeh, S. A. Oliver, B. Fultz and Z. Q. Gao, J. Appl. Phys. **74**, 5117 (1993).

42. Z.Q. Gao, Ph.D. Dissertation, Materials Science, California Institute of Technology, May 18, 1994.

43. F. S. Galasso, Structure and Properties of Inorganic Solids (Pergamon Press, Oxford, England, 1970) p. 8-11.

44. Sargent-Welch Scientific Company, Skokie, 1980 compilation.

Chapter 8. Summary with Perspective

8.1 Driven Alloys

The model of driven alloys proposed by Martin was implemented in our Monte Carlo simulations and theoretical study of disordering –> ordering transformations on square and bcc driven alloys. Though it is an overly simplified physical model of real alloys subject to continuous external driving, it does catch the essential point — the randomness of some atom movements in these alloys. The results from the simulations that only the disordered state can exist if the external driving is strong enough is consistent with experimental observations that almost all alloys are disordered (or amorphous) after ball milling for long times. The results from the simulations that ballistic atom movements cause shifts of phase boundaries in a different way from the shifts caused by temperature are also consistent with our experimental results on two phase coexistence in ball milled Fe-Ni. Both these phenomenon (effects of external driving on critical temperatures and on phase boundaries) were argued to depend on how the enthalpy in the alloy was allowed to increase, given the kinetic mechanisms for atom movements.

8.1.1 Critical Temperature of Ordering Transformations in Driven Alloys

The critical temperature of disordering –> ordering transformations on driven square lattices decreased with ballistic atom movements by the factor of (1 – 1.58 f) for modest f (≤ 0.36). The critical temperature decreased much faster for larger f, and reached 0 above a critical value of f = 0.43. The reasons for the decrease of critical temperature with ballistic jumps were two-fold: (1) the randomness of the ballistic jumps, which are a fraction f of total number of atom jumps, dilute the enthalpy driving force toward ordering

by a factor of (1 – f); (2) the mobility coefficient for the normal thermal atom movements becomes small at low temperatures owing to the high degree of correlation of vacancy diffusion, making thermal atom movements less and less efficient in competing with ballistic atom movements at lower and lower temperatures.

Although my study on critical temperatures of ordering (and spinodal decomposition) was carried out only on square lattices with 1nn pair interactions, I believe that the phenomenon of decreased critical temperature with ballistic atom movements in driven alloys is a general phenomenon. It should be found in ordering transformations of driven alloys on all lattices and with longer-range atomic interactions. A few simulations on bcc and fcc lattices confirmed this, so I approximated the low temperature phase boundaries between disordered A2 and the ordered phases (B2, B32, umx) in driven bcc alloys as in Fig. 4.15b.

Although I believe that the critical temperature will be decreased in driven alloys in general, one cannot know quantitatively how the critical temperature will decrease with ballistic atom movements without a systematic study. From Sections 3.2 and 3.4, there exists no simple general relationship between the dynamical critical temperature and f. The ballistic atom movements are a kinetic process, not a thermodynamic one, so the effects of ballistic atom movements on a critical temperature depend on the mechanism for atom movements and not just f.

8.1.2 Transient Ordering and Low Temperature Phase Diagrams of Driven Alloys

The Monte Carlo study on ordering of driven bcc alloys showed the universality of transient ordering in thermal and driven bcc alloys. In many cases, a phase or state that is not the final equilibrium one appears transiently during the disorder –> order

transformations, but vanishes after long times. The transient ordering was found to be strongest for alloys closest to phase boundaries, probably because of a weaker preference of the final stable phase over the transient phase. The difference in time scale or spatial scale for the formation of a phase also plays a role in determining the extent to which a transient state will develop, and how long it will persist, but this was found not to be the decisive factor (Section 4.2.3). In particular, in Fig. 4.13 we see that the slowly-forming unmixed state can appear transiently (albeit weakly) during the formation of the quickly-forming equilibrium B2 phase.

The relative stabilities of competing phases were affected very strongly by the ballistic atom movements in driven bcc alloys. The stability of the B32 phase was enhanced by ballistic atom movements with respect to both the B2 phase and the unmixed state, while the stability of the B2 phase remained about the same as that of the unmixed state. These changes were attributed to the different response of the different phases to the ballistic atom movements. More specifically, fewer defects and smaller internal energy increase were sustained in the B32 phase than in either the B2 phase or the unmixed state. The accumulation and annihilation of defects is a process controlled by the kinetics of atom movements, which differs for the different phases. The change in relative stabilities caused drastic alterations of transient phase formation and of the steady state phase diagrams. When the relative stability was switched between a pair of phases, the transient state was also switched. Even more dramatically, when two phases had similar stabilities in the presence of the ballistic atom movements, both phases could coexist with each other, and a two-phase coexistence was found in the steady state in the presence of ballistic atom movements.

Although this thesis research focused on bcc alloys of AB stoichiometry, I observed similar phenomena in bcc alloys of other stoichiometries as well. My earliest work on transient ordering of driven alloys was done on driven bcc alloys of AB_3

stoichiometry. With positive 1nn and 2nn pair interaction potentials (V_1 and V_2), these bcc alloys have the DO_3 ordered structure in thermodynamic equilibrium. However, strong transient B32 ordering was observed during disorder –> DO_3 order transformations. The transient B32 order in the thermodynamic case (without ballistic atom movements) was found to be strongly stabilized by the ballistic atom movements of driven alloys. I believe that similar phenomena can also exist in fcc alloys. Due to the complexity of defect generation and annihilation in driven alloys, however, the changes of transient ordering and relative stabilities induced by ballistic atom movements can not be known in detail until a systematic study has been performed . Such a study can also provide useful information on diffusion in various ordered bcc and fcc phases.

Some experimental evidence of transient ordering has been found previously and in my thesis research. Transient DO_3 ordering was observed during annealing of a disordered nanocrystalline Fe_3Ge alloy prepared by mechanical alloying [Chapter 7]. During disorder –> DO_3 order transformations, a transient state with excess B2 order was observed in a ball-milled nanocrystalline Fe_3Si alloy [Chapter 6], while transient B32 order was observed in a piston-anvil quenched Fe_3Al alloy. More experimental evidence could emerge after further kinetics studies.

The formation of transient states in a thermodynamic alloy and the two-phase coexistence (or stabilization of transient states) in a driven alloy are closely related. I propose that the microstructure inhomogeneity, i.e., the distribution of local environments in a alloy, is the common root cause for both phenomena. To elaborate on this point, let us consider an alloy whose thermodynamic equilibrium state is B2 order and in which B32 order appears transiently in the thermodynamic case and coexists with B2 order in the driven alloy case. The local environments of the alloy have a large distribution, especially at the early stages of ordering transformation when it is highly disordered. Some local regions of the alloy are closer to B32 order while others closer to B2 order. At the early

stages of the transformation, these local regions will most easily evolve to their respective closest structures with only a few atom movements. These will result in rapid reduction of the free energy of the alloy as both the B32 and B2 structures have much lower free energy than the disordered structure. The free energy difference between the B32 and B2 structures is typically much smaller and not as important at these stages. The B32 local regions that are formed earlier will make their adjacent local areas come closer to B32 than B2 and therefore easily transfer to the B32 structure later on. So forms and grows the transient B32 order. In the thermodynamic case, however, the B32 order with the higher free energy will eventually give way to the B2 order with the lower free energy after long times. After the transient B32 order vanishes, the total free energy of the alloy is minimized and the thermodynamic equilibrium state is reached. On the other hand in the driven alloy case, the continuous ballistic atom jumps will counteract the thermodynamic atom jumps, which drive the alloy toward B2 order. At favorable conditions such as small free energy difference between B32 and B2 orders, the external driving can balance the small thermodynamic driving force and sustain those local B32 regions. This will result in the B32/B2 two-phase coexistence. This argument based on the microstructure inhomogeneity of the alloys is consistent with the facts that transient states are stronger when closer to the thermodynamic phase boundaries and the two-phase coexistence exists only near the phase boundaries [Chapter 4].

8.2 Nanocrystalline Materials and Mechanical Alloying

Mechanical alloying is now one of the most commonly used methods to synthesize nanocrystalline materials. The experimental part of this thesis research was to study systematically how the various parameters, such as intensity, temperature, and chemical composition, would affect the end products or the process itself. Although this type of

study is important for scaling up of mechanical alloying process and comparing different ball mills or alloy systems, not much has been done previously.

Our experiments on mechanical alloying of nanocrystalline Fe-Ni alloys of various compositions and at two intensities provided rich results. Although the average grain size or strain did not change with either intensity or composition, the phase boundaries changed strongly with milling intensity. The bcc phase was destablized against the fcc phase at higher milling intensity, and the bcc/fcc two-phase region shifted asymmetrically to the bcc phase region. I proposed that spatial heterogeneities in the defect enthalpy of the bcc and fcc phases were responsible for the bcc/fcc two-phase region, and the shift of phase boundaries with milling intensity. A similar phenomenon was observed in our on-going study of nanocrystalline Fe-Cu alloys.

Mechanical alloying of Fe_3X alloys at various ambient temperatures showed that the average grain size was slightly larger for higher milling temperature, while the strain was lower. These were just the same as expected from temperature alone without milling. The subsequent thermal stability of the as-milled nanocrystalline alloys against grain growth, strain release, or equilibrium phase formation was not affected much by the milling temperature.

There were many previous reports of extended solid solubility in mechanically alloyed nanocrystalline alloys, and our study on Fe_3X in Chapter 7 was planned as a systematic study of this subject. The phases of as-milled alloys changed with increasing metallic radii difference between Fe and the solutes, from bcc solid solutions for Ge, Si, Al, and Zn, to B2 order for Sn, to two-phase coexistence of As, Sb, and In. The 25% solubility of mechanically alloyed nanocrystalline alloys could be explained by the Hume-Rothery rules for solid solubility.

The systematic approach taken in these experiments should be useful for other related studies of broader scope. Here I just illustrate one example. Most materials prepared by mechanical alloying are either disordered nanocrystalline solid solutions or amorphous materials. A systematic study of milling intensity, temperature, and composition (I, T, c) on glass-forming alloy systems such as Zr-Al and Ti-Cu should be useful for mapping out the phase regions and boundaries between nanocrystalline and amorphous microstructures of the as-milled products. It would be interesting to see how the change of one or more process parameters leads to the change from one microstructure to the other. Especially if nanocrystalline materials with only 2-3 nm crystal size could be obtained, a study on them can provide insights on how microstructures change from amorphous to nanocrystalline.